

GROWTH OF BaZrS₃ CHALCOGENIDE PEROVSKITE THIN FILMS WITHOUT POST-ANNEALING

 T.M. Razykov^{a,b},  K.M. Kuchkarov^{a,b},  R.T. Yuldoshov^{a,b*},  M.P. Pirimmatov^a,
 R.R. Khurramov^a,  D.Z. Isakov^a, M.A. Makhmudov^{a,b},  S.A. Muzafarova^b,  A. Matmuraov^a

^aPhysical-Technical Institute, Chingiz Aytmatov Street 2B, Tashkent 100084, Uzbekistan

^bInstitute of Semiconductors Physics and Microelectronics, Yangi Olmazor Street 20, Tashkent 100057, Uzbekistan

*Corresponding Author, E-mail: ruhiddin@yahoo.com

Received April 24, 2025; revised August 8, 2025; accepted August 21, 2025

Tandem solar cells based on hybrid organic–inorganic metal halide perovskites have achieved power conversion efficiencies of up to 28%. However, issues related to long-term stability and lead (Pb) toxicity have prompted the search for earth-abundant, chemically stable, and non-toxic alternatives. In this work, we report the first vacuum evaporation synthesis of BaZrS₃ (barium zirconium sulfide) thin films at a substrate temperature of 550 °C. The resulting films exhibit near-stoichiometric Ba:Zr ratios and strong light absorption, with absorption coefficients exceeding 10⁵ cm⁻¹ near 1.9 eV. Under controlled conditions, a baseline oxygen content of 4–6% was consistently observed. The absence of an additional sulfurization step markedly increased the resistance of the thin film and suppressed the dark current by approximately three orders of magnitude, indicating a substantial reduction in carrier density likely resulting from a decreased concentration of sulfur vacancies. These findings highlight the potential of BaZrS₃ as a stable, lead-free absorber for next-generation photovoltaics.

Keywords: BaZrS₃; Chalcogenide perovskites; Energy-dispersive X-ray spectroscopy; Optical bandgap; Photo-response

PACS: 73.61. Le

INTRODUCTION

Chalcogenide perovskites have recently gained significant research interest as promising lead-free, inorganic perovskite semiconductors. Compared to hybrid halide perovskites like CH₃NH₃PbI₃, chalcogenide perovskites exhibit significantly improved structural stability. Most conventional semiconductors are covalent materials characterized by four-fold coordination of both cations and anions. However, in the past decade, organic-inorganic halide perovskites have emerged as competitive alternatives for photovoltaic applications, challenging traditional semiconductors in unprecedented ways. These perovskites are ionic materials with higher coordination, which enhances the Coulomb attraction between cations and anions. Their strong ionicity is believed to reduce the formation of deep-level anti-site defects that contribute to non-radiative carrier recombination.

Unlike conventional semiconductors, halide perovskites exhibit unusually low carrier concentrations (~10¹³/cm³) and extremely long carrier lifetimes (on the order of 1 μs) [1]. The power conversion efficiency (PCE) of solar cells based on halide perovskites has seen a dramatic increase, from an initial 3.8% in 2009 to over 25% in 2019 [2]. Perovskites refer to a class of crystalline compounds with the general formula ABX₃, where the B-site cation has six nearest-neighbor anions (X), and the A-site cation occupies a cavity formed by eight corner-sharing BX₆ octahedra (Figure 1).

The most extensively studied perovskites are complex metal oxides, where X is oxygen. These oxides are technologically significant due to their multifunctionality and tunable properties. Conventional semiconductors and oxide/halide perovskites represent two extremes in the spectrum of covalency and ionicity. Covalent bonding is directional, making electronic and optical properties sensitive to bond distortions, whereas ionic bonding is associated with strong electron correlation due to reduced dielectric screening. Achieving a balance between ionicity and covalency opens pathways to discovering novel semiconductors with enhanced properties. Despite their potential, only limited efforts have been devoted to developing materials that bridge the gap between these bonding characteristics. Recently, chalcogenide perovskites have emerged as a novel class of semiconductors, where sulfur (S) or selenium (Se) replaces oxygen as the anion. Compared to oxide perovskites, chalcogenide perovskites exhibit reduced band gaps, making them well-suited for visible and near-infrared (NIR) light applications. Among these, BaZrS₃ (barium zirconium sulfide) has attracted attention due to its promising optoelectronic properties, initially predicted through theoretical studies. These properties include band gap values suitable for photovoltaics, an exceptionally high absorption coefficient, tolerance to deep defects, strong dielectric screening, favorable phonon characteristics, and isotropic electron mobility for efficient charge transport. [3–11]

Additionally, BaZrS₃ is composed of earth-abundant and non-toxic elements [12, 13]. Although BaZrS₃ and related chalcogenide perovskites were synthesized over half a century ago, they have received minimal attention until recently. After extensive theoretical screening, several ABX₃ chalcogenide materials have been identified as potential candidates

Cite as: T.M. Razykov, K.M. Kuchkarov, R.T. Yuldoshov, M.P. Pirimmatov, R.R. Khurramov, D.Z. Isakov, M.A. Makhmudov, S.A. Muzafarova, A. Matmuraov, East Eur. J. Phys. 3, 413 (2025), <https://doi.org/10.26565/2312-4334-2025-3-43>

© T.M. Razykov, K.M. Kuchkarov, R.T. Yuldoshov, M.P. Pirimmatov, R.R. Khurramov, D.Z. Isakov, M.A. Makhmudov, S.A. Muzafarova, A. Matmuraov, 2025; CC BY 4.0 license

for photovoltaic applications. These materials exhibit strong light absorption and direct bandgap optical transitions, making them very promising for high-performance optoelectronic devices. Notably, BaZrS₃ was confirmed to have a distorted perovskite structure with a band gap of approximately 1.7 eV and strong light absorption, aligning well with theoretical predictions [14]. This material has demonstrated exceptional stability against pressure, moisture, and oxidation, with minimal degradation even four years post-synthesis. However, due to the current lack of high-quality thin films, many fundamental properties of chalcogenide perovskites remain unexplored, posing a challenge to their broader implementation in optoelectronics.

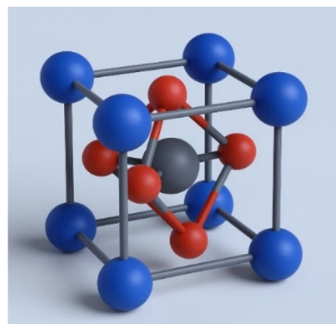


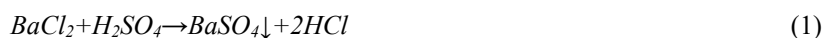
Figure 1. Crystal structures of BaZrS₃. exhibit distorted perovskite structures.

Blue spheres: A-site cations (e.g., Ba²⁺ or Ca²⁺), positioned at the corners. Gray sphere: B-site cation (e.g., Ti⁴⁺, Zr⁴⁺), in the center. Red spheres: anions (O, S²⁻), at the face centers

EXPERIMENTAL PART

BaCl₂ (Barium chloride) (20.800 g, 100 mmol) was first dispersed in 200 mL of deionized water. Subsequently, 5.0 N H₂SO₄ (Sulfuric acid) (33.3 mL, 100 mmol) was slowly added to the dispersion under vigorous stirring while maintaining the reaction mixture in an ice bath [15].

The reaction between BaCl₂, H₂SO₄, and water (H₂O) leads to the formation of barium sulfate (BaSO₄) and hydrochloric acid (HCl):



BaSO₄ is insoluble in water and precipitates out as a white solid. HCl (Hydrochloric acid) remains in solution. This is a double displacement reaction (precipitation reaction), where the sulfate ion (SO₄²⁻) from sulfuric acid displaces the chloride ions from barium chloride, forming the insoluble BaSO₄ precipitate. Since H₂O is already present in the reaction medium (if aqueous solutions are used), it does not directly participate in the reaction but serves as medium for the ions to react.

The reaction was terminated after 5 hours, and BaSO₄ was recovered via centrifugation. The obtained product was subsequently washed with deionized water three times before being dried in an oven at 110 °C overnight. BaS was synthesized by reducing BaSO₄, using a 25% hydrogen-balanced argon atmosphere by chemical molecular beam deposition (CMBD) system at 1000 °C for 1 hour [16]. The resulting BaS product appeared as a white powder, which was immediately transferred into a nitrogen-filled glovebox and finely ground into a homogeneous powder.

A mixture of BaS (7.407 g, 43.732 mmol) and elemental sulfur (S) (2.804 g, 87.46 mmol) was prepared by grinding with an agate mortar and pestle inside the glovebox. The homogenized mixture was then placed into a pre-dried borosilicate glass tube, which was subsequently flame-sealed under vacuum to form an ampule. The ampule was heated in a muffle furnace from room temperature to 400 °C and maintained at this temperature for 12 hours. The furnace was then turned off, allowing the sample to cool to room temperature gradually. BaS₃ and ZrS₂ powders were placed in two separate molybdenum boats under a high-vacuum environment of 10⁻⁵-10⁻⁶ mmHg. The reaction was conducted for 1,5 hours at a substrate temperature of 550 °C. (Figure 2).



Figure 2. Photographic image of the BaS₃ and ZrS₂ in vacuum chamber

The surface morphology of the thin films was characterized using a JSM-IT510 (JEOL) scanning electron microscope (SEM) operating in secondary electron mode at an accelerating voltage of 20 kV. Elemental composition was analyzed via Energy Dispersive X-ray (EDX) spectroscopy using an Aztec Energy Advanced Spectrometer, which offers an energy resolution of 127 eV and a detection sensitivity of 0.5 wt.%. Optical absorption spectra were recorded at room temperature using a Shimadzu UV-1900i UV-Vis-NIR spectrophotometer. Current-voltage (I-V) characteristics were recorded using a Keithley 2460 source meter under AM1.5G simulated sunlight (1600 W xenon lamp, Model No. UHE-NL-250, Sciencetech, Canada).

RESULTS AND DISCUSSIONS

Scanning electron microscopy was employed to examine the morphological characteristics of the BaZrS₃ thin films, while energy-dispersive X-ray spectroscopy was used to verify their elemental composition. The analysis revealed a clear correlation between substrate temperature and the microstructural evolution of the films. Morphology of samples presented in Figure 3 indicates that higher substrate temperatures enhance grain growth and favor the formation of rod-shaped BaZrS₃ grains aligned parallel to the substrate surface. Notably, the sample fabricated at 550 °C exhibited grains exceeding 0.5-1 µm in size, with a uniform distribution across the substrate, indicative of a homogeneous and well-controlled growth process.

The observed increase in grain size with temperature is attributed to enhanced atomic diffusion and coalescence phenomena during the film deposition process, which collectively contribute to improved crystallinity and preferential grain orientation. Although BaZrS₃ films have shown continuity with thicknesses ranging from 350 nm. The results of EDX analysis, as shown in Figure 4 approximately 4% oxygen was detected in the bulk of BaZrS₃ film, with a nearly stoichiometric Ba:Zr composition. Despite efforts to minimize the duration of air exposure prior to measurement, the precursors consistently retained a baseline oxygen content of at least 4-5%, a value that remained unchanged even after several weeks of storage in this environment.

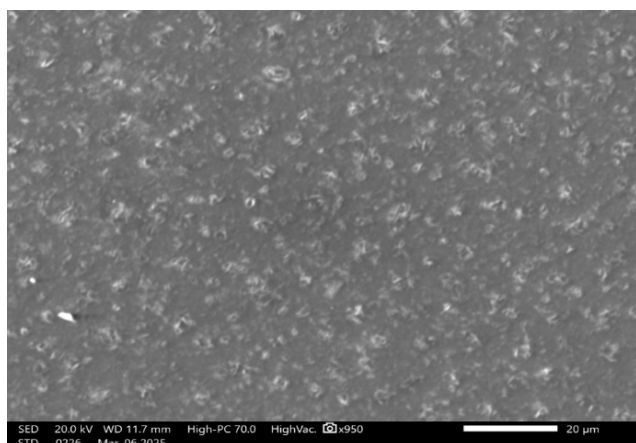


Figure 3. SEM top views of the BaZrS₃ thin films obtained 550 °C substrate temperature

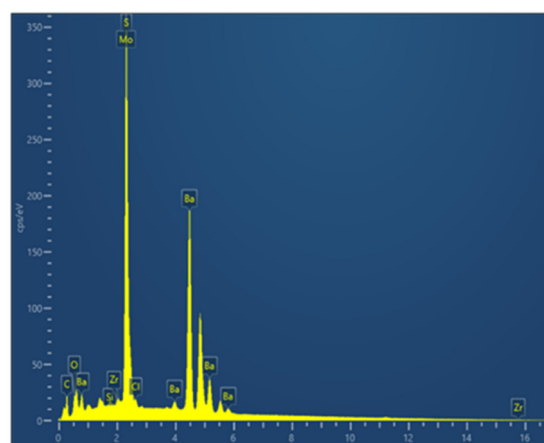


Figure 4. Typical EDX spectra of synthesized BaZrS₃ thin films

In various experimental trials, an increase in oxygen concentration was only observed after annealing the samples, with the oxygen content rising by up to 10%. (These conclusions will be given in detail in subsequent works). This reaction appears to be linked to the presence of excess sulfur in the samples. The precursors were slightly sulfur-rich, and oxidation was notably enhanced when excess sulfur vapor was introduced during the annealing process. During the thermal process, BaZrS₃ crystallizes from the precursor and some of the sulfur-rich material is reduced by sulfur gas evaporation (S(g)), leading to removal of sulfur without oxidation. However, it has been suggested that the stresses generated within the films during this process, which predispose them to oxidation, may contribute to the formation of holes.

The band gaps of BaZrS₃ with distorted perovskite structure have been theoretically calculated to be around 1.7-1.85 eV and have also been experimentally verified to be within the same range [16].

Figure 5 presents the UV-Vis absorption spectrum of the BaZrS₃ thin film deposited at a substrate temperature of 550 °C, plotted as a function of photon energy. The film's geometry enabled the calculation of the absorption coefficient (α). A significant increase in α is observed around 1.9 eV, surpassing 10^5 cm^{-1} , indicating the strong light absorption capability of BaZrS₃. Assuming a direct allowed electronic transition, the optical band gap energy (E_g) was determined using the Tauc relation:

$$(ah\nu)^2 = A(h\nu - E_g) \quad (2)$$

where $h\nu$ is the photon energy, A is a material-dependent constant, and α is the absorption coefficient. The band gap energy was estimated by extrapolating the linear region of the $(ah\nu)^2$ versus $h\nu$ plot to the photon energy axis. Based on this method, the BaZrS₃ thin film exhibited a direct optical band gap of approximately 1.9 eV

The I-V curves under both dark and illuminated conditions are presented in Figure 6. However, the sulfurization process was not performed to enhance the photo-response. This decision was made to avoid potential degradation from prolonged high-temperature exposure, which could induce sulfur vacancies and increase carrier concentration. Indicating a substantial decrease in carrier density due to sulfur vacancies, As shown in Figure 6, the absence of sulfurization significantly increases the junction resistance and reduces the dark current by approximately three orders of magnitude. Nevertheless, the photo-response is notably enhanced. These findings highlight the importance of suppressing dark current by further reducing carrier concentration to achieve optimal photodetector performance. To address sulfur vacancies, we propose high-pressure sulfurization as a strategy. Prolonged high-temperature treatment induces the formation of sulfur vacancies, resulting in an increased carrier concentration

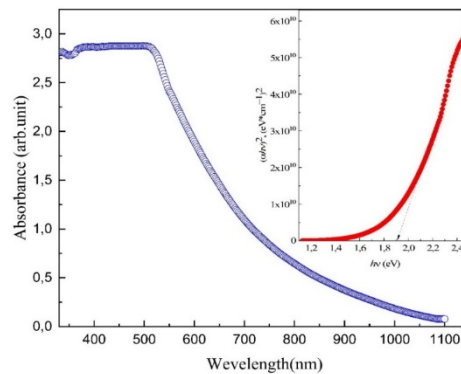


Figure 5. Absorbance for BaZrS₃ thin films and Tauc plots BaZrS₃ thin films

Notably, no additional sulfurization was conducted to further enhance the photo-response. This approach is justified by the high sulfur content in the precursor, as well as the lower substrate temperature employed compared to conventional chalcogenide perovskite layer fabrication methods, which significantly reduce sulfur re-evaporation from the substrate surface. To further enhance performance, we propose that methods such as p-type doping or sulfurization under high-pressure conditions could be utilized. These methods can help passivate sulfur vacancy states, thereby reducing their negative impact on device performance. As shown in figure 6, eliminating the sulfurization without results in a significant increase in the sample resistivity, accompanied by a substantial reduction in the dark current by three orders of magnitude. This observation suggests a marked decrease in the carrier density, which is likely attributed to the reduction in sulfur vacancies. Therefore, these results imply that to achieve improved photodetector performance, it is essential to suppress dark current by effectively reducing the carrier concentration.

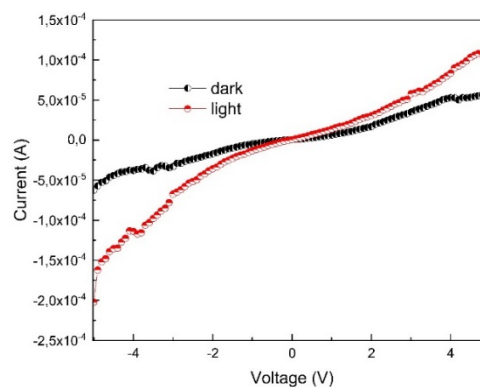


Figure 6. The I-V curves in the dark and under illumination

CONCLUSION

The successful development of a BaS₃ extraction technique, combined with co-deposition of BaS₃ and ZrS₂ powders under high vacuum, enabled controlled synthesis conditions. As a result, BaZrS₃ thin films with an optical bandgap of 1.9 eV and absorption coefficients exceeding 10⁵ cm⁻¹ was successfully fabricated. The elimination of an additional sulfurization step led to a significant increase in film resistivity and a ~1000-fold reduction in dark current. This behavior indicates a notable decrease in free carrier concentration, which is likely due to the suppression of sulfur vacancies - common donor-like defects in chalcogenide semiconductors. These findings highlight the critical role of defect management in optimizing the optoelectronic properties of BaZrS₃-based devices.

Acknowledgements

This work was supported by the Basic Research Program of the Academy of Sciences of the Republic of Uzbekistan, Ministry of innovative development of the Republic of Uzbekistan (Grant № FL-8824063282).

ORCID

✉Takhirdjon. M. Razykov, <https://orcid.org/0000-0001-9738-3308>; ✉Kudrat M. Kuchkarov, <https://orcid.org/0000-0002-2238-7205>; ✉Ruhiddin T. Yuldoshov, <https://orcid.org/0000-0002-7886-1607>; ✉Muhammad M. Pirimmatov, <https://orcid.org/0009-0000-4829-7817>; ✉Ramozan R. Khurramov, <https://orcid.org/0009-0008-1038-0138>; ✉Diyorbek Z. Isakov, <https://orcid.org/0000-0003-4314-5683>; ✉Sultanpasha A. Muzafarova, <https://orcid.org/0000-0001-5491-7699>; ✉Aydos Matmuratov, <https://orcid.org/0009-0005-6121-6424>

REFERENCES

- [1] D.W. de Quilletes, S.M. Vorpahl, S.D. Stranks, H. Nagaoka, G.E. Eperon, M.E. Ziffer, H.J. Snaith, and D.S. Ginger, "Impact of microstructure on local carrier lifetime in perovskite solar cells," *Science*, **348**, 683–686 (2015). <https://doi.org/10.1126/science.aaa5333>
- [2] S. Suragtkhuu, S. Sunderiya, P. Myagmarsereejid, S. Purevdorj, A.S.R. Bati, B. Bold, *et al.*, "Graphene-Like Monoelemental 2D Materials for Perovskite Solar Cells," *Adv. Energy Mater.* **13**, 2204074 (2023). <https://doi.org/10.1002/aenm.202204074>
- [3] A. Swarnkar, W.J. Mir, R. Chakraborty, M. Jagadeeswararao, T. Sheikh, A. Nag, "Are Chalcogenide Perovskites an Emerging Class of Semiconductors for Optoelectronic Properties and Solar Cell?" *Chem. Mater.* **31**, 565–575 (2019). <https://doi.org/10.1021/acs.chemmater.8b04178>
- [4] K.V. Sopiha, C. Comparotto, J.A. Márquez, and J.J.S. Scragg, "Chalcogenide Perovskites: Tantalizing Prospects, Challenging Materials," *Advanced Optical Materials*, **10**, 2101704 (2022). <https://doi.org/10.1002/adom.202101704>
- [5] M. Buffiere, D.S. Dhawale, and F. El-Mellouhi, "Chalcogenide Materials and Derivatives for Photovoltaic Applications," *Energy Technology*, **7**, 1900819 (2019). <https://doi.org/10.1002/ente.201900819>
- [6] C. Comparotto, P. Ström, O. Donzel-Gargand, T. Kubart, and J.J.S. Scragg, "Synthesis of BaZrS₃ Perovskite Thin Films at a Moderate Temperature on Conductive Substrates," *ACS Appl. Energy Mater.* **5**(5), 6335–6343 (2022). <https://doi.org/10.1021/acsaem.2c00704>
- [7] C. Wang, R. Nie, Y. Dai, H. Tai, B. Zhu, L. Zhao, Y. Wu, *et al.*, "Enhancing the inherent stability of perovskite solar cells through chalcogenide-halide combinations," *Energy Environ. Sci.* **17**, 1368–1386 (2024). <https://doi.org/10.1039/D3EE03612J>
- [8] R. Jaramillo, and J. Ravichandran, "In praise and in search of highly- polarizable semiconductors: Technological promise and discovery strategism," *APL Materials*, **7**, 100902 (2019). <https://doi.org/10.1063/1.5124795>
- [9] Y. Nishigaki, T. Nagai, M. Nishiwaki, T. Aizawa, M. Kozawa, K. Hanzawa, Y. Kato, *et al.*, "Extraordinary Strong Band-Edge Absorption in Distorted Chalcogenide Perovskites," *Solar RRL*, **4**, 1900555 (2020). <https://doi.org/10.1002/solr.201900555>
- [10] X. Wu, W. Gao, J. Chai, C. Ming, M. Chen, H. Zeng, P. Zhang, *et al.*, "Defect tolerance in chalcogenide perovskite photovoltaic material BaZrS₃," *Science China Materials*, **64**, 2976–2986 (2021). <https://doi.org/10.1007/s40843-021-1683-0>
- [11] W. Meng, B. Saparov, F. Hong, J. Wang, D.B. Mitzi, and Y. Yan, "Alloying and Defect Control within Chalcogenide Perovskites for Optimized Photovoltaic Application," *Chem. Mater.* **28**, 821–829 (2016). <https://doi.org/10.1021/acs.chemmater.5b04213>
- [12] M. Ishii, and M. Saeki, "Raman and Infrared Spectra of BaTiS₃ and BaNbS₃," *Phys. Stat. Sol. (b)*, **170**, K49 (1992). <https://doi.org/10.1002/pssb.2221700149>
- [13] M. Ishii, M. Saeki, and M. Sekita, "Vibrational spectra of barium-zirconium sulfides," *Mater. Res. Bull.* **28**, 493–500 (1993). [https://doi.org/10.1016/0025-5408\(93\)90132-W](https://doi.org/10.1016/0025-5408(93)90132-W)
- [14] S. Perera, H. Hui, C. Zhao, H. Xue, F. Sun, C. Deng, N. Gross, *et al.*, "Chalcogenide perovskites – an emerging class of ionic semiconductors," *Nano Energy*, **22**, 129–135 (2016). <https://doi.org/10.1016/j.nanoen.2016.02.020>
- [15] R. Yang, J. Nelson, C. Fai, H.A. Yetkin, C. Werner, M. Tervil, A.D. Jess, *et al.*, "A Low-Temperature Growth Mechanism for Chalcogenide Perovskites," *Chemistry of Materials*, **35**(12), 4743–4750 (2023). <https://doi.org/10.1021/acs.chemmater.3c00494>
- [16] T.M. Razykov, K.M. Kuchkarov, B.A. Ergashev, L. Schmidt-Mende, T. Mayer, M. Tivanov, M. Makhmudov, *et al.*, "Growth and characterization of Sb₂(S_xSe_{1-x})₃ thin films prepared by chemical-molecular beam deposition for solar cell applications," *Thin Solid Films*, **807**, 140554 (2024). <https://doi.org/10.1016/j.tsf.2024.140554>
- [17] S. Agarwal, K.C. Vincent, and R. Agrawal, "From synthesis to application: a review of BaZrS₃chalcogenide perovskites," *Nanoscale*, **17**, 4250–4300 (2025). <https://doi.org/10.1039/D4NR03880K>

ВИРОЩУВАННЯ ТОНКИХ ПЛІВОК ХАЛЬКОГЕНІД ПЕРОВСКІТУ BaZrS₃ БЕЗ НАСТУПНОГО ВІДПАЛЮВАННЯ

Т.М. Разиков^{a,b}, К.М. Кучкаров^{a,b}, Р.Т. Юлдошов^{a,b}, М.П. Пірімматов^a, Р.Р. Хуррамов^a, Д.З. Ісаков^a,
М.А. Махмудов^{a,b}, С.А. Музафарова^b, А. Матмуратов^a

¹ Фізико-технічний інститут, вул. Чингіза Айтматова 2Б, Ташкент 100084, Узбекистан

² Інститут фізики напівпровідників і мікроелектроніки, вул. Янгі Олмазор, 20, Ташкент 100057, Узбекистан

Тандемні сонячні батареї на основі гібридних органіко-неорганічних галогенідів металів перовскітів досягли ефективності перетворення електроенергії до 28%.) Однак проблеми, пов'язані з довгостроковою стабільністю та токсичністю свинцю (Pb), спонукали до пошуку поширених у землі, хімічно стабільних і нетоксичних альтернатив. У цій роботі ми повідомляємо про перший синтез тонких плівок BaZrS₃ з (сульфіду барію і цирконію) методом вакуумного випаровування при температурі підкладки 550 °С. Отримані плівки демонструють майже стехіометричне співвідношення Ba:Zr і сильне поглинання світла з коефіцієнтами поглинання, що перевищують 10⁵ см⁻¹ поблизу 1,9 еВ. (У) контрольованих умовах стабільно спостерігався вихідний вміст кисню 4–6%. Відсутність додаткової стадії сульфурвання помітно збільшила опір тонкої плівки та придушила темновий струм приблизно на три порядки величини, що вказує на суттєве зменшення щільності носія, ймовірно, внаслідок зниження концентрації вакансій сірки. Ці висновки підкреслюють потенціал BaZrS₃ як стабільного безсвинцевого поглиначка для фотоелектричних пристроїв нового покоління.

Ключові слова: BaZrS₃; халькогенідні перовскіти; енергодисперсійна рентгенівська спектроскопія; оптична заборонена зона; фотовідгук

TUNABLE MATCHING LAYER METHOD FOR IDENTIFYING IMPURITIES IN LIQUIDS AT MICROWAVES

 Mykola M. Biletskii^a,  Sergey Yu. Polevoy^{a*},  Sergiy I. Tarapov^{a,b,c}

^a*O.Ya. Usikov Institute for Radiophysics and Electronics of NASU, Kharkiv, 61085, Ukraine*

^b*V.N. Karazin Kharkiv National University, Kharkiv, 61022, Ukraine*

^c*Gebze Technical University, Gebze, Kocaeli, 41400, Turkey*

*Corresponding Author E-mail: polevoy@ire.kharkov.ua

Received May 31, 2025; revised August 5, 2025; accepted August 10, 2025

The work aims to develop a method for contactless identification of impurity concentration in liquids of a given type in the microwave frequencies. The work presents the theoretical analysis of the novel method for identifying impurities in liquids at microwave frequencies, based on the use of a tunable matching layer (a dielectric layer of variable thickness). To find the reflection coefficient of an electromagnetic wave from the layered structure, a technique consisting of determining the electromagnetic fields in each region and imposing continuity conditions for the field components at each boundary of the layer was used. Numerical estimations of the method's sensitivity are provided using the example of determining ethanol impurity concentrations in water. The results are compared with experimental data reported in other publications. It has been shown that this method has a high sensitivity to impurity concentration.

Keywords: Matching layer; Impurity concentration in liquids; Contactless; Reflection coefficient; Microwave frequencies

PACS: 41.20.Jb

INTRODUCTION

High-frequency methods for monitoring and characterizing the dielectric properties of liquids remain an active area of research [1-6]. Among the most advanced approaches is the method presented in [1], which enables non-contact, remote measurement of the real and imaginary parts of a liquid's permittivity in the microwave frequency range. The authors of [1] employed a specially designed cylindrical dielectric resonator as the measurement cell.

We subsequently developed the method proposed in [1] in works [7–10]. In our studies, instead of the traditional dielectric resonator (which operates in a narrow frequency range), a so-called one-dimensional photonic crystal [7] was used. This made it possible to identify liquids over a relatively wide frequency range. The use of a one-dimensional photonic crystal with a defect in a microstrip implementation improved the accuracy of liquid identification and enhanced the technical capabilities of the method described in [1]. It should be noted, however, that the method described in [7–10] exhibits several limitations. Despite being well-suited for liquid identification, it is poorly suited for high-precision tuning of sensitivity to specific types of liquids. In the given paper, we propose a method for relatively accurate non-contact measurement of impurity concentrations in specific types of liquids (e.g., aqueous alcohol solutions) in the microwave wavelength range. This approach provides comparatively high accuracy in measuring impurity concentrations in liquids due to the use of a tunable matching layer.

PROBLEM FORMULATION AND RESULTS DISCUSSION

In this work, the reflection coefficient R of the electromagnetic wave from a layered structure (shown in Fig. 1) is calculated.

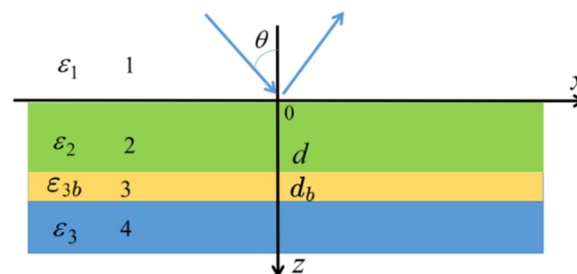


Figure 1. Geometry of the problem: 1 – the free space; 2 – the tunable matching layer; 3 – the wall of the container with the test liquid; 4 – the liquid under test.

It is assumed that the electromagnetic wave is incident from medium (1), with permittivity ϵ_1 , at normal incidence $\theta = 0^\circ$ on the boundary at $z = 0$. The region $0 < z < d$ is occupied by a dielectric layer with permittivity ϵ_2 . This layer

(referred to as the tunable matching layer) (2) is used to control the reflection coefficient of the electromagnetic wave from the whole layered structure by varying its thickness.

The test liquid is assumed to be placed in a flat container. The container wall (3) has a thickness of d_b and the permittivity ϵ_{3b} . The spatial region $z > d + d_b$ is occupied by the test liquid (4) with permittivity ϵ_3 . The second boundary of the flat container is not considered in our model, since its effect on the reflection coefficient is assumed to be negligible.

To determine the reflection coefficient R of the electromagnetic wave from the considered structure, the known standard approach was used. This approach consists of determining the electromagnetic field components in each region and applying the boundary conditions for the continuity of these field components at each interface of the structure. It is assumed that the permittivity of the test liquid is a complex-valued function, accounting for both its dispersive and absorptive properties.

Let us consider the components of the electromagnetic fields in each region of the layered structure.

In the region $z < 0$:

$$H_{y1}(z) = e^{ik_{z1}z} + r \cdot e^{-ik_{z1}z},$$

$$E_{y1}(z) = \frac{ck_{z1}}{\omega\epsilon_1}(e^{ik_{z1}z} - r \cdot e^{-ik_{z1}z}).$$

In the region $0 < z < d$:

$$H_{y2}(z) = H_2^+ e^{ik_{z2}z} + H_2^- e^{-ik_{z2}z},$$

$$E_{y2}(z) = \frac{ck_{z2}}{\omega\epsilon_2}(H_2^+ e^{ik_{z2}z} - H_2^- e^{-ik_{z2}z}).$$

In the region $d < z < d + d_b$:

$$H_{y3b}(z) = H_{3b}^+ e^{ik_{z3b}(z-d)} + H_{3b}^- e^{-ik_{z3b}(z-d)},$$

$$E_{y3b}(z) = \frac{ck_{z3b}}{\omega\epsilon_{3b}}(H_{3b}^+ e^{ik_{z3b}(z-d)} - H_{3b}^- e^{-ik_{z3b}(z-d)}).$$

In the region $z > d + d_b$:

$$H_{y3}(z) = t \cdot e^{ik_{z3}(z-d-d_b)},$$

$$E_{y3}(z) = \frac{ck_{z3}}{\omega\epsilon_3} t \cdot e^{ik_{z3}(z-d-d_b)}.$$

Here, r , t are amplitudes of the reflected and transmitted electromagnetic waves, respectively. The values H_2^+ , H_{3b}^+ represent the amplitudes of the forward-propagating electromagnetic waves, while H_2^- , H_{3b}^- denote the amplitudes of the backward-propagating waves in media with permittivity ϵ_2 and ϵ_{3b} , respectively. The wave numbers are given by $k_{z1,2,3b,3} = \frac{\omega}{c} \sqrt{\epsilon_{1,2,3b,3}}$, where ω is the angular frequency and c is the speed of light in vacuum.

From the continuity conditions of the tangential field components at each interface of the considered structure, we determine the amplitude r of the reflected electromagnetic wave. The reflection coefficient R of the electromagnetic wave at the boundary $z = 0$ is defined as follows:

$$R = |r|^2.$$

The amplitude of the reflected electromagnetic wave r should be determined by the following expression:

$$r = \frac{x_2 p_- \cos(k_{z2}d) - i \cdot s_- \sin(k_{z2}d)}{x_2 p_+ \cos(k_{z2}d) - i \cdot s_+ \sin(k_{z2}d)},$$

where

$$p_{\pm} = x_1 y_{\pm} \pm x_{3b} y_{\pm},$$

$$s_{\pm} = x_1 x_{3b} y_{\pm} \pm x_2^2 y_{\pm},$$

$$y_+ = x_{3b} \cos(k_{z3b}d_b) - i \cdot x_3 \sin(k_{z3b}d_b),$$

$$y_- = x_3 \cos(k_{z3b}d_b) - i \cdot x_{3b} \sin(k_{z3b}d_b),$$

$$x_{z1,2,3b,3} = 1/\sqrt{\epsilon_{1,2,3b,3}}.$$

Let the investigated liquid be contained in a dielectric (plastic) container with thickness $d_b = 0.05$ cm and the permittivity $\epsilon_{3b} = 2.4$. We assume that the thickness d of the tunable matching dielectric layer can vary, and its permittivity is $\epsilon_2 = 5.5$. We also assume $\epsilon_1 = 1.0$.

Let introduce the dimensionless thickness of the tunable matching dielectric layer as $\delta = 2\pi d/\lambda$, where λ is the wavelength of the electromagnetic wave in free space. The value of λ is taken as $\lambda = 3$ cm. Figure 2 shows the dependence of the reflection coefficient $R(\delta)$ for the water, with the real part of its permittivity $\epsilon'_3 = 62.6$ and the imaginary part $\epsilon''_3 = 29.4$ at the chosen wavelength. It can be seen from Fig. 2 that obtained dependence is a periodic function of δ .

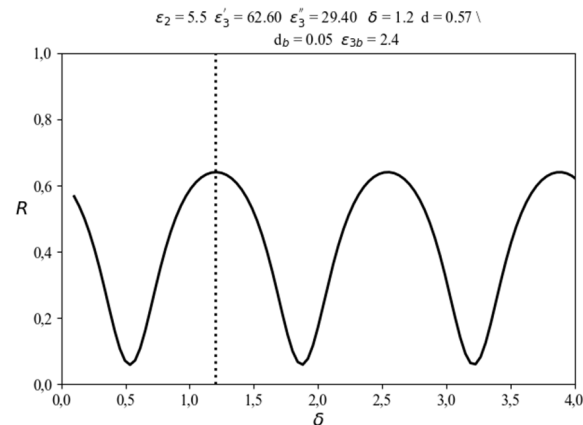


Figure 2. Dependence of reflection coefficient $R(\delta)$ on the dimensionless thickness of the tunable matching layer for pure water

Let's $\delta = 1.2$. This value corresponds to the maximum reflection coefficient R . The chosen value of δ is indicated by a dashed line in Fig. 2. For the selected values of λ and δ , the thickness is $d = 0.57$ cm.

Now, let us consider how the reflection coefficient R changes in the presence of ethanol impurities in water. The results of the performed calculations are presented in Table 1.

Table 1. Reflection coefficient R from the layered structure (Fig. 1) for ethanol-water solutions of varying concentration.

#1	#2	#3	#4
Concentration of ethanol in water, %	Real part of permittivity ϵ'_3 ($\lambda = 3$ cm, experiment [11])	Imaginary part of permittivity ϵ''_3 ($\lambda = 3$ cm, experiment [11])	R ($d = 0.57$ cm)
0	62.5	30.0	0.641
1	61.0	30.8	0.640
5	55.8	32.0	0.634
10	49.5	33.0	0.627
20	37.5	32.2	0.609
40	21.0	24.5	0.560

The first column of Table 1 shows the percentage concentration of ethanol in water. The next two columns list the real and imaginary parts of the permittivity of water containing ethanol impurities. These data are taken from reference [11]. The fourth column of the table presents the calculated values of the reflection coefficient R of the electromagnetic wave from the structure shown in Fig. 1.

From Table 1, it is evident that the presence of ethanol in water significantly affects the reflection coefficient of the electromagnetic wave. As the ethanol concentration in water increases, the reflection coefficient R decreases. This very fact forms the basis of the novel non-contact method we propose for determining impurity concentration (using ethanol as an example) in water.

Let us estimate now the sensitivity of the given method from Table 1 as the minimal measurable increment in ethanol concentration in water for the two cases described below.

In the first case, we consider pure water with low ethanol impurity concentrations ranging from 0% to 5%. It is known that in typical experiments using the standard vector network analyzer N5230A [7–10, 12], a measurement accuracy of the reflection coefficient R for the layered structure on the order of $\Delta R_{\text{exp}} = 0.1\%$ can be easily achieved. With this method, it is experimentally possible to measure such an increment in ethanol concentration that corresponds to a change in R no smaller than the aforementioned accuracy. From Table 1, it follows that R changes by $\Delta R_1 = 1.1\%$ when ethanol concentration varies from 0% to 5%. Thus, for small ethanol concentrations in water, the accuracy of determining its concentration by the new method is approximately $\Delta R_{\text{exp}} / \Delta R_1 \cdot 5\% = 0.45\%$. In the second case, when the ethanol concentration changes from 20% to 40%, the reflection coefficient varies by $\Delta R_2 = 8.75\%$. For this diapason of impurities, the accuracy of determining ethanol concentration in water is approximately $\Delta R_{\text{exp}} / \Delta R_2 \cdot 20\% = 0.23\%$.

For comparison, in reference [12], the accuracy of the method for determining the dielectric permittivity of liquids in a coaxial cell was significantly lower (the errors in determining the dielectric permittivity of water were no better than 5%).

CONCLUSIONS

Thus, in this work:

1. The new remote method for determining impurities concentration in liquids has been developed. The method is based on measuring the reflection coefficient of the electromagnetic wave from a flat plastic container with liquid, using a tunable matching dielectric layer of adjustable thickness.

2. It is demonstrated that, compared to established methods based on permittivity measurements using coaxial line or photonic crystals, the proposed method offers substantially higher sensitivity to impurities. This enhanced sensitivity arises from the implementation of a tunable matching layer with adjustable thickness.

The work is funded by the Project “Microwave express detection of flammable and potentially explosive substances using planar technologies” (Agreement №2.7/25-П on 01.01.2025 between the National Academy of Sciences (NAS) and the O.Ya. Usikov Institute for Radiophysics and Electronics of the NAS of Ukraine).

ORCID

©Sergey Yu. Polevoy, <https://orcid.org/0000-0001-6765-3127>; Mykola M. Biletskii <https://orcid.org/0000-0002-3194-7251>,

©Sergiy I. Tarapov, <https://orcid.org/0000-0002-8958-5003>

REFERENCES

- [1] N. Klein, H.-J. Krause, S. Vitusevich, H. Rongen, A. Kurakin, and O.N. Shaforost, in: *2011 IEEE MTT-S International Microwave Symposium*, (Baltimore, USA, 2011), pp. 1–4. <https://doi.org/10.1109/MWSYM.2011.5972696>
- [2] G. Alsharahi, A. Driouach, and A. Faize, *Procedia Technology*, **22**, 570 (2016). <https://doi.org/10.1016/j.protcy.2016.01.118>
- [3] Y. Jiang, Y. Ju, and L. Yang, *J. Nondestruct. Eval.* **35**(7), (2016). <https://doi.org/10.1007/s10921-015-0322-8>
- [4] S. Dubey, K. Ta, and J.-C. Chiao, in: *2017 IEEE Sensors conference*, (Glasgow, UK, 2017), pp. 1–3, <https://doi.org/10.1109/ICSENS.2017.8234305>.
- [5] D. Zhou, S. Qiu, J. Tan, X. Li, and C. Chen, *Int. J. Patt. Recogn. Artif. Intell.* **33**(02), 1958003 (2019). <https://doi.org/10.1142/S0218001419580035>
- [6] T. Ozturk, *Sci. Rep.* **9**(1), 12571 (2019). <https://doi.org/10.1038/s41598-019-49102-3>
- [7] S.Y. Polevoy, A.S. Vakula, S.V. Nedukh, and S.I. Tarapov, *Telecom. Rad. Eng.* **76**(3), 237 (2017). <https://doi.org/10.1615/TelecomRadEng.v76.i3.40>
- [8] S.Yu. Polevoy, V.A. Michaylichenko, A.S. Vakula, S.V. Nedukh, and S.I. Tarapov, *Telecom. Rad. Eng.* **77**(18), 1639 (2018). <https://doi.org/10.1615/TelecomRadEng.v77.i18.60>
- [9] S. Nedukh, S. Polevoy, S. Tarapov, and A. Vakula, “Identification of liquids in different containers using a microwave planar metamaterial,” *Radiofiz. Elektron.* **22**(4), 69 (2017). <https://doi.org/10.15407/rej2017.04.069>
- [10] S.Y. Polevoy, A.S. Vakula, S.V. Nedukh, and S.I. Tarapov, *URSI Radio Sci. Bull.* **2019**(371), 53 (2019). <https://doi.org/10.23919/ursirsb.2019.9117244>
- [11] X. Bohigas, and J. Tejada, *Food Research International*, **43**(6), 1607 (2010). <https://doi.org/10.1016/j.foodres.2010.04.021>
- [12] K.Yu. Sova, A.S. Vakula, S.Yu. Polevoy, S.I. Tarapov, A.G. Belous, and S.O. Solopan, *Telecom. Rad. Eng.* **79**(18), 1663 (2020). <https://doi.org/10.1615/TelecomRadEng.v79.i18.60>

МЕТОД РЕГУЛЮВАЛЬНОГО УЗГОДЖУВАЛЬНОГО ШАРУ ДЛЯ ІДЕНТИФІКАЦІЇ ДОМІШОК У РІДИНАХ НА МІКРОХВИЛЬОВИХ ЧАСТОТАХ

Микола М. Білецький^a, Сергій Ю. Полевой^a, Сергій І. Тарапов^{a,b,c}

^aІнститут радіофізики та електроніки ім. О.Я. Усикова НАН України, 12, вул. Акад. Проскури, Харків, 61085, Україна

^bХарківський національний університет імені В. Н. Каразіна, майдан Свободи 4, Харків, 61022, Україна

^cТехнічний Університет Гебзе, Гебзе, Коджаелі, 41400, Туреччина

Метою роботи є розробка методу безконтактної ідентифікації концентрації домішок у рідинах заданого типу на мікрохвильових частотах. У роботі представлено теоретичний аналіз нового методу ідентифікації домішок у рідинах на мікрохвильових частотах, заснованого на використанні регульованого узгоджувального шару (діелектричного шару змінної товщини). Для визначення коефіцієнта відбиття електромагнітної хвилі від шаруватої структури була використана методика, яка полягає у визначенні електромагнітних полів у кожній області та накладенні умов безперервності для компонент поля на кожній межі шару. Наведено чисельні оцінки чутливості методу на прикладі визначення концентрації домішок етанолу у воді. Результати порівняно з експериментальними даними в інших публікаціях. Показано, що цей метод має високу чутливість до концентрації домішок.

Ключові слова: узгоджувальний шар; концентрація домішок у рідинах; безконтактний; коефіцієнт відбиття; мікрохвильові частоти

SEMI-EMPIRICAL MODELS OF ELECTRON BEAM CONTROL FOR RADIATION STERILIZATION

 Igor O. Girka,  Valentin T. Lazurik*

V.N. Karazin Kharkiv National University, Kharkiv, Ukraine

*Corresponding Author e-mail: vtlazurik@karazin.ua

Received May 17, 2025; revised July 13, 2025; accepted August 15, 2025

To carry out radiation sterilization, one needs to determine the permissible irradiation modes, which is carried out using computer dosimetry methods. Nowadays, the choice of optimal irradiation modes can be based on the models of the depth-dose curve at different incidence angles of the electron beam on the layer of matter. In the present paper, the distribution of transferred energy in the volume of the target initiated by the normal incidence of a point beam of radiation on the surface of a semi-infinite medium (*Dose-Map* object) is used to develop such models. Semi-empirical models of the *Dose-Map* object are designed based on two assumptions. One is that the target has axial symmetry relative to the direction of the radiation particle incidence on the target. The second is that the dose spatial distribution is uniform or normal (Gaussian distribution) in the cross-sections of the *Dose-Map* object at all depths. For a two-parameter approximation of the *Dose-Map* object, three-dimensional geometric figures are suggested, which surfaces are formed by rotating the plots of power functions around the abscissa axis. Semi-empirical models are developed based on the assumption that the parameters of the *Dose-Map* object in its eigen coordinate system do not change when the beam incidence angle changes. Expressions are obtained for calculating the depth-dose curves from radiation incident on the target at an angle θ in the form of an integral transformation of the depth-dose curve for normal incidence of the radiation beam on the target. Software has been developed for calculating depth-dose curves in a semi-infinite medium under uniform irradiation by an electron beam. The implemented algorithms for calculating the depth-dose curves from an electron beam incident on the target at the angle θ are tested. Satisfactory agreement is established between the results obtained using the developed semi-empirical models and the results of Monte Carlo modeling of the depth-dose curves at different incidence angles of the electron beam on the target. Good agreement is established between the results obtained using the semi-empirical model "Cone" and the results obtained using the developed two-parameter semi-empirical models *SEM2U* and *SEM2N*. The capabilities of the developed two-parameter models for a more complete description of the technological characteristics of the radiation sterilization process are investigated using the numerical methods. Examples are provided where the developed two-parameter models allow for the simultaneous description of two technological characteristics of the two-sided irradiation process: the optimal target thickness and the dose uniformity ratio (*DUR*) in the target. Consistent data on these characteristics allow choosing optimal modes of electron beam irradiation during radiation sterilization in a reasonable manner. The possibilities of using the approach suggested in the present paper for developing a set of semi-empirical models of computer dosimetry of irradiation processes in radiation technologies are noted.

Keywords: *Electron beam dosimetry; Depth-Dose curve; Sterilization processes; Control of optimal modes; Semi-empirical model; Monte-Carlo method*

PACS: 87.53.Bn, 02.60.Cb

INTRODUCTION

The tasks of optimizing irradiation processes arose simultaneously with the introduction of radiation technologies [1-11]. Optimization of irradiation processes is ensured by minimizing the level of non-uniformity of the irradiation dose in the volume of the target being processed [12-20]. For electron beams, the method of two-sided irradiation provides high uniformity of the irradiation dose in the layer [4, 5]. The effective application of this method needs the irradiated layer to be of an optimal thickness H_{opt} , which is determined from the condition of equality of the minimum dose value in the center of the layer to the dose value at the boundary of the layer. For the fixed thickness of the irradiated layer, a strong dependence of the ratio $DUR = D_{max}/D_{min}$ on the electron energy is observed. Here D_{max} is the maximum dose value, and D_{min} is the minimum dose value. This dependence causes difficulties in planning and controlling the irradiation process, which are associated with technical problems arising from the need to vary the electron energy.

Varying the angle of the electron beam incidence on the irradiated object surface is considered as a possible solution to technical problems in implementing the two-sided irradiation method [21-27]. Figure 1 shows the depth-dose curves in polyethylene layers of fixed mass thickness $H_1 = 8.25 \text{ g/cm}^2$ and $H_2 = 6.06 \text{ g/cm}^2$ under two-sided irradiation with electron beams. The doses under normal incidence of an electron beam with energy $E = 10 \text{ MeV}$ are shown by red dashed curves. The dose in the H_1 layer for the incidence angle of $\theta_1 = 20^\circ$ of the electron beams with the energy $E = 10 \text{ MeV}$ as well as that in the H_2 layer at the incidence angle of $\theta_2 = 45^\circ$ are given by the black dashed curves, both are calculated in the semi-empirical model [23]. The beam incidence angles for each layer are selected to provide the optimal thicknesses for two-sided irradiation. The results of Monte Carlo simulation of depth-dose curves are presented in Fig. 1 by solid curves for comparison [12,13]. The depth-dose curves for normal incidence of an electron beam with energy $E_1 = 9.3 \text{ MeV}$ on the H_1 layer as well those for an electron beam with energy $E_2 = 6.9 \text{ MeV}$ incidence on the H_2 layer are shown by

dotted curves. For each layer, the electron energy is chosen in such a way that the layer thickness is the optimal one for two-sided irradiation.

One can see in Fig. 1, that the dose non-uniformity **DUR** at normal incidence of an electron beam with an energy of 10 MeV (see red dashed curves) can significantly exceed the dose non-uniformity during irradiation with electrons with a specially selected energy (which is the essence of optimization method 1) or with a specially selected beam incidence angle (which is the essence of optimization method 2).

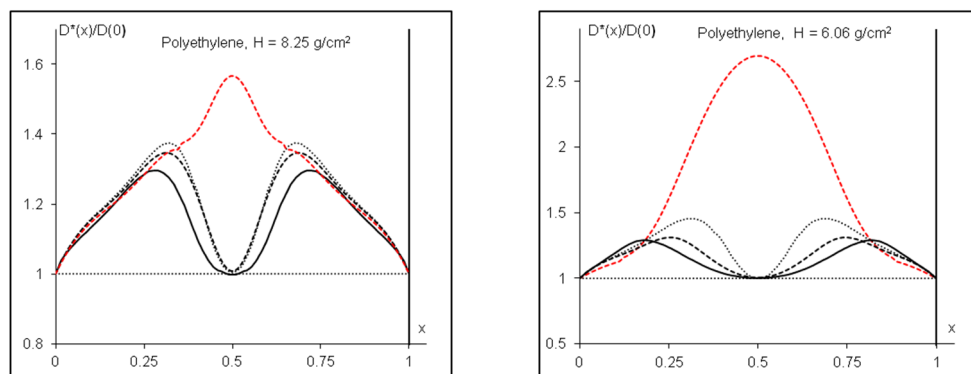


Figure 1. Depth-dose curves for two-sided irradiation of a layer of fixed thickness H

Comparison of **DUR** values in layers of fixed thickness under electron irradiation using optimization method 1 (dotted curves) with those calculated using optimization method 2 (black dashed curves) shows that optimization method 2 provides more uniform dose distribution in the layer. Let compare also the Monte Carlo simulation of the depth-dose curves, presented in Fig.1 by solid curves, with the results calculated within the semi-empirical model (black dashed curves). One can see that the errors in calculating the **DUR** values within the semi-empirical model can be significant.

Therefore, further development of models and methods for describing depth-dose curves at different incidence angles of the electron beam on the layer of matter is the actual problem. The development is necessary when using method 2 to optimize the irradiation parameters in the practical implementation of radiation sterilization.

Development of models and methods for implementing the optimization method 2 was presented in [23-27]. The Monte Carlo method based on the detailed physical model was used in [13] to simulate the depth-dose curves for different incidence angles of the electron beam on the layer. Unfortunately, large arrays of numerical data were the key results of the modeling. These arrays are of little use in searching for optimal irradiation parameters for the practical activities of radiation sterilization centers. Semi-empirical models of the depth-dose curve were developed in [23, 27] for a limited range of incidence angles of the electron beam on the layer. The distribution of the transferred energy in the volume of the target, initiated by the passage of one particle of radiation through the target, was considered as the basic object of the model (the **Dose-Map** object) in the development of these models. Since the passage and transfer of energy by a radiation particle to a substance is a stochastic process, the **Dose-Map** is defined as the average value of the dose distribution over a large number of radiation particles. The semi-empirical model was presented in [27], in which the geometric shape of a cone with one adjustable parameter, the cone angle, was used to approximate the **Dose-Map** object. The model parameter was determined in the result of fitting the data calculated using the semi-empirical model to the data obtained by Monte Carlo simulation in a detailed physical model. For example, for the ISE model [27], the model parameter was determined using data on the optimal layer thicknesses at different incidence angles of the electron beam on the layer [23]. Note that application of single-parameter semi-empirical models, unfortunately, can provide a good description of only one of the technological indicators of the irradiation.

In the present paper, two-parameter semi-empirical models are suggested that can simultaneously describe the optimal layer thickness and the dose uniformity index **DUR** for two-sided irradiation. This is necessary to make a decision on the appropriateness of using irradiation parameters to carry out the radiation sterilization. To design such models, a generalized model of the **Dose-Map** object is developed at the first stage of the present research, which can ensure the elaboration of semi-empirical models for the depth-dose curve in a semi-infinite medium at a given incidence angle of radiation particles on the target.

DISTRIBUTION OF ENERGY TRANSFERRED FROM ONE RADIATION PARTICLE TO THE TARGET VOLUME

Let us start with considering the case of normal incidence of radiation particles on a semi-infinite medium. The material of the medium is assumed to be isotropic with respect to the processes of passage and scattering of particles in the medium. In this case, the distribution of energy transferred from one radiation particle to the target volume (**Dose-Map** object) has axial symmetry relative to the direction of incidence of the radiation particle (X axis) on the medium. To determine the parameters of the **Dose-Map** object model, the well-known fact is applied, that with uniform irradiation of the surface of the medium, the dose at any depth x in the medium is proportional to the integral value of the energy released in the cross-section of the **Dose-Map** object by the plane at depth x . This means that if the flux of radiation

particles $\Phi(y, z)$ incident on the surface ($x=0$) does not depend on the coordinates (y, z) along the surface ($\Phi(y, z) \equiv \Phi_0$), then the dependence of the depth-dose curve $D(x)$ on the depth x in the medium is determined by the expression [27]

$$D(x) = \Phi_0 \int_{G(x)} D_p(x, y, z) \cdot dS, \quad dS = dydz, \quad (1)$$

where $D_p(x, y, z)$ is the dose distribution in the volume of the medium, which is produced by one radiation particle entering the medium, i.e. the mathematical description of the **Dose-Map** object. $G(x)$ is the cross-section of the **Dose-Map** object at depth x . Relation (1) makes it possible to determine the integral values of the dose $E(x)$ in the cross-section $G(x)$ of the **Dose-Map** object based on the data on the depth-dose curve under uniform irradiation of the surface of the medium

$$E(x) \equiv D(x)/\Phi_0. \quad (2)$$

Note that relations (1) and (2) are valid for radiation fluxes of any type and for any angles of incidence of a radiation particle on the boundary of the medium. Therefore, the depth-dose curve $D(x, \theta)$ from the radiation entering the medium at an angle θ can be calculated based on the integral value of the dose $E(x, \theta)$ in the cross-section $G(x, \theta)$ in accordance with the following expressions

$$E(x, \theta) = \int_{G(x, \theta)} D_p(x, y, z, \theta) \cdot dS, \quad dS = dydz, \quad (3)$$

$$D(x, \theta) = \Phi_0 \cdot E(x, \theta),$$

where $D_p(x, y, z, \theta)$ is the dose distribution in the volume of the medium, which is produced by one radiation particle entering the medium at an angle θ .

The depth-dose curves for uniform irradiation of a semi-infinite medium for particles of various types of radiation (electrons, gamma quanta, protons, X-rays) falling normally on the surface of the medium have been studied in detail. For example, for electron irradiation, a semi-empirical model [28] and the implementation of the program for calculating the depth-dose curves in various materials are known. Therefore, for electron irradiation, the integral values of the dose $E(x)$ can be calculated according to (2), based on these data. Therefore, to complete the stage of determining the parameters of the **Dose-Map** object, it is sufficient to establish the characteristics of the dose distribution in the cross-sections $G(x)$ at all depths x in the target.

Uniform distribution and normal (Gaussian) distribution are the simplest types of distribution. Due to the axial symmetry of the **Dose-Map** object, to describe the uniform distribution it is sufficient to know the dependence of the radius $R(x)$ of the circle on the depth x in the medium. The Gaussian distribution requires the variance $\sigma(x)$ to depend on the depth x in the medium. These dependencies should be described by continuous positive functions.

In the present paper, power functions are used as model dependences of dose distributions on x in cross-sections of the **Dose-Map** object:

$$F(x) = \alpha \cdot L_{\max} \left(\frac{x}{L_{\max}} \right)^Q, \quad Q \geq 0, \quad 0 < x \leq L_{\max}. \quad (4)$$

In (4), L_{\max} is the path depth of the radiation particles in the medium [4]. Thus, the **Dose-Map** object model is completely formed and has two model parameters. First, α determines the maximum value of the function $F_{\max} = \alpha \cdot L_{\max}$. And, second, Q is the exponent of the power function.

DEPTH-DOSE CURVES FOR A GIVEN ANGLE OF INCIDENCE OF RADIATION PARTICLES ON A SEMI-INFINITE MEDIUM

Basic assumptions in developing semi-empirical models

The statement that the parameters of the Dose-Map object in its eigen coordinate system $[x^*, y^*, z^*]$ do not change with a change in the angle θ is the main assumption in developing the semi-empirical models. This assumption obviously is valid only for those angles θ , for which the influence of the boundary of the target on the dose distribution in the Dose-Map object can be neglected.

As follows from (3), to calculate the depth-dose curve $D(x, \theta)$ in a medium from radiation incident at an angle θ , it is sufficient to calculate the integral values of the dose $E(x, \theta)$ in the section $G(x, \theta)$ of the dose distribution $D_p(x, y, z, \theta)$ (see Fig. 2). To determine the magnitude of the integral dose values $E(x, \theta)$ in the region $G(x, \theta)$, the contributions $\Delta(x, x^*, \theta)$ are integrated from each of the regions $G(x^*, \theta)$, which are located perpendicular to the X^* axis from $x^*=0$ of the boundary of the medium to $x^*=L_{\max}$ of the maximum depth of the **Dose-Map** object. Then, the relation (3) for the depth-dose curve $D(x, \theta)$ from the radiation entering the medium at an angle θ read

$$D(x, \theta) = \Phi_0 \int_0^{L_{\max}} \Delta(x, x^*, \theta) dx^*. \quad (5)$$

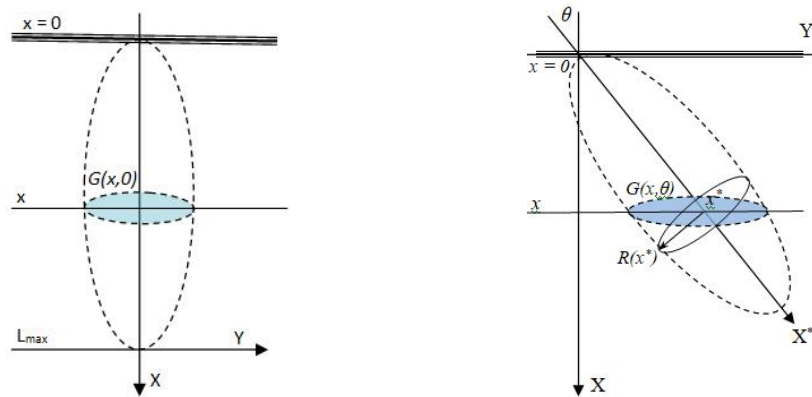


Figure 2. A model of the distribution of transferred energy in a volume of the target, which is initiated by the passage of one particle of radiation through the matter - a *Dose-Map* object

Uniform dose distribution in the cross-sections of the *DOSE-MAP* object

For a uniform dose distribution in the sections of the Dose-Map object, the dependence of the radius $R(x)$ in the cross sections $G(x, \theta)$ on the depth x in the medium is assumed to be known. Then the conditions of intersection of the region $G(x^*, \theta)$ with the plane perpendicular to the X axis at the depth x in the medium are checked while integrating eq. (5)

$$h(x, x^*) < R(x^*), \quad h(x, x^*) = \frac{x - x^* \cdot \cos(\theta)}{\sin(\theta)}, \quad (6)$$

where $h(x, x^*)$ is the distance from point x^* on the plane perpendicular to the X^* axis to the line of intersection of this plane with the plane perpendicular to the X axis at the depth x in the medium (see Fig. 3).

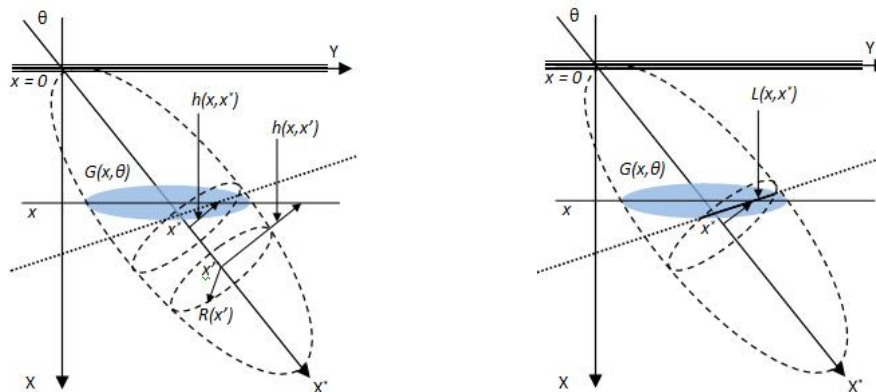


Figure 3. To calculating the depth-dose curve in a semi-infinite medium.

If condition (6) is met, then the contribution of the region $G(x^*, \theta)$ to the dose value in the region $G(x, \theta)$ is proportional to the chord length $L(x, x^*)$ (see Fig. 3):

$$L(x, x^*) = 2 \cdot \sqrt{R^2(x^*) - h^2(x, x^*)}. \quad (7)$$

In accordance with the assumption that the parameters of the *Dose-Map* object in its eigen coordinate system $[x^*, y', z']$ do not change with a variation of the angle θ , the dose distribution in the medium $D_p(x^*, y', z', \theta)$ can be represented as

$$D_p(x^*, y', z', \theta) \equiv \begin{cases} \frac{E(x^*)}{\pi R^2(x^*)} & y'^2 + z'^2 \leq R^2(x^*) \\ 0 & y'^2 + z'^2 > R^2(x^*) \end{cases},$$

$$E(x) = \int_{G(x)} D_p(x, y, z) dS, \quad dS = dydz, \quad (8)$$

where $R(x)$ is the radius of the section $G(x)$ of the *Dose-Map* object. In this case, the contribution $\Delta(x, x^*, \theta)$ from the region $G(x^*, \theta)$ of the *Dose-Map* object to the region $G(x, \theta)$ reads

$$\Delta(x, x^*, \theta) = \frac{E(x^*)}{\pi R^2(x^*)} \cdot \frac{L(x, x^*)}{\sin(\theta)}. \quad (9)$$

In (9), the multiplier $1/\sin(\theta)$ determines the effective area of intersection of the plane perpendicular to the X^* axis at point x^* with the plane perpendicular to the X axis at depth x in the medium.

According to (5), the depth-dose curve $D(x, \theta)$ from radiation entering the medium at an angle θ is determined by the relation

$$D(x, \theta) = \Phi_0 \int_0^{L_{\max}} \frac{E(x^*)}{\pi R^2(x^*)} \cdot \frac{L(x, x^*)}{\sin(\theta)} dx^*. \quad (10)$$

This relationship can easily be represented as an integral transformation of the depth-dose curve $D(x, 0)$ from radiation entering the medium at an angle 0° .

$$D(x, \theta) = \frac{1}{\pi \sin(\theta)} \int_0^{L_{\max}} D(x^*, 0) \cdot \frac{L(x, x^*)}{R^2(x^*)} dx^*. \quad (11)$$

Note that in (11), the dependence $R(x)$ can be any continuous positive function. In particular, when choosing $R(x) \equiv R_0$, one obtains the model “Cylinder”. If one chooses $R(x) \equiv x \cdot \tan(\omega)$, the equivalent of the model “Cone” [27] is obtained. In the present paper, the two-parameter model of the Dose-Map object is applied, $R(x) \equiv F(x)$ (see eq. (4)), and two-parameter (α, Q) semi-empirical model SEM2U is designed for the depth-dose curve in a semi-infinite medium at a given incidence angle of electrons on the medium.

Normal dose distribution in cross-sections of the DOSE-MAP object

For a normal dose distribution in the cross-sections of the Dose-Map object, the dependence of the variance $\sigma(x)$ of the distribution in the cross-sections on the depth x in the medium is assumed to be known. This model uses a dose distribution in the cross-sections of the Dose-Map of the type of axially symmetric spatial distribution of the Gaussian type on a plane, i.e.

$$D_p(x^*, y', z', \theta) \equiv \frac{E(x^*)}{2\pi\sigma^2(x^*)} \cdot e^{-\frac{(y'^2 + z'^2)}{2\sigma^2(x^*)}}, \quad (12)$$

$$E(x) = \int_{G(x)} D_p(x, y, z) dS, \quad dS = dydz,$$

where $\sigma(x)$ is the dependence of the variance of the dose distribution in the **Dose-Map** cross sections on the depth x in the medium; x^*, y', z' are the coordinates of the **Dose-Map** object in its eigen coordinate system.

For a normal dose distribution in the cross-sections of the **Dose-Map** object, the contribution from the region $G(x^*, 0)$ to the dose value in the region $G(x, \theta)$ can be determined by integrating the contributions along the line of intersection of the plane perpendicular to the X^* axis at point x^* with the plane perpendicular to the X axis at depth x (see Fig. 3, dotted line).

According to the basic assumptions, the **Dose-Map** object has axial symmetry relative to the direction of incidence of the radiation particle (axis X^*) on the target and in its eigen coordinate system does not change when the incidence angle of the radiation particle varies. Therefore, one can choose the Z' axis parallel to the dotted line - the intersection of the planes shown in Fig. 3. Note that with this choice of coordinate system orientation, the Y' axis is perpendicular to the intersection line of the planes. In this case, the contribution $\Delta(x, x^*, \theta)$ from the region $G(x^*, 0)$ of the **Dose-Map** object to the region $G(x, \theta)$ can be represented as follows

$$\Delta(x, x^*, \theta) = \frac{1}{\sin(\theta)} \int_{-\infty}^{+\infty} D_p(x^*, y', z', \theta) dz'. \quad (13)$$

Using (12) and integrating in eq. (13), one obtains

$$\Delta(x, x^*, \theta) = \frac{1}{\sqrt{2\pi} \cdot \sin(\theta)} \frac{E(x^*)}{\sigma(x^*)} e^{-\frac{h^2(x, x^*, \theta)}{2\sigma^2(x^*)}}, \quad (14)$$

where $h(x, x^*, \theta)$ is the distance along the Y' axis to the intersection line of the planes.

According to (5), for the depth-dose curve $D(x, \theta)$ from radiation entering the medium at an angle θ , we have the relation

$$D(x, \theta) = \frac{1}{\sqrt{2\pi} \cdot \sin(\theta)} \int_0^{L_{\max}} \frac{D(x^*)}{\sigma(x^*)} \cdot e^{-\frac{h^2(x, x^*, \theta)}{2\sigma^2(x^*)}} dx^* . \quad (15)$$

In this version of the computational scheme, the dependence $\sigma(x)$ can be chosen as an arbitrary continuous positive function. However, ensuring a given error in the calculation results requires numerical methods that take into account the features of the chosen dependence. In the present paper, two-parameter model of the Dose-Map object, $\sigma(x) \equiv F(x)$ (see eq. (4)) is used, and two-parameter (α, Q) semi-empirical model SEM2N is designed for the depth-dose curve in a semi-infinite medium at a given incidence angle of electrons on the medium.

NUMERICAL STUDY OF TWO-PARAMETER EMPIRICAL MODELS

Study of two-parameter SEM2U model

Software for calculating depth-dose curves using the SEM2U model is developed. The calculation results obtained using the SEM2U model are compared with those obtained using the “Cone” model. To do this, one has to take the model parameter $Q = 1$, and the value of the parameter α is determined by the value of the parameter ω of the “Cone” model, $\alpha = \tan(\omega)$. For the angles $\theta \leq 60^\circ$, when the influence of the medium boundary on the dose distribution in the Dose-Map object can be neglected, good agreement between the calculation results obtained using these models is observed. It should be noted that the observed differences are associated only with the error in the numerical integration of the relationships for calculating the depth-dose curve in a semi-infinite medium.

Figure 4 shows the depth-dose curves in a semi-infinite medium and in a layer with two-sided irradiation. The black solid curves correspond to the calculations in the “Cone” model and the SEM2U model with the model parameters $Q_u = 1$, $\alpha_u = 0.47$. Dotted curves relate to the calculations in the SEM2U model with the model parameters: $Q_u = 1.5$, $\alpha_u = 0.53$ (curve 1); $Q_u = 1.1$, $\alpha_u = 0.55$ (curve 2); $Q_u = 0.9$, $\alpha_u = 0.40$ (curve 3); and $Q_u = 0.5$, $\alpha_u = 0.65$ (curve 4). Red solid curves are calculated in the result of modeling the depth-dose curves using the Monte Carlo method.

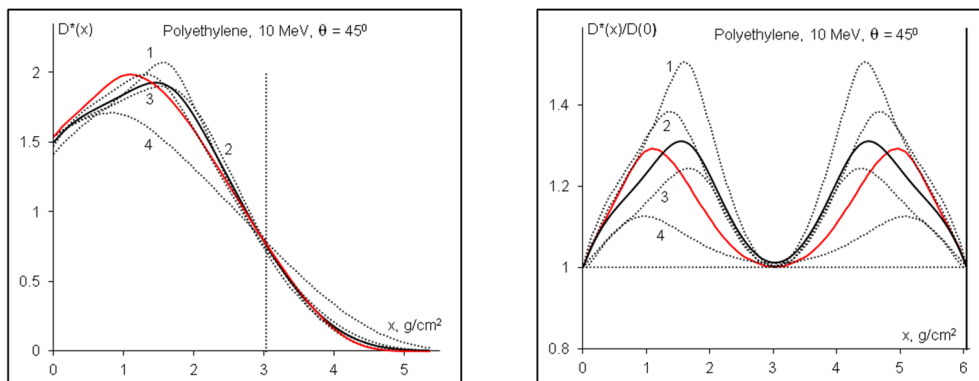


Figure 4. Depth-dose curves in a semi-infinite medium (left) and in a layer of optimal thickness $H_{\text{opt}} = 6.06 \text{ g/cm}^2$ with two-sided irradiation (right).

One can see in Fig. 4, that the selected combinations of model parameter values (Q, α) describe a set of depth-dose curves for which the value of the optimal layer thickness for two-sided irradiation is fixed. At the same time, the value of the dose distribution uniformity characteristic DUR in this set varies in a wide range – from 1.1 to 1.5. This confirms that in the two-parameter SEM2U model, it is possible to select the values of the model parameters in such a way that the calculated depth-dose curves simultaneously describe two technological characteristics of the irradiation.

Study of two-parameter SEM2N model

Software for calculating depth-dose curves using the SEM2N model is produced. The calculation results obtained using the SEM2N model are compared with those obtained using the “Cone” model. Figure 5 shows the depth-dose curves calculated in the “Cone” model (solid curve) for the model parameter value $\omega = 24.75^\circ$ [23]. The depth-dose curves calculated in the SEM2N model with the model parameters: $Q_n = 1$, $\alpha_n = 0.36$ (curve 1); $Q_n = 1$, $\alpha_n = 0.09$ (curve 2), and $Q_n = 1$, $\alpha_n = 0.23$ (dashed curve) are displayed in Fig. 5 for comparison.

One can see from Fig. 5, that the results obtained in the “Cone” model are in good agreement with those obtained in the SEM2N model for the parameters $(Q_n = 1, \alpha_n = 0.23)$. Note that the results obtained in the “Cone” model coincide with the results obtained in the SEM2U model for the model parameters $(Q_u = 1, \alpha_u = 0.46)$. Calculations of the depth-dose curves for different beam incidence angles $\theta < 60^\circ$ show that there is satisfactory agreement between the results obtained in the “Cone” model and in the SEM2N model, if one assumes that the model parameter $Q_n = 1$, and the value of the parameter α_n is determined by the value of the “Cone” model parameter: $\alpha_n = 0.5 \cdot \tan(\omega)$.

The results obtained from comparing the “Cone” model with the SEM2U and SEM2N models indicate that, at a qualitative level, there is agreement between the results obtained in the SEM2N model and the SEM2U model. Numerical

comparison of depth-dose curves calculated using these models demonstrate that the calculation results are in good agreement for angles $\theta < 60^\circ$ if the model parameters are linked by the following relations: $Q_n = Q_u$ and $\alpha_n = 0.5 \cdot \alpha_u$.

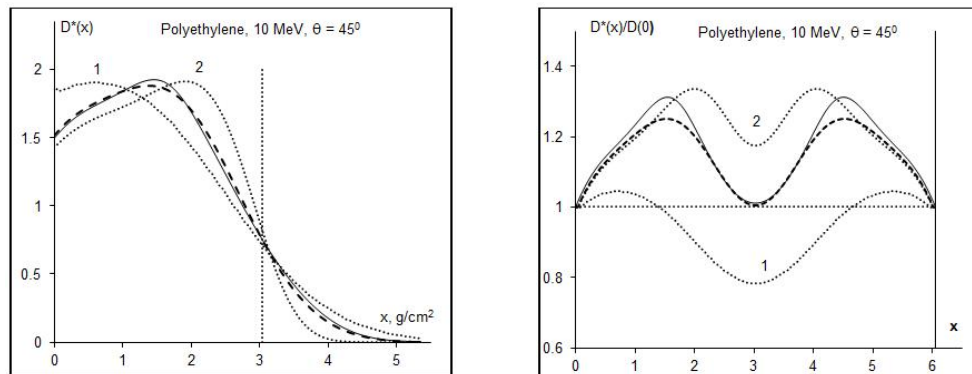


Figure 5. Depth-dose curves in a semi-infinite medium (left) and in a layer of optimal thickness $H_{\text{opt}} = 6.06 \text{ g/cm}^2$ with two-sided irradiation (right).

The depth-dose curves in the layer of optimal thickness under two-sided electron irradiation, calculated in the “Cone” model and in the SEM2N model, are shown in Fig. 6. The parameter of the “Cone” model is chosen as $\omega = 24.75^\circ$ (solid curve). And for the SEM2N model the following model parameters are chosen: $Q_n = 1$, $\alpha_n = 0.23$ (dashed curve), and $Q_n = 1.1$, $\alpha_n = 0.27$ (dotted curve). The depth-dose curve calculated using the Monte Carlo method is presented by solid red curve for comparison.

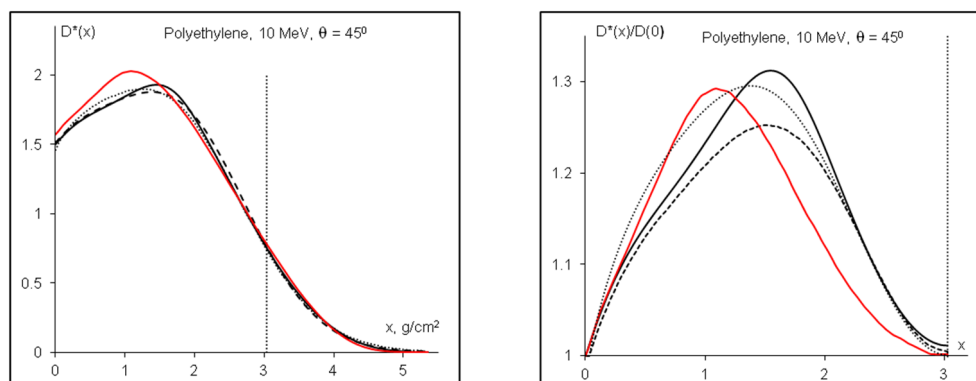


Figure 6. Depth-dose curves calculated for a semi-infinite medium (left) and for a layer of optimal thickness $H_{\text{opt}} = 6.06 \text{ g/cm}^2$ with two-sided irradiation (right).

One can see in Fig. 6, that the depth-dose curve calculated by the SEM2N model can correctly describe both the value of the optimal layer thickness and the uniformity of the dose distribution in the layer. This follows from the fact that the maximum value of the dotted curve is close to the maximum value of the dose in the layer calculated by the Monte Carlo method, and the minimum value equal to 1 is in the middle of the layer of optimal thickness. Thus, the two-parameter SEM2N model provides the possibility to calculate a depth-dose curve that can simultaneously describe two technological characteristics of the radiation sterilization process – the optimal layer thickness and the uniformity of the dose distribution in the layer.

CONCLUSIONS

The spatial distribution of transferred energy in the volume of a target, initiated by the normal incidence of a point beam of radiation on the surface of a semi-infinite medium, is used as a basic object (Dose-Map object) for the development of computer dosimetry models. For a two-parameter approximation of the Dose-Map object, three-dimensional geometric figures are suggested, whose surfaces are formed by rotating the plots of power functions around the abscissa axis.

The two-parameter semi-empirical models of the object are designed on the base of two assumptions. First, the Dose-Map object has axial symmetry relative to the direction of the radiation particle incidence on the target. Second, the dose spatial distribution is uniform or normal (Gaussian distribution) in the *Dose-Map* object cross sections at all the depths.

Semi-empirical models SEM2U and SEM2N are developed for calculating the depth-dose curves from radiation incident on the target at the angle θ . Doing this, the following assumption is applied. The parameters of the Dose-Map object in its eigen coordinate system do not change with a change in the beam incidence angle θ .

Expressions for calculating the depth-dose curves from radiation incident on the target at the angle θ are obtained in the form of the integral transformation of the depth-dose curve known for normal incidence of the radiation beam on the

target. Software is produced for calculating the depth-dose curves in a semi-infinite medium with uniform irradiation of the medium surface by the electron beam.

Satisfactory agreement is established between the results obtained using the developed herein semi-empirical models SEM2U and SEM2N and the results obtained in the semi-empirical model "Cone" and Monte Carlo modeling of depth-dose curves at different incidence angles of the electron beam on the target.

Examples are provided for which the developed two-parameter models make it possible to simultaneously and consistently describe two technological characteristics of the two-sided irradiation process: the optimal target thickness and the dose uniformity coefficient in the target. Consistent data regarding these characteristics allow for the reasonable choice of optimal electron beam irradiation modes for radiation sterilization.

The present paper describes in detail the procedure of developing the semi-empirical models for calculating the depth-dose curves of the electron beam in a semi-infinite medium. The described approach to developing the semi-empirical models can be further applied to developing models for computer dosimetry of other types of penetrating radiation, for example, bremsstrahlung or gamma quanta, which are widely, used nowadays as penetrating radiation for radiation technologies.

ORCID

✉ Igor O. Girka, <https://orcid.org/0000-0001-6662-8683>; ✉ Valentín T. Lazurik, <https://orcid.org/0000-0002-8319-0764>

REFERENCES

- [1] S. Schiller, U. Heisig, and S. Panzer, *Electron Beam Technology*, (John Wiley & Sons Inc, 1995).
- [2] M. Reiser, *Theory and Design of Charged Particle Beams*, (John Wiley & Sons, 2008).
- [3] R.C. Davidson, and H. Qin, *Physics of Intense Charged Particle Beams in High Energy Accelerators*, (World Scientific, Singapore, 2001).
- [4] ICRU REPORT 35, *Radiation dosimetry: electron beams with energies between 1 and 50 MeV*, (ICRU, 1984), p. 168.
- [5] R.J. Woods, and A.K. Pikaev, *Applied radiation chemistry: radiation processing*, (Wiley, New York, 1994).
- [6] ISO/ASTM Standard 51649, *Practice for dosimetry in an e-beam facility for radiation processing at energies between 300 keV and 25 MeV*, (ASTM Standards, vol. 12.02, 2005).
- [7] Yu. Pavlov, and P. Bystrov, *Radiation Physics and Chemistry*, **196**, 110110 (2022). <https://doi.org/10.1016/j.radphyschem.2022.110110>
- [8] Z. Zimek, *Radiation Physics and Chemistry*, **189**, 109713 (2021). <https://doi.org/10.1016/j.radphyschem.2021.109713>
- [9] S. Howard, and V. Starovoitova, *Applied Radiation and Isotopes*, **96**, 162 (2015). <https://doi.org/10.1016/j.apradiso.2014.12.003>
- [10] R. Pomatsalyuk, S. Romanovskyi, V. Shevchenko, and V. Uvarov, *Problems of Atomic Science and Technology*, (5), 131 (2024). <https://doi.org/10.46813/2024-153-131>
- [11] R.I. Pomatsalyuk, S.K. Romanovsky, V.O. Shevchenko, V.Yu. Titov, D.V. Titov, and V.L. Uvarov, *Problems of Atomic Science and Technology*, (5), 117 (2024). <https://doi.org/10.46813/2024-153-117>
- [12] ASTM E2232-21 *Standard Guide for Selection and Use of Mathematical Methods for Calculating Absorbed Dose in Radiation Processing Applications*, (ASTM, 2021), p. 19. <https://doi.org/10.1520/E2232-21>
- [13] F. Salvat, J. Fernandez-Varea, J. Sempau, *PENELOPE 2011: A Code System for Monte Carlo Simulation of Electron and Photon Transport*, (Nuclear Energy Agency, 2012), p. 385.
- [14] S.-T. Jung, S.-H. Pyo, W.-G. Kang, Y.-R. Kim, J.-K. Kim, C.M. Kang, Y.-C. Nho, and J.-S. Park, *Radiation Physics and Chemistry*, **186**, 109506 (2021). <https://doi.org/10.1016/j.radphyschem.2021.109506>
- [15] M. Rezzoug, M. Zerfaoui, Y. Oulhouq, A. Rrhiaua, S. Didi, and D. Bakari, *Radiation Physics and Chemistry*, **235**, 112828 (2025). <https://doi.org/10.1016/j.radphyschem.2025.112828>
- [16] D.J.S. Findlay, *Nucl. Instrum. Methods A*, **276**(3), 598 (1989). [https://doi.org/10.1016/0168-9002\(89\)90591-3](https://doi.org/10.1016/0168-9002(89)90591-3)
- [17] V.L. Uvarov, A.A. Zakharchenko, N.P. Dikiy, Yu.V. Lyashko, R.I. Pomatsalyuk, V.A. Shevchenko, and Eu.B. Malets, *Problems of Atomic Science and Technology*, (6), 180 (2023). <https://doi.org/10.46813/2023-148-180>
- [18] V.L. Uvarov, A.A. Zakharchenko, N.P. Dikiy, R.I. Pomatsalyuk, and Yu.V. Lyashko, *Applied Radiation and Isotopes*, **199**, 110890 (2023). <https://doi.org/10.1016/j.apradiso.2023.110890>
- [19] V.G. Rudychev, M.O. Azarenkov, I.O. Girka, V.T. Lazurik, and Y.V. Rudychev, *Radiation Physics and Chemistry*, **206**, 110815 (2023). <https://doi.org/10.1016/j.radphyschem.2023.110815>
- [20] V.L. Uvarov, A.A. Zakharchenko, N.P. Dikiy, Yu.V. Lyashko, and R.I. Pomatsalyuk, *Radiation Physics and Chemistry*, **214**, 111547 (2024). <https://doi.org/10.1016/j.apradiso.2024.111547>
- [21] V.G. Rudychev, V.T. Lazurik, and Y.V. Rudychev, *Radiation Physics and Chemistry*, **186**, 109527 (2021). <https://doi.org/10.1016/j.radphyschem.2021.109527>
- [22] M. Rosenstein, H. Eisen, and J. Silverman, *Journal of Applied Physics*, **43**, 3191 (1972). <https://doi.org/10.1063/1.1661684>
- [23] V. Lazurik, S. Sawan, V. Lazurik, and O. Zolotukhin, in: *4th International Maghreb Meeting of the Conference on Sciences and Techniques of Automatic Control and Computer Engineering Proceedings*, (IEEE, Maghreb, 2024), pp. 649–653. <https://doi.org/10.1109/MI-STA61267.2024.10599694>
- [24] I. Melnyk, A. Pochynok, and M. Skrypka, *System Research and Information Technologies*, (4), 133 (2024). <https://doi.org/10.20535/SRIT.2308-8893.2024.4.11>
- [25] S.V. Denbnovetsky, V.I. Melnik, I.V. Melnik, and B.A. Tugay, in: *XVIII-th International Symposium on Discharges and Electrical Insulation in Vacuum Proceedings*, (IEEE, Eindhoven, 1998), pp. 637–640. <https://doi.org/10.1109/DEIV.1998.738530>
- [26] I.V. Melnik, and B.A. Tugay, *Radioelectronics and Communications Systems*, **55**, 514 (2012). <https://doi.org/10.3103/S0735272712110064>
- [27] V. Lazurik, S. Sawan, V. Lazurik, and V. Rudychev, in: *3rd International Maghreb Meeting of the Conference on Sciences and Techniques of Automatic Control and Computer Engineering Proceedings*, (IEEE, Maghreb, 2023), pp. 25–29. <https://doi.org/10.1109/MI-STA57575.2023.10169519>

- [28] T. Tabata, P. Andreo, and K. Shinoda, Radiation Physics and Chemistry, **53**, 205 (1998). [https://doi.org/10.1016/S0969-806X\(98\)00102-9](https://doi.org/10.1016/S0969-806X(98)00102-9)

НАПІВЕМПІРИЧНІ МОДЕЛІ КЕРУВАННЯ ЕЛЕКТРОННИМ ПРОМЕНЕМ ДЛЯ РАДІАЦІЙНОЇ СТЕРИЛІЗАЦІЇ

Ігор О. Гірка, Валентин Т. Лазурик

Харківський національний університет імені В. Н. Каразіна, Харків, Україна

Для проведення радіаційної стерилізації необхідно визначати допустимі режими опромінення, що здійснюється за допомогою методів комп'ютерної дозиметрії. На сьогодні вибір оптимальних режимів опромінення може ґрунтуватися на моделях кривої залежності дози від глибини при різних кутах падіння електронного пучка на шар речовини. У цій роботі для розробки таких моделей використано розподіл переданої енергії в об'ємі мішені, ініційований нормальним падінням точкового пучка випромінювання на поверхню напівбезкінечного середовища (об'єкт Dose-Mар). Напівемпіричні моделі об'єкта Dose-Mар розроблені на основі двох припущень. Одна з них полягає в тому, що мішень має осьову симетрію відносно напрямку падіння частинок випромінювання на мішень. Друге полягає в тому, що просторовий розподіл дози є рівномірним або нормальним (розподіл Гауса) у поперечних перерізах об'єкта Dose-Mар на всіх глибинах. Для двопараметричної апроксимації об'єкта Dose-Mар запропоновано тривимірні геометричні фігури, поверхні яких утворюються обертанням графіків степеневих функцій навколо осі абсцис. Напівемпіричні моделі розроблені на основі припущення, що параметри об'єкта Dose-Mар у його власній системі координат не змінюються при зміні кута падіння променя. Отримано вирази для розрахунку кривих глибинної дози від випромінювання, що падає на мішень під кутом θ , у вигляді інтегрального перетворення кривої глибинної дози для нормального падіння пучка випромінювання на мішень. Розроблено програмне забезпечення для розрахунку кривих залежності дози від глибини в напівбезмежному середовищі при рівномірному опроміненні електронним пучком. Тестово реалізовані алгоритми розрахунку кривих залежності дози від глибини від електронного пучка, що падає на мішень під кутом θ . Встановлено задовільну узгодженість між результатами, отриманими за допомогою розроблених напівемпіричних моделей, та результатами моделювання методом Монте-Карло кривих залежності дози від глибини при різних кутах падіння електронного променя на мішень. Встановлено добру узгодженість між результатами, отриманими за допомогою напівемпіричної моделі "Конус", та результатами, отриманими за допомогою розроблених двопараметричних напівемпіричних моделей SEM2U та SEM2N. За допомогою числових методів досліджено можливості розроблених двопараметричних моделей для більш повного опису технологічних характеристик процесу радіаційної стерилізації. Наведено приклади, де розроблені двопараметричні моделі дають можливість одночасно описувати дві технологічні характеристики процесу двостороннього опромінення: оптимальну товщину мішені та коефіцієнт рівномірності дози (DUR) у мішені. Узгоджені дані щодо цих характеристик дають можливість обґрунтовано вибирати оптимальні режими опромінення електронним променем під час радіаційної стерилізації. Зазначено можливості використання запропонованого в цій статті підходу для розробки набору напівемпіричних моделей комп'ютерної дозиметрії процесів опромінення в радіаційних технологіях.

Ключові слова: дозиметрія електронного пучка; крива глибинної дози; процеси стерилізації; контроль оптимальних режимів; напівемпірична модель; метод Монте-Карло

JUSTIFICATION OF A HIGH-ENERGY REGIME FOR WATER DISINFECTION BY AN ELECTRON BEAM

 Stepan H. Karpus^{a*,b},  Oleh O. Shopen^b,  Dmytro A. Zakharchuk^a,  Tetiana O. Narozhna^c

^aLuts'k National Technical University, Lvivska Str., 75, Luts'k, 43018, Ukraine

^bNational Scientific Centre "Kharkiv Institute of Physics and Technology", Akademichna Str., 1, Kharkiv, 61108, Ukraine

^cZinkiv Support Lyceum No. 1 of Zinkiv City Council, Sobornosti Str. 62, Poltava Region, 38100, Ukraine

*Corresponding Author e-mail: s.karpus@lntu.edu.ua

Received May 22, 2025; revised July 31, 2025; accepted August 10, 2025

The challenge of providing safe and clean drinking water requires reliable disinfection methods. Electron beam processing is a promising technology, but its industrial application is often limited by regulatory constraints, which typically cap the electron energy at 10 MeV to prevent induced radioactivity. This paper presents a theoretical justification for the radiological safety of using a higher, sub-threshold energy regime. This paper proposes operating in the 10–15.6 MeV range (using 14.9 MeV as a case study) and demonstrate that this approach allows for the treatment of significantly thicker water layers compared to the standard 10 MeV regime, while ensuring radiological safety. A comprehensive numerical model was used to simulate the process, calculating the bremsstrahlung photon spectrum and the induced activity from potential photonuclear reactions. A quantitative analysis of induced activity was performed for the main components of water (^{16}O , ^2H) and typical trace impurities according to Ukrainian standards (DSanPiN 2.2.4-171-10). The analysis proves that the induced radioactivity is negligible. The primary activation channel on oxygen is energetically forbidden, and the activity from trace elements is short-lived and falls far below the intervention levels set by Ukrainian radiation safety norms (NRBU-97). This work provides a strong physics-based rationale that a high-energy, sub-threshold regime is radiologically safe, which allows for a reconsideration of existing energy limitations in the design of electron beam water treatment facilities.

Keywords: Water disinfection; Electron beam; Bremsstrahlung; Induced activity; Photonuclear reactions; Computer simulation; Sub-threshold energy

PACS: 61.80.Fe, 81.40.Wx, 87.55.N-

1. INTRODUCTION

Providing access to clean and safe drinking water is one of the key global challenges of our time and a cornerstone of public health. Traditional disinfection methods, such as chlorination, while widespread, can lead to the formation of potentially toxic and carcinogenic organochlorine by-products. Alternative methods, like ultraviolet (UV) irradiation, are safe but their effectiveness drops sharply in turbid media, limiting their application. In this context, radiation processing using accelerated electron beams appears to be a promising, fast, and highly efficient technology capable of achieving a high degree of water sterilization regardless of its optical properties.

A major factor limiting the widespread adoption of radiation processing is the concern over induced radioactivity in the treated products. For this reason, international and national standards typically limit the maximum energy of electron beams used for processing food and water to 10 MeV. This limitation ensures the absence of photonuclear reactions in most light and medium nuclei. However, from a physics standpoint, the penetration depth of electrons is directly dependent on their energy. At the same time, the primary disinfecting agent in direct electron irradiation is the electron beam itself, through the formation of highly reactive radiolytic products caused by the ionization and excitation of water molecules. A detailed description of these processes can be found in foundational texts such as Spinks and Woods [1]. The key products include hydrated electrons (e_{aq}^-), hydroxyl radicals ($\cdot\text{OH}$), and hydrogen peroxide (H_2O_2), which effectively destroy microorganisms by damaging their DNA and cell membranes. The secondary bremsstrahlung radiation, however, is the source of photons that can induce radioactivity, creating a conflict between the desire for greater penetration depth (high energy) and the strict requirement for radiological safety (low energy).

The purpose of this work is to provide a theoretical justification and quantitative proof, by means of computer simulation, that using an electron beam with an energy higher than 10 MeV but strictly below the threshold of the main water activation reaction $^{16}\text{O}(\gamma, n)^{15}\text{O}$ (15.66 MeV) allows for a significant increase in the treatment depth without creating radiologically significant induced activity in the water. This paper presents a calculation of the absorbed dose and a quantitative analysis of possible activation channels for water that complies with the Ukrainian standards DSanPiN 2.2.4-171-10 [2].

2. NUMERICAL MODEL AND METHODS

To quantitatively assess the efficiency and safety of the proposed irradiation regime, a numerical model was developed using the Python programming language (version 3.x) [6]. All mathematical calculations and array manipulations were performed using the NumPy library [7], and the results were visualized using the Matplotlib library [8]. The model allows for the calculation of the bremsstrahlung spectrum, absorbed dose, and induced activity in water for a given experimental configuration.

2.1. General simulation setup

The model utilizes a one-dimensional geometry, representing the dose distribution along the central axis of the beam. In a practical application, a beam scanning system would be employed to distribute the dose uniformly over the width of the treatment channel. The simulation follows the passage of a monoenergetic electron beam sequentially through three media: 1) the accelerator exit window (100 μm thick titanium foil); 2) an air gap (10 cm); and 3) the water target. The baseline parameters for the calculations were an initial electron beam energy of $E_0 = 14.9$ MeV and a current of $I = 1$ μA , normalized to a cross-sectional area of $S = 1$ cm^2 . The water composition was assumed to comply with DSanPiN 2.2.4-171-10 [2].

2.2. Calculation of physical quantities

The simulation is based on a step-by-step calculation of three key physical quantities: the absorbed dose, the bremsstrahlung photon spectrum, and the induced activity.

Absorbed Dose. The absorbed dose distribution was estimated using a simplified one-dimensional model. The calculation is based on the energy deposited by the electron beam, E_{dep} [J], in a given mass layer, m_{layer} [kg]. For this first-order approximation, the fundamental definition of absorbed dose was used [11], with energy loss, dE/dx , based on stopping power data from the NIST ESTAR database [9]:

$$D = \frac{E_{dep}}{m_{layer}} = \frac{(dE/dx) \cdot \Delta x \cdot N_e \cdot t_{irr}}{m_{layer}}$$

where N_e is the number of electrons per second, and Δx is the thickness of the water layer. We acknowledge that this linear model is an approximation valid for thin absorbers and does not account for electron scattering effects. For precise dosimetry in a thick target, more advanced methods like Monte Carlo simulations are required. However, for the primary purpose of this paper—the safety analysis—this model is sufficient for a general estimation.

Bremsstrahlung Spectrum. The bremsstrahlung photon flux, $\Phi_\gamma(E_\gamma)$, was calculated to assess the potential for photonuclear activation. For this purpose, a conservative estimation approach was adopted. The calculation was based on the Schiff theory [10], which accurately describes the spectrum from a thin target. This model was applied using the initial electron energy ($E_0 = 14.9$ MeV), effectively assuming the entire photon flux is generated in a thin layer without prior energy loss of the electrons.

This approach is intentionally conservative for a safety analysis involving a thick target, such as the water layer. In a thick medium, electrons lose energy as they penetrate, which "softens" the resulting bremsstrahlung spectrum, reducing the fraction of high-energy photons. By using the thin-target Schiff formula for the maximum initial energy, the model overestimates the flux of high-energy photons responsible for activation. Therefore, if the calculated induced activity is found to be negligible under this conservative assumption, the actual activity in a real-world scenario will be even lower.

Induced Activity. The rate of formation of the i -th radionuclide, R_i [nuclei/s], was calculated based on the fundamental activation equation, as described in standard texts like Krane [12]:

$$R_i = n_i \int_{E_{th}}^{E_0} \Phi_\gamma(E_\gamma) \sigma_i(E_\gamma) dE_\gamma$$

where n_i is the number of target nuclei of type i , $\Phi_\gamma(E_\gamma)$ is the calculated photon flux spectrum, $\sigma_i(E_\gamma)$ is the cross-section for the specific photonuclear reaction, and the integration is performed from the reaction threshold energy E_{th} up to the initial electron energy E_0 . The cross-section data were obtained from the TALYS code [4] and international nuclear data libraries. The time-dependent activity, $A(t)$, was then calculated using the standard activation and decay equation.

3. RESULTS AND DISCUSSION

Based on the developed model, calculations of the absorbed dose and induced activity were performed for the baseline configuration of the facility ($E_0 = 14.9$ MeV, $I = 1$ μA , $S = 1$ cm^2).

3.1. Absorbed Dose Distribution and Penetration Depth

A key indicator of the radiation processing capability is the absorbed dose distribution as a function of depth in the target. The calculations, based on the model described in the Methods section, indicate a significant difference in penetration depth for electron beams with initial energies of 10 MeV and 14.9 MeV.

The model shows that the 10 MeV beam is completely absorbed within a ~ 5.2 cm layer of water, whereas the 14.9 MeV beam provides effective treatment through a layer of ~ 7.8 cm. This demonstrates the technical advantage of the higher-energy regime: it allows for the treatment of significantly thicker water layers in a single pass. It is important to clarify that this increase in penetration and treatable volume is a direct consequence of the higher beam power (for a given current) and does not imply a higher energy efficiency per unit mass of treated water. The value of this approach lies in a significant expansion of technological capabilities. The ability to treat a thicker water layer in a single pass simplifies the hydraulic engineering of the flow system, potentially eliminating the need for complex weirs or thin-film flow designs that are necessary for lower-energy beams. This simplifies the overall design and operation of the treatment facility.

The calculated surface dose rate (≈ 2 kGy/s) indicates that a sterilizing dose of 10 kGy, recommended by the IAEA, can be delivered to the water in a matter of seconds, confirming the high-throughput nature of the electron beam method.

3.2. Radiological safety analysis

To illustrate the underlying principle of the sub-threshold safety regime, the calculated bremsstrahlung photon spectrum is superimposed with the cross-section of the dominant photonuclear reaction, $^{16}\text{O}(\gamma, n)^{15}\text{O}$, in Fig. 1.

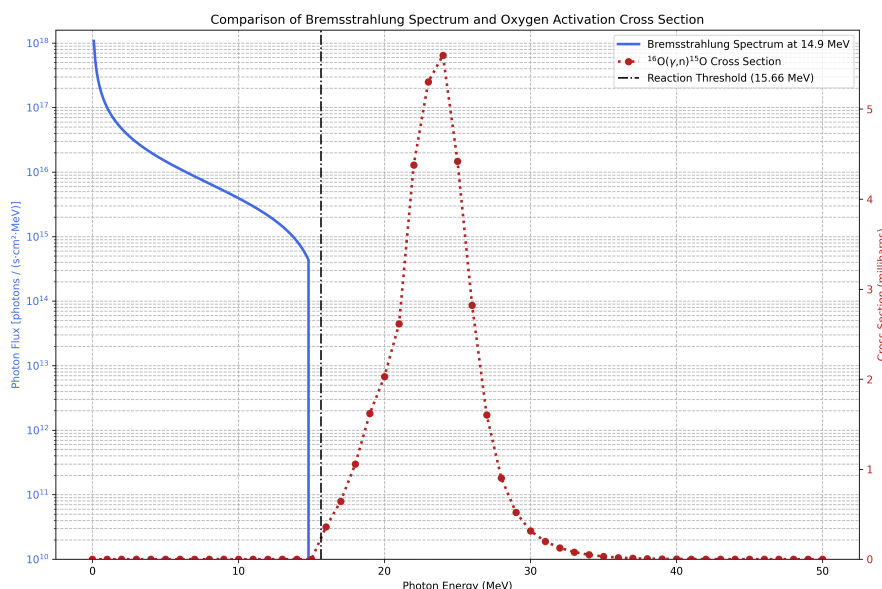


Figure 1. Comparison of the calculated bremsstrahlung photon spectrum with the experimental photonuclear reaction cross-section for $^{16}\text{O}(\gamma, n)^{15}\text{O}$.

The photon spectrum was calculated using the Schiff theory based on the simulation parameters outlined in the Methods section: an initial electron beam energy of 14.9 MeV, a current of 1 μA , and a cross-sectional area of 1 cm^2 , after passage through a 100 μm titanium accelerator window and a 10 cm air gap. The cross-section data were obtained from international nuclear data libraries. The lack of significant overlap between the two curves visually demonstrates the principle of the sub-threshold safety regime.

As can be seen from Fig. 1, the reaction rate, which is determined by the overlap region of the two curves, is negligible because the photon spectrum effectively ends before the reaction cross-section becomes significantly non-zero. A quantitative analysis confirms this:

- **Activation of Oxygen-16:** The induced activity from the formation of ^{15}O is theoretically zero, as the maximum energy of the electron beam (14.9 MeV) is below the $^{16}\text{O}(\gamma, n)^{15}\text{O}$ reaction threshold (15.66 MeV). This primary activation channel, which is dominant at above-threshold energies, is physically forbidden in the proposed regime.
- **Photodisintegration of Deuterium.** The $^2\text{H}(\gamma, n)^1\text{H}$ reaction (threshold ≈ 2.225 MeV) does occur, generating a fast neutron flux of approximately $10^7 - 10^8$ $\text{n}/(\text{s}\cdot\text{cm}^2)$. It is important to emphasize that this process does not produce radioactive isotopes in the water (the products are stable protium and a neutron) and thus does not create residual

radioactivity after the beam is turned off. The resulting prompt neutron field is a standard engineering consideration for the shielding design of any high-energy accelerator facility.

- **Activation of Impurities:** A comprehensive safety assessment requires a multi-step analysis of trace elements present in the water according to DSaPiN standards [2]. Such an analysis involves calculating the absorbed dose and the resulting time-integrated photon flux, followed by the calculation of radionuclide production for each potential impurity. The final step is to determine the total and spectral activity at the end of the irradiation cycle and predict its decay over time.

Following this methodology, a preliminary conservative analysis was performed. It shows that for all relevant photonuclear reactions, such as $^{35}\text{Cl}(\gamma, n)^{34}\text{Cl}$ (product $T_{1/2} = 32$ min) or $^{14}\text{N}(\gamma, n)^{13}\text{N}$ (product $T_{1/2} = 9.97$ min), the half-life of the produced radionuclide is orders of magnitude longer than the typical water irradiation time (which is on the order of seconds). Because the irradiation time t_{irr} is much shorter than the half-life $T_{1/2}$, the activity cannot build up to a significant level, reaching only a minuscule fraction of its potential saturation value. This comprehensive analysis confirms that for all likely impurities, the induced activity falls many orders of magnitude below the intervention levels established in the national standard NRB-97 [3].

4. CONCLUSIONS

Based on the performed theoretical analysis and computer modeling, the following conclusions can be drawn:

1. A high-energy, sub-threshold approach to radiation-based water disinfection has been proposed and theoretically justified. It involves using an accelerated electron beam with an energy higher than the standard 10 MeV limit but strictly below the threshold of the main water activation reaction, $^{16}\text{O}(\gamma, n)^{15}\text{O}$ (15.66 MeV).
2. It has been demonstrated through the developed computer model that operating in the proposed regime (using 14.9 MeV as an example) allows for the treatment of significantly thicker layers of water (7.8 cm) compared to the standard 10 MeV regime (5.2 cm). This represents an expansion of the technological capabilities for designing single-pass water treatment systems, rather than an increase in energy efficiency per unit mass.
3. A quantitative analysis of radiological safety has proven that the induced activity in the water is negligible in the proposed regime. The activation of the main water component, oxygen, is physically forbidden by selecting an energy below the reaction threshold. The prompt neutron flux from deuterium photodisintegration is a standard shielding design consideration and does not cause residual radioactivity. The induced activity from trace impurities is short-lived and rapidly decays to levels several orders of magnitude below the intervention levels set by the Ukrainian Radiation Safety Norms.
4. Thus, the proposed approach is physically justified and has been shown to be radiologically safe. It offers an expanded technological capability for water disinfection and provides a strong basis for reconsidering the current 10 MeV regulatory limit in the design and modernization of advanced water treatment facilities.
5. It is established that for a more detailed assessment of the induced activity in treated water samples, a separate comprehensive study is required. This future work should include: a) calculation of the absorbed dose and the corresponding time-integrated photon flux for the specific irradiation regime; b) analysis of the complete list of potential impurities according to DSaPiN standards; c) calculation of the production rate for each possible radionuclide; and d) determination of the total and spectral activity at the moment the irradiation is complete, followed by a forecast of its decay over time.

REFERENCES

- [1] J.W.T. Spinks, and R.J. Woods, *An Introduction to Radiation Chemistry*, 3rd ed. (Wiley-Interscience, New York, 1990).
- [2] State Sanitary Norms and Rules DSaPiN 2.2.4-171-10, *Hihienichni vymohy do vody pytnoi, pryznachenoi dlia spozhyvannia liudynoiu* [Hygienic requirements for drinking water intended for human consumption] (Kyiv, 2010). (in Ukrainian).
- [3] Radiation Safety Standards of Ukraine (NRBU-97), *Normy radiatsiinoi bezpeky Ukrainy* [Radiation Safety Standards of Ukraine] (Kyiv, 1997). (in Ukrainian).
- [4] Koning, A., Hilaire, S. Goriely, S. TALYS: modeling of nuclear reactions. *Eur. Phys. J. A* **59**, 131 (2023). <https://doi.org/10.1140/epja/s10050-023-01034-3>
- [5] IAEA-TECDOC-1570, "Radiation Treatment for Disinfection of Water and Wastewater," (International Atomic Energy Agency, Vienna, 2008).
- [6] G. Van Rossum, and F. L. Drake, *Python 3 Reference Manual* (CreateSpace, Scotts Valley, CA, 2009).
- [7] C.R. Harris, et al., "Array programming with NumPy," *Nature*, **585**, 357-362 (2020). <https://doi.org/10.1038/s41586-020-2649-2>
- [8] J.D. Hunter, "Matplotlib: A 2D graphics environment," *Computing in Science & Engineering*, **9**, 90-95 (2007). <https://doi.org/10.1109/MCSE.2007.55>

- [9] M.J. Berger, J.S. Coursey, M.A. Zucker, and J. Chang, "ESTAR: Stopping-Power and Range Tables for Electrons," National Institute of Standards and Technology, Gaithersburg, MD. [Online]. Available: <https://www.nist.gov/pml/stopping-power-range-tables-electrons-protons-and-helium-ions>
- [10] L. I. Schiff, "Energy-Angle Distribution of Thin Target Bremsstrahlung," *Physical Review*, **83**, 252 (1951). <https://doi.org/10.1103/PhysRev.83.252>
- [11] F. H. Attix, *Introduction to Radiological Physics and Radiation Dosimetry* (Wiley-VCH, 2004).
- [12] K. S. Krane, *Introductory Nuclear Physics* (John Wiley & Sons, 1988).

ОБҐРУНТУВАННЯ ВИСОКОЕНЕРГЕТИЧНОГО РЕЖИМУ ДЕЗІНФЕКЦІЇ ВОДИ ЗА ДОПОМОГОЮ ПУЧКА ЕЛЕКТРОНІВ

Степан Г. Карпусь^{a,b}, Олег О. Шопен^b, Дмитро А. Захарчук^a, Тетяна О. Нарожна^c

^aЛуцький національний технічний університет, вул. Львівська, 75, Луцьк, 43018, Україна

^bНаціональний науковий центр «Харківський фізико-технічний інститут», вул. Академічна, 1, Харків, 61108, Україна

^cЗінківський опорний ліцей № 1 Зінківської міської ради, вул. Соборності, 62, Полтавська область, 38100, Україна

Завдання забезпечення безпечною та чистою питною водою вимагає надійних методів дезінфекції. Електронно-променева обробка є перспективною технологією, але її промислове застосування часто обмежене нормативними обмеженнями, які зазвичай обмежують енергію електронів на рівні 10 МеВ для запобігання індукованій радіоактивності. У цій статті представлено теоретичне обґрунтування радіологічної безпеки використання вищого, підпорогового енергетичного режиму. У статті пропонується робота в діапазоні 10–15,6 МеВ (на прикладі 14,9 МеВ) та демонструється, що цей підхід дозволяє обробляти значно товстіші шари води порівняно зі стандартним режимом 10 МеВ, забезпечуючи при цьому радіологічну безпеку. Для моделювання процесу було використано комплексну числову модель, розраховано спектр гальмівного фотона та індуковану активність від потенційних фотоядерних реакцій. Було проведено кількісний аналіз індукованої активності для основних компонентів води (^{16}O , ^2H) та типових мікроелементів відповідно до українських стандартів (ДСанПіН 2.2.4-171-10). Аналіз доводить, що індукована радіоактивність є незначною. Первинний канал активації на кисні енергетично заборонений, а активність від мікроелементів є короткочасною та значно нижчою за рівні втручання, встановлені українськими нормами радіаційної безпеки (НРБУ-97). Ця робота надає вагоме фізичне обґрунтування того, що високоенергетичний підпороговий режим є радіологічно безпечним, що дозволяє переглянути існуючі енергетичні обмеження при проектуванні електронно-променевих водоочисних установок.

Ключові слова: дезінфекція води; електронний промінь; гальмівне випромінювання; індукована активність; фотоядерні реакції; комп'ютерне моделювання; підпорогова енергія

ANALYSIS OF TEMPERATURE-DEPENDENT SURFACE PROPERTIES IN THE Ni/SiO₂/Si SYSTEM DURING ELECTRON BEAM DEPOSITION

A.A. Rakhimov,  I.Kh. Khudaykulov*, A.A. Ismatov,  M.M. Adilov

U.A. Arifov Institute of Ion-Plasma and Laser Technologies, Academy of Sciences of Uzbekistan

100125, Durmon Yuli str. 33, Tashkent, Uzbekistan

*Corresponding Author E-mail: i_khudaykulov@mail.ru

Received May 8, 2025; revised June 7, 2025; accepted July 29, 2025

In this study, we investigated the morphological properties of nickel (Ni) island-shaped thin films formed on a SiO_x/Si substrate using the electron beam evaporation method. The morphology was examined using Scanning Electron Microscopy (SEM) and Atomic Force Microscopy (AFM). SEM images were analyzed using ImageJ software to determine the size, density, distribution, and coverage ratio of the islands. The results showed a strong dependence of island morphology on substrate temperature: at 20 °C, the islands had an irregular shape with a density of 103 μm⁻², while at 250 °C and 500 °C, the islands became more spherical in shape, and their densities increased to 751.8 and 1212.4 μm⁻², respectively. AFM analysis confirmed the uniform distribution of the islands and their average height (15.4 nm). EDS analysis revealed the presence and uniform distribution of Si, O, and Ni elements on the surface. These findings confirm that substrate temperature is a critical factor in the island formation process.

Keywords: Nickel nanoparticles; Silicon oxide; Electron beam physical vapor deposition; Layer morphology; Vacuum; Substrate surface; Nanocatalyst

PACS: 81.15.-z; 68.47.Fg

1. INTRODUCTION

Nickel nanoparticles and thin films possess unique physical and chemical properties that ensure high efficiency and have a wide range of applications. Specifically, they are effectively used in the synthesis of carbon nanotubes [1], hydrogenation [2] and oxidation reactions [3], spintronics [4], electronics [5], magnetic devices [6], as well as energy storage systems [7] and sensor devices [8].

These applications are mainly attributed to the high catalytic activity, thermal and chemical stability, and distinctive electronic structure of nickel nanoparticles [9]. Nickel nanoparticles embedded in an oxide matrix provide a valuable platform for in-depth investigation of various physical phenomena. Compared to bulk nickel metal, oxide-supported nickel nanoparticles exhibit different catalytic activity, stability, and electronic properties [10]. These features are especially important in heterogeneous catalysis processes [11]. Among the key factors influencing catalytic performance, the composition of the support material, as well as the size and shape of the nanoclusters, deserve special attention [12].

Research shows that these factors can significantly alter the reactivity and thermodynamic stability of nickel nanoparticles [12]. Therefore, controlling the size and shape of nickel catalyst particles during their growth process is one of the key challenges [13]. Currently, buffer layers formed on SiO_x substrates play a crucial role in regulating the growth mechanism of metal nanoparticles. These layers help manage the chemical and physical interactions between the substrate and metal nanoparticles [14]. At the same time, they contribute to improving the morphological and crystalline structure of the nanoparticles [15]. Buffer layers based on oxide play an important role in the formation of nanostructured materials. In particular, nickel nanoparticles grown on a SiO_x surface exhibit high dispersion, which facilitates an increase in their activity [16].

Moreover, these layers play an important role in determining the chemical composition, electronic properties, and thermodynamic stability of the nanoparticles [17]. The primary objective of this study is to investigate the growth mechanisms of nickel nanoparticles from the vapor phase via electron beam evaporation on a SiO_x buffer layer surface. This involves examining the formation process of Ni nanoparticles, as well as their morphological and structural characteristics depending on the substrate temperature. Additionally, the study explores how the synthesis conditions influence the formation and controllability of the nanoparticles' properties [18]. The obtained results are expected to contribute to a deeper understanding of nickel nanoparticle formation within oxide-based buffer layer matrices. Furthermore, the study aims to identify more efficient ways to control nanoparticle formation processes based on these mechanisms. The findings will serve as a valuable scientific foundation for applications in catalytic processes and nanomaterials engineering.

2. EXPERIMENTAL

A monocrystalline Si (111) wafer was used as the substrate. To remove various organic compounds from the surface, the substrate was first immersed in acetone ((CH₃)₂CO) and methanol (CH₃OH) baths at a temperature of 55 °C for 15 minutes. It was then rinsed with deionized water and dried under a nitrogen atmosphere. To form an oxide layer on the

silicon substrate, it was annealed in a SNOL furnace at 1000 °C for two hours. The thickness of the resulting SiO_x layer was analyzed using a SER-850 model spectral ellipsometer manufactured by SENTECH. Based on the Cauchy layer model, the measurements showed that the thickness of the SiO_x layer was 60 nm.

In the present study, a thin nickel island layer was deposited onto the SiO_x/Si substrate via electron beam physical vapor deposition (EB-PVD). This method enables high-purity film growth under controlled vacuum conditions. The schematic diagram of the deposition setup used in the experiment is presented in Figure 1.

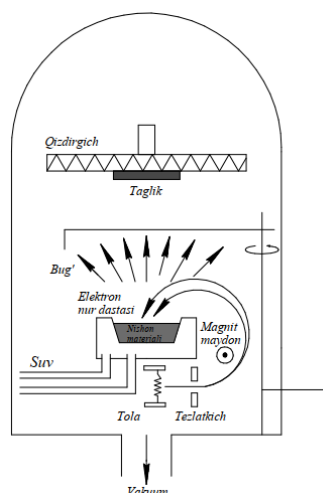


Figure 1. Schematic representation of the thin film deposition process via electron beams physical vapor deposition (EB-PVD)

The device is equipped with an electron beam evaporation system (model SEB-06) with a power capacity of 6 kW, capable of operating with an external voltage of up to 10 kV and an electron emission current of up to 600 mA. A high vacuum of up to 10^{-8} Torr is achieved in the chamber using a turbomolecular pump. This minimizes the contribution of impurities from the sample and the crucible during the evaporation process. Nickel (Ni) vapor was deposited onto the substrate surface under a vacuum of 10^{-6} Torr, using an electron beam with a current of 30 mA and a voltage of 10 kV for a duration of 3 seconds.

The surface morphology of the obtained thin films was studied using a Thermo Fisher Scientific (Apreo 2S SEM). During the investigation, accelerating voltages ranging from 2 kV to 20 kV were used. Low accelerating voltage (2 kV) was applied to obtain surface morphological images of the sample, while high voltage (20 kV) was used for elemental composition analysis. SEM images were captured at various magnification levels (from $\times 5,000$ to $\times 100,000$), allowing the assessment of film uniformity and the identification of potential structural anomalies on the surface.

3. RESULTS AND DISCUSSION

To evaluate the surface morphology of the samples, scanning electron microscopy (SEM) analyses were performed. The ImageJ software was used to determine the size and surface distribution of Ni islands from the SEM images. This software allows for the identification of individual island areas and quantities within the image, which in turn helps calculate the island diameter, surface density, and coverage coefficient. Figure 1 shows the SEM images of the Ni island structure grown on SiO/Si at different substrate temperatures (20°C, 250°C, and 500°C) for 4 seconds. The shape of the islands was idealized as spherical, and their diameters were determined. The histograms of Ni nanoparticles diameters were displayed in Figure 1(d-f).

Figure 1(a) shows the SEM image of the surface morphology of the Ni island structure formed at a substrate temperature of 20°C using the electron beam heating method. It can be seen that the islands have an irregular shape and are arranged in a way that they are not entirely separated from each other.

The values of parameters such as the diameter, area, surface density, and surface coverage ratio of Ni nanoparticles obtained from the SEM images (a–c) in Figure 1 using the ImageJ software are presented in Table 1. Using the ImageJ software for image analysis, the average diameter of the islands was found to be 52.9 nm, and the surface density was $103 \mu\text{m}^{-2}$. These values indicate that at low temperatures, the mobility of metal atoms is limited. As a result, many voids may form in the structure. For this reason, the islands are unevenly distributed on the substrate and have an irregular shape.

Table 1. Results of SEM analysis for the size and surface density of Ni island structures grown on the substrate at 20°C, 250°C, and 500°C temperatures.

SiO _x /Si temperature (°C)	Area ($10^{-4} \mu\text{m}^2$)	Diameter (nm)	Density (μm^{-2})	Coverage (%)
20	21.9 ± 7.2	52.9	103 ± 0.2	62.70
250	5.81 ± 2.8	27.2	751.8 ± 0.4	43.610
500	2.3 ± 1.2	17.3	1212.4 ± 0.3	28.7

In Figure 1(b), it is observed that as the substrate temperature increased up to 250°C during the deposition process, the shape of the islands became more orderly, approaching a spherical form. At this temperature, the mobility of atoms increases, causing them to start approaching a more energetically stable configuration, that is, transitioning to a shape that minimizes surface energy. According to the analysis results, at 250°C, the average diameter of the islands decreased to 27.2 nm, and the surface density increased to 751 μm^{-2} , with the islands being fully separated from each other and evenly distributed across the surface.

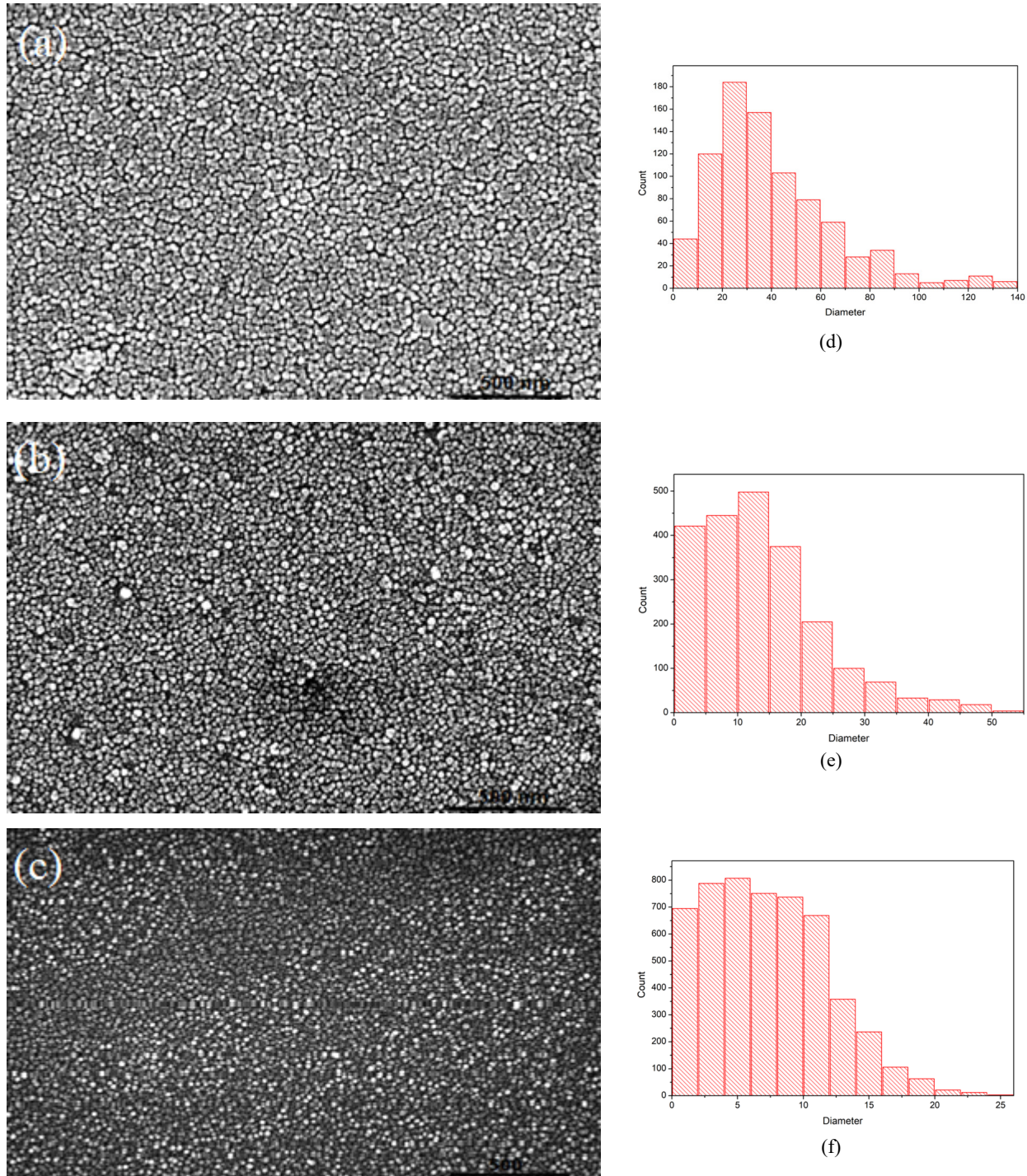


Figure 1. SEM images of Ni nanoparticles formed on the SiO_x/Si substrate surface at substrate temperatures of 20°C, 250°C, and 500°C and the histograms of Ni nanoparticles diameters (a, b, s). Scale bar – 500 nm.

In Figure 1(c), at a substrate temperature of 500°C during the deposition process, the size of the islands further decreased, with the average diameter reaching 17.3 nm and the surface density increasing to 1212 μm^{-2} . These results indicate that at higher temperatures, the activation of atomic diffusion leads to an increase in the number of islands and a decrease in their size.

Furthermore, the coverage ratio of the islands was found to vary with the substrate temperature. Specifically, the coverage coefficient was 42.7% at 20°C, 46.3% at 250°C, and 48.9% at 500°C. This indicates that as the temperature increases, both the density of the islands and the overall surface coverage increase. These analyses confirm that substrate temperature is a decisive factor in the process of metal island formation.

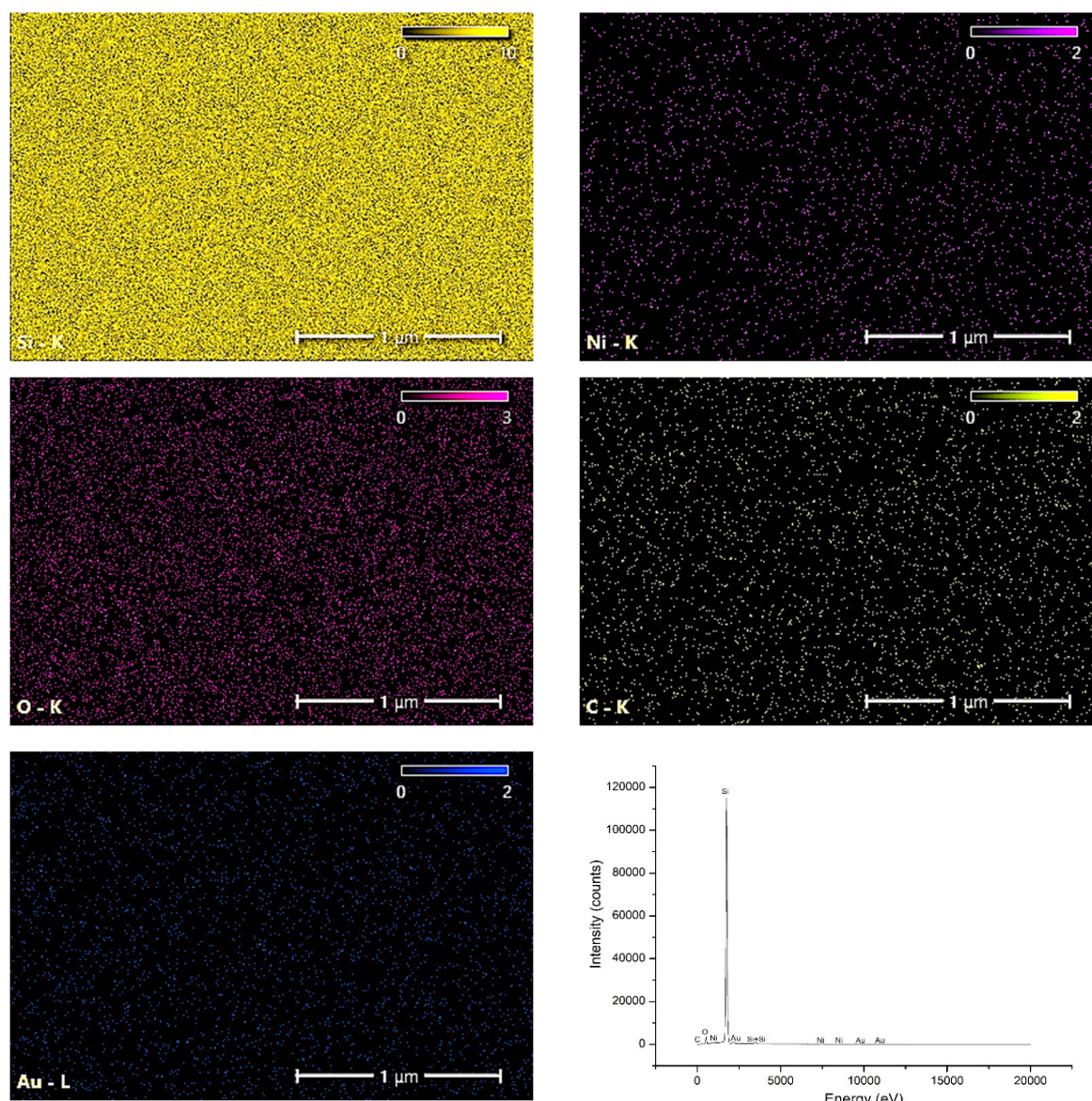


Figure 2. Elemental mapping/EDS spectrum of Ni/SiO_x/Si

Energy dispersive spectroscopy (EDS) analysis was performed on a sample grown at a substrate temperature of 250°C to determine the chemical composition of the Ni/SiO_x/Si structure. This analysis allowed for the determination of the elemental composition in the sample as well as their distribution across the surface.

According to the EDS elemental mapping results, the presence of silicon (Si), oxygen (O), and nickel (Ni) elements in the Ni/SiO/Si structure was confirmed, and their uniform distribution across the substrate surface was observed. Specifically, it was noted that nickel nanoparticles and their aggregates were not localized but were almost uniformly distributed on the sample surface.

The Au element identified in the EDS spectrum was deposited on the sample surface in a very thin (3 nm) layer prior to analysis. Its purpose is to enhance the SEM image quality and contrast, as well as to improve the electrical conductivity of the sample. This is a standard practice widely used in SEM analyses. The presence of carbon (C) observed in the spectrum is mainly explained by the effect of the carbon tape used to attach the sample during the SEM analysis. That is, the C element is not a constituent part of the sample itself, but is present in the composition due to the technical support material. Based on the EDS spectrum, the atomic percentages of the identified elements were determined as follows: Si - 70.7%, O - 16.3%, C - 11.2%, Ni - 1.3%, and Au - 0.4%.

It was determined that the main composition of the sample consists of Si and O elements, indicating the dominance of the SiO_x substrate. The relatively small amount of Ni nanoparticles is located in the upper parts of the layer, and it is

these that play a key role in morphological analysis and determining functional properties. In general, the results of the EDS analysis, in agreement with the SEM and AFM analyses presented above, qualitatively explained the presence or absence of foreign impurities, reflecting the elemental composition in the Ni/SiO_x/Si structure.

To further assess the surface unevenness of the Ni island structure and the spatial distribution of the islands, Atomic Force Microscopy (AFM) analysis was conducted. The 3D AFM image (Figure 3) provided detailed information about the surface topography and roughness of the Ni/SiO_x/Si sample, which was obtained at a substrate temperature of 250°C.

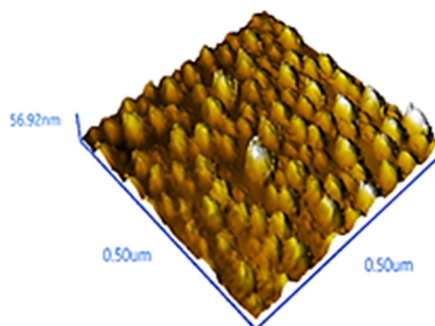


Figure 3. 3D topographic AFM image for the Ni/SiO_x/Si sample

The image reveals that the distribution of the Ni islands across the substrate surface is relatively uniform and exhibits a clear structure. The islands are located close to each other, with some of them not fully separated, forming a dense mass. This observation aligns with the results from the SEM analysis, showing that the islands exhibit irregular shapes and vary somewhat in size. The height profile from the AFM image indicates that the surface roughness is relatively stable, with minimal variations between individual islands. The average height (R_m) of the Ni islands was found to be approximately 15.4 nm. This suggests that the surface relief of the thin film does not have significant differences between peaks and valleys, and the islands grew at nearly the same height. These findings are consistent with the data obtained from the SEM analysis, demonstrating that at higher substrate temperatures, Ni islands adopt a more uniform shape and higher density distribution.

4. CONCLUSIONS

In this study, the morphological characteristics of Ni island-shaped thin films formed on the SiO_x/Si substrate surface using the electron beam physical vapor deposition (EB-PVD) method were investigated through scanning electron microscopy (SEM) and atomic force microscopy (AFM) techniques. Data obtained from SEM images using the ImageJ software allowed for the determination of the islands' size, surface distribution, density, and coverage coefficient. According to the results, the geometric parameters and distribution of the Ni islands were directly dependent on the substrate temperature. At a temperature of 20 °C, the islands exhibited irregular shapes and were located close to each other, with an average diameter of 52.9 nm and a density of 103 μm^{-2} . As the temperature increased to 250°C and 500°C, the shape of the islands became closer to spherical, their size decreased, and their density increased to 751.8 μm^{-2} and 1212.4 μm^{-2} , respectively. These changes were attributed to the islands striving for a thermodynamically stable state and minimizing the surface energy. Moreover, AFM images confirmed that the islands were evenly distributed on the surface, with an average height of approximately 15.4 nm. The elemental composition was determined using EDS analysis, which showed the presence of Si, O, and Ni elements on the surface, evenly distributed. Thus, the results of the study demonstrated that the morphology and surface properties of the Ni island structure are strongly dependent on the substrate temperature.

Funding

The authors gratefully acknowledge the financial and technical support provided by the Ministry of Higher Education, Science, and Innovation under project number IL-5421101842.

ORCID

✉ I.Kh. Khudaykulov, <https://orcid.org/0000-0002-2335-4456>; ✉ M.M. Adilov, <https://orcid.org/0000-0003-0312-2356>

REFERENCES

- [1] J. Cheng, X. Zhang, and Y. Ye, "Synthesis of nickel nanoparticles and carbon encapsulated nickel nanoparticles supported on carbon nanotubes," *Journal of Solid-State Chemistry*, **179**(1), 91-95 (2006). <https://doi.org/10.1016/j.jssc.2005.10.001>
- [2] J. Xia, G. He, L. Zhang, X. Sun, and X. Wang, "Hydrogenation of nitrophenols catalyzed by carbon black-supported nickel nanoparticles under mild conditions," *Applied Catalysis B: Environmental*, **180**, 408-415 (2016). <https://doi.org/10.1016/j.apcatb.2015.06.043>
- [3] A. Singh, S.L. Chang, R.K. Hocking, U. Bach, and L. Spiccia, "Highly active nickel oxide water oxidation catalysts deposited from molecular complexes," *Energy & Environmental Science*, **6**(2), 579-586 (2013). <https://doi.org/10.1039/C2EE23862D>
- [4] J. Mroziński, "New trends of molecular magnetism," *Coordination chemistry reviews*, **249**(21-22), 2534-2548 (2005). <https://doi.org/10.1016/j.ccr.2005.05.013>

- [5] R. Poulain, G. Lumbeeck, J. Hunka, J. Proost, H. Savolainen, H. Idrissi, *et al.*, "Electronic and chemical properties of nickel oxide thin films and the intrinsic defects compensation mechanism," *ACS Applied Electronic Materials*, **4**(6), 2718-2728 (2022). <https://doi.org/10.1021/acsaelm.2c00230>
- [6] S. Nadaf, G.K. Jena, N. Rarokar, N. Gurav, M. Ayyanar, S. Prasad, and S. Gurav, "Biogenic and biomimetic functionalized magnetic nanosystem: Synthesis, properties, and biomedical applications," *Hybrid Advances*, **3**, 100038 (2023). <https://doi.org/10.1016/j.hybadv.2023.100038>
- [7] D. Zhou, X. Guo, Q. Zhang, Y. Shi, H. Zhang, C. Yu, and H. Pang, "Nickel-based materials for advanced rechargeable batteries," *Advanced Functional Materials*, **32**(12), 2107928 (2022). <https://doi.org/10.1002/adfm.202107928>
- [8] S.G. Danjumma, Y. Abubakar, and S. Suleiman, "Nickel oxide (NiO) devices and applications: a review," *J. Eng. Res. Technol.*, **8**, 12-21 (2019). <https://doi.org/10.17577/IJERTV8IS040281>
- [9] B. Han, B. Yu, J. Wang, M. Liu, G. Gao, K. Xia, *et al.*, "Understanding the electronic metal-support interactions of the supported Ni cluster for the catalytic hydrogenation of ethylene," *Molecular Catalysis*, **511**, 111731 (2021). <https://doi.org/10.1016/j.mcat.2021.111731>
- [10] Z. Shang, S. Li, L. Li, G. Liu, and X. Liang, "Highly active and stable alumina supported nickel nanoparticle catalysts for dry reforming of methane," *Applied Catalysis B: Environmental*, **201**, 302-309 (2017). <https://doi.org/10.1016/j.apcatb.2016.08.019>
- [11] L. Liu, and A. Corma, "Metal catalysts for heterogeneous catalysis: from single atoms to nanoclusters and nanoparticles," *Chemical reviews*, **118**(10), 4981-5079 (2018). <https://doi.org/10.1021/acs.chemrev.7b00776>
- [12] T.K. Turdaliev, K.B. Ashurov, and R.K. Ashurov, "Morphology and Optical Characteristics of TiO₂ Nanofilms Grown by Atomic-Layer Deposition on a Macroporous Silicon Substrate," *Journal of Applied Spectroscopy*, **91**(4), 769-774 (2024). <https://doi.org/10.1007/s10812-024-01783-z>
- [13] I.J. Abdusaidov, S.G. Gulomjanova, I.K. Khudaykulov, and K.B. Ashurov, "The Low-Temperature Growth of Carbon Nanotubes Using Nickel Catalyst," *East European Journal of Physics*, (3), 355-358 (2024). <https://doi.org/10.26565/2312-4334-2024-3-41>
- [14] F.A. Silva, V.M.M. Salim and T.S. Rodrigues, "Controlled Nickel Nanoparticles: A Review on How Parameters of Synthesis Can Modulate Their Features and Properties," *Applied Chem.* **4**(1), 86-106 (2024). <https://doi.org/10.3390/appliedchem4010007>
- [15] P. Camilos, C. Varvenne, and C. Mottet, "Size and shape effects on chemical ordering in Ni–Pt nanoalloys," *Physical Chemistry Chemical Physics*, **26**(21), 15192-15204 (2024). <https://doi.org/10.1039/D4CP00979G>
- [16] A.S. Al-Fatesh, N.A. Bamatraf, S.B. Alreshaidan, J.K. Abu-Dahrieh, N. Patel, A.A. Ibrahim, *et al.*, "Cost-effective single-step synthesis of metal oxide-supported Ni catalyst for H₂-production through dry reforming of methane," *Arabian Journal for Science and Engineering*, **49**(6), 8031-8047 (2024). <https://doi.org/10.1007/s13369-023-08576-0>
- [17] S. Mehravar, B.M. Garmejani, and S. Fatemi, "Nickel-Deposited Hexagonal Boron Nitride Composites via Chemical Vapor Deposition: Unlocking Enhanced Magnetic Properties for Advanced Technologies," *Journal of Materials Chemistry C*, **13**, 6823-6830 (2025). <https://doi.org/10.1039/D4TC05281A>
- [18] X. Chen, Z. Li, Y. Zhao, C. Qi, S. Li, and F. Li, "Wetting and interfacial phenomena between a Ni-based superalloy and silica-based ceramic cores with ZrSiO₄ additions," *Journal of Physics: Conference Series*, **2671**(1), 012025 (2024). <https://doi.org/10.1088/1742-6596/2671/1/012025>
- [19] B.C. Bayer, D.A. Bosworth, F.B. Michaelis, R. Blume, G. Habler, R. Abart, *et al.*, "In situ observations of phase transitions in metastable nickel (carbide)/carbon nanocomposites," *The Journal of Physical Chemistry C*, **120**(39), 22571-22584 (2016). <https://doi.org/10.1021/acs.jpcc.6b01555>

АНАЛІЗ ТЕМПЕРАТУРНО-ЗАЛЕЖНИХ ПОВЕРХНЕВИХ ВЛАСТИВОСТЕЙ У СИСТЕМІ Ni/SiO₂/Si ПІД ЧАС ЕЛЕКТРОННО-ПРОМЕНЕВОГО ОСАДЖЕННЯ

А.А. Рахімов, І.Х. Худайкулов, А.А. Ісмаєв, М.М. Аділов

*Інститут іонно-плазмових та лазерних технологій імені У.А. Аріфова, Академія наук Узбекистану
100125, вул. Дурмон Юлі, 33, Ташкент, Узбекистан*

У цьому дослідженні ми вивчали морфологічні властивості тонких плівок нікелю (Ni) у формі острівців, сформованих на підкладці SiO_x/Si за допомогою методу електронно-променевого випаровування. Морфологію досліджували за допомогою скануючої електронної мікроскопії (СЕМ) та атомно-силової мікроскопії (АСМ). Зображення СЕМ аналізували за допомогою програмного забезпечення ImageJ для визначення розміру, щільності, розподілу та коефіцієнта покриття острівців. Результати показали сильну залежність морфології островів від температури підкладки: при 20°C острови мали неправильну форму з щільністю 103 мкм⁻², тоді як при 250°C та 500°C острови набували більш сферичної форми, а їх щільність збільшувалася до 751,8 та 1212,4 мкм⁻² відповідно. АСМ-аналіз підтвердив рівномірний розподіл островів та їх середню висоту (15,4 нм). EDS-аналіз виявив наявність та рівномірний розподіл елементів Si, O та Ni на поверхні. Ці результати підтверджують, що температура підкладки є критичним фактором у процесі формування островів.

Ключові слова: наночастинки нікелю; оксид кремнію; електронно-променеве фізичне осадження з парової фази; морфологія шару; вакуум; поверхня підкладки; нанокаталізатор

INVESTIGATION OF THE BEHAVIOR OF NICKEL IMPURITY ATOMS IN THE SILICON LATTICE BASED ON FIRST PRINCIPLES

✉ Bayrambay K. Ismaylov^{a,b}, ✉ Kanatbay A. Ismailov^a, ✉ Nurulla F. Zikrillaev^b,
✉ Atabek E. Atamuratov^c, ✉ Sergey V. Koveshnikov^b, ✉ Zoir T. Kenzhaev^a,
✉ Makhkam M. Khalilloev^c, ✉ Parakhat K. Dilimbetov^a

^aKarakalpak State University named after Berdakh, Uzbekistan, 230112, Nukus, Ch. Abdirova St.1

^bTashkent State Technical University, Uzbekistan, 100095, Tashkent, University St.2

^cUrgench State University, Uzbekistan, 220100, Urgench, Kh. Olimjan St.14

*Corresponding Author E-mail: ismaylovb81@gmail.com

Received May 1, 2025; revised June 23, 2025; accepted June 27, 2025

This work presents a comprehensive theoretical and experimental study of the behavior of nickel impurity atoms in the silicon crystal lattice. The focus is on analyzing diffusion mechanisms, the energetic characteristics of interstitial nickel atoms, their interaction with defects and other impurities, as well as the formation of stable clusters within the crystal volume. First-principles quantum mechanical modeling was employed using the QuantumATK software, applying the Linear Combination of Atomic Orbitals (LCAO) method and the Local Density Approximation (LDA) exchange-correlation functional. Special attention was given to calculating the binding energy of nickel atoms in interstitial sites and estimating the activation energy for their migration along various crystallographic directions ([100] and [010]). The modeling results revealed that nickel atoms predominantly diffuse in interstitial positions with an activation energy around 0.31 eV, which aligns well with previously reported experimental data. It was found that interactions of nickel with oxygen, carbon impurities, and point defects have a minimal impact on diffusion processes. However, interactions with vacancies lead to the formation of stable nickel silicides and cause an increased concentration of nickel near the surface. The experimental part of the study confirmed the formation of nickel clusters under high-temperature treatments. Scanning Electron Microscopy (SEM), Secondary Ion Mass Spectrometry (SIMS), and Infrared (IR) microscopy revealed a high density and uniform distribution of clusters throughout the crystal volume. Cluster sizes ranged from 20 to 100 nm, with concentrations reaching approximately 10^{10} cm^{-3} . These findings demonstrate that nickel acts as an effective gettering impurity, enhancing the electrophysical properties of silicon. The results provide valuable insights for optimizing the fabrication processes of high-efficiency silicon solar cells and microelectronic devices.

Keywords: Nickel; Silicon; Diffusion; Clusters; Interstitial atoms; First-principles; Activation energy; Quantum mechanical modeling; Gettering; Semiconductors

PACS: 68.37.Rt, 68.37.Ps

INTRODUCTION

Silicon is a key semiconductor material widely used in microelectronics, photonics, and solar energy. The electrophysical properties of silicon are largely determined by the level of crystalline purity and the presence of impurity atoms. Of particular importance is the influence of such impurities on the lifetime of minority charge carriers - a critical parameter that determines the efficiency of solar cells. Transition metals, in particular nickel, form deep energy levels in the silicon bandgap, acting as recombination centers and reducing the carrier lifetime, which leads to degradation of semiconductor device performance. At the same time, nickel exhibits pronounced gettering properties, facilitating the removal of contaminating impurities from the active region, which conversely increases carrier lifetime and improves photovoltaic parameters.

The present study aims to investigate the behavior of nickel atoms in silicon, their impact on recombination processes, gettering effects, as well as the stability and durability of silicon structures. Using quantum-mechanical modeling methods based on first principles, the microscopic mechanisms of interaction between nickel and the crystal lattice are analyzed, enabling the proposal of new approaches to improve the efficiency and reliability of semiconductor devices. Previous studies [1-3] and foreign researchers [4-7] have examined the diffusion mechanisms of nickel impurities, the state of impurity atoms in the lattice, and their influence on the electrical parameters of silicon. The majority of nickel atoms diffuse in silicon in an electronically neutral state and primarily occupy interstitial positions. The maximum solubility of nickel atoms is nearly two orders of magnitude higher (see Table 1) than that of other transition group elements. To deepen the understanding of the diffusion processes of nickel impurity atoms in silicon, this work performs first-principles calculations of the activation energy of interstitial nickel atoms in the silicon crystal lattice.

The diffusion coefficient of interstitial nickel atoms depends weakly on temperature and is approximately $\sim 10^{-5} \div 10^{-4} \text{ cm}^2/\text{s}$. To calculate the diffusion coefficient of nickel in silicon, the equations given in Table 2 can be used.

Cite as: B.K. Ismaylov, K.A. Ismailov, N.F. Zikrillaev, A.E. Atamuratov, S.V. Koveshnikov, Z.T. Kenzhaeva, M.M. Khalilloev, P.K. Dilimbetova, East Eur. J. Phys. 3, 442 (2025), <https://doi.org/10.26565/2312-4334-2025-3-48>

© B.K. Ismaylov, K.A. Ismailov, N.F. Zikrillaev, A.E. Atamuratov, S.V. Koveshnikov, Z.T. Kenzhaeva, M.M. Khalilloev, P.K. Dilimbetova, 2025; CC BY 4.0 license

Table 1. Solubility of nickel atoms in silicon [2]

State of atoms	Calculation formula	Solubility at T=1250 °C, cm ⁻³
in nodes	$Ni_s(T)=10^{26} \cdot \exp(-3.1 \text{ eV}/kT)$	$5 \cdot 10^{14}$
in the internodes	$Ni_i(T)=1.23 \cdot 10^{24} \cdot \exp(-1.68 \text{ eV}/kT)$	$7 \cdot 10^{17} \div 10^{18}$
	$Ni_i(T) = 1,4 \times 10^{25} \exp(-2.3 \text{ eV}/kT)$	$7 \cdot 10^{17}$

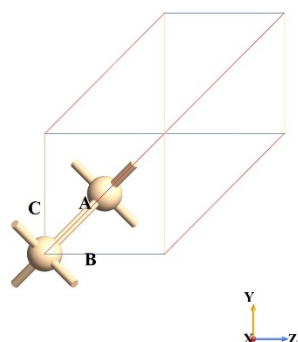
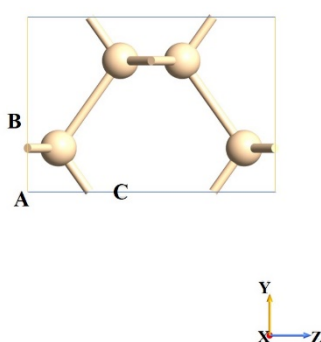
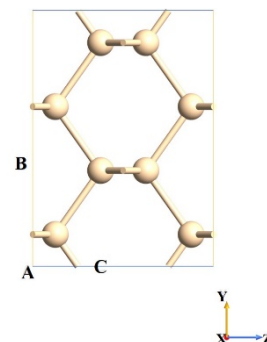
Table 2. Diffusion coefficient of nickel atoms in silicon [3]

Temperature range T, °C	Calculation formula	D, cm ² /c
900÷1300	$D(Ni_i)=2.3 \cdot 10^{-3} \cdot \exp(-0.47 \text{ eV}/kT)$	$(3 \div 8) \times 10^{-5}$
600÷900	$D(Ni_i) = (1.69 \pm 0.74) \times 10^{-4} \exp(-0.15 \text{ eV}/k_B T)$	$(2 \div 4) \times 10^{-5}$

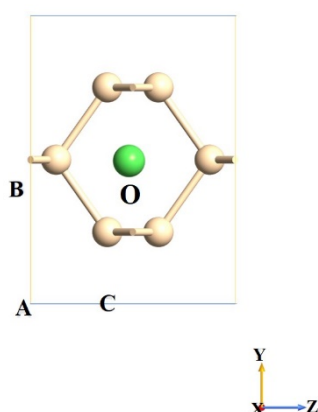
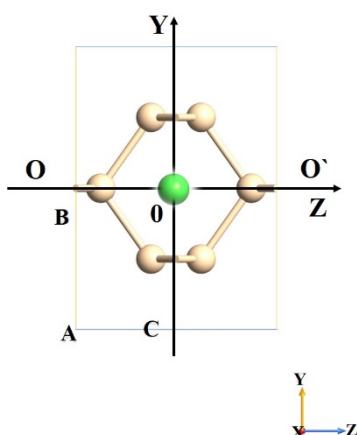
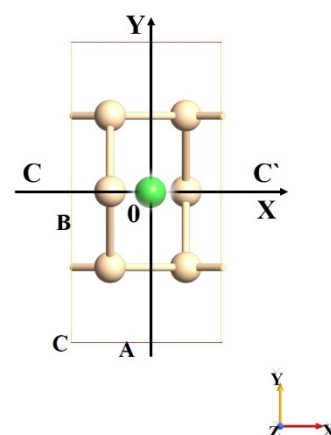
RESEARCH METHODOLOGY

In this work, the behavior of the energy of an interstitial nickel atom in the silicon crystal lattice was studied. For this purpose, based on first principles, the dependence of the lattice energy on the position of the interstitial nickel atom was analyzed. Figure 1 shows the primitive unit cell of the silicon crystal.

To calculate the dependence of the lattice energy on the position of the interstitial nickel atom, a minimal region of the silicon lattice was selected, constructed based on the primitive unit cell. For this, a lattice slice (lattice projection) in the (100) direction was considered (Fig.2). To form the first coordination sphere around the Ni atom, the cell shown in Figure 2 was translated in the Y direction (Fig.3).

**Figure 1.** Primitive unit cell of the silicon crystal**Figure 2.** Section of the silicon lattice in the (100) direction**Figure 3.** A silicon lattice cell obtained by translating the cut shown in Fig. 2 in the direction of the Y axis

The position of the nickel atom was considered relative to point O at the center of the obtained cell (Fig.3), so atoms located farther from this region, which did not belong to the first coordination sphere, were removed (Fig.4).

**Figure 4.** Cell and silicon atoms included in the first coordination sphere for the nickel impurity atom located in the region around point O**Figure 5.** Illustration of the OO' axis (Z-axis direction) along which various positions of the interstitial Ni atom were considered**Figure 6.** Illustration of the CC' axis (X-axis direction) along which various positions of the interstitial Ni atom were considered

The lattice energy was calculated for various positions of the interstitial Ni atom along the OO' axis (direction along the Z-axis) passing through the center of the formed cell (Fig. 5). The origin of the coordinate system was taken as the point corresponding to the center of volume O of the considered lattice cell. The dependence of the total energy on the position of the nickel atom was analyzed along two mutually perpendicular directions: along the OO' axis (direction along the Z-axis) and perpendicular to it along the CC' axis (direction along the X-axis), which also passes

through the center of the volume of the considered lattice (Fig. 6). The origin along this axis was also taken as the point corresponding to the center of the volume of the considered lattice.

When examining the energetic behavior of nickel impurity atoms, the most important characteristic is the binding energy of nickel atoms in the silicon lattice. To determine the binding energy of a Ni atom in the silicon lattice cell, it is necessary to subtract the total energy of the silicon cell and the Ni atom from the total energy of the system:

$$E_{\text{binding}} = E_{\text{total}} - E_{\text{Si}} - E_{\text{Ni}}$$

By performing these calculations for each position of the Ni atom within the silicon unit cell, one can obtain the dependence of the Ni atom's binding energy as it moves both along the OO' direction (Z axis) and along the CC' direction (X axis).

The calculations were carried out from first principles using the QuantumATK software. The molecular orbital method was employed, specifically the LCAO method (Linear Combination of Atomic Orbitals). To determine the electronic structure, the exchange-correlation functional Local Density Approximation (LDA) was chosen. The interatomic interactions were modeled using the PseudoDojo pseudopotential.

To increase the accuracy of the electronic density calculation, the density cutoff parameter of the computational grid was set to 75 Ry. The k-point mesh was chosen with a density of $4 \times 4 \times 0 \text{ \AA}^{-1}$, which is an optimal choice for electronic property calculations.

To study the behavior of the nickel atom during its transition from one cell to a neighboring one, the energy behavior was considered during movement along two adjacent cells both in the OO' (OZ) direction and in the CC' (OX) direction (Figs. 7 and 8). In the calculations, 12 silicon atoms were fixed, while the movement of the nickel atom was restricted to only one direction at a time, with the other two directions left free.

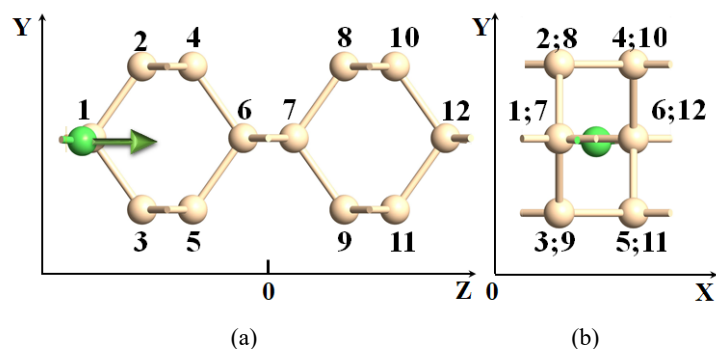


Figure 7. Structure of the considered silicon crystal cell with a nickel impurity atom (colored green) and the direction of nickel atom diffusion along the OZ axis (a) and view of the cell in cross-section (b). The numbers in the Figure mean the order number of atoms

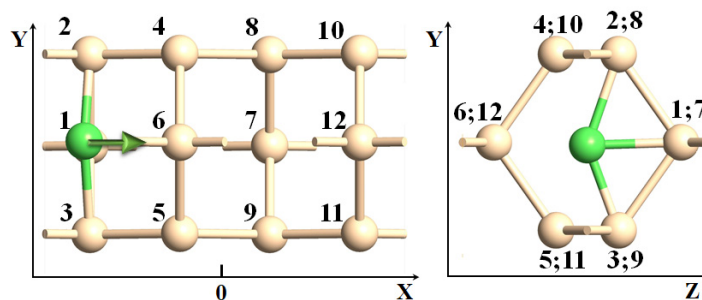


Figure 8. Structure of the considered silicon crystal cell with a nickel impurity atom (colored green) and the direction of nickel atom diffusion along the OX axis (a) and view of the cell in cross-section (b). The numbers in the Figure mean the order number of atoms

Structure optimization was also performed using the Optimize Geometry function of the program. During optimization, the force tolerance was set to 0.05 eV/Å, and the stress tolerance was set to 0.1 GPa [17, 18]. The maximum number of iterations was limited to 200, and the maximum step size was not allowed to exceed 0.2 Å. The optimization process was carried out using the LBFGS algorithm (Limited-memory Broyden-Fletcher-Goldfarb-Shanno).

For the optimized structure, the total energy was calculated, which allowed determination of the thermodynamically stable states of the system and the energetic configurations of the nickel atom in the silicon matrix. The applied methods provide high accuracy in calculating the electronic and structural properties of the system.

RESULTS AND DISCUSSION

The results of calculating the binding energy dependence of the interstitial nickel impurity atom on its position along two mutually perpendicular directions are shown in Figures 9 and 10. These graphs show that the activation

energy, defined as the energy required to transition from one equilibrium position to another, depends on the direction of movement within the lattice.

During diffusion of the nickel atom along the Z direction, several equilibrium positions appear with energies of 0.26, 0.32, 0.44, and 0.67 eV. The maximum energy required to overcome the barrier (diffusion activation energy) in this direction is 0.91 eV. During diffusion along the X direction, several equilibrium positions also appear, with approximately equal energies around 0.31 eV.

The activation energy values obtained from first-principles calculations (0.31 eV) lie between the values of 0.51 eV and 0.15 ± 0.04 eV reported in studies [8, 9], respectively.

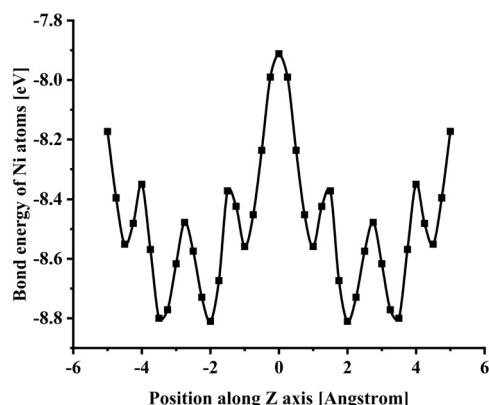


Figure 9. Dependence of the binding energy on the position of the Ni atom along the CC' axis (along the Z direction).

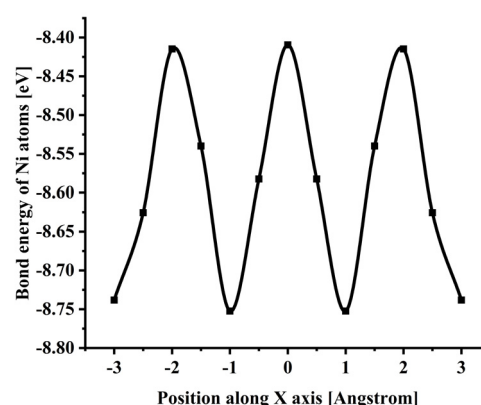


Figure 10. Dependence of the binding energy on the position of the Ni atom along the X direction.

However, when calculating diffusion parameters in real crystals, it is also necessary to take into account the influence of impurities (including electrically inactive ones) and point defects that have a significant concentration in semiconductor silicon under diffusion conditions. These include oxygen, carbon, boron, vacancies, divacancies, and interstitial silicon.

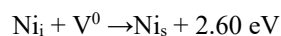
Since Ni_i is in a neutral charge state [7], there is no Coulomb attraction to small dopant impurities (such as boron).

The interaction between Ni_i and substitutional carbon (C_s) occurs with an energy of -0.31 eV [8]. This energy is comparable to the activation energy of nickel diffusion in pure silicon, so the carbon impurity does not affect diffusion.

The interaction between Ni_i and interstitial oxygen (O_i) is very weak: the formation energy of the complex is -0.07 eV [7]. This trapping energy is significantly lower than the activation energy of interstitial nickel atoms, which is 0.31 eV for diffusion in silicon [8,9]. Therefore, O_i does not impede Ni_i diffusion.

In work [7], the interaction of Ni_i with intrinsic interstitial silicon atoms (Si_i^0) and vacancies (V^0) was calculated. The interaction between interstitial nickel and silicon has little effect on nickel diffusion processes in silicon because the concentration of Si_i^0 is low [$\sim 10^9 \div 10^{11} \text{ cm}^{-3}$], and the binding energy is estimated to be $0.07 \div 0.10$ eV [7].

The interaction between Ni_i and V^0 is much stronger [10], since Ni becomes substitutional and forms four covalent Ni–Si bonds:



Such a reaction is highly likely to lead to the formation of chemical compounds—silicides—at the nickel-silicon interface. The flux of vacancies and divacancies from the silicon lattice volume slows down nickel diffusion and results in an increased concentration of substitutional nickel near the surface, forming a nickel-enriched layer.

The maximum nickel excess in the surface layer can reach $\exp(2.6/0.31) \approx 4 \times 10^3$ times the solubility of nickel in the lattice (10^{18} cm^{-3}). This allows estimating the maximum nickel concentration at the surface to be on the order of 10^{22} cm^{-3} . This roughly corresponds to experimental data [11].

During the cooling process after diffusion, the state of nickel atoms can easily change. Nickel, having high mobility in the silicon lattice, can form complexes with impurities (carbon, oxygen) and with each other, forming "nickel clusters."

As shown in [9], nickel atoms diffuse in silicon as electronically neutral atoms but with a changed quantum state ($3d^8 4s^2 \rightarrow 3d^{10} 4s^0$). According to Hund's rule, nickel atoms thus acquire a more stable state. At the same time, the atomic radius of nickel decreases from 12.5 nm to 10 nm . This enables nickel atoms to occupy interstitial sites and move through the interstitial positions without significant deformation of the silicon lattice. Since the size of the interstitial sites in silicon (12.7 nm) is larger than the radius of the nickel atom, it can be assumed that the cluster consists of electronically neutral nickel atoms located at interstitial positions in the silicon lattice and additionally bonded to each other, most likely by metallic-type bonding.

Based on the above, it can be assumed that electronically neutral nickel atoms in the clusters occupy the nearest equivalent interstitial positions and form a cubic nickel sublattice similar to the regular silicon lattice, with a lattice constant approximately equal to that of silicon.

We calculated [12] that the binding energy of nickel atoms to a nickel cluster is $\Delta E_k \approx 1.39$ eV, and the concentration of nickel atoms in the clusters is 6 to 8 orders of magnitude higher than the residual nickel concentration in the silicon lattice.

To verify the formation of clusters and silicides on the surface due to the high nickel concentration, the following studies were conducted:

Polished silicon wafers of grade KDB-0.5 were used. A layer of pure nickel, 1 μm thick, was deposited on the surface of the samples in a vacuum, followed by diffusion at $T_{\text{diff}} = 800 \div 950^\circ\text{C}$ for 30 to 60 minutes, and at $T_{\text{diff}} = 1000 \div 1200^\circ\text{C}$ for 5 to 60 minutes in an air atmosphere. The samples were cooled in air at a rate of approximately $50 \div 60^\circ\text{C}/\text{sec}$.

To determine the composition and distribution of nickel clusters, samples with clusters were studied using scanning electron microscopy (SEM) equipped with X-ray microanalysis, as well as by SIMS and IR microscopy methods.

During this experiment, it was found (see Fig. 11) that the surface density of nickel clusters is approximately 5×10^6 to 10^7 cm^{-2} on the silicon surface and about $(4 \div 5) \times 10^6 \text{ cm}^{-2}$ in the bulk. The distribution of clusters in the bulk is practically uniform, and their size is less than $0.5 \mu\text{m}$ (estimated by us to be from 20 to 100 nm), which confirms the results of studies [13–15].

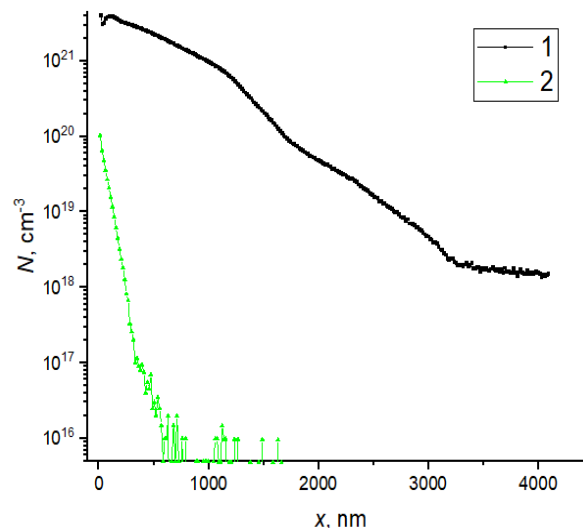


Figure 11. Distribution of nickel atoms in the front (1) and back (2) layers of silicon after diffusion from a metallic nickel film deposited on one surface of the silicon

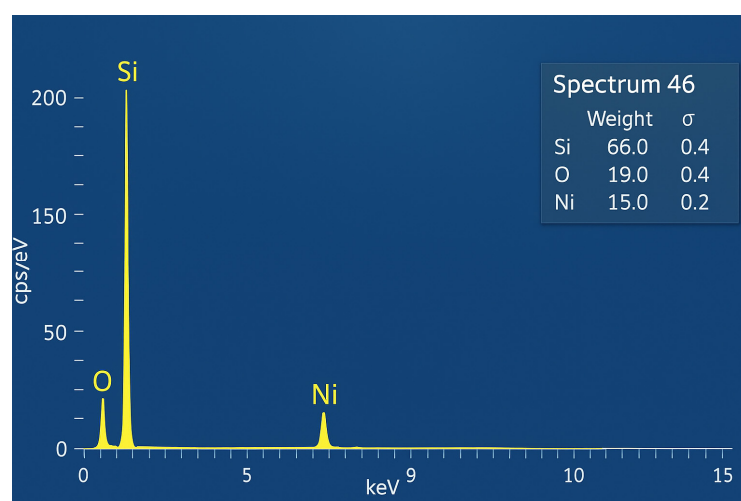


Figure 12. Spectrum and composition of clusters of nickel primium atoms on the silicon surface, obtained using a MIRA 3 TESCAN scanning electron microscope (Field-Emission Scanning Electron Microscope (FE-SEM)).

Fig. 12, shows the arrangement of nickel atom clusters on the silicon surface obtained using a MIRA 3 TESCAN (Field-Emission Scanning Electron Microscope (FE-SEM)). To verify that the observed clusters are nickel atom clusters, we studied their composition using the method (energy dispersive X-ray spectroscopy EDS).

Additional thermal annealing at relatively low temperatures should lead to the redistribution of isolated interstitial nickel atoms and to the growth of cluster sizes. The additional thermal annealing was carried out at $T_{ann} = 700 \div 900$ °C for 30 to 60 minutes in an air atmosphere. The cooling rate of the samples after annealing was not significant. The increase in cluster size makes it possible to study nickel clusters in silicon using infrared microscopy (on the INFRAM-I microscope).

As seen in Fig. 13, the nickel atoms introduced by diffusion are present in the lattice as clearly visible clusters, uniformly distributed throughout the crystal volume, which confirms the results of [16-18].

The cluster size depends on the presence of defects in the silicon lattice and the conditions of additional thermal treatment (degree of supersaturation). Based on the results of infrared microscopy, it can be concluded that the average cluster diameter increases to several microns after annealing, and the cluster concentration is on the order of $\sim 10^{10} \text{ cm}^{-3}$.

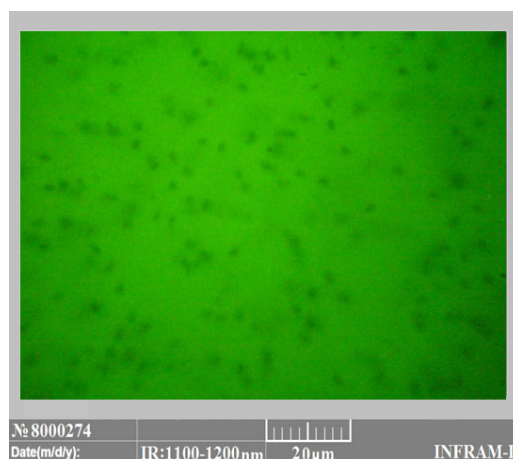


Figure 13. Clusters of impurity nickel atoms in the silicon lattice

CONCLUSION

As a result of the conducted study, it was established that nickel atoms in silicon predominantly diffuse through interstitial positions with the lowest activation energy along the crystallographic direction [100], with a value of 0.31 eV. It was found that at high nickel concentrations under thermal treatment conditions, stable clusters are formed, uniformly distributed throughout the crystal volume. These results confirm the important role of nickel as an effective gettering impurity and as a basis for controlling the recombination properties of silicon structures.

ORCID

©Bayrambay K. Ismaylov, <https://orcid.org/0000-0002-5880-4568>; ©Kanatbay A. Ismailov, <https://orcid.org/0000-0003-2867-0826>; ©Nurulla F. Zikrillayev, <https://orcid.org/0000-0002-6696-5265>; ©Atabek E. Atamuratov, <https://orcid.org/0000-0003-2173-3783>; ©Sergey V. Koveshnikov, <https://orcid.org/0000-0002-6897-4683>; ©Zoir T. Kenzhaev, <https://orcid.org/0000-0002-5335-0405>; ©Makhkam M. Khalilloev, <https://orcid.org/0000-0001-5497-6410>; ©Parakhat K. Dilimbetov, <https://orcid.org/0009-0009-1579-4273>

REFERENCES

- [1] B.K. Ismaylov, N.F. Zikrillayev, K.A. Ismailov, and Z.T. Kenzhaev, *Physical Sciences and Technology*, **10**(1), 13 (2023). <https://doi.org/10.26577/phst.2023.v10.i1.02>
- [2] M.K. Bakhadyrkhanov and S.Z. Zaynobidinov, *Semiconductors*, **14**, 412 (1980). (in Russian)
- [3] N.F. Zikrillayev, S.V. Koveshnikov, Levent Trabzonb, G.Kh. Mavlonova, B.K. Ismaylov, T.B. Ismailov, and F. E. Urakova, *Surface Engineering and Applied Electrochemistry*, **61**(1), 75 (2025). <https://doi.org/10.3103/S1068375524700571>
- [4] H. Kitagawa, *Sol. Stat. Phenom.* **71**, 51 (2000). <https://doi.org/10.4028/www.scientific.net/SSP.71.51>
- [5] A.A. Istratov, P. Zhang, R.J. McDonald, A.R. Smith, M. Seacrist, J. Moreland, J. Shen, *et al.*, *Journal of Applied Physics*, **97**, 023505 (2005). <https://doi.org/10.1063/1.1836852>
- [6] J. Lindroos, D.P. Fenning, D.J. Backlund, E. Verlage, A. Gorgulla, S.K. Estreicher, H. Savin, and T. Buonassisi, *Journal of Applied Physics*, **113**, 204906 (2013). <http://dx.doi.org/10.1063/1.4807799>
- [7] J. Lindroos, D. Sc. Thesis, "Copper-related light-induced degradation in crystalline silicon", Aalto University, 2015.
- [8] H. Kitagawa, and Sh. Tanaka, *Physica B: Condensed Matter*, **273**, 391 (1999). [https://doi.org/10.1016/S0921-4526\(99\)00487-1](https://doi.org/10.1016/S0921-4526(99)00487-1)
- [9] B.K. Ismaylov, N.F. Zikrillayev, K.A. Ismailov, and Z.T. Kenzhaev, *Semiconductor Physics, Quantum Electronics & Optoelectronics*, **27**(3), 294 (2024). <https://doi.org/10.15407/spqeo27.03.294>
- [10] Z.T. Kenzhaev, Kh.M. Iliev, K.A. Ismailov, G.Kh. Mavlonov, S.V. Koveshnikov, B.K. Ismaylov, and S.B. Isamov, *Physical Sciences and Technology*, **11**(1), 13 (2024). <https://doi.org/10.26577/phst2024v11i1a2>
- [11] K.A. Ismailov, N.F. Zikrillayev, B.K. Ismaylov, Kh. Kamalov, S.B. Isamov, and Z.T. Kenzhaev, *J. Nano- Electron. Phys.* **16**(5), 05022 (2024). [https://doi.org/10.21272/jnep.16\(5\).05022](https://doi.org/10.21272/jnep.16(5).05022)

- [12] Z.T. Kenzhaev, H.M. Iliev, V.B. Odzhaev, G.H. Mavlonov, V.S. Prosolovich, E.I. Kosbergenov, B.K. Ismailov, *et al.*, Surface Engineering and Applied Electrochemistry, **60**(6), 851 (2024). <https://doi.org/10.3103/S1068375524700467>
- [13] M.O. Tursunov, Kh.M. Iliev and B.K. Ismaylov, Physical Sciences and Technology, **11**(1), 4 (2024). <https://doi.org/10.26577/phst2024v11i1a1>
- [14] K.A. Ismailov, X.M. Iliev, M.O. Tursunov, and B.K. Ismaylov, Semiconductor Physics, Quantum Electronics & Optoelectronics, **24**(3), 255 (2021). <https://doi.org/10.15407/spqeo24.03.255>
- [15] I. Bayrambay, I. Kanatbay, K. Khayratdin, and S. Gulbadan, AIP Conference Proceedings, **2552**, 060015 (2022). <https://doi.org/10.1063/5.0129486>
- [16] N.F. Zikrillayev, S.V. Koveshnikov, X.S. Turekeev, and B.K. Ismailov, Journal of Surface Investigation: X-ray, Synchrotron and Neutron Techniques. **18**(1), 69 (2024). <https://doi.org/10.1134/S102745102401021X>
- [17] X.M. Iliyev, V.B. Odzhaev, S.B. Isamov, B.O. Isakov, B.K. Ismaylov, K.S. Ayupov, S.I. Hamrokulov, and S.O. Khasanbaeva, East Eur. J. Phys. (3), 363 (2023). <https://doi.org/10.26565/2312-4334-2023-3-38>
- [18] N.F. Zikrillayev, F.E. Urakova, A.R. Toshev, G.A. Kushiev, T.B. Ismailov, Y.A. Abduganiev, and N. Norkulov, East Eur. J. Phys. (1), 184 (2025). <https://doi.org/10.26565/2312-4334-2025-1-18>

ДОСЛІДЖЕННЯ ПОВЕДІНКИ АТОМІВ НІКЕЛЕВОЇ ПРИМІСІ В КРИСТАЛІЧНІЙ РІШІТЦІ КРЕМНІЮ НА ОСНОВІ ПЕРШИХ ПРИНЦИПІВ

Байрамбай К. Ісмаїлов^a, Канатбай А. Ісмаїлов^a, Нурулла Ф. Зікрілаєв^b, Атабек Е. Атамуратов^c,
Сергій В. Ковешніков^b, Зоїр Т. Кенжаєв^a, Махамм М. Халіллоєв^c, Парахат К. Ділімбетов^a

^aКаракалтакський державний університет імені Бердаха, Узбекистан, 230112, Нукус, вул. Ч. Абдірова, 1

^bТашкентський державний технічний університет, Узбекистан, 100095, Ташкент, вул. Університетська, 2

^cУргенцький державний університет, 220100, вул. Х. Олімжана, 14, Ургенч, Узбекистан

Ця робота представляє всебічне теоретичне та експериментальне дослідження поведінки атомів нікелевої домішки в кристалічній решітці кремнію. Основна увага приділяється аналізу механізмів дифузії, енергетичних характеристик міжвузлових атомів нікелю, їх взаємодії з дефектами та іншими домішками, а також утворенню стабільних кластерів у об'ємі кристала. Для моделювання з першопринципним підходом застосовувалося квантово-механічне програмне забезпечення QuantumATK із використанням методу лінійної комбінації атомних орбіталей (LCAO) та функціоналу обміну-кореляції локальної густини (LDA). Особливу увагу було приділено розрахунку енергії зв'язку атомів нікелю у міжвузлових положеннях та оцінці енергії активації їх міграції вздовж різних кристалографічних напрямків ([100] та [010]). Результати моделювання показали, що атоми нікелю переважно дифундують у міжвузлових положеннях з енергією активації близько 0,31 еВ, що добре узгоджується з раніше опублікованими експериментальними даними. Виявлено, що взаємодія нікелю з киснем, вуглецевими домішками та точковими дефектами має незначний вплив на процеси дифузії. Однак взаємодія з вакансіями призводить до утворення стабільних силіцидів нікелю та збільшення концентрації нікелю поблизу поверхні. Експериментальна частина дослідження підтвердила утворення кластерів нікелю при термічній обробці за високих температур. Методами скануючої електронної мікроскопії (SEM), вторинної іонної мас-спектрометрії (SIMS) та інфрачервоної (ІЧ) мікроскопії було виявлено високу щільність і рівномірний розподіл кластерів по всьому об'єму кристала. Розміри кластерів варіювалися від 20 до 100 нм, а концентрації досягали приблизно 10^{10} см⁻³. Ці результати демонструють, що нікель виступає як ефективна геттеруюча домішка, покращуючи електрофізичні властивості кремнію. Отримані дані є цінним внеском для оптимізації технологічних процесів виготовлення високоефективних кремнієвих сонячних елементів та мікроелектронних пристроїв.

Ключові слова: нікель; кремній; дифузія; кластери; міжвузлові атоми; першопринципне моделювання; енергія активації; квантовомеханічне моделювання; геттерування; напівпровідники

INVESTIGATION OF THE INFLUENCE OF NICKEL ON THE BEHAVIOR OF THERMAL DONORS IN SILICON

 Bayrambay K. Ismaylov^{a,c,*},  Nurulla F. Zikrillayev^b,  Kanatbay A. Ismailov^a,
 Khayratdin U. Kamalov^a,  Alloberdi K. Saparov^a

^aKarakalpak State University, Ch. Abdirov st. 1, Nukus, Karakalpakstan, 230100, Uzbekistan

^bTashkent state technical university, Uzbekistan, 100095, Tashkent, University St., 2

^cUniversity of Business and Science, Yakkabog MFY Gavhar street, house 1, Tashkent, Uzbekistan

*Corresponding Author E-mail: ismaylovb81@gmail.com; i.bayram@karsu.uz

Received June 1, 2025; revised July 8, 2025; accepted July 18, 2025

It has been established that doping silicon with nickel in the temperature range $T = 1000\div 1250^\circ\text{C}$ makes it possible to almost completely suppress the generation of thermal donors during thermal annealing in the temperature range $T = 100\div 700^\circ\text{C}$. It has been established that impurity nickel atoms form clusters and precipitates in silicon that absorb oxygen atoms. The most effective technological method for producing silicon with stable electrophysical parameters has been proposed. The proposed method for gettering uncontrolled impurity atoms can be used in the production of various electronic devices, especially in the development of efficient silicon-based solar cells.

Keywords: Diffusion; Cluster; Nickel; Oxygen; Thermal donor; Silicon

PACS: 78.30. Am

INTRODUCTION

Impurity nickel atoms, unlike other elements of transition groups, have not only the highest diffusion coefficient in silicon, but also high solubility in the crystal lattice ($N_{\text{Ni}} \sim 10^{18} \text{ cm}^{-3}$) [1,2]. However, the maximum concentration of electroactive impurity nickel atoms is less than $\sim 0.1\%$ of the total solubility of atoms at a given temperature, which means that the bulk of impurity nickel atoms in silicon are in an electrically neutral state.

The authors in [3-8] showed that some of the nickel atoms located in the interstices of the silicon crystal lattice can form impurity clusters and precipitates. The structure, size and distribution of the formed clusters are mainly determined by the defectiveness of the original silicon, the conditions of diffusion doping, the cooling rate after diffusion annealing, as well as the temperature and time of additional thermal annealing.

This work is devoted to the study of the electrophysical parameters of silicon doped with nickel impurity atoms at various temperatures, as well as its behavior during additional heat treatments in a wide range of temperatures (in which intensive generation of thermal donors occurs) and time.

MATERIALS AND METHODS

Single-crystalline silicon, grade KDB-1, grown by the Czochralski method of p - type conductivity with a boron concentration of $N_B \sim 2 \cdot 10^{15} \text{ cm}^{-3}$ was chosen as the starting material. The size of the samples was $1 \times 5 \times 10 \text{ mm}^3$. The concentration of residual oxygen in the studied silicon samples was $N_{\text{O}_2} \sim 6 \cdot 10^{17} \text{ cm}^{-3}$, the dislocation density $S \sim 10^3 \text{ cm}^{-2}$.

Ni diffusion was carried out from a layer of pure metallic nickel deposited on the surface of a silicon sample, both in open air and in evacuated quartz ampoules up to $P \sim 10^{-6} \text{ atm.}$ in the temperature range $T = 1000\div 1200^\circ\text{C}$. The diffusion time was chosen in such a way as to ensure a uniform distribution of nickel atoms in the volume of silicon. In separate ampoules, control silicon samples, without nickel admixture, were annealed under similar conditions in order to evaluate the effect of diffusion annealing on the electrical parameters of the original silicon samples. After diffusion annealing, the silicon samples were ground off on all sides by $5\div 10 \mu\text{m}$ to remove the surface layer enriched in nickel, and then etched by $5\div 7 \mu\text{m}$ with an alkaline etchant. Mechanical and chemical treatment of all samples was carried out under identical conditions. The electrical parameters of the samples were measured by the Van der Pauw method using an ECOPIA HALL HMS-3000 installation.

Table 1 shows the electrical parameters of silicon samples before and after diffusion of nickel impurity atoms at various temperatures and a duration of 120 minutes. As can be seen from the experimental results, samples doped with impurity nickel atoms at $T = 1220^\circ\text{C}$ practically retain their original electrical parameters, that is, no significant changes in parameters are observed in them, and in control samples annealed under the same conditions, but without impurity nickel atoms, resistivity increases 30 times

These experimental results show that at this thermal annealing temperature $T = 1220^\circ\text{C}$ the generation of thermal donors occurs, bound by oxygen atoms in the silicon lattice, and the concentration of thermal donors reaches ($N_d > 2 \cdot 10^{15} \text{ cm}^{-3}$), which is in good agreement with the results of the work [9-12].

As can be seen from Table 1, with a decrease in the diffusion annealing temperature, the resistivity of the control samples increases significantly (by 3 and 4 orders of magnitude) and reaches $\rho = 4 \cdot 10^4$ and $\rho = 2 \cdot 10^5 \Omega \cdot \text{cm}$ at annealing temperatures $T = 1170$ and 1120°C , respectively. At the same time, in samples doped with impurity nickel atoms, the electrical parameters practically do not change. These experimental results make it possible to determine the optimal conditions for doping silicon with nickel, which almost completely suppress the generation of thermal donors.

Table 1. Electrical parameters of control and nickel-doped silicon samples at different diffusion temperatures

no.	Before diffusion			Diffusion mode			After diffusion		
	Type conductivity	ρ , $\Omega \cdot \text{cm}$	μ , $\text{cm}^2/\text{V} \cdot \text{s}$	$T, ^\circ\text{C}$	t , min	Impurity	Type conductivity	ρ , $\Omega \cdot \text{cm}$	μ , $\text{cm}^2/\text{V} \cdot \text{s}$
		Resistivity	Mobility	Temperature	Time			Resistivity	Mobility
1	<i>p</i>	9.8	317	1220	120	<i>Ni</i>	<i>p</i>	9.2	354
	<i>p</i>	10.3	319		120	<i>Ni</i>	<i>p</i>	8.3	325
	<i>p</i>	10.1	285		120	<i>Control</i>	<i>n</i>	295	1075
2	<i>p</i>	9.5	355	1170	120	<i>Ni</i>	<i>p</i>	9.1	370
	<i>p</i>	10.4	327		120	<i>Ni</i>	<i>p</i>	9.75	335
	<i>p</i>	10.2	332		120	<i>Control</i>	<i>n</i>	$4 \cdot 10^4$	1052
3	<i>p</i>	10.8	335	1120	120	<i>Ni</i>	<i>p</i>	9.2	279
	<i>p</i>	9.6	322		120	<i>Ni</i>	<i>p</i>	9.9	314
	<i>p</i>	9.3	325		120	<i>Control</i>	<i>i</i>	$2 \cdot 10^5$	505
4	<i>p</i>	10.2	270	1070	120	<i>Ni</i>	<i>p</i>	9.75	315
	<i>p</i>	10.5	290		120	<i>Ni</i>	<i>p</i>	9.42	306
	<i>p</i>	9.7	297		120	<i>Control</i>	<i>p</i>	11.5	295
5	<i>p</i>	40.3	338	1170	120	<i>Ni</i>	<i>p</i>	45.5	340
	<i>p</i>	39.6	345		120	<i>Control</i>	<i>n</i>	$1.5 \cdot 10^3$	1130

Ni – nickel doped silicon samples, *C* – silicon control samples

The electrical parameters of the samples doped with nickel impurity atoms and the control samples annealed at the annealing temperature $T = 1070^\circ\text{C}$ do not differ significantly. This may be due to the fact that the concentration of thermal donors at this temperature and annealing time will be noticeably lower than the concentration of holes in the original samples. The results showed that in this case, the control silicon samples change their type of conductivity, that is, they become *n* - type with a resistivity of $\rho \sim 1.5 \cdot 10^3 \Omega \cdot \text{cm}$.

From an analysis of the research results, it was established that the influence of impurity nickel atoms on the generation of thermal donors does not depend on the conditions of nickel diffusion (in air or evacuated quartz ampoules).

In this regard, at the next stage of work, higher-resistance silicon samples of *p* and *n* type conductivity with different resistivity values were used as the starting material (Table 2).

Table 2. Technological parameters of the nickel alloying process.

Parameters of the original silicon		Ni diffusion temperature	Diffusion time	Heat treatment parameters after diffusion		Changing parameters after heat treatment	
Type conductivity	ρ , $\Omega \cdot \text{cm}$	$T, ^\circ\text{C}$	t , min	$T, ^\circ\text{C}$	t , hour	ρ , $\Omega \cdot \text{cm}$	τ , %
	Resistivity	Temperature	Time	Temperature	Time	Resistivity	Life time change
<i>n</i>	≤ 10	1100÷1150	15÷20	100÷700	$t=1 \div 20$	11÷13	does not change
<i>n</i>	≤ 40	1060÷1100	25	100÷600	$t=1 \div 20$	41÷46	+ 0 ÷ + 12
<i>n</i>	≤ 100	1050	30÷35	100÷500	$t=1 \div 20$	97÷105	+ 0 ÷ + 16
<i>p</i>	≤ 10	1150÷1100	15÷20	100÷700	$t=1 \div 20$	8÷12	little changes
<i>p</i>	≤ 40	1100÷1050	20÷25	100÷700	$t=1 \div 20$	43÷48	+16 ÷ +19
<i>p</i>	≤ 100	1050÷1000	30÷35	100÷500	$t=1 \div 20$	97÷106	9÷16

Table 2 shows the main technological conditions for doping with nickel impurities, under which the original electrical and recombination parameters of silicon are preserved after the diffusion process and after subsequent thermal annealing.

It has been established that the electrical and recombination parameters of silicon samples with nickel clusters remain unchanged during additional thermal annealing for a time $t = 1 \div 20$ hours in a wide range of heat treatment temperatures ($T = 100 \div 700^\circ\text{C}$).

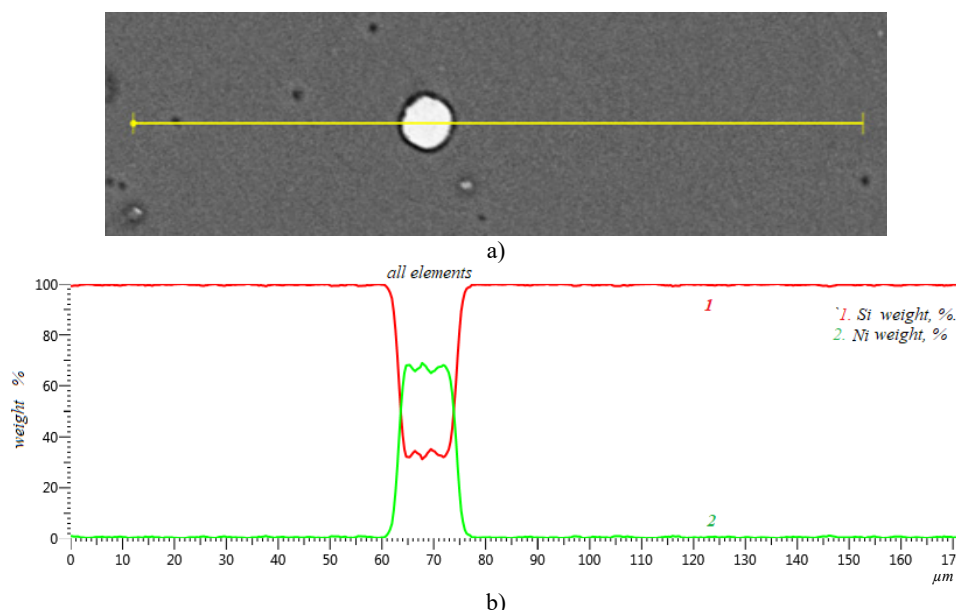


Figure 1. Distribution of nickel atoms on the surface of silicon samples

a) clusters of nickel atoms on the silicon surface, b) elemental composition of silicon doped with impurity nickel atoms

Analysis of the research results showed that electrically neutral nickel atoms in silicon are involved in the formation of clusters (Fig. 1), the size of which is on average $1 \div 10 \mu\text{m}$ and depends on the diffusion temperature and the cooling rate after diffusion annealing.

The composition of such clusters was studied using energy-dispersive X-ray spectroscopy (EDS). In Fig. 2 presents the results of these studies.

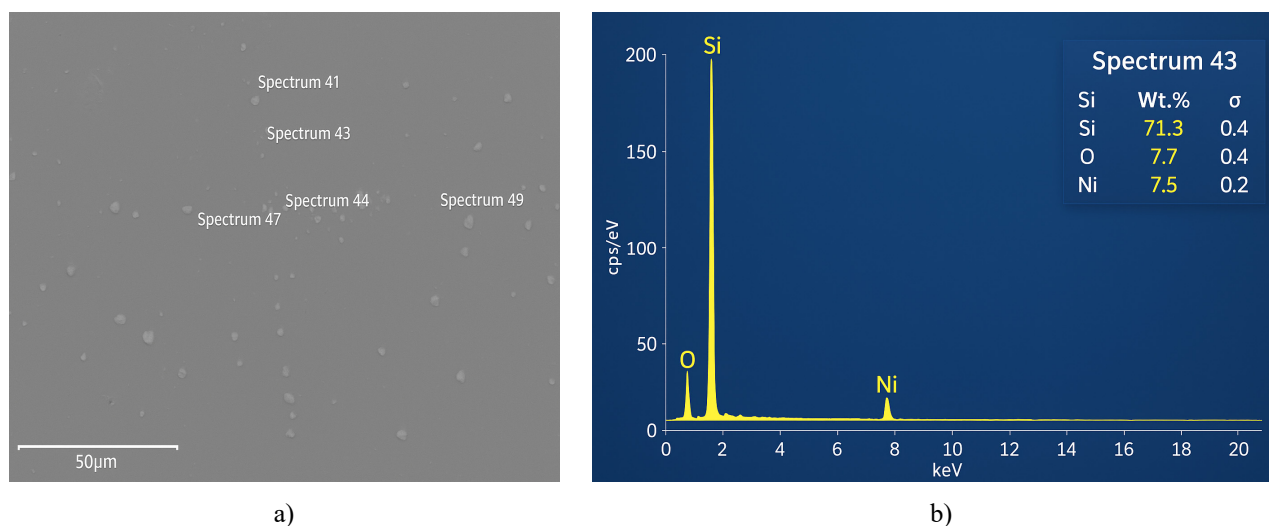


Figure 2. a) image of the surface, and b) elemental analysis of the surface of silicon doped with impurity nickel atoms at the “Spectrum 43” point

As can be seen from Table 3, the clusters consist of silicon, nickel and oxygen atoms. On average, the content of elements in them is: silicon atoms - 60%, nickel atoms - 3%, oxygen atoms - 11%. Based on these research results, it can be argued that impurity nickel atoms getter oxygen atoms when forming clusters. This means that clusters are a region of silicon enriched in nickel and oxygen atoms.

As is known from the literature, oxygen atoms in silicon are a source of thermal donors and also act as recombination centers [13]. This behavior is clearly manifested in control silicon samples (without nickel impurities). Thus, it can be assumed that electrically neutral nickel atoms form clusters that capture and retain a significant concentration of oxygen atoms and other uncontrolled impurities, and suppress the generation of thermal donors, which in turn ensures the stability of electrical parameters and recombination properties during various heat treatment processes [14-18].

Table 3. Result of elemental analysis of a sample of silicon doped with nickel atoms!

Element	Type line	Weight, %	σ , %	Atomic, %
Si	K series	71,3	0,4	59,9
O	K series	7,7	0,4	11,3
Ni	K series	7,5	0,2	3,03

CONCLUSIONS

From the analysis of the research results, it can be stated:

1. Impurity nickel atoms in the silicon lattice are mainly in electrically neutral states, easily forming clusters and precipitates.

2. Clusters of impurity nickel atoms can act as active getter centers for oxygen atoms and other impurities in silicon, thereby significantly suppressing the generation of thermal donors and other recombination centers in the silicon lattice.

3. The experimental results obtained show that the presence of impurity nickel atoms in silicon leads to stabilization of the initial electrical parameters of the samples, regardless of the type of conductivity and the concentration of the initial impurity boron and phosphorus atoms.

4. The optimal thermodynamic conditions for obtaining silicon samples with clusters of impurity nickel atoms and electrical parameters that are stable during heat treatment have been determined.

Acknowledgment

The authors express their gratitude to senior lecturer *S.V. Koveshnikov* for assistance in conducting experiments and discussing the results.

ORCID

Bayrambay K. Ismaylov, <https://orcid.org/0000-0002-5880-4568>; Nurulla F. Zikrillayev, <https://orcid.org/0000-0002-6696-5265>
 Kanatbay A. Ismailov, <https://orcid.org/0000-0003-2867-0826>; Khayratdin U. Kamalov, <https://orcid.org/0000-0002-1358-141X>;
 Alloverdi K. Saparov, <https://orcid.org/0009-0002-3049-5668>

REFERENCES

- [1] J. Lindroos, D.P. Fenning, D.J. Backlund, *et al.*, Nickel: "A very fast diffuser in silicon," *Journal of Applied Physics*, **113**(20), 204906 (2013). <https://doi.org/10.1063/1.4807799>
- [2] A.S. Astashenkov, D.I. Brinkevich, and V.V. Petrov, "Properties of Silicon Doped with Nickel Impurity by Diffusion," *Dokladi BGUIR*, **38**(8), 37-43 (2018). (in Russian)
- [3] B.K. Ismaylov, N.F. Zikrillayev, K.A. Ismailov, and Z.T. Kenzhaev, "Clusters of impurity nickel atoms and their migration in the crystal lattice of silicon," *Physical Sciences and Technology*, **10**(1-2), 13-18 (2023). <https://doi.org/10.26577/phst.2023.v10.i1.02>
- [4] K.A. Ismailov, N.F. Zikrillayev, B.K. Ismaylov, Kh. Kamalov, S.B. Isamov, and Z.T. Kenzhaev, "Nickel Clusters in the Silicon Lattice," *J. Nano- Electron. Phys.* **16**(5), 05022 (2024). [https://doi.org/10.21272/jnep.16\(5\).05022](https://doi.org/10.21272/jnep.16(5).05022)
- [5] M.K. Bakhadyrkhanov, B.K. Ismaylov, S.A. Tachilin, K.A. Ismailov, and N.F. Zikrillayev, "Influence of electrically neutral nickel atoms on electrical and recombination parameters of silicon," *Semiconductor Physics, Quantum Electronics and Optoelectronics*, **23**(4), 361-365 (2020). <https://doi.org/10.15407/spqeo23.04.361>
- [6] M.G. Milvidsky, and V.V. Chaldyshev, "Nanometer-size atomic clusters in semiconductors—a new approach to tailoring material properties," *Semiconductors*, **32**(5), 513-522 (1998). <https://doi.org/10.1134/1.1187418>
- [7] B.K. Ismaylov, N.F. Zikrillayev, K.A. Ismailov, and Z.T. Kenzhaev, "Physical mechanism of gettering of impurity Ni atom clusters in Si lattice. *Semiconductor Physics*," *Quantum Electronics & Optoelectronics*, **27**(3), 294-297 (2024). <https://doi.org/10.15407/spqeo27.03.294>
- [8] N.A. Turgunov, E.Kh. Berkinov, and R.M. Turmanova, "The effect of thermal annealing on the electrophysical properties of samples n-Si<Ni, Cu>," *East Eur. J. Phys.* (3), 287 (2023). <https://doi.org/10.26565/2312-4334-2023-3-26>
- [9] V.V. Voronkov, G.I. Voronkova, A.V. Batunina, V.N. Golovina, M.G. Milvidskiy, *et al.*, "Generation of thermal donors in silicon influence of self-interstitial atoms," *Fizika tverdogo tela*, **42**(11), 1965-1975 (2000). (in Russian)
- [10] V.B. Neymash, Ye.A. Puzenko, A.N. Kabaldin, A.N. Kraychinskiy, and N.N. Krasko, "On the nature of nuclei for the formation of thermal donors in silicon," "Fizika i tekhnika poluprovodnikov". **33**(12) 1423-1427 (1999). (in Russian)
- [11] V.M. Babich, *et al.*, *Oxygen in silicon single crystals*, (Interpres LTD", Ukraine, 1997), pp. 46.
- [12] P.A. Selishev, "Kinetics of formation of oxygen-containing thermodonors in silicon and formation of their non-uniform distribution," *Fizika i tekhnika poluprovodnikov*, **35**(1) 11-14 (2001). (in Russian)
- [13] Yu.A. Yakimov, and E.A. Klimanov, "Modeling of gettering processes of generation-recombination centers in silicon during diffusion of phosphorus and boron," *Prikladnaya fizika*, **5**(1), 15-20 (2015). (in Russian)
- [14] M.K. Bakhadyrkhanov, Z.T. Kenzhaev, Kh.S. Turekeev, B.O. Isakov, and A.A. Usmonov, "Gettering properties of nickel in silicon photocells," *Technical Physics*, **11**(14), 2217-2220 (2021). <https://doi.org/10.21883/JTF.2021.11.51529.99-21>
- [15] I. Bayrambay, I. Kanatbay, K. Khayratdin, and S. Gulbadan, "Suppression of Harmful Impurity Atoms With Clusters of Nickel Impurity Atoms in a Silicon Lattice," *AIP Conference Proceedings*, **2552**, 060015 (2022). <https://doi.org/10.1063/5.0129486>
- [16] K.A. Ismailov, Z.T. Kenzhaev, S.V. Koveshnikov, E.Z. Kosbergenov, and B.K. Ismaylov, "Radiation Stability of Nickel Doped Solar Cells", *Physics of the Solid State*, **64**(3), 154–156 (2022). <https://doi.org/10.1134/S1063783422040011>
- [17] A. Galashev, and A. Vorobev, "Electronic properties and structure of silicene on Cu and Ni substrates," *Materials*, **15**(2), 3863 (2022). <https://doi.org/10.3390/ma15113863>

- [18] Z.T. Kenzhaev, Kh.M. Iliev, K.A. Ismailov, G.Kh. Mavlonov, S.V. Koveshnikov, B.K. Ismaylov, and S.B. Isamov, "Physical mechanisms of gettering properties of nickel clusters in silicon solar cells," *Physical Sciences and Technology*, **11**(1-2), 13-22 (2024). <https://doi.org/10.26577/phst2024v11i1a2>

ДОСЛІДЖЕННЯ ВПЛИВУ НІКЕЛЮ НА ПОВЕДІНКУ ТЕПЛОВИХ ДОНОРІВ У КРЕМНІЇ
**Байрамбай К. Ісмаїлов^{а,с}, Нурулла Ф. Зікриллаєв^б, Канатбай А. Ісмаїлов^а, Хайратдін У. Камалов^а,
Аллоберді К. Сапаров^а**

^а*Каракалпакський державний університет. 1 ч. Abdirov st., Нукус, Каракалпакстан 230100, Узбекистан*

^б*Ташкентський державний технічний університет, Узбекистан, 100095, м. Ташкент, вул. Університетська, 2*

^с*Університет бізнесу і науки, вул. Яккабог МФУ Гавхар, 1, Ташкент, Узбекистан*

Встановлено, що легування кремнію нікелем в інтервалі температур $T = 1000 \div 1250$ °С дозволяє практично повністю придушити генерацію термодонорів під час термічного відпалу в інтервалі температур $T = 100 \div 700$ °С. Встановлено, що домішкові атоми нікелю утворюють у кремнії кластери та осади, які поглинають атоми кисню. Запропоновано найбільш ефективний технологічний спосіб отримання кремнію зі стабільними електрофізичними параметрами. Запропонований метод гетерування неконтрольованих домішкових атомів може бути використаний у виробництві різних електронних пристроїв, особливо при розробці ефективних сонячних елементів на основі кремнію.

Ключові слова: дифузія; кластер; нікель; кисень; термодонор; кремній

INFLUENCE OF AN ADDITIONAL P3HT LAYER ON THE PERFORMANCE OF P3HT: IC₆₀BA POLYMER SOLAR CELL

 Chittur Devarajan Ramabadran^{a,b§},  K. Sebastian Sudheer^{a*}

^aDepartment of Physics, Opto-electronic Device Simulation Research Lab, Christ College [Autonomous], Irinjalakuda, Thrissur, 680125, University of Calicut, Kerala, India

^bDepartment of Physics, Government College, Chittur, Palakkad, 678104, University of Calicut, Kerala, India

Corresponding Author e-mail: [§]ramabadrandc@christcollegeijk.edu.in; *e-mail: sudheersebastian@christcollegeijk.edu.in

Received May 9, 2025; revised July 11, 2025; accepted July 17, 2025

A simulation study utilizing SCAPS 1-D software was conducted to explore the effects of an additional P3HT (Poly 3-hexylthiophene) layer on the performance of bulk heterojunction polymer solar cells, specifically with the active layer P3HT: IC₆₀BA. The investigated cell structure is ITO/PEDOT:PSS/P3HT/P3HT:IC₆₀BA/ZnO NPs/Al. Following the standardization of the software, we determined the optimal parameters of the solar cell structure by analyzing various factors influencing cell performance across different layers. Subsequently, after optimizing the structure, the power conversion efficiency (PCE) improved significantly, rising from 5.18% without additional layer to 15.26% with additional layer.

Keywords: Bulk heterojunction polymer solar cell; Fullerene; SCAPS 1-D; Active Layer; ETL; HTL

PACS: 84.60.Jt; 81.05.Lg; 07.05.Tp

1. INTRODUCTION

A polymer solar cell (PSC) is an organic solar cell that utilizes polymers as the primary component for converting sunlight into electrical energy. The operation of PSCs relies on photoinduced charge transfer between a donor (the polymer) and an acceptor, typically a fullerene derivative. When exposed to sunlight, excitons are generated within the polymer, which then separate into electrons and holes at the donor-acceptor interface. These charge carriers are subsequently collected at the electrodes, producing an electric current. Key characteristics of PSCs include their ease of fabrication, adaptability, and low production costs. Additionally, they can be made partially transparent. However, a significant limitation is their relatively low power conversion efficiency (PCE), comparable to that of traditional silicon solar cells. While PSCs hold environmental advantages, they often exhibit lower stability and increased susceptibility to environmental changes.

Polymer solar cells (PSCs) can be broadly categorized into four main types: tandem PSCs, bulk heterojunction PSCs (the most prevalent and favored type), single-layer PSCs, and bilayer PSCs. These solar cells find applications in wearable technology, portable electronics, integrated photovoltaics, and energy harvesting for the Internet of Things. One of the key materials used in bulk heterojunction (BHJ) polymer solar cells is poly(3-hexylthiophene) (P3HT), which is notable for its high hole mobility, environmental stability, and extended absorption in the red region. Consequently, [6,6]-phenyl-C61-butyric acid methyl ester (PCBM), a soluble C60 derivative, has emerged as one of the most widely utilized organic semiconductors for acting as an electron acceptor [1-3]. P3HT:PCBM solar cells have demonstrated an open circuit voltage (Voc) of approximately 0.6 V [4], attributed to the low LUMO energy levels of PCBM, which is around -3.8 eV. In 2009, a novel C60 derivative named indene-C60 bisadduct (IC₆₀BA) was introduced, and due to its higher LUMO energy levels of approximately -3.74 eV, IC₆₀BA has increasingly replaced PCBM as the preferred acceptor material in these solar cells [14]. This substitution has resulted in improved efficiencies and a higher Voc of about 0.84 V [5-9].

Bulk heterojunction organic solar cells (OSCs), in which the donor and acceptor materials are combined to form the active layer, were first proposed by Yu et al. in 1995. Since the introduction of this bulk heterojunction (BHJ) structure, the power conversion efficiency (PCE) of BHJ OSCs has significantly improved, rendering it a promising technology. Heeger and colleagues [10] were the first to utilize the BHJ structure for polymer-fullerene blends. Subsequent research revealed that increasing the diameters of the donor and acceptor domains through various additive techniques leads to enhanced performance [11,12]. In an effort to improve results and address the limitations associated with the poly(3-hexylthiophene) and [6,6]-phenyl-C61-butyric acid methyl ester (P3HT:PCBM) blend, which exhibits a relatively low open-circuit voltage (Voc) of 0.6 V, Li et al. demonstrated the use of indene-C60 bisadduct (IC₆₀BA) as an electron acceptor in BHJ PSCs [13]. This P3HT:IC₆₀BA combination resulted in higher PCE values and an increased Voc of approximately 0.84 V [14,15].

In this study, the solar cell comprised of P3HT:IC₆₀BA (poly(3-hexylthiophene): (indene-C60 bisadduct) was simulated using SCAPS 1-D Software [16]. The simulation software was standardized by comparing the simulated output with experimental data [17]. In the numerical simulation of the polymer solar cell (PSC), the hole transport layer (HTL) is represented by PEDOT:PSS, the active layer by the fullerene blend P3HT: IC₆₀BA, and the electron transport layer (ETL) by ZnO nanoparticles (ZnONPs). Aluminum (Al) and indium tin oxide (ITO) serve as the electrode materials in

this structure. The performance of a polymer solar cell with P3HT: IC₆₀BA as the active layer is improved when P3HT is added as an extra layer. Based on previous investigations, the operational performance and efficiency of the device were augmented to 26.5% through the incorporation of an ultrathin P3HT polymeric layer serving as an interfacial medium between the hole transport material and the perovskite layer [18]. In order to effectively separate and collect charges, P3HT helps to increase the mobility of electrons and holes, which adds to improved charge transport qualities. It assists in maximizing the open-circuit voltage and current density by maximizing energy level alignment at the heterojunction interface [19,20]. P3HT can improve the active layer's structural ordering and crystallinity, resulting in bigger crystal domain sizes that strengthen the interpenetrating network necessary for efficient charge transfer [17]. Furthermore, P3HT's solubility in common solvents makes it possible to use simple solution-processing processes, which increases the layers' scalability and compatibility with a range of production methods [21]. All things considered, these characteristics help the solar cells' power conversion efficiency to rise noticeably. To the best of our knowledge, this is the first simulation study reporting the impact of using P3HT on Polymer solar cell with P3HT:IC₆₀BA as active layer. In this simulation, we specifically investigated the impact of adding P3HT layer to the structure above.

2. DEVICE SIMULATION METHODOLOGY

The one-dimensional Solar Cell Capacitance Simulator (SCAPS) version 3.3.08 was employed as the numerical simulation tool in this investigation. This software is capable of solving both optical and electrical models throughout the entire configuration. We utilized a 1.5 AM spectrum for illumination. Previous simulations have focused on various types of solar cells, including perovskite, fullerene, non-fullerene bulk heterojunction (BHJ), and tandem solar cells (Abdelaziz et al., 2019, 2020; Gupta and Dixit, 2018; Bahrami et al., 2019). The application allows users to modify parameters and select the desired output across its various panels. Additionally, the software numerically solves Burgelman et al.'s generic semiconductor equations to obtain a steady-state operating point solution [16]

Equations foundational to semiconductors, including the Poisson equation, continuity equations, drift equations, and diffusion current equations, are used to efficiently evaluate the electrical performance of electronic devices when stimulated. The stimulation can take the form of heat energy, photons, or voltages. This indicates that we can compute the electrical performance of the devices and analyze their I-V characteristics using these equations. Consequently, these equations provide a theoretical basis for interpreting and assessing the measured performance of the devices. Furthermore, they can be employed to reduce experimental labor costs and to evaluate and predict the performance of new device structures, potentially leading to significant savings in both time and money.

They can be applied to streamline mathematical analysis and determine the ideal device structure parameters. The local microscopic behaviour of the material is described by these differential equations. The local electric field change resulting from the volumetric charge density at a particular location within a material is described by the Poisson equation [Equation 1]. The conservation of electrons and holes at a specific place in the material is expressed by the continuity equations [Equation 2]. In this instance, an electric field (drift current) or a concentration gradient (diffusion current) is driving the electron and hole currents [Equations 4-5]. [22]

$$\frac{\partial \epsilon_0 \epsilon}{\partial x} \frac{\partial \Psi}{\partial x} = -q (p - n + N_D - N_A + \frac{\rho_{def}}{q}), \quad (1)$$

$$-\frac{\partial J_n}{\partial x} - Un + G = \frac{\partial n}{\partial t}, \quad (2)$$

$$-\frac{\partial J_p}{\partial x} - Up + G = \frac{\partial p}{\partial t}, \quad (3)$$

$$J_n = -\frac{\mu_n n}{q} \frac{\partial E_{Fn}}{\partial x}, \quad (4)$$

$$J_p = +\frac{\mu_p p}{q} \frac{\partial E_{Fp}}{\partial x}. \quad (5)$$

In the abovementioned equations, the charge is denoted by q , and the electrostatic potential is denoted by Ψ . The symbols p , n , stand for free holes and electrons, respectively. Ionised donor-like and ionised acceptor-like doping concentrations are denoted by N_D and N_A . Here, ϵ signifies absolute permittivity, while ϵ_0 denotes permittivity in free space. The terms J_n and J_p signify electron and hole current densities, respectively, whereas Un denotes electron recombination rate. G is the generation rate, while Up is the rate of hole recombination. In contrast to what has been described so far, E_{Fn} and E_{Fp} stand for the electron and hole quasi-Fermi levels, whereas n and p indicate the electron and hole mobility, respectively

The glass substrate/ITO/PEDOT: PSS/P3HT:IC₆₀BA/ZnONPS/Al simulated bulk heterojunction structure is shown in Figure 1. The simulation's material properties, such as electron affinity (χ), bandgap energy (E_g), and relative permittivity (ϵ_r), are displayed in Table 1. Hole and electron mobilities are μ_p and μ_n , respectively. Donor and acceptor densities are denoted by N_D and N_A , respectively. The effective densities of states in the valence and conduction bands are denoted by N_v and N_c , respectively, while the defect density is represented by N_t . 4.8 and 4.2 eV are the settings for the anode and cathode work functions, respectively. The capture cross section for holes and electrons is set to $1 \times 10^{-25} \text{ cm}^2$ across all layers, and the thermal velocity is set to 10^7 cm/s .

The four primary output parameters of a solar cell are power conversion efficiency (PCE), fill factor (FF), short circuit current (Jsc), and open circuit voltage (Voc). The necessary material parameters for simulation and absorption spectra have been compiled from the literature [16,17, 21–35]. A comparison analysis of the simulated and experimental data for SCAPS 1-D calibration is presented in Table 2. Additionally, Figure 2 illustrates the simulated polymer solar cell structure with additional P3HT layer.

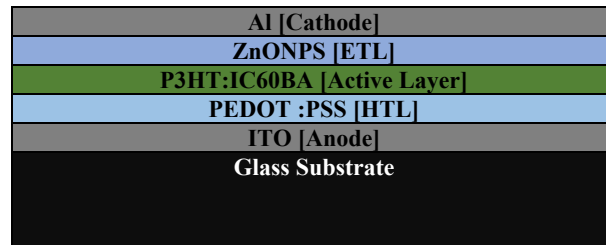


Figure 1. Simulated Bulk Heterojunction Polymer Solar Cell Structure for Standardization of SCAPS 1D

Table 1. Simulation parameters of Bulk Heterojunction Polymer Solar Cell

Parameters	HTL	Active Layer	ETL
Thickness [nm]	27	250	46
E _g (eV)	1.6	1.68	3.2
χ (eV)	3.4	3.880	4.6
ε _r	3.0	3.3	9.0
μ _n cm ² /vs	10	10 ⁷	10 ⁷
μ _p cm ² /vs	400	10 ⁷	10 ⁷
N _A (cm ⁻³)	10 ¹⁵	0	0
N _D (cm ⁻³)	0	3.2×10 ¹⁸	1.1×10 ¹⁸
N _C (cm ⁻³)	2.2×10 ¹⁵	1.6×10 ²⁰	2.2×10 ¹⁹
N _V (cm ⁻³)	1.8×10 ¹⁸	10 ¹⁹	1.8×10 ¹⁹
N _t (cm ⁻³)	10 ¹⁵	10 ¹⁶	10 ¹⁵

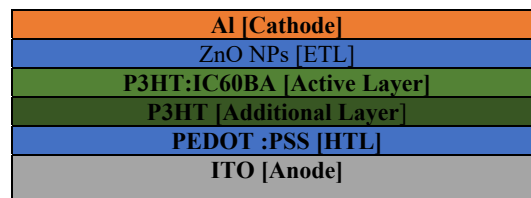


Figure 2. Simulated Polymer Solar Cell Structure

Table 2. Comparison of simulated parameters with experimental results

Parameters	Experimental	Simulated
Voc (V)	0.84	0.85
Jsc(mA/cm ²)	8.36	8.21
FF(%)	59	57
PCE(%)	4.1	3.97

3. RESULTS AND DISCUSSION

We will analyze the solar cell structure shown in Figure 2 in greater detail. Each layer of the structure is examined to determine its performance under various parameters for optimal results. To achieve these optimal outcomes, new device structures are developed and their performance is thoroughly investigated. The following section provides an explanation of the simulation studies that were conducted.

3.1 Effect of Active Layer thickness

The thickness of the active layer is varied between 100 and 300 nm to assess the characteristics related to solar cell performance. The parameters Voc, Jsc, FF, and PCE demonstrate similar trends, with all reaching their optimal values at a thickness of 300 nm. These improvements at the ideal thickness can be attributed to reduced recombination and enhanced light absorption. Increasing the active layer thickness may enhance Jsc by allowing more light to be absorbed. However, this relationship is nonlinear; beyond an optimal thickness, it is affected by increased charge recombination and decreased charge transport efficiency, leading to diminishing returns [36, 37]. While Voc is not directly influenced by the thickness of the active layer, it is primarily determined by the energy levels of the donor and acceptor materials.

Nevertheless, recombination dynamics and the quality of the interface may play significant roles in its behavior [38, 39]. Certain experiments have demonstrated that increasing the thickness of the active layer can improve the power conversion efficiency (PCE) to a certain extent. The relevant graph is presented in Figure 3.

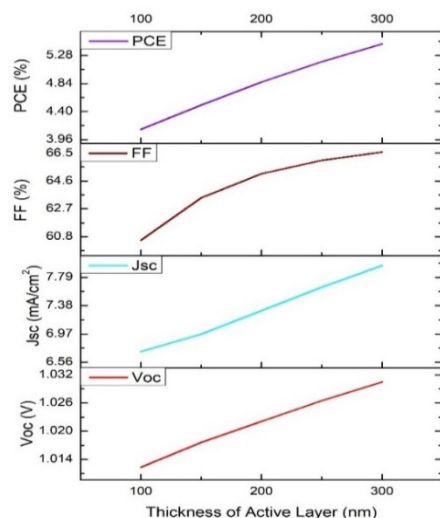


Figure 3. Influence of Active Layer Thickness

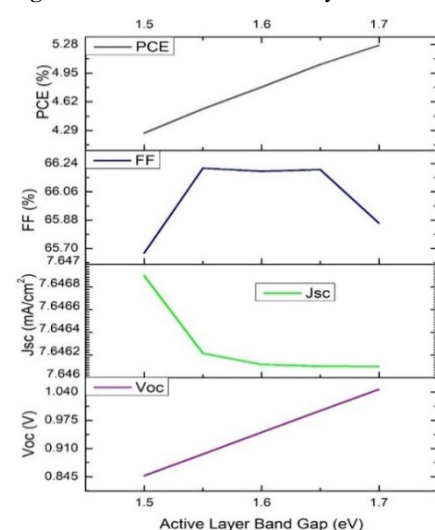


Figure 4. Influence of Active Layer Bandgap

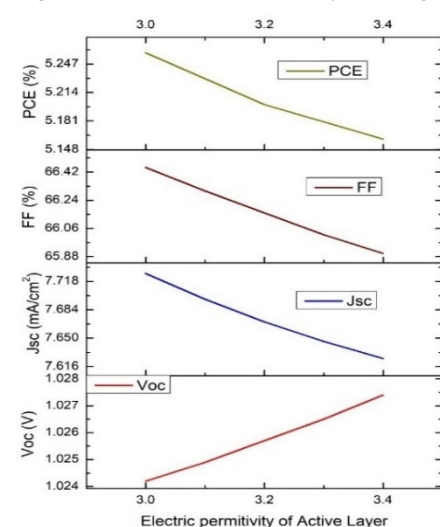


Figure 5. Influence of Electric Permittivity of Active Layer

3.2 Influence of Active Layer Band Gap

The active layer band gap is varied from 1.5 eV to 1.7 eV, and both power conversion efficiency (PCE) and open-circuit voltage (Voc) exhibit similar variations with bandgap. Both PCE and Voc reach their maximum at 1.7 eV. In organic solar cells, Voc is determined by the difference between the lowest unoccupied molecular orbital (LUMO) of the acceptor material and the highest occupied molecular orbital (HOMO) of the donor material. As the bandgap of the active layer increases, the Voc tends to increase as well, reflecting either a higher LUMO level of the donor or a lower HOMO level of the acceptor. This relationship is influenced by the energy levels of the donor and acceptor materials, which impact Voc in connection with the difference between the quasi-Fermi levels of the electrons and holes. A larger bandgap reduces the energy loss between the bandgap energy (E_g) and Voc. However, in organic solar cells, the Voc is generally lower than the bandgap energy due to non-radiative recombination and other losses. As the bandgap increases, Voc approaches E_g , resulting in an overall increase in Voc. Furthermore, the power conversion efficiency of a solar cell is calculated by multiplying its fill factor (FF), open-circuit voltage (Voc), and short-circuit current (Jsc).

As mentioned earlier, an increase in the bandgap can lead to a higher open-circuit voltage (Voc), which may subsequently enhance the power conversion efficiency (PCE). However, a wider bandgap often results in reduced solar spectrum absorption by the solar cell, particularly in the infrared region, which can lower the short-circuit current (Jsc). Nevertheless, in some cases, the increase in Voc associated with a wider bandgap can compensate for the decrease in Jsc, resulting in an overall increase in PCE. Additionally, the fill factor (FF) may improve with an increasing bandgap due to enhanced charge carrier transfer [40], although this trend is not always consistent. With further increases in bandgap, FF may remain stable or even decline, possibly due to the effects of recombination processes and exciton lifetimes [41, 42]. The relationship between FF and bandgap is complex and depends on the specific materials and cell architecture used in the organic solar cell. The relevant graph illustrating these dynamics is presented in Figure 4.

3.3 Effect of Electric Permittivity of Active Layer

In this section, we have analyzed the impact of the active layer's electric permittivity [ϵ] on the performance of the polymer solar cell. The electric permittivity is varied from 3.0 to 3.4. The findings indicate that while the open-circuit voltage (Voc) increases with ϵ , all other parameters are found to decrease. The electric permittivity of the active layer influences the dielectric properties of the material, which in turn affects the open-circuit voltage of polymer solar cells (PSCs). Consequently, a higher electric permittivity in the active layer may lead to an increase in Voc due to its effect on the dynamics of charge carriers within the solar cell.

A higher electric permittivity enhances charge carrier separation and reduces recombination losses by decreasing the Coulombic interaction between charge carriers [43]. This improvement can result in a stronger built-in electric field and more efficient charge extraction, both of which contribute to an increased open-circuit voltage (Voc). However, optimizing the performance of polymer solar cells (PSCs) requires a comprehensive understanding

of all contributing parameters, as a higher permittivity can indeed enhance Voc. The electric permittivity of the active layer also influences the short-circuit current (Jsc), fill factor (FF), and power conversion efficiency (PCE) of PSCs by affecting the dissociation of photogenerated electron-hole pairs and the movement of charge carriers within the device. Elevated Coulombic attraction between opposing charges can occur with high electric permittivity, potentially hindering their separation and reducing Jsc [44]. Additionally, a larger permittivity may negatively impact charge carrier mobility, leading to increased recombination rates and declines in both FF and PCE. The relevant graph illustrating these relationships is presented in Figure 5.

3.4: Effect of Conduction Band Density of States of Active Layer

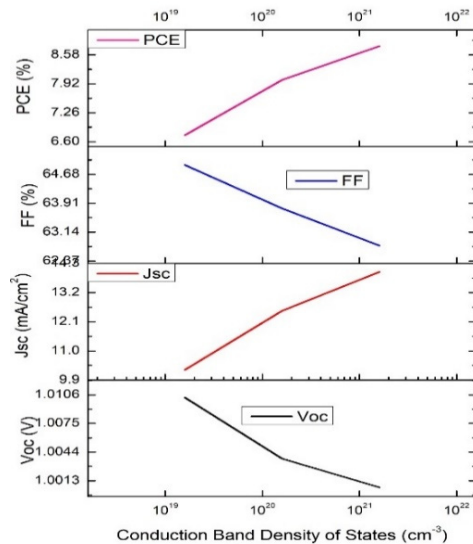


Figure 6. Influence of CB density of states of Active Layer

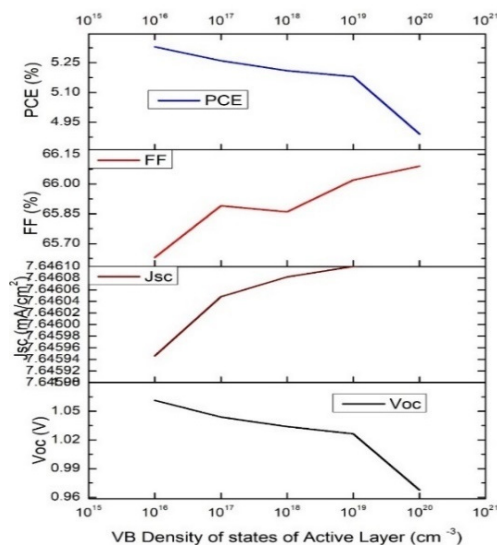


Figure 7. Influence of VB density of states of Active Layer

seem beneficial, it generates more energy states that facilitate non-radiative recombination processes and hinder charge transport, which adversely affects both PCE and Voc [47-48]. Figure 7 shows the respective graph.

3.6. Effect of Shallow Uniform Density of States of Active Layer

The shallow uniform density of states in the active layer experiences a significant shift from 3.2×10^{14} to $3.2 \times 10^{16} \text{ cm}^{-3}$. As this density increases, parameters such as open-circuit voltage (Voc), fill factor (FF), and power conversion efficiency (PCE) tend to improve, while the short-circuit current (Jsc) shows a decline. An elevated donor density can enhance the intrinsic potential across the junction by increasing the availability of charge carriers. This rise in potential positively impacts Voc, which is crucial for the efficient operation of solar cells, as it reduces losses during charge separation. Furthermore, an increase in donor density leads to enhanced conductivity within the active layer, which

In this section, we examine how varying the conduction band density of states in the active layer from 1.6×10^{19} to $1.6 \times 10^{21} \text{ cm}^{-3}$ affects the performance metrics of polymer solar cells. Figure 6 illustrates the corresponding data. The graph indicates that while short-circuit current (Jsc) and power conversion efficiency (PCE) fluctuate similarly, the open-circuit voltage (Voc) and fill factor (FF) do not exhibit the same trend. The decline in Voc with an increase in the conduction band density of states in the active layer is primarily attributed to enhanced recombination losses and shifts in the Fermi level.

Recombination events are more likely to occur when the density of states is higher, as this provides more energy levels for charge carriers to occupy [45]. The increase in short-circuit current density (Jsc) associated with a higher conduction band density of states (DOS) in the active layer can be attributed to increased charge carrier generation and improved collection efficiency. A greater DOS enhances the availability of conduction states, leading to more efficient photon absorption and, consequently, a higher production of electron-hole pairs. This directly correlates with an increase in Jsc [46]. However, the rise in power conversion efficiency (PCE) and the decline in fill factor (FF) of polymer solar cells with an increasing conduction band DOS result from a combination of enhanced charge generation and increased recombination losses. While a higher DOS contributes to improved charge carrier absorption and generation, it also results in more opportunities for recombination, which negatively impacts the FF [45].

3.5 Effect of Valence Band Density of States of Active Layer

The valence band density of states in the active layer is varied from 1×10^{16} to $1 \times 10^{20} \text{ cm}^{-3}$, and its impact on the characteristics of polymer solar cells is evaluated. The analysis reveals that while short-circuit current density (Jsc) and fill factor (FF) change in a similar manner, open-circuit voltage (Voc) and power conversion efficiency (PCE) do not exhibit the same trend. The decline in PCE and Voc with an increase in valence band density of states (DOS) is primarily due to enhanced recombination rates and increased charge carrier trapping. Although a higher valence band DOS might initially

in turn lowers series resistance. This reduction in series resistance facilitates a higher fill factor by minimizing voltage drops during operation [49]. The graphical representation is given in Figure 8. However, a noticeable increase in shallow donor density can also result in a higher defect density within the active layer. This heightened defect density may give rise to additional recombination centers that foster nonradiative recombination of charge carriers. Consequently, this adverse effect results in fewer charge carriers contributing to the photocurrent, thereby reducing the short-circuit current [50].

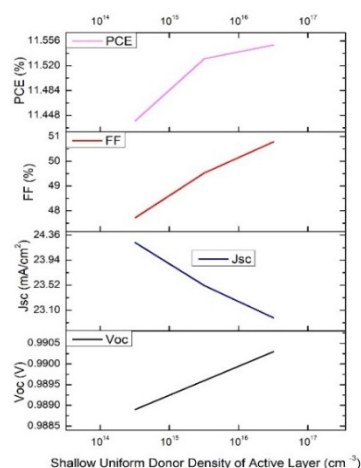


Figure 8. Influence of Shallow Uniform Donor Density of states of Active Layer

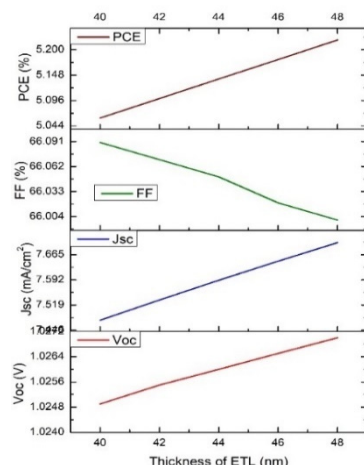


Figure 9. Influence of ETL Thickness

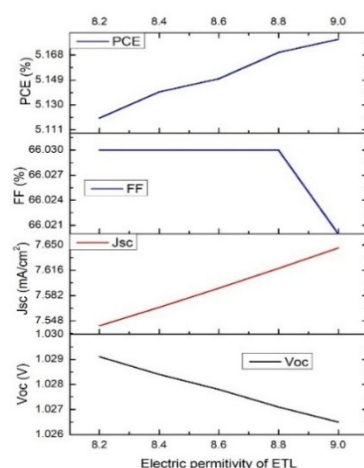


Figure 10. Effect of Electric Permittivity of ETL

3.7. Effect of Thickness of ETL

This study examines the effect of varying the thickness of the electron transport layer (ETL) made from zinc oxide nanoparticles (ZnONPs), changing it from 40 nm to 48 nm. The optimal performance was identified at a thickness of 48 nm, where the power conversion efficiency (PCE) peaked at 5.22%, the open circuit voltage (Voc) reached 1.0270 V, and the short-circuit current density (Jsc) was measured at 7.699979 mA/cm². At 40 nm thickness, the fill factor (FF) was observed to achieve a higher value of 66.09%. The analysis of output parameters indicates that as the thickness increases, the fill factor tends to decrease, while Voc, Jsc, and PCE show an upward trend. Thicker ETLs can enhance the open circuit voltage (Voc) in polymer solar cells by slowing down charge recombination processes. By expanding the electron transport pathway, a thicker ETL minimizes the likelihood of electron-hole recombination before charge carriers reach the electrodes. This increased thickness facilitates a more effective collection of photo-generated electrons due to the greater transit space afforded to the electrons. Consequently, as more charge carriers efficiently reach the electrodes with minimal losses from trapping or recombination, this improvement in charge transport can lead to higher Jsc [51]. However, the decline in the fill factor in polymer solar cells at greater ETL thicknesses is primarily attributed to increased series resistance, reduced charge carrier mobility, elevated recombination rates, and interfacial charge transfer resistance [52]. The power conversion efficiency (PCE) of polymer solar cells can improve with increased thickness of the ETL, up to a certain optimal point, largely due to better light absorption, enhanced charge extraction, and superior charge transport capabilities [53]. The respective graph is shown in Figure 9.

3.8 Effect of Electric Permittivity of ETL

This section provides a comprehensive analysis of how the electric permittivity of the electron transport layer (ETL) affects polymer solar cells, as illustrated in Figure 10. The findings reveal that changing the electric permittivity from 8.2 to 9.0 results in a decrease in the open-circuit voltage (Voc), while both the short-circuit current density (Jsc) and overall efficiency experience an increase. Specifically, a permittivity value of 9.0 yields the best optimized performance. For effective charge transfer, the energy levels of the ETL and the active layer must be closely aligned. Higher permittivity in the ETL may disrupt this alignment at the ETL/polymer interface, leading to voltage loss and a reduction in Voc due to ineffective charge transfer. Quality issues within the ETL can further diminish Voc and impede charge transfer, even if the permittivity is elevated. Since successful charge collection relies on the interactions between charge carriers and their respective layers, any adverse effects on the electrostatic potential exacerbated by materials with high dielectric constants [54] can contribute to a lower Voc. Conversely, increased electric permittivity facilitates faster charge transfer at the donor-acceptor interface, significantly reducing non-geminate recombination losses. By minimizing these losses, more charge carriers become available for collection, enhancing the overall performance of the solar cell.

Ultimately, improved charge dynamics and reduced recombination lead to higher values of Jsc and power conversion efficiency (PCE), which can be attributed to a favourable dielectric environment [55]. However, flaws or suboptimal interfaces can still generate recombination losses, which may diminish the fill factor's responsiveness to changes in permittivity.

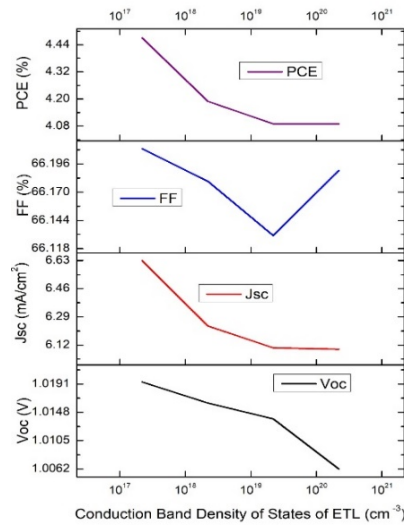


Figure 11. Influence of Conduction Band Density of States of ETL

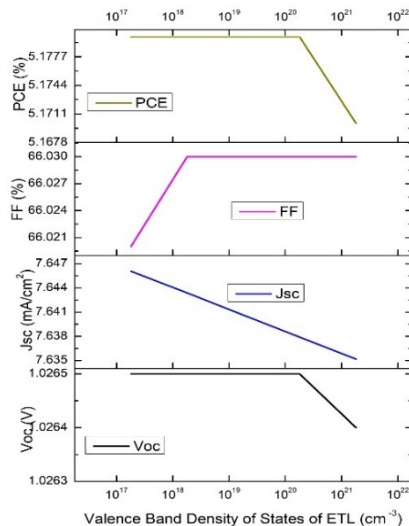


Figure 12. Influence of Valence Band Density of States of ETL

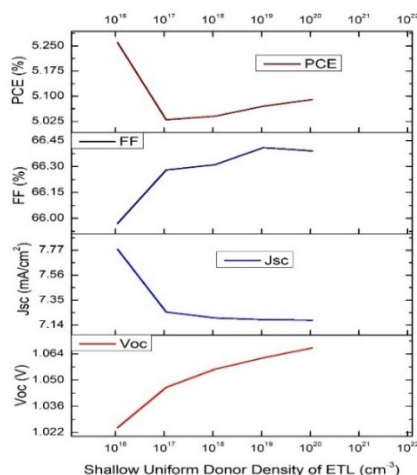


Figure 13. Influence of Shallow Donor Density of ETL

3.9 Effect of Conduction Band Density of States of ETL

This section investigates the influence of the conduction band density of states (CBDoS) of a polymer cell on the performance of its electron transport layer (ETL). For this analysis, the CBDoS is varied from 2.2×10^{17} to $2.2 \times 10^{20} \text{ cm}^{-3}$. It was observed that the short-circuit current density (Jsc) and power conversion efficiency (PCE) exhibited similar trends, while the fill factor (FF) initially decreased before increasing at higher CBDoS values. The performance was found to be optimized at $2.2 \times 10^{17} \text{ cm}^{-3}$, as illustrated in Figure 11. The decline in Jsc and PCE with increasing CBDoS is primarily attributed to increased carrier trapping, higher recombination rates, and potential misalignment of energy levels [56]. As the CBDoS rises, the presence of additional trap states hinders charge extraction and facilitates enhanced carrier recombination, leading to a reduction in open-circuit voltage (Voc). The behaviour of the fill factor (FF) is influenced by the complex interactions among energy level alignment, trap states, and carrier dynamics. This results in a non-linear relationship, where the competing effects of increased recombination and improved carrier mobility contribute to the observed patterns in FF.

3.10 Effect of Valence Band Density of States of ETL

This section focuses on the changes in the valence band density of states of the electron transport layer in polymer solar cells, varying from 1.8×10^{17} to $1.8 \times 10^{21} \text{ cm}^{-3}$. Figure 12 provides a graphical representation of these changes.

It was found that the optimal performance, characterized by a maximum efficiency of 5.18%, occurs at a density of $1.8 \times 10^{17} \text{ cm}^{-3}$. Variations in the valence band density of states within the electron transport layer can lead to complex changes in the output characteristics of polymer solar cells. The effects on short-circuit current density (Jsc), open-circuit voltage (Voc), fill factor (FF), and power conversion efficiency (PCE) are determined by optimizing the density of states, alongside the ratio of charge transport to recombination and the alignment of interfacial energy levels. The respective graph is given in Figure 12.

3.11 Effect of Shallow Donor Density of ETL

This section analyzes the fluctuations in the shallow donor density of the electron transport layer, which ranges from 1.1×10^{16} to $1.1 \times 10^{20} \text{ cm}^{-3}$. Figure 13 provides the corresponding graph illustrating these fluctuations. The findings indicate that while the variations in short-circuit current density (Jsc) and power conversion efficiency (PCE) are comparable, the changes in open-circuit voltage (Voc) and fill factor (FF) exhibit a similar trend. Voc typically increases with a higher shallow donor density, as this leads to improved charge extraction and reduced recombination losses. Additionally, as charge transport and extraction enhance, the fill factor (FF) also rises with the shallow donor density. However, excessive concentrations of shallow donors can lead to significant recombination, ultimately resulting in a decrease in PCE.

3.12 Effect of Thickness of Additional P3HT Layer

In this case, the thickness of the P3HT layer is varied from 16 nm to 24 nm, with the optimal performance observed at 16 nm.

This is illustrated in Figure 14, which provides a graphical representation of the findings. The investigation reveals that while the fill factor (FF) shows a different trend, the open-circuit voltage (Voc), short-circuit current density (Jsc), and power conversion efficiency (PCE) fluctuate similarly. As the P3HT layer increases in thickness, the pathways for charge transport become longer and more convoluted.

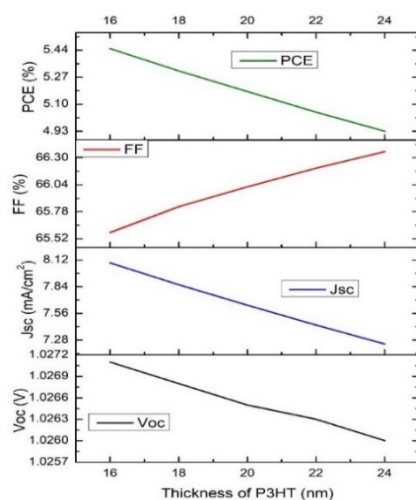


Figure 14. Influence of P3HT Thickness

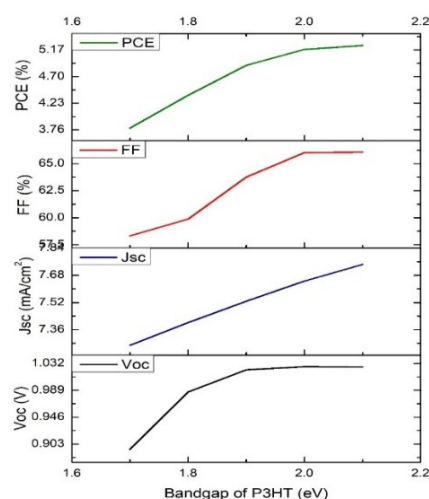


Figure 15. Effect of Band gap of P3HT

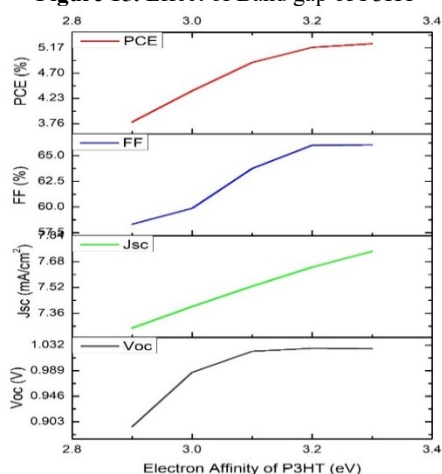


Figure 16. Influence of Electron Affinity of P3HT

declines due to higher defect densities and shorter diffusion lengths, ultimately reducing the overall efficiency of the solar cell. The maximum efficiency is observed at a valence band density of $1.8 \times 10^{17} \text{ cm}^{-3}$. The decrease in Jsc for polymer solar

Consequently, charge carrier mobility diminishes, which is crucial for the effective transfer of electrons and holes to their respective electrodes. This increase in the distance that charge carriers must traverse can lead to a higher likelihood of recombination before reaching the electrodes, potentially resulting in reduced Jsc and PCE. Moreover, the drop in Voc may be attributed to lower charge extraction efficiency in thicker layers and higher energy losses associated with elevated recombination rates. Key factors contributing to the decline in FF in polymer solar cells (PSCs) as the P3HT layer thickness increases include enhanced bimolecular recombination, inefficient charge transport, and imbalanced charge carrier mobilities [57].

3.13. Effect of Bandgap of Additional P3HT Layer

The bandgap of P3HT varies from 1.7 eV to 2.1 eV, with observations indicating that all output parameters increase alongside the bandgap. This trend is illustrated in Figure 15. There is a direct correlation between the open-circuit voltage (Voc) and the energy levels of the polymer's lowest unoccupied molecular orbital (LUMO) and highest occupied molecular orbital (HOMO). Generally, a larger bandgap ensures a higher HOMO energy level, which can enhance Voc. Additionally, higher bandgap materials are more effective at absorbing high-energy photons, potentially leading to increased short-circuit current density (Jsc). Increasing the bandgap creates a larger energy difference necessary for charge separation, which reduces the likelihood of exciton recombination. This mechanism ultimately contributes to an improvement in both fill factor (FF) and power conversion efficiency (PCE).

3.14 Effect of Electron Affinity of Additional P3HT Layer

This section investigates the influence of P3HT's electron affinity on the performance of polymer solar cells. The electron affinity is varied from 2.9 eV to 3.3 eV, revealing that all output parameters of the cell respond similarly to these changes. Figure 16 illustrates this correlation. In general, a higher electron affinity results in an elevated LUMO energy level, which can lead to an increase in the open-circuit voltage (Voc) when no current is flowing. Larger electron affinities create greater energy offsets, facilitating the efficient movement of electrons and potentially enhancing the short-circuit current density (Jsc). Furthermore, a polymer donor with a higher electron affinity can reduce recombination losses, leading to improved fill factor (FF) and power conversion efficiency (PCE) [58].

3.15 Effect of Valence Band Density of States of Additional P3HT Layer

The present study investigates the effect of varying the valence band density of states of P3HT from 1.8×10^{16} to $1.8 \times 10^{20} \text{ cm}^{-3}$ on the output parameters of polymer solar cells. While the short-circuit current density (Jsc) shows a differential response among the output parameters, the open-circuit voltage (Voc), fill factor (FF), and power conversion efficiency (PCE) exhibit similar trends. This relationship is illustrated in Figure 17.

Improvements in metrics such as PCE, FF, and Voc can be attributed to better energy level alignment and enhanced charge transport. However, as the valence band density increases, performance declines due to higher defect densities and shorter diffusion lengths, ultimately reducing the overall efficiency of the solar cell. The maximum efficiency is observed at a valence band density of $1.8 \times 10^{17} \text{ cm}^{-3}$. The decrease in Jsc for polymer solar

cells, particularly those utilizing P3HT, is primarily caused by increased defect density and shorter charge carrier diffusion lengths associated with high density states.

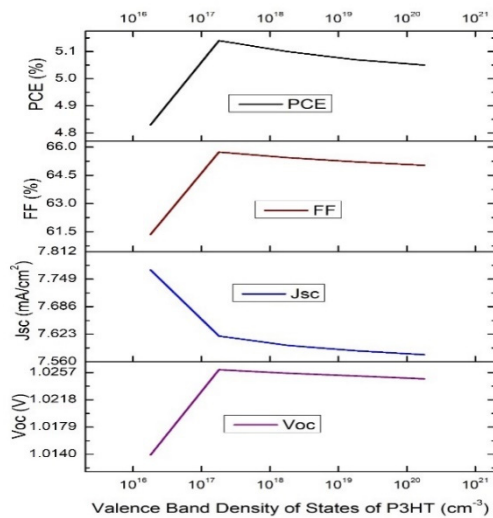


Figure 17. Influence of Valence Band Density of States of P3HT

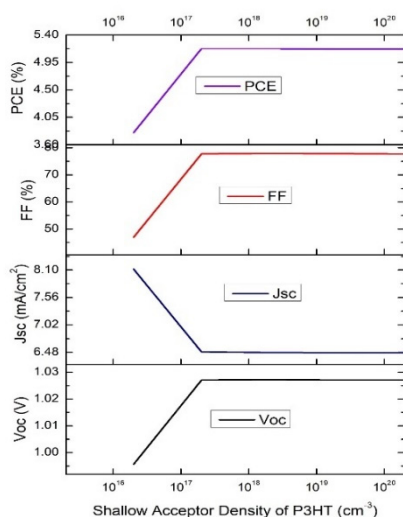


Figure 18. Influence of Shallow Acceptor Density of States of P3HT

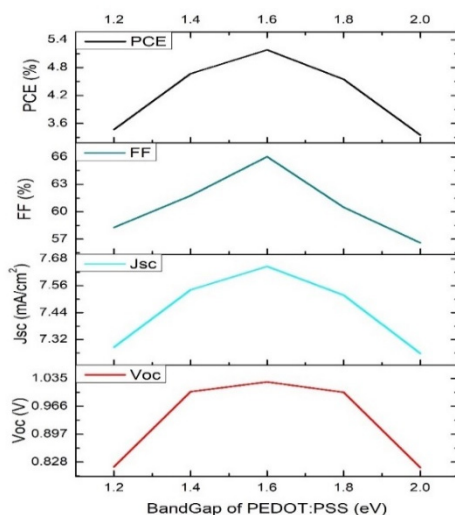


Figure 19. Influence of Bandgap of PEDOT : PSS

3.16 Effect of Shallow Acceptor Density of States of Additional P3HT Layer

In our subsequent endeavor, we adjusted the shallow acceptor density of states in the P3HT layer, conducting a study that encompassed values ranging from 2×10^{16} to $2 \times 10^{20} \text{ cm}^{-3}$. The optimal performance was observed at a density of $2 \times 10^{17} \text{ cm}^{-3}$, as illustrated in Figure 18, which displays the graphical variations. The fluctuations in performance were similar to those seen with the layer's valence band density of states. This similarity arises because both factors significantly influence the solar cell's charge transport, carrier density, trap formation, and recombination dynamics. The sensitivity of performance to these concentrations highlights the delicate balance required to enhance charge mobility while minimizing the adverse effects of defects.

3.17 Effect of Bandgap of PEDOT: PSS [HTL]

This study investigates the impact of changing the bandgap of the hole transport layer, PEDOT:PSS, from 1.2 eV to 2.0 eV on the output parameters of polymer solar cells. All parameters were observed to fluctuate similarly, with maximum efficiency achieved at a bandgap of 1.6 eV, as illustrated in Figure 19. Increasing the PEDOT:PSS bandgap can enhance the open-circuit voltage (Voc) in polymer solar cells. However, a higher bandgap limits sunlight absorption, resulting in lower charge carrier production. Due to the significantly high bandgap of PEDOT:PSS, sunlight absorption is reduced, which subsequently decreases the short-circuit current density (Jsc). Additionally, the hydrophilic nature and instability of the hole transport layer (HTL) may lead to increased series resistance, further affecting the fill factor (FF). The power conversion efficiency (PCE) increases initially but subsequently declines as the hole transport bandgap is raised.

3.18 Effect Electron Affinity of PEDOT:PSS [HTL]

PEDOT:PSS demonstrates a shift in electron affinity ranging from 3.0 eV to 3.8 eV, with optimized values achieved at 3.4 eV, as illustrated in Figure 20. The output parameters of polymer solar cells exhibit similar changes as the bandgap and electron affinity of PEDOT:PSS are increased. This similarity arises from the interplay between energy level alignment and charge transport dynamics, both of which are simultaneously influenced by these two characteristics.

CONCLUSION

In this modeling work, a P3HT layer was integrated into a polymer solar cell structure using SCAPS 1-D software, with P3HT:IC₆₀BA serving as the active layer. The study revealed that the structure exhibited significantly better performance with the inclusion of P3HT. The P3HT layer enhances charge transit and maximizes Voc and Jsc by aligning energy levels at the heterojunction surfaces. After optimization, the following output parameters were achieved: power conversion efficiency (PCE) = 15.26%, fill factor

(FF) = 51.62%, short-circuit current density (J_{sc}) = 26.577140 mA/cm², and open-circuit voltage (V_{oc}) = 1.1126 V. Before optimization, we recorded an efficiency of only 5.18%. These results are quite promising and will contribute to the advancement of photovoltaic research in the future.

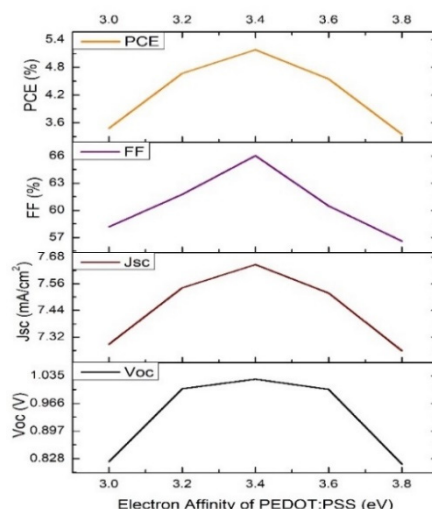


Figure 20. Influence of Electron Affinity of PEDOT: PSS

Statements and Declarations:

Data availability statement: The data that support the findings of this study are available on request from the corresponding author.

Acknowledgements. For providing SCAPS 1-D software for the simulation investigation, the authors would like to thank Pr.M. Burgelman of the University of Gent in Belgium.

CRedit authorship contribution statement.: Ramabadran C.D.: Conceptualization, Data curation, Methodology, Software, Investigation, Validation, Formal analysis, Writing – original draft. Sudheer K.S.: Supervision, Conceptualization, Software, Writing – review & editing

Conflict of interest. The authors declare that they have no conflict of interest.

ORCID

Chittur Devarajan Ramabadran, <https://orcid.org/0009-0003-2255-3087>; K. Sebastian Sudheer, <https://orcid.org/0000-0002-9019-4405>

REFERENCES

- [1] Y. He, G. Zhao, B. Peng, and Y. Li, "High-Performance Polymer Solar Cells with P3HT:PCBM Bulk Heterojunction: A Combined Experimental and Simulation Study," *Advanced Functional Materials*, **20**(19), 3383–3389 (2010). <https://doi.org/10.1002/adfm.201000973>
- [2] C. Bendenia, H. Merad-Dib, S. Bendenia, and B. Hadri, "Numerical simulation of CIGS solar cells with SCAPS-1D: Optimization of the absorber band gap grading and thickness," *Optik*, **174**, 167–172 (2018). <https://doi.org/10.1016/j.ijleo.2018.08.058>
- [3] A. Hazra, I. Mal, D. Samajdar, and T. Das, "Device simulation of lead-free CH₃NH₃SnI₃ perovskite solar cells with high efficiency," *Optik*, **168**, 747–753 (2018). <https://doi.org/10.1016/j.ijleo.2018.04.117>
- [4] Y. Sun, C. Cui, H. Wang, and Y. Li, "Fabrication of Flexible, Free-Standing, Ultralight Carbon Nanotube Aerogel Films for Supercapacitor Electrodes," *Advanced Energy Materials*, **1**(6), 1058–1061(2011). <https://doi.org/10.1002/aenm.201100322>
- [5] Y. He, H.-Y. Chen, J. Hou, and Y. Li, "Indene-C60 Bisadduct: A New Acceptor for High-Performance Polymer Solar Cells," *Journal of the American Chemical Society (JACS)*, **132**(4), 1377–1382 (2010). <https://doi.org/10.1021/ja908602j>
- [6] G. Zhao, Y. He, and Y. Li, "6.5% Efficiency of Polymer Solar Cells Based on poly(3-hexylthiophene) and Indene-C60 Bisadduct by Device Optimization," *Advanced Materials*, **22**(39), 4355–4358 (2010). <https://doi.org/10.1002/adma.201001339>
- [7] Z. Tan, D. Qian, W. Zhang, L. Li, Y. Ding, Q. Xu, F. Wang, and Y. Li, "Efficient and stable polymer solar cells with a solution-processable small molecule as anode buffer layer," *Journal of Materials Chemistry A*, **1**(3), 657–664 (2013). <https://doi.org/10.1039/C2TA00575F>
- [8] S. Gartner, M. Christmann, S. Sankaran, H. Röhm, E.-M. Prinz, F. Pentz, A. Pütz, *et al.*, "Design Rules for High-Efficiency Polymer Solar Cells with Low Energy Loss and High Fill Factor," *Advanced materials*, **26**(38), 6653–6657 (2014). <https://doi.org/10.1002/adma.201402932>
- [9] E.F. Oliveira, L.C. Silva, and F.C. Lavarda, "Electronic structure and charge transport properties of star-shaped molecules with 1,3,5-triazine core and thiophene arms for photovoltaic applications," *Structural Chemistry*, **28**, 1133–1140 (2017). <https://doi.org/10.1007/s11224-017-0926-y>
- [10] G. Yu, J. Gao, J.C. Hummelen, F. Wudl, and A.J. Heeger, "Polymer Photovoltaic Cells: Enhanced Efficiencies via a Network of Internal Donor-Acceptor Heterojunctions," *Science*, **270**, 1789–1791 (1995). <https://doi.org/10.1126/science.270.5243.1789>
- [11] J. Peet, J.Y. Kim, N.E. Coates, W.L. Ma, D. Moses, A.J. Heeger, and G.C. Bazan, "Efficiency enhancement in low-bandgap polymer solar cells by processing with alkane dithiols," *Nature materials*, **6**(7), 497–500 (2007). <https://doi.org/10.1038/nmat1928>
- [12] J.K. Lee, W.L. Ma, C.J. Brabec, J. Yuen, J.S. Moon, J.Y. Kim, K. Lee, *et al.*, "Processing additives for improved efficiency from bulk heterojunction solar cells," *Journal of the American Chemical Society*, **130**(11), 3619–3623 (2008). <https://doi.org/10.1021/ja710079w>

- [13] N. Loew, S. Komatsu, H. Akita, K. Funayama, T. Yuge, T. Fujiwara, and M. Ihara, "Development of a novel glucose sensor using engineered glucose dehydrogenase," *ECS Transactions*, **58**(45), 77- 82 (2014). <https://doi.org/10.1149/05845.0077ecst>
- [14] P. Matavulj, M.K. Islam, and C.S. Živanović, "Numerical simulation of organic solar cells: Impact of interface layers on device performance," in: *Proceedings of the International Conference on Numerical Simulation of Optoelectronic Devices (NUSOD)*, (IEEE, Copenhagen, Denmark, 2017), pp. 133–134. <https://doi.org/10.1109/NUSOD.2017.8010026>
- [15] S.-A. Gopalan, A.-I. Gopalan, A. Vinu, K.-P. Lee, and S.-W. Kang, "A new strategy for designing high-efficiency cascaded solar cells: Optical and electrical modeling using SCAPS-1D," *Solar Energy Materials and Solar Cells*, **174**, 112-123 (2018). <https://doi.org/10.1016/j.solmat.2017.08.033>
- [16] M. Burgelman, P. Nollet, and S. Degraeve, "Modelling polycrystalline semiconductor solar cells," *Thin Solid Films*, **361-362**, 527-532 (2000). [https://doi.org/10.1016/S0040-6090\(99\)00825-1](https://doi.org/10.1016/S0040-6090(99)00825-1)
- [17] B. Xu, G. Sai-Anand, A.-I. Gopalan, Q. Qiao, and S.-W. Kang, "Improving Photovoltaic Properties of P3HT:IC₆₀BA through the Incorporation of Small Molecules," *Polymers*, **10**(2), 121 (2018). <https://doi.org/10.3390/polym10020121>
- [18] S. Hosseini, M. Bahramgour, N. Delibaş, and A. Niaie, "Investigation of a Perovskite Solar Cell and Various Parameters Impact on Its Layers and the Effect of Interface Modification by Using P3HT as an Ultrathin Polymeric Layer Through SCAPS-1D Simulation," *Sakarya University Journal of Science*, **25**(5), 1168-1179 (2021). <https://doi.org/10.16984/aufenbilder.947735>
- [19] A. Maillard and A. Rochefort, "Quantum transport properties of graphene nanoribbons with embedded heptagon-pentagon defects," *Organic Electronics*, **15**(9), 2091-2098 (2014). <https://doi.org/10.1016/j.orgel.2014.05.028>
- [20] H. Lee, (2015). "Optimization of energy level alignment for efficient organic photovoltaics," *Vacuum Magazine*, **2**(2), 12-16 (2015). <https://doi.org/10.5757/VACMAG.2.2.12> (in Korean)
- [21] S. Holliday, et al., "High-efficiency and air-stable P3HT solar cells with a new non-fullerene acceptor," *Nature Communications*, **7**, 11585 (2016). <https://doi.org/10.1038/ncomms11585>
- [22] A. Kumar, and R. Singh, "Numerical Modelling Analysis for Carrier Concentration Level Optimization of CdTe Heterojunction Thin Film-Based Solar Cell with Different Non-Toxic Metal Chalcogenide Buffer Layers Replacements: Using SCAPS-1D Software," *Crystals*, **11**(12), 1454 (2021). <https://doi.org/10.3390/cryst11121454>
- [23] K. Nithya, and K. Sudheer, "Numerical modelling of non-fullerene organic solar cell with high dielectric constant ITIC-OE acceptor," *Journal of Physics Communications*, **4**(2), 025012 (2020). <https://doi.org/10.1088/2399-6528/ab772a>
- [24] S.W. Heo, E.J. Lee, K.W. Seong, and D.K. Moon, "Enhanced stability in polymer solar cells by controlling the electrode work function via modification of indium tin oxide," *Solar energy materials and solar cells*, **115**, 123–128, (2013). <https://doi.org/10.1016/j.solmat.2013.03.023>
- [25] S. Loser, C.J. Bruns, H. Miyauchi, R.P. Ortiz, A. Facchetti, S.I. Stupp, and T.J. Marks, "A Naphthodithiophene-Diketopyrrolopyrrole Donor Molecule for Efficient Solution-Processed Solar Cells," *Journal of the American Chemical Society*, **133**(21), 8142– 8145 (2011). <https://doi.org/10.1021/ja202791n>
- [26] G. Li, Y. Yao, H. Yang, V. Shrotriya, G. Yang, and Y. Yang, "Solvent annealing' effect in polymer solar cells based on poly(3-hexylthiophene) and methanofullerenes," *Advanced Functional Materials*, **17**(10), 1636–1644 (2007). <https://doi.org/10.1002/adfm.200600624>
- [27] Z. He, F. Liu, C. Wang, J. Chen, L. He, D. Nordlund, H. Wu, T.P. Russell, and Y. Cao, "Simultaneous Enhancement of Open-Circuit Voltage, Short-Circuit Current Density, and Fill Factor in Polymer Solar Cells," *Materials Horizons*, **2**(6), 592–597(2015). <https://doi.org/10.1039/C5MH00164A>
- [28] X. Zhu, K. Lu, B. Xia, J. Fang, Y. Zhao, T. Zhao, Z. Wei, et al., "Improving the Performances of Random Copolymer Based Organic Photovoltaics by Incorporating Fluorine Substituents," *Polymers*, **8**(1), 4 (2015). <https://doi.org/10.3390/polym8010004>
- [29] L. Lu, et al., "High-performance ternary blend polymer solar cells involving both energy transfer and hole relay processes," *Nat. Commun.* **6**, 7327 (2015). <https://doi.org/10.1038/ncomms8327>
- [30] M.M. Stylianakis, D. Konios, C. Petridis, G. Kakavelakis, E. Stratakis, and E. Kymakis, "Efficient and stable hybrid perovskite-graphene solar cells via interfacial passivation with 2D–2D heterostructures," *2D Materials*, **4**(4), 042005 (2017). <https://doi.org/10.1088/2053-1583/aa87b6>
- [31] B.N. Ezealigo, A.C. Nwanya, A. Simo, R.U. Osuji, R. Bucher, M. Maaza, and F.I. Ezema, "Optical and electrochemical capacitive properties of copper (I) iodide thin film deposited by SILAR method," *Arabian Journal of Chemistry*, **12**(8), 5380–5391 (2019). <https://doi.org/10.1016/j.arabjc.2017.01.008>
- [32] J. Liu, Y. Zhang, C. Liu, M. Peng, A. Yu, J. Kou, W. Liu, et al., "High-Performance UV Photodetector Based on a Heterojunction of a ZnO Nanowire Array and a Few-Layer MoS₂ Film," *Nanoscale research letters*, **11**, 1–7 (2016). <https://doi.org/10.1186/s11671-016-1291-2>
- [33] Z. El Jouad, M. Morsli, G. Louarn, L. Cattin, M. Addou, and J.C. Bernède, "Improving the efficiency of subphthalocyanine based planar organic solar cells through the use of MoO₃/CuI double anode buffer layer," *Solar Energy Materials and Solar Cells*, **141**, 429– 435 (2015). <https://doi.org/10.1016/j.solmat.2015.06.017>
- [34] M.I. Hossain, F.H. Alharbi, and N. Tabet, "Copper oxide as inorganic hole Transport material for lead halide perovskite based solar cells," *Solar Energy*, **120**, 370–380 (2015). <https://doi.org/10.1016/j.solener.2015.07.037>
- [35] B.M. Omer, A. Khogali, and A. Pivrikas, "Combined effects of carriers charge mobility and electrodes work function on the performance of organic photovoltaic devices," in: *37th IEEE Photovoltaic Specialists Conference*, pp. 000734–000743 (IEEE, 2011). <https://doi.org/10.1109/LED.2011.2117953>
- [36] O.D. Iakobson, O.L. Gribkova, A.R. Tameev, and J.-M. Nunzi, "Polymeric semiconductors for hybrid organic-inorganic solar cells: A comparative study of water-soluble polythiophenes," *Scientific Reports*, **11**, 3697 (2021). <https://doi.org/10.1038/s41598-021-84452-x>
- [37] N. Sharma, S.K. Gupta, and C.M. Singh Negi, "Enhanced performance of organic solar cells by using zinc oxide and graphene quantum dots as electron transport layer," *Superlattices and Microstructures*, **135**, 106278 (2019). <https://doi.org/10.1016/j.spmi.2019.106278>
- [38] K. Weng, L. Ye, L. Zhu, J. Xu, J. Zhou, X. Feng, G. Lu, et al., "Molecular design of benzodithiophene-based organic photovoltaic materials to achieve both high VOC and JSC," *Nature Communications*, **11**, 2855 (2020). <https://doi.org/10.1038/s41467-020-16621-x>

- [39] Y. Zhang, X. Li, T. Dai, D. Xu, J. Xi, and X. Chen, "Charge transport and extraction of PTB7:PC71BM organic solar cells: effect of film thickness and thermal-annealing," *RSC Advances*, **9**(31), 17857-17864 (2019). <https://doi.org/10.1039/c9ra02877c>
- [40] A. Gusain, R.M. Faria, and P.B. Miranda, "Controlling the morphology and performance of bulk heterojunctions in solar cells: Lessons from interfacial forces," *Frontiers in Chemistry*, **7**, 61 (2019). <https://doi.org/10.3389/fchem.2019.00061>
- [41] M. Zhang, X. Xu, L. Yu, and Q. Peng, "High-performance ternary organic solar cells with controllable morphology via sequential layer-by-layer deposition," *Journal of Power Sources*, **506**, 229961 (2021). <https://doi.org/10.1016/j.jpowsour.2021.229961>
- [42] D. Spoltore, W.D. Oosterbaan, S. Khelifi, J.N. Clifford, A. Viterisi, E. Palomares, M. Burgelman, *et al.*, "A combined experimental and modeling study of the factors limiting the performance of polymer:fullerene solar cells processed from chlorobenzene and 1,2-dichlorobenzene," *Advanced Energy Materials*, **3**(2), 227-236 (2013). <https://doi.org/10.1002/aenm.201200674>
- [43] M.R. Khan, and B. Jarzabek, "Recent Advances in Polymer-Based Materials for High-Performance Perovskite Solar Cells," *Polymers*, **15**(18), 3674 (2023). <https://doi.org/10.3390/polym15183674>
- [44] C. Deibel, Photocurrent in organic solar cells – Part 1, Blog post, Notes on Disordered Matter (2009). <https://blog.disorderedmatter.eu/2009/07/20/photocurrent-in-organic-solar-cells-part-1>
- [45] B. Qi, and J. Wang, "Fill factor in organic solar cells," *Journal of Materials Chemistry*, **22**(46), 24315- 24325 (2012). <https://doi.org/10.1039/c2jm33719c>
- [46] M. Wright, and A. Uddin, "Organic-inorganic hybrid perovskites: A solution for cost-effective solar cells," *Solar Energy Materials, and Solar Cells*, **107**, 87–117 (2012). <https://doi.org/10.1016/j.solmat.2012.07.006>
- [47] S. Galindo, M. Ahmadpour, L.G. Gerling, A. Marsal, C. Voz, R. Alcubilla, and J. Puigdollers, "Analysis of the origin of open circuit voltage in organic solar cells with different device architectures," *Organic Electronics*, **15**(11), 3034-3041 (2014). <https://doi.org/10.1016/j.orgel.2014.07.011>
- [48] Z. Liu, and Y. Lin, "Recent advances in polymer-based interfacial materials for efficient and stable organic solar cells," *Polymer Testing*, **131**, 108387 (2024). <https://doi.org/10.1016/j.polymertesting.2024.108387>
- [49] A. Kumar, and S. Sharma, "Performance analysis of organic solar cells with different anode buffer layers," *IOSR Journal of Electrical and Electronics Engineering (IOSR-JEEE)*, **14**(4), 49-54 (2019). <https://www.iosrjournals.org/iosr-jeee/Papers/Vol14%20Issue%204/Series-1/G1404014954.pdf>
- [50] J. Yang, X. Wang, X. Yu, J. Liu, Z. Zhang, J. Zhong, and J. Yu, "Recent advances in organic solar cells with non-fullerene acceptors: From morphology control to device optimization," *Nanomaterials*, **13**(21), 2899 (2023). <https://doi.org/10.3390/nano13212899>
- [51] S. Valsalakumar, S. Bhandari, A. Roy, T.K. Mallick, J. Hinshelwood, and S. Sundaram, "Machine learning-based optimization of hole transport layer-free carbon-based perovskite solar cells," *Npj Computational Materials*, **10**(1), 94 (2024). <https://doi.org/10.1038/s41524-024-01383-7>
- [52] T.M. Mukametkali, B.R. Ilyassov, A.K. Aimukhanov, T.M. Serikov, A.S. Baltabekov, L.S. Aldasheva, and A.K. Zeinidenov, "Optical and electronic properties of monolayer MoS₂ under different strains: DFT study," *Physica B: Condensed Matter*, **660**, 414784 (2023). <https://doi.org/10.1016/j.physb.2023.414784>
- [53] S. Sakib, M.Y. Mohd Noor, M.R. Salim, A.S. Abdullah, A.I. Azmi, M.H. Ibrahim and M.H. Ibrahim, "Effect of different composition ratio on structural and morphological properties of TiO₂ nanoparticles synthesized by sol-gel method," *Mater. Today: Proc.* **76**, 176–182 (2023). <https://doi.org/10.1016/j.matpr.2022.11.4564>
- [54] C. Poelking, J. Benduhn, D. Spoltore, M. Schwarze, S. Roland, F. Piersimoni, D. Neher, *et al.*, "Interfacial electrostatics control open-circuit voltage in organic solar cells," *Communications Physics*, **5**(1), 332 (2022). <https://doi.org/10.1038/s42005-022-01084-x>
- [55] M.R. Khan, and B. Jarzabek, "The effect of 3D printing process parameters on the mechanical properties of PLA polymer and polymer composites: A review," *Polymers*, **15**(18), 3674 (2023). <https://doi.org/10.3390/polym15183674>
- [56] S.A. Moiz, M.S. Alzahrani, and A.N.M. Alahmadi, "Influence of process parameters on mechanical properties of natural fiber-reinforced polymer composites: A review," *Polymers*, **14**(17), 3610 (2022). <https://doi.org/10.3390/polym14173610>
- [57] D. Bartesaghi, I. del C. Pérez, J. Kniepert, S. Roland, M. Turbiez, D. Neher, and L.J.A. Koster, "Competition between charge extraction and recombination determines the fill factor in organic solar cells," *Nature Communications*, **6**, 7083 (2015). <https://doi.org/10.1038/ncomms8083>
- [58] J.C. Nolasco, R. Cabré, J. Ferré-Borrull, L.F. Marsal, M. Estrada, and J. Pallarès, "Design of two-dimensional silicon photonic crystals by means of a guided-mode resonant filter structure," *Journal of Applied Physics*, **107**(2), 023108 (2010). <https://doi.org/10.1063/1.3296294>

ВІПЛИВ ДОДАТКОВОГО ШАРУ РЗНТ НА ПРОДУКТИВНІСТЬ ПОЛІМЕРНОГО СОНЯЧНОГО ЕЛЕМЕНТА РЗНТ: ІС₆₀ВА

Чіттур Девараджан Рамабадран^{a,b}, К. Себастьян Судхір^a

^aКафедра фізики, дослідницька лабораторія моделювання оптоелектронних пристроїв, Коледж Христа [Автономний],
Ірінджалакуда, Тріссур, 680125, Університет Калікута, Керала, Індія

^bКафедра фізики, Урядовий коледж, Чіттур, Палаккад, 678104, Університет Калікута, Керала, Індія

Було проведено моделювання з використанням програмного забезпечення SCAPS 1-D для вивчення впливу додаткового шару РЗНТ (полі-3-гексилтіофен) на продуктивність сонячних елементів з об'ємним гетеропереходом, зокрема з активним шаром РЗНТ: ІС₆₀ВА. Досліджувана структура елемента - ІТО/PEDOT:PSS/РЗНТ/РЗНТ:ІС₆₀ВА/ZnO NPs/Al. Після стандартизації програмного забезпечення ми визначили оптимальні параметри структури сонячного елемента, проаналізувавши різні фактори, що впливають на продуктивність елемента в різних шарах. Згодом, після оптимізації структури, ефективність перетворення енергії (PCE) значно покращилася, збільшившись з 5,18% без додаткового шару до 15,26% з додатковим шаром.

Ключові слова: сонячний елемент з об'ємного гетероперехідного полімеру; фулерен; SCAPS 1-D; активний шар; ETL; HTL

A 31% EFFICIENT CIGS-BASED SOLAR CELL USING SPIRO MATERIAL AS A BUFFER LAYER: NUMERICAL SIMULATION

 **Mohamed Hamdaoui^{a*}**,  **Lhoussayne Et-taya^a**,  **Abdellah Benami^a**,  **Malika Ouhadou^a**,
 **Abderrahman El Boukili^b**,  **Jaouad Fosh^c**

^a*Optoélectronique et Techniques Energétiques Appliquées, Department of Engineering Sciences, Faculty of sciences and techniques, Moulay Ismail University of Meknès BP 509 Boutalamine, Errachidia, Morocco*

^b*Physique Moderne, Rayonnement et Applications, Department of Engineering Sciences, Faculty of sciences and techniques, Moulay Ismail University of Meknès BP 509 Boutalamine Errachidia, Morocco*

^c*Électronique et Systèmes Intelligents, Optoelectronics and Applied Energy Technics (OAET), Department of Engineering Sciences, Faculty of sciences and techniques, Moulay Ismail University of Meknès BP 509 Boutalamine Errachidia, Morocco*

*Corresponding Author E-mail: m.hamdaoui@umi.ac.ma

Received March 31, 2025; revised June 26, 2025; accepted July 15, 2025

This study investigates the potential boost of (Cu(In,Ga)Se₂) based solar cells through numerical simulations using SCAPS-1D software to optimize their performance. Various parameters were analyzed, including the thickness, acceptor concentration, and band gap of the CIGSe active layer, as well as the donor concentration and thickness of the ZrS₂ buffer layer. The impact of operating temperature was also considered. The optimized output characteristics of the proposed cell design include a V_{OC} of 1.13V, J_{SC} of 32.61mA/cm², FF of 89.12, and a PCE of 32.91. These findings can aid in advancing the development of high-efficiency CIGSe-based thin-film solar cells.

Keywords: SCAPS; Operating temperature; Thickness; Work function; Parameter of solar cells

PACS: 42.79.Ek, 78.20.Bh, 72.80.Le, 73.30.y, 73.40.Kp

1. INTRODUCTION

Despite the depletion of fossil resources, the need for energy is growing every year, which is vital for worldwide technological and economic development [1]. As an environmentally advantageous technology that decreases worldwide CO₂ emissions, solar cells are recognized one of the most important renewable energy sources.

Like a hybrid of organic and inorganic materials, PSCs, or perovskite solar cells, have advanced remarkably during the past ten years; their energy conversion efficiency has improved from 3.8% in 2009 to 25.5% in 2024. An essential factor for generating effective and stable PSCs is the choosing of hole transport layers (HTLs).

As a clean energy source, solar cells are in demand, and copper indium gallium selenide (CIGS) is showing talent [1]. Because of its direct bandgap, A significant optical absorption coefficient is present in CIGS, allowing active materials to use thin layer (1–2 μm) [2]. But as virgin spiro-OMeTAD has limited hole mobility and does not fulfill device performance parameters, chemical doping is necessary to boost its conductivity and, consequently, its hole extraction capacity [3].

First and foremost, the goal of this research is to increase a simple solar cell's efficiency as defined by [4]. As a result, we suggest using an HTL hole transport layer in this study and experimenting with the energy gap and charge carrier concentration to get the best performance. This study investigates how two crucial solar cell characteristics affect the photovoltaic performance of simple CIGS/ZrS₂ devices: The thickness and band gap of the active layer (absorber).

However, to maximize perovskite solar cells' optical and electrical performance, the hole transport layer is an essential component that improves the optoelectronic properties of the cells. Spiro-OMeTAD is widely used as a hole transport material in perovskite solar cells (PSCs). However, the mobility and conductivity of virgin or oxygen-oxidized spiro-OMeTAD are restricted [5]. Cumene hydroperoxide-oxidized spiro-OMeTAD, which has several benefits as an HTL, is used in this study. It is undeniable that the reduction of particle density, the optimization of the perovskite energy-to-layer ratio, and the ease of carrier movement all contribute to improved cellular efficiency.

2. MODELING FRAMEWORK AND MATERIAL PARAMETERS

We utilized a solar cell structure that was derived from the research conducted by [4]. for the purposes of this investigation. Figure 1.a shows the framework that will be used to improve these results, while Figure 1.b shows the suggested framework based on a modified version of the foundational structure that includes a spiro layer. In order to investigate potential methods of improving the device's efficacy, we implemented a sequence of alterations to the cell structure. An innovative addition has been incorporated into our proposed configuration we inserted a HTL the absorbent layer and the contact layer behind by using the SPIRO material (refer to Figure 1.b).

As shown in Table 1, the physical parameters for the different material layers in this work were carefully collected using a mix of theoretical considerations, well-researched literature sources, and careful estimate, it's noted that the thermal velocity of the electron and the hole is established at 1×10^7 cm/s for all layers.

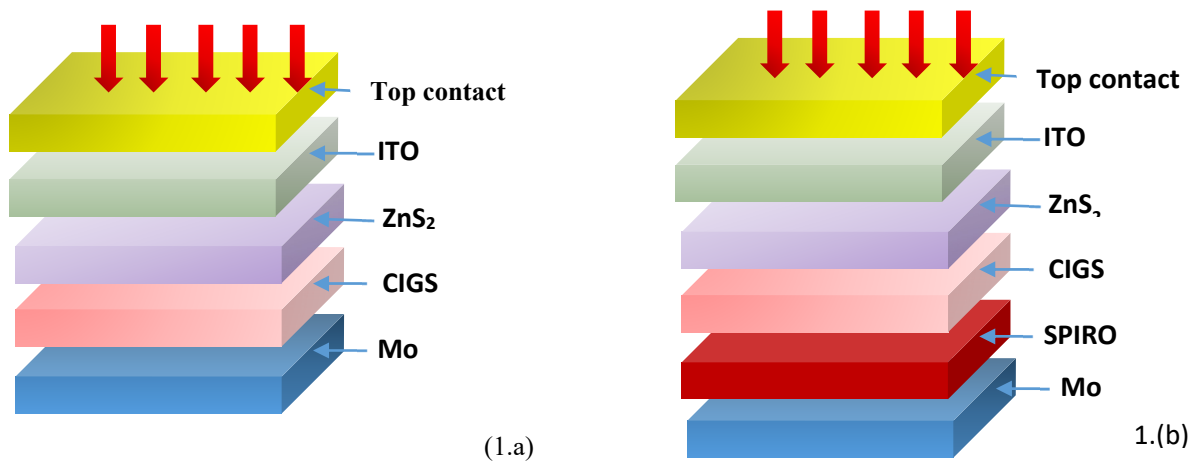


Figure 1. structure of the solar cell without HTL (1.a) and with HTL (1.b).

Table 1. Key material properties that were employed in this simulation

Materials Parameters	ITO [6]	n-ZrS ₂ [7]	p-CIGSe [5]	CuSbS ₂ [8]	P3HT [9]	Cu ₂ O[9]	Spiro [10, 11]
Bandgap (eV)	3.6	1.5-1.9	1.4	1.58	1.7	2.17	1.6
Thickness (nm)	40	100-400	200-2000	50	50	50	50
Dielectric permittivity	8.9	16.4	13.6	14.6	3	7.2	3
Electron affinity (eV)	4.5	4.7	4.5	4.2	4.5	3.2	4.07
C _B density of states (cm ⁻³)	2.2×10 ¹⁸	2.2×10 ¹⁸	2.2×10 ¹⁸	2×10 ¹⁸	2×10 ¹⁸	2.5×10 ²⁰	2.5×10 ¹⁸
V _B density of states (cm ⁻³)	1.8×10 ¹⁹	1.8×10 ¹⁹	1.8×10 ¹⁹	1×10 ¹⁹	1.8×10 ¹⁹	2.5×10 ²⁰	2.2×10 ¹⁹
Hole mobility (cm ² /Vs)	10	1300	25	49	1.8×10 ⁻²	8600	18
Electron mobility (cm ² /Vs)	10	2300	200	49	1.8×10 ⁻³	200	100
Donor density (cm ⁻³)	1×10 ¹⁸	1×10 ¹⁴ -1×10 ¹⁸	0	1×10 ¹⁸	0	-	0
Acceptor density (cm ⁻³)	0	0	1×10 ¹⁴ -1×10 ¹⁸	0	1×10 ¹⁸	1×10 ¹⁹	1×10 ¹⁸

2.1. Numerical simulation

Within the framework of our research, we used SCAPS-1D, a digital simulation program known for its sophistication and usefulness in the analysis and comprehension of physical phenomena produced by photovoltaic devices. This tool has enabled us to model and assess our solar cells. The standard test conditions (STC) were implemented in each SCAPS-1D simulation with a luminescence intensity of AM 1.5 (100 mW/cm²).

The displacement of charge carriers along the superposition axis is described by the solution of the Poisson equations in conjunction with the continuity equations for the electrons and the trous [12].

Solving Poisson's equations in combination with the continuity equations for holes and electrons characterizes the passage of charge carriers down the superposition axis [13].

$$\frac{d^2}{dx^2} \psi(x) = \frac{q}{\epsilon} [p(x) - n(x) + N_D - N_A + N_t] \quad (1)$$

$$\frac{1}{q} \frac{d}{dx} J_n = R_n(x) - G_{op}(x) \quad (2)$$

$$\frac{1}{q} \frac{d}{dx} J_p = G_{op}(x) - R_n(x) \quad (3)$$

Where;

- ψ denotes the electrostatic potential,
- N_t represents the defect density,
- q signifies the elemental charge, ϵ indicates permittivity,
- p refers to the concentrations of free electrons,
- n refer to concentrations of holes,
- N_A correspond to the densities of ionized acceptors,
- N_D is to the densities of ionized donors,
- J_n and J_p represent the current densities of electrons and holes,
- G_{op} denote the rates of electron-hole pair generation,
- R_n represent the rates of electron-hole pair recombination.

3. RESULTS AND DISCUSSION

3.1. Optimization of a Conventional Solar Cell

As it's mentioned, as our reference cell for the sake of this investigation, we used a solar cell structure that was motivated by the findings of [5]. We implemented a number of modifications to the cell structure in order to investigate possible methods to progress the device's competence.

In this section, we will first examine how the thickness of the absorption layer, the band gap, and density sensors affect the primary photovoltaic characteristics: open circuit tension (V_{oc}), closed circuit current density (J_{sc}), filling factor (FF), and cell efficiency (η), respectively.

As seen in Figure 2, the photovoltaic cell model used in this simulation study consists of the following components: the metal/metal electrode (HTL), CIGS (perovskite absorption layer), ZnS_2 (ETL), and FTO (transparent conductive oxide). Table 1 displays the characteristics established for the solar cell structure in this simulation, such as thickness, band gap, electrical permittivity, electronic affinity, electron/hollow mobility, and thermal electron/hole velocity.

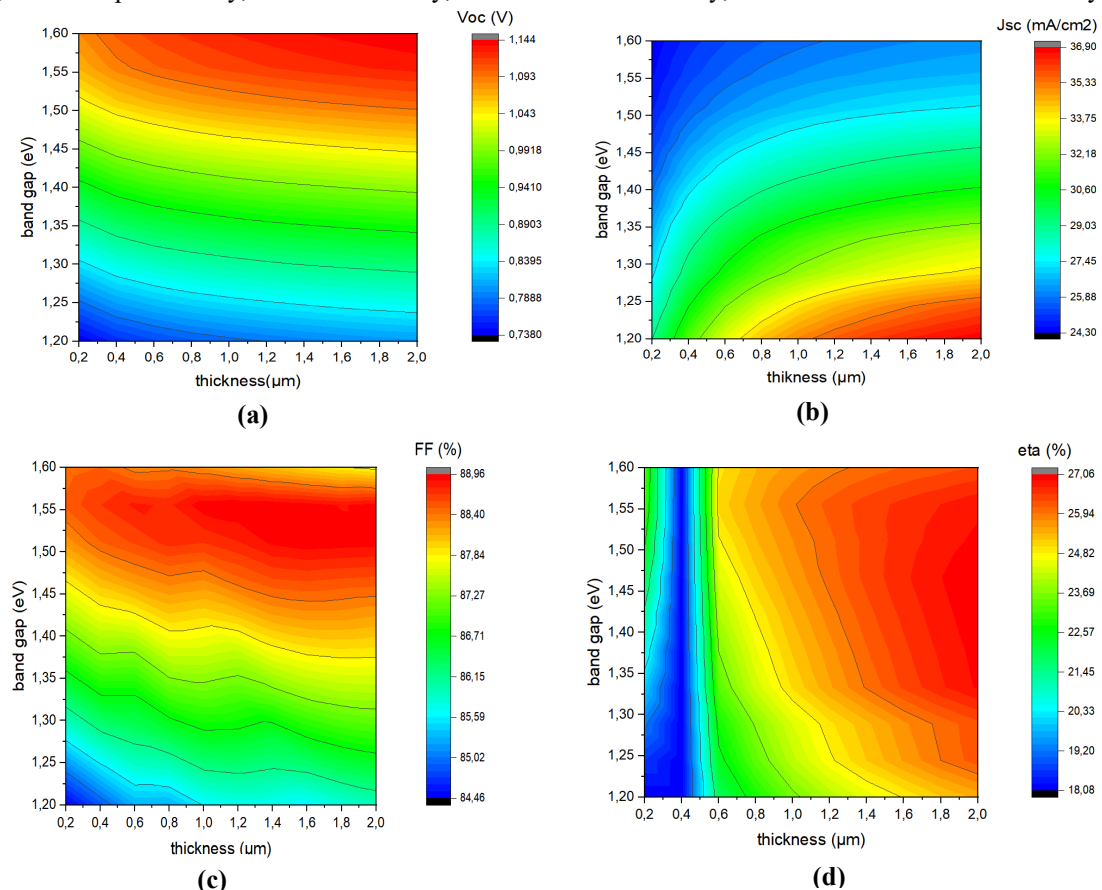


Figure 2. The simulated solar cells basic parameters including V_{oc} (a), J_{sc} (b), FF (c), and η (d) as function on

This section aims to explain how the photovoltaic performance of the basic CIGS/ ZrS_2 structure is impacted by two important solar cell parameters: the thickness and the absorber and tampon cushion band gaps. The thickness and the interdict band were changed from 0.2 to 2.0 μm and 1.2 to 1.6 V, respectively, in the first phase. In the second step, we examine how the thickness of the ZrS_2 couche and its energy difference affect solar cell performance in order to optimize the couche tampon's parameters. The final step is to ascertain how the concentration of donors ZrS_2 and acceptors CIGS (NA) affects the main parameter of the solar cell under study.

3.1.1. Exploring the impact of the CIGC thickness and band gap on conventional solar cell properties

It is commonly recognized that the absorber layer's thickness, band gap, and carrier concentration have a significant impact on how effectively solar cells work. The impact of the CIGS layer's thickness and band gap on solar cell performance was investigated in order to maximize the absorber layer properties.

It is well acknowledged that the properties of the absorbent layer, such as its thickness, band separation, and porteur density, are crucial for optimizing the performance of solar panels [14,15]. We have investigated how the thickness and band gap of the CIGS layer affect the efficiency of solar cells in order to enhance the properties of the absorption layer.

The contour plot depicting the interplay between absorber thickness and band energy of the CIGS layer of the basic structure is illustrated in Fig. 2, and how these variables impact the performance metrics of the device. We take a range of thickness from 0.2 to 2 μm and the gap energy from 1.2 to 1.6 eV. It is clear from this figure, that J_{SC} decreases

from about 36.90 mA/cm² at E_g of 1.2 eV to about 24.30 mA/cm² of 1.6 eV for the thickness greater to 0.8 μm however the variation of the J_{SC} with absorber thickness growth from 0.2 to 2 μm . The V_{oc} and FF decrease when the thickness increases but they rise with the variation of E_g . The efficiency decreases as the thickness of CIGS increases while remaining constant at E_g greater than 1.3 eV. The reason for this is that 1.3 eV represents the ideal value for a solar cell, enabling it to absorb the maximum quantity of solar radiation, which in turn leads to the generation of electron-hole pairs and an enhancement of the cell's efficiency [16]. Consequently, research indicates that CIGS serves as the most effective material to minimize usage. The optimal parameters determined for our new cell design are as follows: $V_{OC} = 1.06\text{V}$, $J_{SC} = 28.76 \text{ mA/cm}^2$, $FF = 88.55\%$, $\eta = 27.5\%$, with a thickness of 2 μm and an energy band gap of 1.46 eV.

Since it has been noted in the literature that device performance declined when E_g approached 1.3 eV, the impact of a larger uniformly variable energy band-gap has not been fully examined [17].

These results may be explained by expanding the interdigit band, the local efficacy of the luminescent absorption collection, and the interface between the p-CIGS chopped and n-ZnS₂ films. According to the following equation, this would raise the porters' output rate and, as a result, dramatically raise the V_{oc} value [18]:

$$V_{oc} = \frac{k_B T}{q} \ln \left(1 + \frac{I_{ph}}{I_0} \right) \quad (4)$$

In this equation, k_B , T and I_{ph} are the Boltzmann constant, the ambient temperature, and the photogenerated current respectively.

Additionally, this said that a clifflike band alignment is thought to enhance the charge separation process based on the CIGS and ZnS₂ bandgap values [7].

3.1.2. Exploring the effect of the ZrS₂ thickness and band gap on conventional Solar Cell properties

Having determined the optimal values of the mouthpiece thickness and the band gap of the absorber layer of the basic structure, we are now interested in the influence of these two factors on the performance of the buffer layer. as shown in the following figures.

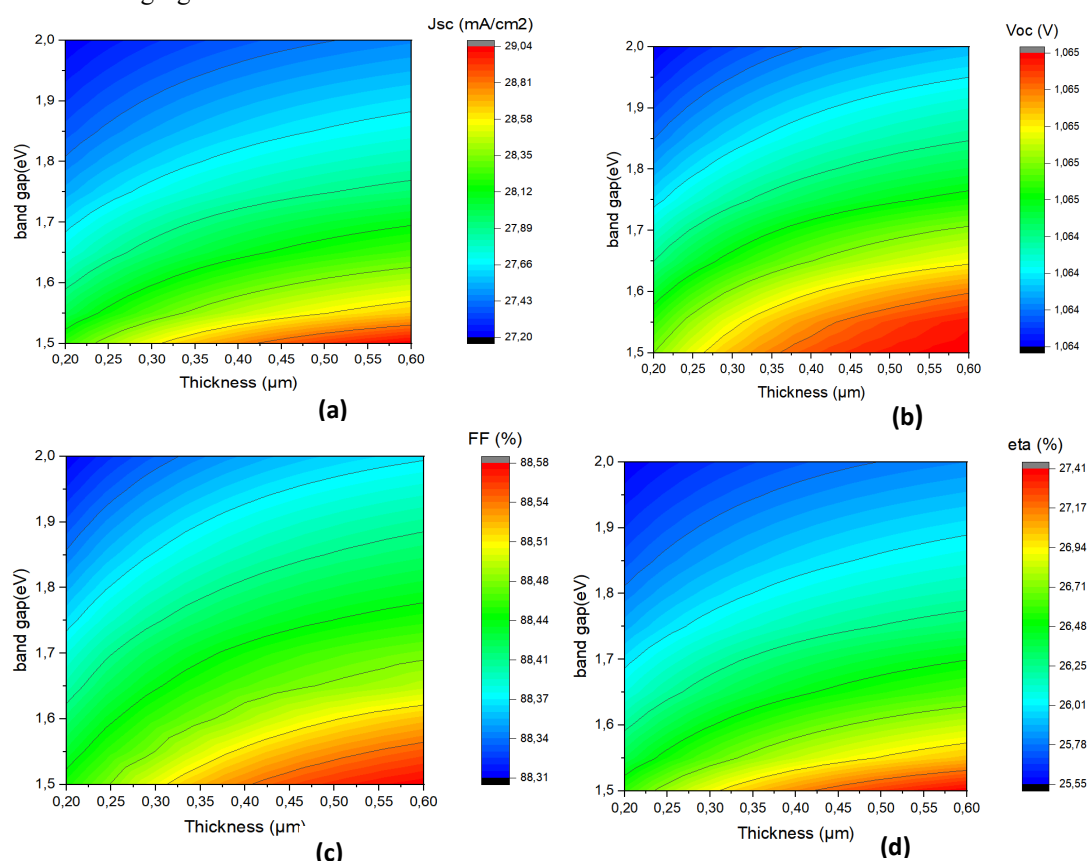


Figure 3. The fundamental parameters of solar cell simulations: V_{oc} (a), J_{sc} (b), FF (c), and η (d), are displayed according to the thickness of the tampon couch (axis des x) and the concentration of the carriers (axis des y).

Next, we examine how the ZrS₂ buffer layer's thickness and band gap affect the device performance as seen in the contour plot in Figure 3. The ZrS₂ buffer layer's thickness and band gap energy ranges from 0.20 to 0.60 μm and 1.5 to 2 eV, respectively. There is a consistent relationship among the photovoltaic output metrics V_{oc} , J_{sc} , FF , and efficiency. This suggests that the cell's overall performance increases when the ZrS₂ layer's thickness expands, but they decline with band gap rise. The development of structural flaws at the buffer layer interface might be connected to this phenomenon.

As a result, ZrS_2 's strong lattice mismatch strain reduces optical absorption, which might harm solar cells' overall performance [19, 20]. the best performances found are as follows: $V_{OC}=1.06\text{V}$, $J_{SC}=29.03\text{mA/m}^2$, $FF= 88.57\%$ and $\eta=27.40\%$ at $0.6\mu\text{m}$ and 1.5eV of thickness and band energy of ZrS_2 buffer layer, respectively.

3.1.3. Exploring the Impact of CIGS Na and ZrS_2 N_d on conventional solar cell properties

In order to maximize the efficiency of these solar cells with CIGS based, the impact of variations in ZrS_2 porteurs and CIGS couches on the key parameters of the cited structure has been examined. Fig. 4 exhibits the effect of the acceptor (Na) and donor (N_d) carrier concentration of CIGS and ZrS_2 , respectively, Na and N_d varied from 10^{12} to 10^{18} cm^{-3} . The V_{OC} , FF , η rise from 0.77 to 1.06 V , from 81.1 to 82.62% and from 19.14% to 27.42% ; when the Na increases. However, when the acceptor concentration of the CIGS layer increases, the J_{sc} drops from 29.83 to 29mA/cm^2 . Because of dominating recombination and the material's increased resistivity, it is harder to capture photo-generated electrons at larger concentrations, which accounts for the slight decrease in J_{sc} [21, 22]. However, further increasing the donor concentration in the ZrS_2 thin film does not affect the J_{SC} value between 10^{12} and 10^{18} cm^{-3} . increasing N_d of ZrS_2 has no major effect on cell performance.

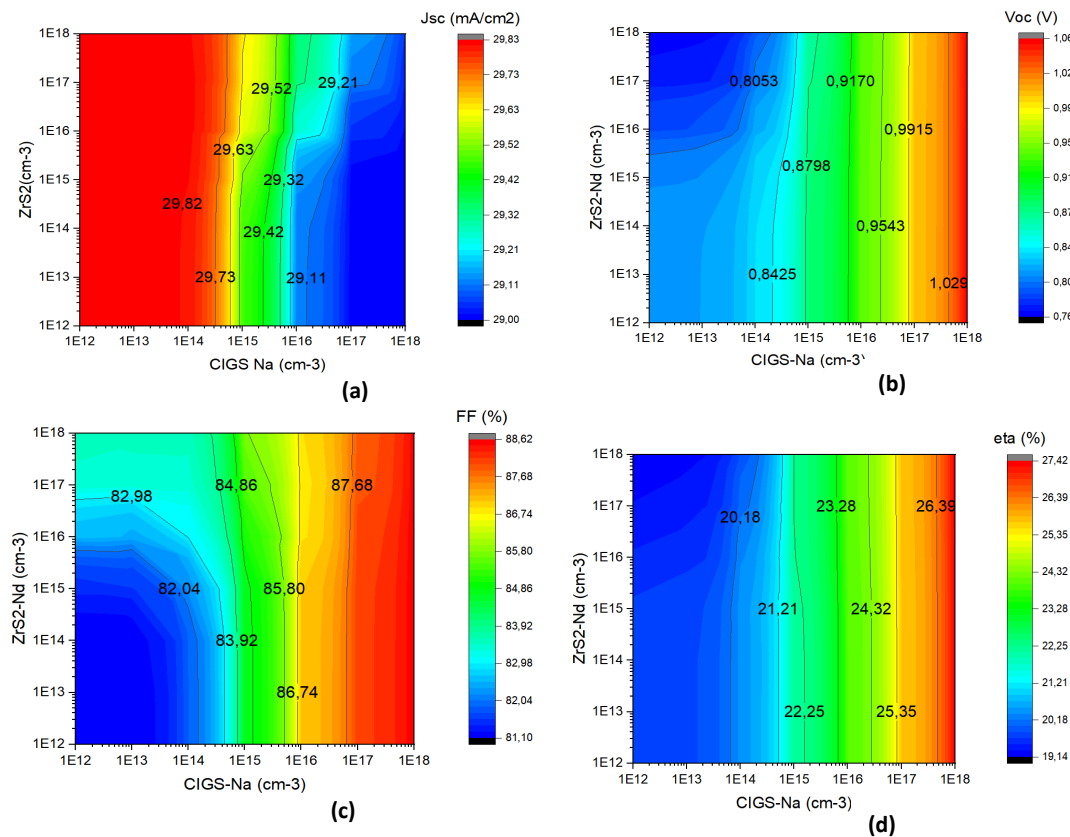


Figure 4. simulated solar cells basic parameters including V_{oc} (a), J_{sc} (b), FF (c), and η (d) as function on CIGS-Na (x-axis) and ZrS_2 N_d (y-axis)

III- Study of solar cell device with HTL material

Spiro-OMeTAD, one of the most widely used hole-transport materials (HTMs) in optoelectronic devices, often requires chemical doping with a lithium compound (LiTFSI) to get sufficient conductivity and efficient hole extraction [23]. Spiro-OMeTAD is a highly researched and effective hole transport layer material (HTL) owing to its ease of application and superior performance in organic-inorganic electronic systems spiro [24]. The spiro-linked molecule offers a high glass transition temperature (T_g), morphological stability, and facile processability, while preserving excellent electrical characteristics.

To indicate the influence of HTL on power conversion efficiency solar cell CIGS based design, the numerical simulations are done and the results are presented. The material properties used for HTL couches are taken from other published works in the literature. Table 1 compiles the essential HTL layer characteristics that were collected from [11, 12] to enhance the solar cell's performance. The impact of altering this layer's band gap on the most crucial solar cell properties using an HTL layer is seen in Figure 5 below. Nutrients improve all of the solar cell's parameters by jointly expanding the hole transport layer's band gap. In detail we notice an improvement in the surface current from 31.46 to 32.61mA/cm^2 , from 0.71 to 1.04 V for V_{OC} ; We also have a form factor improvement of 80.47 percent to 86.49% and an efficiency improvement of 19.04 to 29.36% [25].

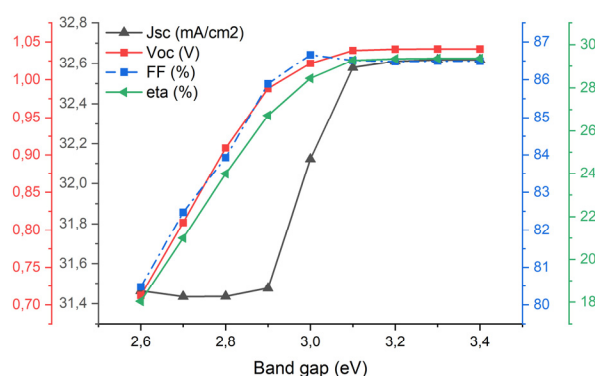


Figure 5. impact of altering the HTL layer's band gap on the solar cell's primary parameters.

It is well known that the band gap affects the mobility of charge carriers (holes) inside the HTL [26]. By facilitating the flow of holes from the active layer to the anode, a suitable band gap can raise the overall efficiency of the solar cell.

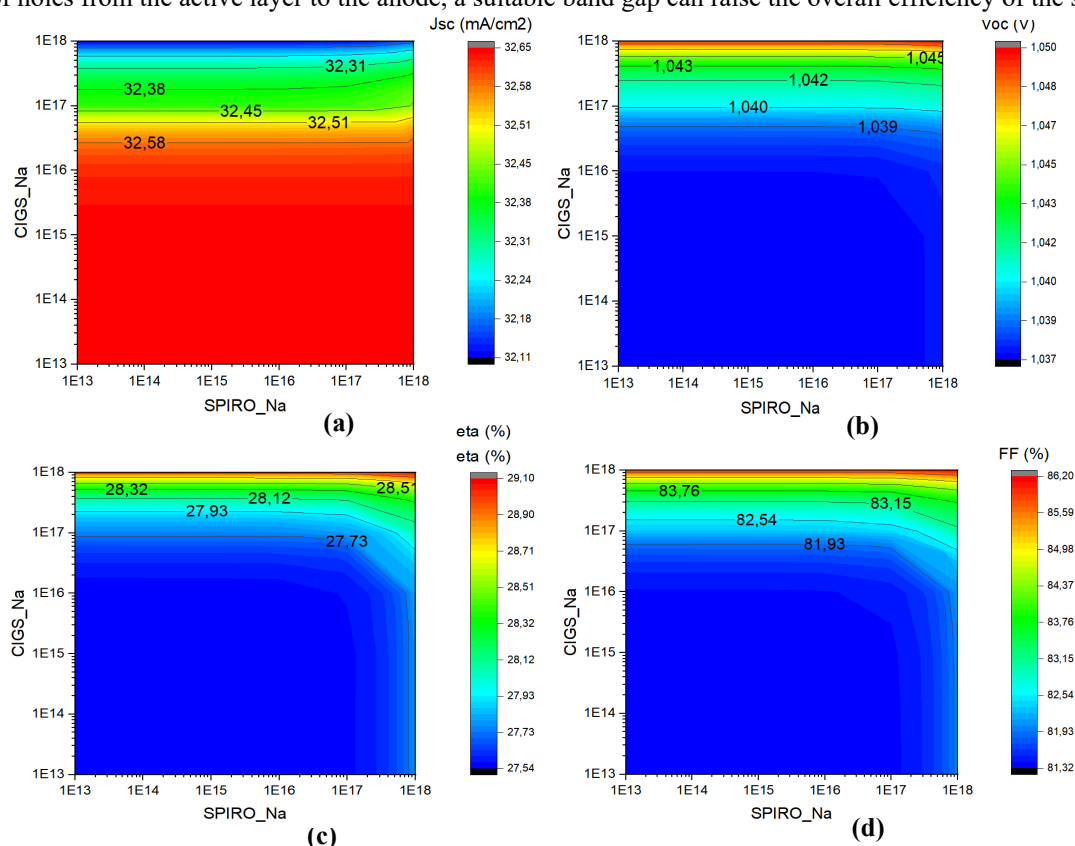


Figure 6. Contour plot of simulated solar cells parameters including Voc, Jsc, FF, and η as function on the Spiro Na (x-axis) and CIGS Na (y-axis)

On the other hand, the alignment of energy levels between the HTL and the active layer (such organic materials or perovskites) is influenced by the band gap. An appropriately matched band gap can promote effective charge transfer and lower interface energy losses [27]. Dance usually we adopted the value 3 eV for the gap because this is the value in which we found the best optimization of the solar cell.

To investigate the effects of acceptor density in the two layers, namely Spiro and CIGS, the following study was carried out, we vary the density of the acceptors for the two layers between an exponential 1.10^{12} and $1.10^{18}/\text{cm}^3$. Based on figure 6, we can assume that since all parameters essentially stay the same, changes in the layer's total acceptor density have no consequence on the solar cell's efficiency. The value of $\text{Na} = 10^{18}/\text{cm}^3$ has been set at for the two layers based on the results.

3.2. Operating temperature effects on the efficiency of solar cells

In this paragraph, in Fig. 7, the influence of operating temperature on the fundamental parameters of the basic structure and the optimal CIGS/ZrS₂/Spiro solar cell was explored. The following graphs show how the operational temperature affects two different configuration types: the basic setup without HTL and the suggested design that relies

on SPIRO-MeTAD as a HTL layer. These curves clearly show that the suggested cell's performance is not much impacted by temperature increases. Which is consistent with other previously published studies. It can be confirmed that the construction exhibits good stability in the face of temperature changes. which states that when temperature rises and the charge carrier recombination probability increases, the opposite saturation current (I_0) increases and, therefore, the V_{oc} , J_{sc} , and η values decrease [28].

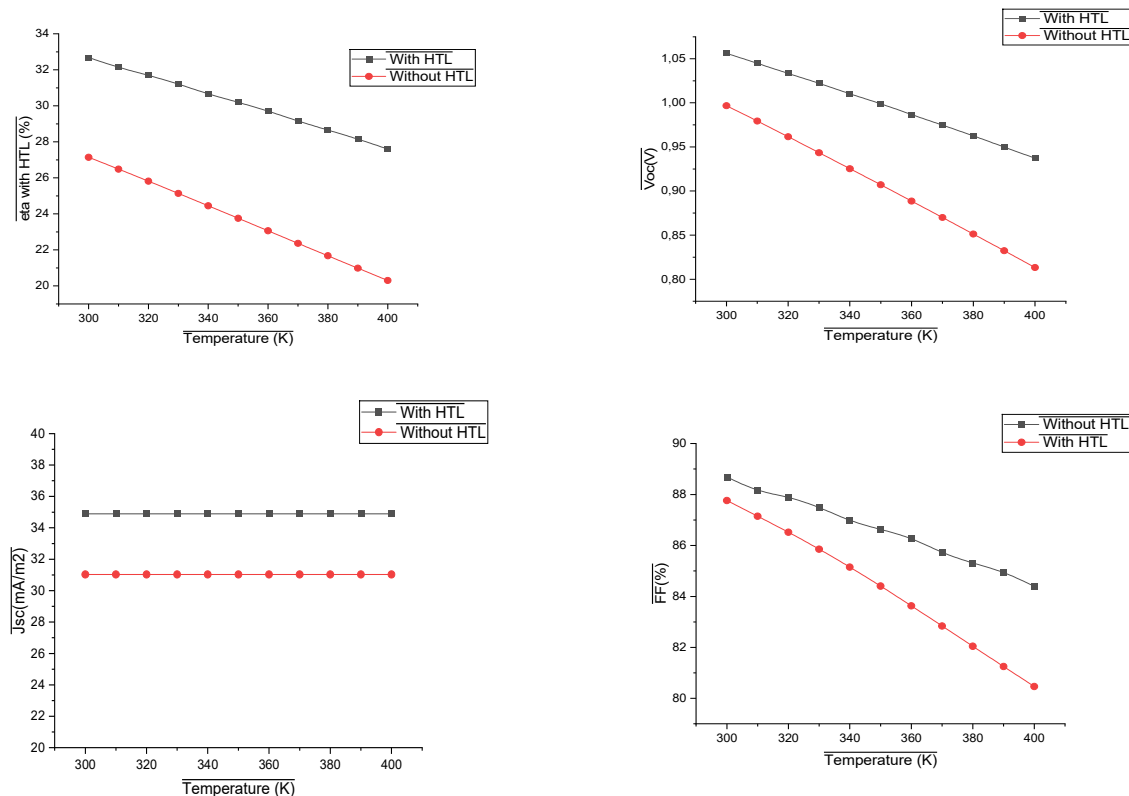


Figure 7. Impacts of the and temperature solar cell performances with and without HTL

4. COMPARATIVE STUDY OF THE PROPOSED STRUCTURE

4.1. Comparative analysis with another HTL layers

In the preceding paragraph, we demonstrated the value of including an HTL sofa into the structure using Spiro MeTAD; nevertheless, it is necessary to test more HTL materials and observe their impact on the building's performance. Consequently, many HTMs (ZrS_2 , $CuSbSe_2$, P3HT, Cu_2O and Spiro-OMeTAD) have been used to enhance simulation and guide experimental research in order to justify the use of spiro-OMeTAD as HTL. Table 1 displays the input parameters for the various HTL couches mentioned. The photovoltaic parameters obtained using various devices based on various HTL are shown in Table 2. It's noted that the total defect density (N_t) for each layer is taken for $1.00 \times 10^{14} \text{ cm}^{-3}$.

Table 2. The input characteristics for the various HTL layer mentioned

HTL	Voc(V)	Jsc(mA/cm ²)	FF(%)	PCE(%)	Ref
ZrS_2	0.997	31.03	88.00	27.22	[7]
$CuSbS_2$	1.07	32.62	87.35	30.69	[8]
P3HT	1.07	32.60	79.89	28.05	[9]
Cu_2O	1.07	32.59	84.95	29.83	[9]
Spiro	1.02	35.41	87.84	31.71	This work

This configuration of Spiro-HTL-based showed an excellent photovoltaic conversion yield of 31.71%, which was greater than that of other devices based on other HTMs, according to our testing of many HTMs based on the structure proposed in this study. Compared to the ather configurations with HTL, Spiro-OMeTAD-HTL we were able to get higher values for J_{sc} , FF and PCE. ($J_{sc}=35.41 \text{ mA/m}^2$, $FF=87.84\%$ and $PEC=31.71$).

4.2. Comparative study with other works

Using various tampon couches from other works, Table 3 compares the performance of the solar cells under investigation with that of the CIGS solar cells examined in other studies. The data makes it clear that the optimal efficiency we achieved in our research is 26.75%, which compares well with the results of other studies on solar cells CIGS.

An overview of certain published works has been done in order to arrange the solar cell in such an optimal manner. This course demonstrates that the optimized structure has one of the best configurations at the performance level that touches more than 31.71%.

Table 3. Comparative studies with other works

Cell structur	Voc(V)	Jsc(mA/cm ²)	FF(%)	PCE(%)	Ref
SnO ₂ / ZnSe/ CIGS/ / Mo	0.8242	21.08	79.70%,	13.85%	[29]
ZnO/CdS/CIGS/Mo	0.7436	34.47	83.09	21.3	[30]
ITO/ZrS ₂ /CIGS/Mo	1.0063	30.35	88.24	26.95	[4]
ZnO:Al/ZnO-i/Cd/CIGS /Mo	0.82	43.3	84%,	29.82%,	[31]
ZnO:Al/ZnS ₂ /CIGS/SPIRO/Mo	1.02	35.41	87.84	31.71	This work

4.3. Parameters of the optimal final cell

The following Figure 7 present the four fundamental parameters of the suggested cell output with Spiro as a HTL layer. As can be seen in this figure, the developed cell presents the following values. The most interesting is its exceptional efficiency of 31.7%. Given these considerations, this structure can be an alternative solution for photovoltaic systems.

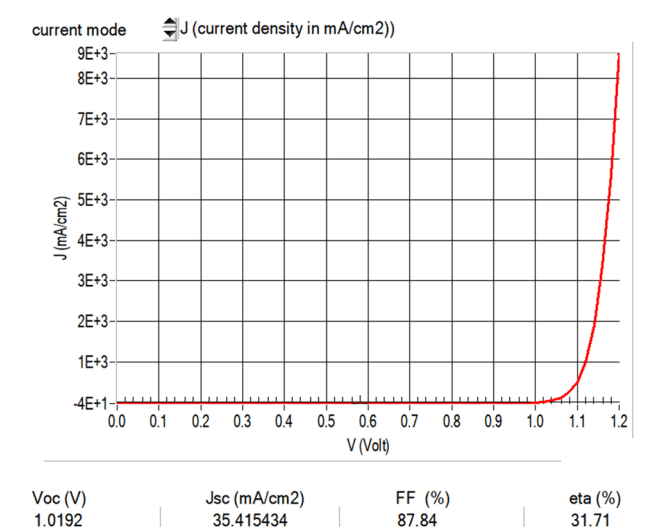


Figure 7. the main parameters of the optimized structure with HTL

5. CONCLUSION

We have utilized the SCAPS-1D software in this work to do numerical simulations and illustrate the potential of solar cells in Cu(In,Ga)Se₂ in order to maximize their performance. Among the many fundamental structural characteristics examined were the thickness, acceptor concentration, and band gap of the ZrS₂ tampon couche, as well as the donor concentration and thickness of the CIGSe absorber layer. The performance of the cells was further enhanced in the other section of this study by adding a Spiro as a buffer. Additionally taken into account was the effect of operational temperature. The suggested cell design's optimal output statistics include a PCE of 31.71%, a JSC of 35.41 mA/cm², an FF of 87.84%, and a V_{OC} of 1.02 V. These findings might contribute to the advancement of thin-film solar cells based on CIGSe that have excellent efficiency.

ORCID

- Mohamed Hamdaoui**, <https://orcid.org/0009-0008-9063-0984>;
 Lhoussayne Et-taya, <https://orcid.org/0000-0002-9815-3667>
Abdellah Benami, <https://orcid.org/0000-0001-5516-5660>;
 Malika Ouhadou, <https://orcid.org/0000-0002-9751-2381>
Abderrahman El Boukili, <https://orcid.org/0000-0002-3277-9640>;
 Jaouad Foshi, <https://orcid.org/0000-0002-8509-6130>

REFERENCES

- [1] A. Azmand and A.H. Kafashan, "Al-doped ZnS thin films: Physical and electrochemical characterizations," *J. Alloys Compd.* **779**, 301-313 (2019). <https://doi.org/10.1016/j.jallcom.2018.11.268>
- [2] R.N. Bhattacharya, M.-K. Oh and Y. Kim, "CIGS-based solar cells prepared from electrodeposited precursor films," *Sol. Energy Mater. Sol. Cells*, **98**, 198–202 (2012). <https://doi.org/10.1016/j.solmat.2011.10.026>
- [3] Qi Chen, et al., "Spiro-OMeTAD doped with cumene hydroperoxide for perovskite solar cells," *Electrochemistry Communications*, **126**, 107020 (2021). <https://doi.org/10.1016/j.elecom.2021.107020>
- [4] H. Kafashan and A. Bahrami, "CIGS solar cells using ZrS₂ as buffer layer: Numerical simulation," *Optik - International Journal for Light and Electron Optics*, **298**, 171594 (2024). <https://doi.org/10.1016/j.ijleo.2023.171594>
- [5] P. Ganesan, et al., "A simple spiro-type hole transporting material for efficient perovskite solar cells," *Energy. Environ. Sci.* **8**(7), 1986–1991 (2015). <https://doi.org/10.1039/C4EE03773A>

- [6] M. Al-Hattab, et al., “Numerical simulation of a new heterostructure CIGS/GaSe solar cell system using SCAPS-1D software,” *Sol. Energy*, **227**, 13–22 (2021). <https://doi.org/10.1016/j.solener.2021.08.084>
- [7] M. Moustafa, T. Al Zoubi and S. Yasin, “Exploration of CZTS-based solar using the ZrS₂ as a novel buffer layer by SCAPS simulation,” *Opt. Mater.* **124**, 112001 (2022). <https://doi.org/10.1016/j.optmat.2022.112001>
- [8] M. Ameri, E. Mohajerani, M. Ghafarkani, N. Safari and S.A. Alavi, “The investigation of the unseen interrelationship of grain size, ionic defects, device physics and performance of perovskite solar cells,” *J. Phys. D Appl. Phys.* **52**, 125501 (2019). <https://doi.org/10.1088/1361-6463/AAFEA9>
- [9] Y. Raoui, H. Ez-Zahraoui, N. Tahiri, O. El Bounagui, S. Ahmad and S. Kazim, “Performance analysis of MAPbI₃ (3) based perovskite solar cells employing diverse charge selective contacts: Simulation study,” *Sol. Energy*, **193**, 948–955 (2019). <https://doi.org/10.1016/j.solener.2019.10.009>
- [10] S. Karthick, J. Boucle and S. Velumani, “Effect of bismuth iodide (BiI₃) interfacial layer with different HTL’s in FAPI based perovskite solar cell-SCAPS-1D study,” *Sol. Energy*, **218**, 157–168 (2021). <https://doi.org/10.1016/j.solener.2021.02.041>
- [11] A. Hima, N. Lakhdar and A. Saadoun, “Effect of Electron Transporting Layer on Power Conversion Efficiency of Perovskite-Based Solar Cell: Comparative Study,” *Journal of Nano- and Electronic Physics*, **11**, 01026 (2019). [https://doi.org/10.21272/jnep.11\(1\).01026](https://doi.org/10.21272/jnep.11(1).01026)
- [12] D. Valencia, J. Conde, A. Ashok, C.A. Meza-Avendaño, H. Vilchis and S. Velumani, “Optimization of Cu(In, Ga)Se₂ (CIGSe) thin film solar cells parameters through numerical simulation and experimental study,” *Sol. Energy*, **224**, 298–308 (2021). <https://doi.org/10.1016/j.solener.2021.05.075>
- [13] H. Aissat, H. Arbouz and J.P. Vilcot, “Optimization and improvement of a front graded bandgap CuInGaSe₂ solar cell,” *Solar Energy Materials and Solar Cells*, **180**, 381–385 (2018). <https://doi.org/10.1016/j.solmat.2017.09.017>
- [14] A. Belghachi and N. Limam, “Effect of the absorber layer band-gap on CIGS solar cell,” *Chinese Journal of Physics*, **55**(4), 1127–1134 (2017). <https://doi.org/10.1016/j.cjph.2017.01.011>
- [15] S. Bechlaghem, B. Zebentout and Z. Benamara, “The major influence of the conduction-band offset on Zn (O, S)/CuIn_{0.7}Ga_{0.3}Se₂ solar cells,” *Results in Physics*, **10**, 650–654 (2018). <https://doi.org/10.1016/j.rinp.2018.07.006>
- [16] L. Et-taya, T. Ouslimane and A. Benami, “Numerical Simulation of Third-Generation Solar Cells Based on Kesterite CZTSSe Using SCAPS-1D,” in: *Proceedings of the 3rd International Conference on Electronic Engineering and Renewable Energy Systems. ICEERE*, 2022. Lecture Notes in Electrical Engineering, edited by H. Bakkay, A. Mellit, A. Gagliano, A. Rabhi, and A. Koulali, vol. **954**. (Springer, Singapore, 2022). http://dx.doi.org/10.1007/978-981-19-6223-3_31
- [17] Y. Osman, M. Fedawy, M. Abaza and M.H. Aly, “Optimized CIGS based solar cell towards an efficient solar cell: impact of layers thickness and doping”, *Optical and Quantum Electronics*, **53**, 245 (2021). <https://doi.org/10.1007/s11082-021-02873-4>
- [18] M. Abdelfatah, et al., “Fabrication and characterization of low cost Cu₂O/ZnO: Al solar cells for sustainable photovoltaics with earth abundant materials,” *Sol. Energy Mater. Sol. Cells*, **145**, 454–461 (2016). <https://doi.org/10.1016/j.solmat.2015.11.015>
- [19] H. Kafashan and A. Bahrami, “CIGS solar cells using ZrS₂ as buffer layer: Numerical simulation,” *Optik*, **298**, 71594 (2024). <https://doi.org/10.1016/j.ijleo.2023.171594>
- [20] T. AlZoubi and M. Moustafa, “Numerical optimization of absorber and CdS buffer layers in CIGS solar cells using SCAPS,” *International Journal of Smart Grid and Clean Energy*, **8**, 291–298 (2019). <https://doi.org/10.12720/sgcc.8.3.291-298>
- [21] L. Et-Taya, A. El Khalfi, M. Ouhadou, A. El Boukili, Md.F. Rahman and A. Benami, “Design and simulation of a new kesterite solar cell structure with and without a perovskite back surface field layer to exceed 32% efficiency,” *Physica Scripta*, **99**(5), 055922 (2024). <https://doi.org/10.1088/1402-4896/ad3684>
- [22] L. Et-taya, T. Ouslimane and A. Benami, “Numerical analysis of earth-abundant Cu₂ZnSn(SxSe_{1-x})₄ solar cells based on Spectroscopic Ellipsometry results by using SCAPS-1D,” *Solar Energy*, **201**, 827–835 (2020). <https://doi.org/10.1016/j.solener.2020.03.070>
- [23] X. Liu, B. Zheng, L. Shi, et al., « Perovskite solar cells based on spiro-OMeTAD stabilized with an alkylthiol additive,” *Nat. Photon.* **17**, 96–105 (2023). <https://doi.org/10.1038/s41566-022-01111-x>
- [24] C. Lin, G. Liu, X. Xi, L. Wang, Q. Wang, Q. Sun, M. Li, et al., “The Investigation of the Influence of a Cu₂O Buffer Layer on Hole Transport Layers in MAPbI₃-Based Perovskite Solar Cells,” *Materials*, **15**, 8142 (2022). <https://doi.org/10.3390/ma15228142>
- [25] S. Rabhi, et al., “The impact of CBz-PAI interlayer in various HTL-based flexible perovskite solar cells: A drift-diffusion numerical study”, *Heliyon*, **10**(10), e31138 (2024). <https://doi.org/10.1016/j.heliyon.2024.e31138>
- [26] H.S. Najafabadi, M.A. Meier and G.A. Hallock, “Charge carrier transport and electrical response by driving band gap modulation in semiconductors,” *Applied Materials Today*, **29**, 101608 (2022). <https://doi.org/10.1016/j.apmt.2022.101608>
- [27] L.V.T. Merino, et al., “Impact of the valence band energy alignment at the hole-collecting interface on the photostability of wide band-gap perovskite solar cells”, *Joule*, **8**(9), 2585–2606 (2024). <https://doi.org/10.1016/j.joule.2024.06.017>
- [28] A. Chen and K. Zhu, “Computer simulation of a-Si/c-Si heterojunction solar cell with high conversion efficiency,” *Sol. Energy*, **86**, 393–397 (2012). <https://doi.org/10.1016/j.solener.2011.10.015>
- [29] Rihana, S.F. Ahmed and M. Khalid, “Simulation of CIGS based solar cells with SnO₂ window layer using SCAPS-1D,” in: *2019 International Conference on Power Electronics, Control and Automation (ICPECA)*, (New Delhi, India, 2019), pp. 1–4. <https://doi.org/10.1109/ICPECA47973.2019.8975461>
- [30] H. Heriche, Z. Rouabah and N. Bouarissa, “New ultra-thin CIGS structure solar cells using SCAPS simulation program,” *International Journal of Hydrogen Energy*, **42**, 9524–9532 (2017). <https://doi.org/10.1016/j.ijhydene.2017.02.099>
- [31] M. Hamdaoui, L. Et-Taya, J. Foshi, N. Mansour and A. Benami, “Enhancement of the performance of solar cells based-CIGSe by using SCAPS-1D,” in: *2024 International Conference on Circuit, Systems and Communication (ICCSC)*, (Fes, Morocco, 2024), pp. 1–4, <https://doi.org/10.1109/ICCSC62074.2024.10617204>

СОНЯЧНІ ЕЛЕМЕНТИ З 31% ЕФЕКТИВНІСТЮ НА ОСНОВІ CIGS З ВИКОРИСТАННЯМ МАТЕРІАЛУ SPIRO ЯК БУФЕРНОГО ШАРУ: ЧИСЕЛЬНЕ МОДЕЛЮВАННЯ

Мохамед Хамдауї^a, Луссейн Ет-Тая^a, Абделла Бенамі^a, Маліка Ухаду^a, Абдеррахман Ель Букілі^b, Джауад Фош^c

^a*Департамент інженерних наук, оптоелектроніка та прикладні енергетичні методи, факультет наук і техніки, університет Мулая Ісмаїла в Мекнесе BP 509 Буталамін, Еррахідія, Марокко*

^b*Кафедра інженерних наук, сучасна фізика, радіація та застосування, факультет науки і технологій, університет Мулай Ісмаїла в Мекнесі BP 509 Буталамін, Еррашідія, Марокко*

^c*Департамент інженерних наук, електроніка та інтелектуальні системи, оптоелектроніка та прикладна енергетика (ОАЕТ), факультет наук і техніки, університет Мулай Ісмаїл у Мекнесі, BP 509, Буталамін, Еррашідія, Марокко*

У цьому дослідженні вивчається потенційне підвищення потужності сонячних елементів на основі (Cu(In,Ga)Se₂) за допомогою числового моделювання з використанням програмного забезпечення SCAPS-1D для оптимізації їхньої продуктивності. Були проаналізовані різні параметри, включаючи товщину, концентрацію акцепторів та ширину забороненої зони активного шару CIGSe, а також концентрацію донорів та товщину буферного шару ZrS₂. Також було враховано вплив робочої температури. Оптимізовані вихідні характеристики запропонованої конструкції елемента включають летючу органічну формулу (VOC) 1,13 В, струм опромінення (JSC) 32,61 мА/см², коефіцієнт деградації (FF) 89,12 та коефіцієнт виходу (PCE) 32,91. Ці результати можуть допомогти у розробці високоефективних тонкоплівкових сонячних елементів на основі CIGSe.

Ключові слова: SCAPS; робоча температура; товщина; робота виходу; параметри сонячних елементів

INFLUENCE OF FLUOROSUBSTITUTION ON THE HEAT CAPACITY OF ALIPHATIC ALCOHOLS

Leonid A. Bulavin^{a,b}, Oleksii V. Khorolskyi^c, Bohdan A. Hetalo^c, Andrii M. Hetalo^c,
Yevgenii G. Rudnikov^{a,d,*}

^aTaras Shevchenko National University of Kyiv, 64/13 Volodymyrska str., Kyiv 01601, Ukraine

^bInstitute for Safety Problems of Nuclear Power Plants of the NAS of Ukraine, 12 Lysohirska str., 03028 Kyiv, Ukraine

^cPoltava V. G. Korolenko National Pedagogical University, 2 Ostrohradskoho str., 36003 Poltava, Ukraine

^dNational Technical University of Ukraine "Igor Sikorsky Kyiv Polytechnic Institute",
37 Beresteyskyi Ave. 03056 Kyiv, Ukraine

*Corresponding Author E-mail: erudni67@gmail.com

Received June 9, 2025; revised July 22, 2025; in final form August 12, 2025; accepted August 23, 2025

In this paper, the principle of corresponding states was applied in a comparative analysis of the temperature dependencies of the isobaric heat capacities of aliphatic alcohols and their fluorosubstituted analogues. For the heat capacity, both experimental data from the literature and simulated data, obtained using artificial neural networks, were applied. The isobaric heat capacity for aliphatic alcohols in absolute values over a wide temperature range at constant pressure is smaller than that for the corresponding fluorosubstituted analogues. The comparison of the heat capacity data on the aliphatic alcohols and their fluorosubstituted analogues with the heat capacity of water, for which there is a hydrogen bond network, and comparison of the corresponding data with the heat capacity of hydrogen peroxide, where there are hydrogen bonds, but the network is absent, indicates that the change in the physical properties of alcohols upon fluorosubstitution is associated with the hydrogen bond density.

Keywords: Aliphatic alcohols; Fluorosubstituted alcohols; Water; Hydrogen peroxide; Heat capacity; Principle of corresponding states

PACS: 61.20.-p., 61.25.Em

INTRODUCTION

The study of the thermodynamic properties of fluorosubstituted monohydric aliphatic alcohols in comparison with their unsubstituted analogues is one of the essential problems of the up-to-date physics of liquids and liquid systems. The comparison of the thermodynamic properties of liquids within one homologous series and the substitution series, obtained by substituting hydrogen atoms with fluorine atoms in their molecules, enables the analysis of the characteristics of the mechanisms of molecular processes that occur in fluorosubstituted liquids. Such research is now relatively scarce and sometimes contradictory.

At the same time, the fluorosubstituted alcohols are currently widely used in pharmacology and organic synthesis as specific solvents and cosolvents, components of high-temperature heat carriers, lubricants, and adhesives, in the manufacture of pesticides and polymeric materials [1]. Fluorosubstituted alcohols continue to master new scopes of application, in particular, they are used in biotechnology for peptides stabilization [2], enzymes biomodification [3], change of the protein macromolecules structure [4], modification of the lipid membranes properties [5], as well as for modulation of the nicotinic acetylcholine receptors function [6], the mechanosensitive channel of small conductance, KcsA channels and potassium channels Kv1.3 [7,8], etc. However, despite the widespread use of fluorosubstituted alcohols in various industries, their thermodynamic properties remain poorly studied.

Thermodynamic coefficients of individual liquids allow analyzing the intermolecular bond energy, to relate the microscopic and macroscopic parameters of the system state with the changes in the molecular structure of the liquid. The analysis of literature sources has shown that the low-molecular representatives of homologous series (such as 2,2,2-trifluoroethanol and 1,1,1,3,3,3-hexafluoropropan-2-ol), which have found wide use in the chemical industry and biochemical engineering as specific solvents, can be considered as the best studied fluorosubstituted alcohols. As an example, in [9] the quantum-chemical calculations at the Gaussian M-062x/6-31+g (d,p) level were applied to determine the standard enthalpy, entropy, and heat capacity for various fluorosubstituted alcohols, emphasizing the importance of vibrational and rotational contributions to the specified properties. In [10] the authors provided new experimental data on the surface tension for 1H,1H-perfluoroalcohols of $\text{CF}_3(\text{CF}_2)_n\text{CH}_2\text{OH}$ ($n=0-5$) type, supplemented by molecular dynamics simulation to determine the phase equilibria and bulk properties, including the enthalpy of vaporization.

Papers [11-13] are devoted to the helical conformation of fluorosubstituted hydrocarbon chains, what can be explained by the fact that the fluorocarbon chains, due to steric repulsion of fluorine atoms, acquire a stable helical shape, but not the usual linear zigzag conformation of aliphatic alcohols. The manifestation of the steric effect is a change in the bond length and the valence angle between the carbon skeleton and halogen, thus causing tension in the

intramolecular structure and its change: the zigzag structure of the aliphatic alcohol molecule turns into a helical arrangement of fluorine atoms in the fluorosubstituted alcohol molecule. The steric hindrance of the substituent atom can affect the formation of hydrogen bonds and significantly reduce the acidic properties of alcohols. The reason for this is the negative inductive effect ($-I$ -effect) inherent in the strong electron-withdrawing fluorine substituent [13].

The transition from aliphatic alcohols to their fluorosubstituted analogues must affect the nature of intermolecular hydrogen bonds [14]. In [11], the quantum-chemical calculations, based on the semiempirical molecular orbital theory Parametric Method 3 (PM3), were applied to study the structural and thermodynamic properties of the formation of monomers ($n=1-14, 34$), dimers ($n=1-14, 34$), trimers and tetramers ($n=1-8$) of fluorosubstituted alcohols of the type $C_nF_{2n+1}CH_2CH_2OH$ at the air-water interface. From the analysis of the enthalpy, entropy, and Gibbs energy of the clusterization, it was concluded that the dimerization of fluorosubstituted alcohols at the air-water interface occurs in case, when the number of hydrocarbon links in the alcohol skeleton exceeds 6, while for the ordinary alcohols this number of the homologous series is 11. Such studies contribute to a deeper understanding of the surface and thermodynamic properties of fluorosubstituted alcohols, which is of crucial importance for practical applications. For this purpose, we have compared the thermodynamic properties of the studied alcohols with the corresponding properties of water, for which there is a continuous network of hydrogen bonds, and with the properties of hydrogen peroxide, for which the hydrogen bonds exist, but do not form a network.

At the present stage of predicting the thermodynamic properties of halogen-substituted organic compounds from the point of view of their molecular structure, special attention is paid to the application of artificial neural networks. As is well known, neural networks require reliable experimental data, and the quality of their prediction is higher the more relevant data are available within the homologous series. However, the fluorosubstituted alcohol heat capacity remains insufficiently studied experimentally today. These studies are aimed at clarifying the change in the molecular structure of the liquid at its transition from aliphatic alcohols [15,16] to their fluorosubstituted analogues. Explanation of the fluorosubstituted alcohol stabilizing properties at the molecular level, as well as comparison of the saturated acids stabilizing properties with physical mechanisms [17], remains an urgent task of condensed matter physics, which is important for modern biomedicine.

The object of this paper is to compare the temperature dependences of the isobaric heat capacity of liquid aliphatic alcohols within the same homologous series with the properties of their fluorosubstituted analogues using available experimental data and data obtained from artificial neural networks.

TECHNIQUE FOR THE ALCOHOL HEAT CAPACITY CALCULATION BY THE PRINCIPLE OF CORRESPONDING STATES

Utilizing the principle of corresponding states [18,19], the authors used the data for aliphatic alcohols, their fluorosubstituted analogues, water, and hydrogen peroxide, which are presented in up-to-date reference books [20,21], experimental databases [22-27], and databases simulated by artificial neural networks [28,29], or calculated by up-to-date statistical methods [30]. The theoretical foundations of simulations using artificial neural networks are presented in [31,32], and the examples of the artificial neural networks application for simulating the thermodynamic and transport properties of liquids are given in [33-35].

The utilized simulation approach [28] includes quantum-chemical calculations based on conformer analysis to determine the most stable structure of the molecule. In this case, optimization of the molecules spatial structure, comparison of the molecules energy levels and analysis of the relationship between the structure of the molecule and the property of the substance were carried out. The database [28] contains thermodynamic, physico-chemical, transport, spectral, biomedical, and other properties, as well as molecular descriptors. Both basic molecular descriptors, indicating the relative number of different atoms in a molecule, the structure of the molecule and the type of chemical bonds in the molecule, and special quantum-chemical descriptors, in particular topological ones (about 2000 descriptors in total), were used. The predicted data were compared with the experimental data, if available.

Note that the experimental data on the temperature dependences of isobaric heat capacity for the fluorosubstituted alcohols, as well as their critical parameters, are practically absent in the literature today. Therefore, for the fluorosubstituted alcohols, the simulations by artificial neural networks [28,29] were used. It should be noted that over the past 10 years, the simulation methods, based on artificial intelligence, have achieved significant development, thus allowing calculations of physical quantities with an error that is close to those occurring when these quantities are determined in the up-to-date experimental studies [28].

The principle of corresponding states [18,19] was used to compare the properties of aliphatic alcohols with those of their fluorosubstituted analogues. The isobaric heat capacity $C_p = T \cdot (\partial S / \partial T)_p = (\partial H / \partial T)_p$ was made dimensionless using critical values of temperature, density, and pressure:

$$C_r = \left(\frac{\partial H}{\partial T} \right)_p \cdot \frac{T_c \rho_c}{P_c}. \quad (1)$$

Here S is entropy, H is enthalpy, both referred to a mass unit (or to the number of moles) of the liquid; T_c , P_c , ρ_c are the critical values of temperature, pressure, and density, respectively. By the content of this dimensionlessness,

the enthalpy has the energy dimensionality, which is provided by the combination of critical parameters $P_c / \rho_c = P_c \cdot V_c$.

The temperature dependences of the heat capacity as well as the critical parameters were taken from literature sources [20-24] or simulated using the artificial neural networks [28,29]. Table 1 presents the utilized values of the studied liquids critical parameters.

Table 1. Critical parameters of aliphatic alcohols, their fluorosubstituted analogues, water, and hydrogen peroxide with their CAS identification

Substance	CAS	T_c , K	P_c , kPa	$\rho_c \cdot 10^4$, m ³ /mol
methanol	67-56-1	519.368	8012.12	1.15
ethanol	64-17-5	515.071	6137.06	1.69
propanol-1	71-23-8	535.940	5197.28	2.24
butanol-1	71-36-3	560.307	4452.95	2.77
pentanol-1	71-41-0	583.979	3839.56	3.34
hexanol-1	111-27-3	610.024	3425.08	3.89
heptanol-1	111-70-6	628.259	3095.95	4.43
octanol-1	111-87-5	646.665	2888.66	4.97
nonanol-1	143-08-8	662.673	2510.61	5.51
3F-ethanol-1	75-89-8	499	4863	2.04
5F-propanol-1	422-05-9	511	3862	2.56
7F-butanol-1	375-01-9	522	3199	3.07
9F-pentanol-1	355-28-2	536	2550	3.62
11F-hexanol-1	423-46-1	549	2263	4.15
13F-heptanol-1	375-82-6	563	1942	4.65
15F-octanol-1	307-30-2	582	1685	5.15
17F-nonanol-1	423-56-3	604	1515	5.69
water	7722-18-5	647.1	22064	0.563
hydrogen peroxide	7722-84-1	727.98	22000	0.777

TEMPERATURE DEPENDENCES OF THE ALCOHOL ISOBARIC HEAT CAPACITY ALONG THE LIQUID–VAPOR COEXISTENCE CURVE

Let us consider the temperature dependences of the isobaric heat capacity of aliphatic alcohols and their fluorosubstituted analogues applying the principle of corresponding states. For the alcohols we studied, the literature lacks both experimental data on the temperature dependences of the heat capacity and the values of the critical parameters that are necessary when applying the principle of corresponding states. In the view of the availability of only simulated data for the fluorosubstituted alcohols under study (Table 1), the data, simulated by the same technique [28,29] for both aliphatic alcohols and their fluorosubstituted analogues, are used in the paper.

Our analysis have shown that for aliphatic alcohols the difference between the simulated data on heat capacity [28] and similar data, but obtained experimentally [15, 36], generally increases with an increase in the number of carbon atoms. We estimated the relative deviation $\delta = C_p - \tilde{C}_p$ of the simulated heat capacity value \tilde{C}_p from the experimental value C_p at the same temperature as $\Delta = 2 \cdot (C_p - \tilde{C}_p) / (C_p + \tilde{C}_p)$. The maximum relative deviation $\Delta_{\max} = 2 \cdot (C_p - \tilde{C}_p) / (C_p + \tilde{C}_p)$ on the side of higher temperatures varied from 0.5% for ethanol to 9% for nonanol (see Table 2). At the same time, the arithmetic mean absolute deviation $\bar{\delta}$ and relative deviation $\bar{\Delta}$ for each alcohol at equidistantly selected temperatures are at least half their maximum values $|\delta_{\max}|$ and $|\Delta_{\max}|$, respectively.

Table 2. Modulus of the maximum absolute $|\delta_{\max}|$ and relative $|\Delta_{\max}|$ deviations of the simulated data on the heat capacity of aliphatic alcohols from the similar data obtained experimentally

Substance	Modulus of maximum absolute deviation $ \delta_{\max} $, J/(mol·K)	Modulus of maximum relative deviation $ \Delta_{\max} $
ethanol	0.678	0.0049
propanol-1	1.69	0.0089
butanol-1	6.50	0.0255
pentanol-1	20.9	0.0671
hexanol-1	22.8	0.0723
heptanol-1	26.7	0.0666
octanol-1	39.2	0.0885
nonanol-1	42.8	0.0883

The critical parameters of fluorosubstituted alcohols were obtained by artificial neural networks [28,29]. The temperature dependences of the dimensionless isobaric heat capacity C_r according to (1) on the reduced temperature $\tau = T/T_c$ for the aliphatic alcohols and their fluorosubstituted analogues are presented in Fig. 1 and 2, respectively.

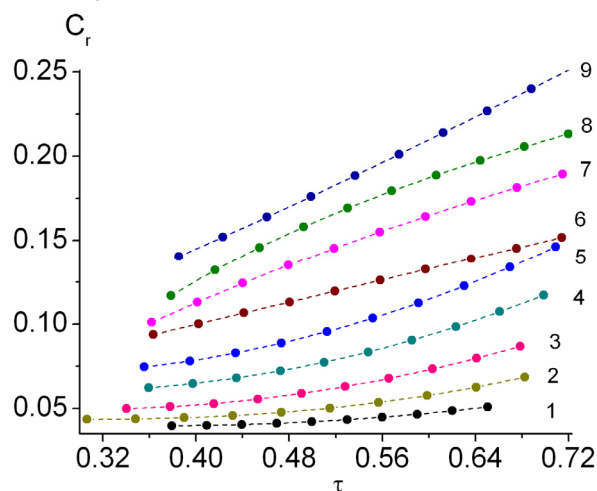


Figure 1. Temperature dependences of the reduced isobaric heat capacity of aliphatic alcohols in the liquid phase along the liquid–vapor coexistence curve: 1 – methanol, 2 – ethanol, 3 – propanol, 4 – butanol, 5 – pentanol, 6 – hexanol, 7 – heptanol, 8 – octanol, 9 – nonanol

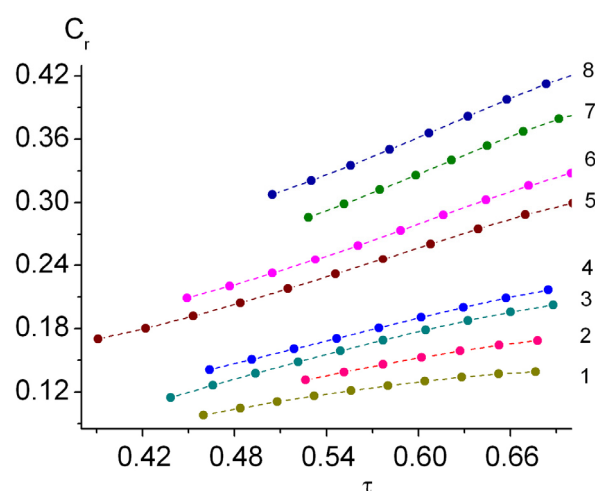


Figure 2. Temperature dependences of the reduced isobaric heat capacity of fluorosubstituted alcohols in the liquid phase along the liquid–vapor coexistence curve: 1 – 3F-ethanol, 2 – 5F-propanol, 3 – 7F-butanol, 4 – 9F-pentanol, 5 – 11F-hexanol, 6 – 13F-heptanol, 7 – 15F-octanol, 8 – 17F-nonanol

The analysis of Fig. 1 and 2 shows that the temperature dependences of the isobaric heat capacity for aliphatic alcohols and their fluorosubstituted analogues are monotonic, but under certain conditions have inflection points. Moreover, in a wide temperature range along the liquid–vapor coexistence curve, the isobaric heat capacity of the aliphatic alcohols is almost half the isobaric heat capacity of the fluorosubstituted alcohols. Fig. 3 presents the temperature dependences of the reduced isobaric heat capacity for some pairs aliphatic alcohol – its fluorosubstituted analogue.

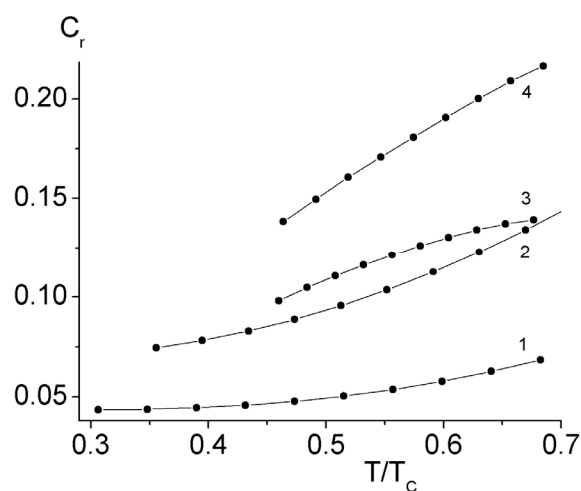


Figure 3. Temperature dependences of the reduced isobaric heat capacity of liquids along the liquid–vapor coexistence curve: 1 – ethanol, 2 – pentanol, 3 – 3F-ethanol, 4 – 9F-pentanol

As Figure 3 shows, curves 1 and 2, which correspond to aliphatic alcohols, have a positive second derivative of the heat capacity with respect to temperature, while curves 3 and 4, which correspond to fluorosubstituted alcohols, have a negative corresponding derivative. Our research has shown that for ethanol $(\partial^2 C_r / \partial T^2)_p > 0$, while for trifluoroethanol $(\partial^2 C_r / \partial T^2)_p < 0$; in the vicinity of the melting temperature for hexanol $(\partial^2 C_r / \partial T^2)_p < 0$, while for 11F-hexanol $(\partial^2 C_r / \partial T^2)_p > 0$. Such features of the behavior of fluorosubstituted alcohols as compared to the aliphatic alcohols may indicate to structural differences of the alcohols in the liquid state under study. The research described in [11,12,13] indicates the significant differences according to which the molecules of fluorosubstituted alcohols can be located more densely due to the helical conformation of the fluorosubstituted hydrocarbon chains. In our opinion, this may occur due to the destruction of a certain number of hydrogen bonds.

DISCUSSION OF RESULTS

To understand the reasons for significant difference in the values of the isobaric heat capacities of the studied alcohols, the attention should be paid to the influence of hydrogen bonds on the value of the heat capacity of liquids along the liquid–vapor coexistence curve. For this purpose, we use the principle of corresponding states to compare the heat capacity of water, in which there is a continuous network of hydrogen bonds, with that of hydrogen peroxide, where the hydrogen bonds exist, but their continuous network is absent. Fig. 4 shows the temperature dependences of the isobaric heat capacity of water and hydrogen peroxide along the liquid–vapor coexistence curve, calculated according to the principle of corresponding states. The indicated curves have minimums at the temperature of 36°C ($T/T_c=0.477$) for water and 155°C ($T/T_c=0.558$) for hydrogen peroxide. The minima in the temperature dependences of the heat capacities of water, hydrogen peroxide, and a number of other substances having a small molar mass [21,22,23,24] indicate the emergence of molecules associates [15] at the temperatures lower than those of the minima. At the same time, for the aliphatic alcohols [15,28] and their fluorine-substituted analogues [28] the minima in the temperature dependences of the heat capacities do not occur. Below the temperatures of the indicated minima, the temperature dependence of the isobaric heat capacities of water and hydrogen peroxide along the liquid–vapor coexistence curve is anomalous as compared to other liquids. When the temperatures are above the indicated minima, the heat capacities of the indicated liquids increase as the temperature grows, as it is shown in Fig. 3 for the studied alcohols.

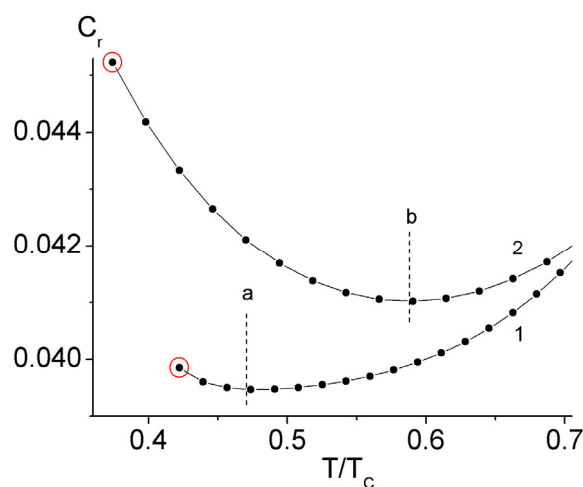


Figure 4. Temperature dependences of the reduced isobaric heat capacity of liquids along the liquid-vapor coexistence curve: 1 – water, 2 – hydrogen peroxide; a - minimum for water, b - minimum for hydrogen peroxide. Circles indicate the triple points

The analysis of Fig. 4 leads to the conclusion that the reduced heat capacity of water exceeds the reduced heat capacity of hydrogen peroxide due to the presence of a continuous network of hydrogen bonds in water. Therefore, it can be assumed that for the fluorosubstituted alcohols, where most of the hydrogen atoms are replaced by fluorine atoms, the hydrogen bonds are less dense, thus resulting in higher values of the reduced isobaric heat capacity (Fig. 3, curves 3 and 4).

Unlike the aliphatic alcohols, the temperature dependences of the isobaric heat capacity of their fluorosubstituted analogues have opposite signs of the second derivative of the heat capacity with respect to the temperature. According to [15], the curves of the temperature dependences of the alcohols heat capacity can have an inflection point associated with the breaking of hydrogen bonds above the inflection temperature. The breaking of the aliphatic alcohol hydrogen bonds corresponds to such inflection points [15] for which $(\partial^2 C_r / \partial T^2)_p > 0$ is below the inflection temperature, while $(\partial^2 C_r / \partial T^2)_p < 0$ is above the inflection temperature. Note, that for the corresponding aliphatic thiols, in whose molecules instead of the oxygen atom there is a heavier sulfur atom, the curves of the temperature dependences of the heat capacity do not have inflection points [15].

Thus, the opposite sign of the second derivative of the heat capacity with respect to the temperature for the aliphatic alcohols and their fluorosubstituted analogues indicates that for the fluorosubstituted alcohols there exists a hydrogen bond breaking dynamics.

CONCLUSIONS

Using the principle of corresponding states, a comparative analysis of the temperature dependences of the isobaric heat capacity of aliphatic alcohols and their fluorosubstituted analogues was carried out in the wide temperature range along the liquid–vapor coexistence curve.

On the basis of literature experimental data and the simulations, performed by artificial neural networks, it is shown that homologous series of aliphatic alcohols and their fluorosubstituted analogues have differences in reduced caloric properties.

It is shown that in a wide temperature range along the liquid–vapor coexistence curve, the reduced isobaric heat capacity of fluorosubstituted alcohols is almost twice as high as the corresponding value of the aliphatic alcohols, which the authors attribute to a decrease in the number of hydrogen bonds in the fluorosubstituted alcohols as compared with the aliphatic ones.

Unlike the aliphatic alcohols, for their fluorosubstituted analogues the second derivative of the heat capacity with respect to temperature along the liquid–vapor coexistence curve is opposite in sign, which indicates to the dynamics of hydrogen bond breaking upon fluorosubstitution in aliphatic alcohols.

Conflict of interest

The authors declare the absence of any conflict of interest related to the research presented in this manuscript.

ORCID

©Leonid A. Bulavin, <https://orcid.org/0000-0002-8063-6441>; ©Oleksii V. Khorolskyi, <https://orcid.org/0000-0001-9272-0395>; ©Bogdan A. Hetalo, <https://orcid.org/0009-0007-8191-3811>; ©Andrii M. Hetalo, <https://orcid.org/0000-0001-8312-089X>; ©Yevgenii G. Rudnikov <https://orcid.org/0000-0002-6328-1650>

REFERENCES

- [1] *Current Fluoroorganic Chemistry: New Synthetic Directions, Technologies, Materials, and Biological Applications*, edited by V.A. Soloshonok, K. Mikami, T. Yamazaki, J.T. Welch, and J.F. Honek, (American Chemical Society, 2007).
- [2] J. Vymětal, L. Bednářová, and J. Vondrášek, “Effect of TFE on the helical content of AK17 and HAL-1 peptides: Theoretical insights into the mechanism of helix stabilization”, *The Journal of Physical Chemistry B*, **120**, 1048-1059 (2016). <https://doi.org/10.1021/acs.jpcb.5b11228>
- [3] A.M. Arnold, P. Dullinger, A. Biswas, C. Jandl, D. Horinek, and T. Gulder, “Enzyme-like polyene cyclizations catalyzed by dynamic, self-assembled, supramolecular fluoro alcohol-amine clusters”, *Nature Communications*, **14**, 813 (2023). <https://doi.org/10.1038/s41467-023-36157-0>
- [4] N. Nakata, R. Okamoto, T. Sumi, K. Koga, T. Morita, and H. Imamura, “Molecular mechanism of the common and opposing cosolvent effects of fluorosubstituted alcohol and urea on a coiled coil protein”, *Protein Science*, **32**, e4763 (2023). <https://doi.org/10.1002/pro.4763>
- [5] V.V. Motov, E.F. Kot, A.V. Shabalkina, S.A. Goncharuk, A.S. Arseniev, M.V. Goncharuk, and K.S. Mineev, “Investigation of lipid/protein interactions in trifluoroethanol–water mixtures proposes the strategy for the refolding of helical transmembrane domains”, *Journal of Biomolecular NMR*, **77**, 15-24 (2023). <https://doi.org/10.1007/s10858-022-00408-x>
- [6] E.L. Godden, R.A. Harris, and T.V. Dunwiddie, “Correlation between molecular volume and effects of n-alcohols on human neuronal nicotinic acetylcholine receptors expressed in *Xenopus* oocytes”, *Journal of Pharmacology and Experimental Therapeutics*, **296**, 716-722 (2001). [https://doi.org/10.1016/s0022-3565\(24\)38808-1](https://doi.org/10.1016/s0022-3565(24)38808-1)
- [7] B. Akitake, R.E. Spelbrink, and S. Sukharev, “2,2,2-Trifluoroethanol changes the transition kinetics and subunit interactions in the small bacterial mechanosensitive channel MscS”, *Biophysical Journal*, **92**, 2771-2784 (2007). <https://doi.org/10.1529/biophysj.106.098715>
- [8] M.I. Lioudyno, M. Broccio, and J.E. Hall, “Effect of synthetic aβ peptide oligomers and fluorosubstituted solvents on Kv1.3 channel properties and membrane conductance”, *PLoS One*, **7**, e35090 (2012). <https://doi.org/10.1371/journal.pone.0035090>
- [9] H. Abdel-Wahab, and J. Bozzelli, “Gaussian M-062x/6-31+g (d,p) calculation of standard enthalpy, entropy and heat capacity of some fluorosubstituted alcohol’s and its radicals at different temperatures”, *American Journal of Physical Chemistry*, **9**, 101-111 (2020). <https://doi.org/10.11648/j.ajpc.20200904.13>
- [10] G.M.C. Silva, J. Justino, P. Morgado, M. Teixeira, L.M.C. Pereira, L.F. Vega, and E.J.M. Filipe, “Detailed surface characterization of highly fluorosubstituted liquid alcohols: Experimental surface tensions, molecular simulations and soft-SAFT theory”, *Journal of Molecular Liquids*, **300**, 112294 (2020). <https://doi.org/10.1016/j.molliq.2019.112294>
- [11] Y.B. Vysotsky, V.S. Bryantsev, F.L. Boldyreva, V.B. Fainerman, and D. Vollhardt, “Quantum chemical semiempirical approach to the structural and thermodynamic characteristics of fluoroalkanols at the air/water interface”, *The Journal of Physical Chemistry B*, **109**, 454-462 (2005). <https://doi.org/10.1021/jp048240e>
- [12] M.P. Krafft, and J.G. Riess, “Chemistry, physical chemistry, and uses of molecular fluorocarbon–hydrocarbon diblocks, triblocks, and related compounds – Unique “apolar” components for self-assembled colloid and interface engineering”, *Chemical Reviews*, **109**, 1714-1792 (2009). <http://doi.org/10.1021/cr800260k>
- [13] A.M. Hetalo, O.V. Khorolskyi, S.A. Stetsenko, S.O. Samoilenko, and O.S. Svechnikova, “Similar behavior of rheological properties and the evaluation of the melting temperatures of fluorosubstituted aliphatic alcohols”, *Ukrainian Journal of Physics*, **65**, 419-427 (2020). <https://doi.org/10.15407/ujpe65.5.419>
- [14] A.M. Hetalo, O.P. Rudenko, O.V. Khorolskyi, S.O. Samoilenko, and L.A. Bulavin, “Temperature dependence of the bulk elasticity modulus of aliphatic alcohols and their fluorosubstituted analogs”, *Ukrainian Journal of Physics*, **63**, 134-137 (2018). <https://doi.org/10.15407/ujpe63.2.134>
- [15] M. Zabransky, M. Bures, and V. Ruzicka Jr., “Types of curves for the temperature dependence of the heat capacity of pure liquids”, *Thermochimica Acta*, **215**, 25-45 (1993). [https://doi.org/10.1016/0040-6031\(93\)80080-T](https://doi.org/10.1016/0040-6031(93)80080-T)
- [16] V. Pogorelov, L. Bulavin, I. Doroshenko, O. Fesjun, and O. Veretennikov, “The structure of liquid alcohols and the temperature dependence of vibrational bandwidth”, *Journal of Molecular Structure*, **708**, 61-65 (2004). <https://doi.org/10.1016/j.molstruc.2004.03.003>
- [17] V.I. Petrenko, M.V. Avdeev, L. Almásy, L.A. Bulavin, V.L. Aksenov, L. Rosta, and V.M. Garamus, “Interaction of monocarboxylic acids in benzene studied by small-angle neutron scattering”, *Colloids and Surfaces A: Physicochemical and Engineering Aspects*, **337**, 91-95 (2009). <https://doi.org/10.1016/j.colsurfa.2008.12.001>
- [18] I.I. Novikov, “Thermodynamic similarity and prediction of the properties and characteristics of substances and processes”, *Journal of Engineering Physics*, **53**, 1227-1232 (1987). <https://doi.org/10.1007/BF00871080>

- [19] H.W. Xiang, *The Corresponding-States Principle and Its Practice. Thermodynamic, Transport and Surface Properties of Fluids*, (Elsevier Science, 2005).
- [20] C. Yaws, *Thermophysical Properties of Chemicals and Hydrocarbons*, (Gulf Professional Publishing, 2014).
- [21] M.Z. Southard, and D.W. Green, *Perry's Chemical Engineers' Handbook*, (McGraw-Hill Education, 2019).
- [22] P.J. Linstrom, and W.G. Mallard (Eds.), *NIST Chemistry WebBook, NIST Standard Reference Database Number 69*, (National Institute of Standards and Technology, 2025). <https://doi.org/10.18434/T4D303>
- [23] *MiniRefprop Database*, (National Institute of Standards and Technology, 2025). <https://trc.nist.gov/refprop/MINIREF/MINIREF.HTM>
- [24] I.H. Bell, J. Wronski, S. Quoilin, and V. Lemort, "Pure and pseudo-pure fluid thermophysical property evaluation and the open-source thermophysical property library CoolProp", *Industrial & Engineering Chemistry Research*, **53**, 2498-2508 (2014). <https://doi.org/10.1021/ie4033999>
- [25] *NIST Reference Fluid Thermodynamic and Transport Properties Database (REFPROP)*, (National Institute of Standards and Technology, 2025). <https://www.nist.gov/srd/refprop>
- [26] *ThermoData Engine Database*, (National Institute of Standards and Technology, 2025). <https://trc.nist.gov/tde.html>
- [27] *NIST/TRC Web Thermo Tables (WTT). NIST Standard Reference Subscription Database*, (National Institute of Standards and Technology, 2025). <https://wtt-pro.nist.gov/wtt-pro/>
- [28] *MOL-Instincts Database*, (ChemEssen, 2025). <https://www.molinstincts.com/>
- [29] *ChemRTP Database*, (ChemEssen, 2025). <http://www.chemrtp.com/>
- [30] M. Zábranský, V. Růžička, and V. Majer, "Heat capacities of organic compounds in the liquid state I. C1 to C18 1-alkanols", *Journal of Physical and Chemical Reference Data*, **19**, 719-762 (1990). <https://doi.org/10.1063/1.555860>
- [31] *Pure Property Calculator*, (Korea Thermophysical Properties Data Bank, 2025). <https://www.mdlkdb.com/calculate/pure>

ВПЛИВ ФТОРЗАМІЩЕННЯ НА ТЕПЛОЄМНІСТЬ АЛІФАТИЧНИХ СПИРТІВ

Леонід А. Булавін^{a,b}, Олексій В. Хорольський^c, Богдан А. Гетало^c, Андрій М. Гетало^c, Євгеній Г. Рудніков^{a,d}

^aКиївський національний університет імені Тараса Шевченка, вул. Володимирська, 64/13, 01601 Київ, Україна

^bІнститут проблем безпеки атомних електростанцій НАН України, вул. Лисогірська, 12, 03028 Київ, Україна

^cПолтавський національний педагогічний університет імені В. Г. Короленка, вул. Остроградського, 2, 36003 Полтава, Україна

^dНаціональний технічний університет України "Київський політехнічний інститут імені Ігоря Сікорського",
просп. Берестейський, 37, 03056 Київ, Україна

Із використанням принципу відповідних станів у статті проведено порівняльний аналіз температурних залежностей ізобарної теплоємності аліфатичних спиртів та їх фторзаміщених аналогів. Для теплоємності використані як літературні експериментальні дані, так і симульовані дані, отримані за допомогою штучних нейронних мереж. Ізобарна теплоємність для аліфатичних спиртів за абсолютними величинами в широкому температурному інтервалі при сталому тиску є меншими, ніж для відповідних фторзаміщених аналогів. Порівняння даних теплоємності аліфатичних спиртів та їх фторзаміщених аналогів із теплоємністю води, для якої існує сітка водневих зв'язків, із відповідними даними для перекису водню, де є водневі зв'язки, але сітка відсутня, вказує на те, що зміна фізичних властивостей спиртів при фторзаміщенні пов'язана зі щільністю водневих зв'язків.

Ключові слова: аліфатичні спирти; фторзаміщені спирти; вода; перекис водню; теплоємність; принцип відповідних станів

DIELECTRIC RELAXATION AND MOLECULAR INTERACTIONS IN ACETIC ACID

©S.T. Azizov^{a,b}, ©O.A. Aliyev^{a,b*}, ©Kh.Kh. Hashimov^b

^aMinistry of Science and Education Republic of Azerbaijan, Institute of Physics, H.Javid ave131., AZ-1143 Baku, Azerbaijan

^bAzerbaijan State Oil and Industry University, Azadligave. 34, Baku AZ1010, Azerbaijan

*Corresponding Author E-mail: o.a.amea@gmail.com

Received April 2, 2025; revised June 21, 2025; accepted June 30, 2025

This article presents the results of measurements of the dielectric coefficients of acetic acid and its solutions. Measurements were carried out at wavelength $\lambda = 40.0; 30.0; 20.0; 10.0; 6.4; 4.4; 2.1; 1.2$; and in the temperature range $20 \div 50^\circ\text{C}$. Models of molecular clustering in liquid acetic acid were studied based on analysis of the dielectric absorption spectrum. The results of a study of the radio frequency absorption spectrum of acetic acid indicate the presence of two polymorphic forms of this compound. The characteristic temperature dependences of the dielectric constant ϵ' of acetic acid have been determined, from which two isothermal rotational transitions are clearly visible. The first - at the melting point - is accompanied by a sharp decrease in the number of dielectrically active units. The second, at a temperature below the melting point, leads to dielectric constant ϵ' values close to the high frequency (HF) limit of the total orientation contribution for microwave absorption in liquid acid. At temperatures above the first and below the second transitions, the values of the dielectric constant ϵ' do not depend on the frequency of the electromagnetic wave; on the contrary, pronounced dispersion is observed in the interval between two transitions.

Keywords: Dielectric spectroscopy; Dielectric relaxation; Complex dielectric constant; Dielectric properties; Acetic acid

PACS: 61.20. – p; 77.22. – d; 77.22.Gm

1. INTRODUCTION

The main goal of dielectric research is to study the patterns of manifestation of the features of molecular interactions and movements in the condensed state of matter. Effective control of chemical and technological processes, revelation of the nature of physical and chemical processes in biological media, synthesis of new polymeric materials that meet specific requirements, creation of high-speed methods of analysis and control - none of these pressing problems can be successfully solved without a deep understanding of the mechanism of molecular movements and interactions.

The extreme diversity of the molecular structures of polar liquids and their solutions that must be taken into account, as well as the difficulties associated with theoretical inter predation, make it extremely necessary to systematically accumulate experimental data on molecular motion and interactions in connection with the microscopic properties of matter. In this aspect, dielectric information acquires special value due to the exceptionally high resolution of the method on a time scale, which makes it possible to observe the movements of atomic groups, individual molecules, and large supra molecular formations - clusters. This feature distinguishes the dielectric method from other widely used spectroscopy methods. However, its implementation is possible only when setting up an experiment within a wide range of frequency variations, which is associated with overcoming great methodological and technical difficulties.

Dielectric studies were carried out in parallel in two directions:

a) mastering the existing methodology, as well as the development and implementation of a new experimental methodology;

b) direct dielectric studies of substances with various types of interactions and molecular structure in liquid and solid states, under conditions of significant variation in external parameters.

The dynamic dielectric properties of acetic acid [1 – 3], in agreement with X-ray data [4,5], indicate the existence of highly polar clusters based on intermolecular hydrogen bonds, as well as kinetic units with a smaller effective dipole moment. In this work, changes in the spectrum of the dispersion caused by the melting of the acid were traced. Analysis of changes in the dispersion spectrum [6,7] shows that, to a first approximation, the spectrum can be described by a superposition of two regions. The HF region has a relaxation nature and is characterized by a symmetrical distribution of relaxation times, increasing with decreasing temperature. The small value of the absorption amplitude and the relatively low (for the solid phase) reorientation barrier (~ 4 kCal/mol) give grounds to assert that the rotational movement of individual molecules creates the high-frequency region.

Low frequency (LF) - the region only partially falls within the overlapped frequency range. A notable feature of this area is the strong dependence of dielectric coefficients on the thermal conditions of sample preparation, which requires special precautions to eliminate or minimize the contribution due to the surface effect. Judging by the long relaxation times and large amplitude, comparable to that in the liquid phase, the main contribution to the LF region is made by the movements of molecules forming hydrogen-bonded multiverse, without the disintegration of the latter.

The purpose of the work was to study the radio frequency absorption spectrum of acetic acid. Determination of the temperature dependences of the dielectric constant ε' of acetic acid.

2. MATERIALS AND METHODS

Acetic acid (United States, Keysight Technologies) was chosen as the object of research. Dielectric constant ε' and dielectric losses ε'' of liquid acetic acid were measured at wavelengths $\lambda = 40.0; 30.0; 20.0; 10.0; 6.40; 4.40; 2.10; 1.20; 0.75$ cm in the temperature range from 20 to 50°C according to the method described in [8 - 11], taking into account amendments [12,13]. Equilibrium dielectric constants ε_0 were measured on a Q - meter VM 560, at a frequency of 1.6 MHz and the same temperatures. The errors are about 2% for the dielectric constant ε' , 3 – 5% for the dielectric loss ε'' and 0.5% for the equilibrium dielectric constant ε_0 . Further details about the methodology and constants of the studied sample are given in [14, 15].

To measure the dielectric constant ε' and dielectric losses ε'' of liquids and solutions in the range of centimeter and millimeter wavelengths, waveguide methods are widely used, characterized by a relatively high measurement accuracy. The expression for the complex propagation constant γ of an electromagnetic wave in a waveguide fill fused by a polar liquid, is written in the form [11, 15 – 17]:

$$\hat{\gamma} = i \frac{2\pi}{\lambda} \sqrt{\varepsilon^* - \left(\frac{\lambda}{\lambda_{kp}}\right)^2} = i \frac{2\pi}{\lambda_g} \left(1 - tg^2 \frac{\Delta}{2}\right). \quad (1)$$

Here $\Delta = \arctg \frac{\varepsilon''}{\varepsilon' - \left(\frac{\lambda}{\lambda_{kp}}\right)^2}$; λ – wavelength in vacuum; λ_{cw} – critical wavelength in a waveguide, determined by the dimensions of the waveguide and the type of waves propagating in the waveguide [18], λ_g – wavelength in the waveguide with the liquid under study, ε^* – complex dielectric constant of a polar liquid. From identity (1) it follows that

$$\varepsilon' = \left(\frac{\lambda}{\lambda_{kp}}\right)^2 + \left(\frac{\lambda}{\lambda_g}\right)^2 \cdot \left(1 - tg^2 \frac{\Delta}{2}\right); \quad \varepsilon'' = 2\left(\frac{\lambda}{\lambda_{kp}}\right)^2 tg \frac{\Delta}{2}. \quad (2)$$

To determine the quantities λ_g and $tg \frac{\Delta}{2}$ included in expression (2), the waveguide method of variable thicknesses is often used [19 – 21], which is acceptable only under the condition that $tg \frac{\Delta}{2} \neq 0$. According to this method, a waveguide cell with the liquid under study, the thickness of which in the cell is controlled by the position of the short-circuiting piston at the rear of the cell, is connected to the end of the waveguide path. The dependence of the standing wave coefficient in the waveguide path η on the thickness of the liquid in the cell l is removed. The minimum values η of this dependence are realized at liquid thicknesses in the cell approximately equal to $l = \frac{\lambda_g}{4} (2k - 1)$, where $k = 1, 2, 3 \dots$ while the ratio of arbitrary maxima η_m and η_n of the same dependence η on l is related to the value of $tg \frac{\Delta}{2}$ by the relation, which to a first approximation has the form:

$$\frac{\eta_m}{\eta_n} = \frac{th(n\pi tg \frac{\Delta}{2})}{th(m\pi tg \frac{\Delta}{2})} \cdot (1 - c_{mn}), \quad (3)$$

$$\text{where } c_{mn} = 4 \sin^2 \frac{\Delta}{4} \left[\frac{1}{1 - \left(\frac{\lambda_g}{\lambda_n}\right)^2 \cdot \cos^2 \frac{\Delta}{2} \cdot th^2(n\pi tg \frac{\Delta}{2})} - \frac{1}{1 - \left(\frac{\lambda_g}{\lambda_m}\right)^2 \cdot \cos^2 \frac{\Delta}{2} \cdot th^2(m\pi tg \frac{\Delta}{2})} \right],$$

here λ_g – wavelength in an empty waveguide [1].

The convenience of calculating $tg \frac{\Delta}{2}$ using expression (3), the functions $\frac{th(n\pi tg \frac{\Delta}{2})}{th(m\pi tg \frac{\Delta}{2})}$ are tabulated. It is usually assumed that c_{mn} values are quite small in magnitude. However, as calculations show, this assumption is valid only for values of the indices $m > 2$ and $n > 2$. For other values of the indices m and n , the value of c_m should be taken into account. When accurately determining the value of λ_g , a systematic error is allowed, which, as a rule, is not always taken into account. In some cases, it can exceed the permissible limits and significantly affect the accuracy of measuring the values of ε' and ε'' of the liquids under study. To take into account the systematic error in determining the value of λ_g , we use the following considerations.

The expression for the standing wave coefficient in a waveguide has the following form [11]:

$$\eta = \frac{1+|\rho|}{1-|\rho|}. \quad (4)$$

Where $|\rho| = \left| \frac{th \gamma l - \left(\frac{\lambda_n}{\lambda_g}\right) \cdot (1 - i tg \frac{\Delta}{2})}{th \gamma l + \left(\frac{\lambda_n}{\lambda_g}\right) \cdot (1 - i tg \frac{\Delta}{2})} \right|$ – modulus of the reflection coefficient of an electromagnetic wave in a waveguide.

The position of the extreme values of the dependence of η on l is determined from the condition.

$$\frac{d\eta}{dl} = \frac{2}{(1-|\rho|)^2} \cdot \frac{d|\rho|}{dl} = 0. \quad (5)$$

We assume that the minimum values of ρ , and therefore η , are realized at liquid thicknesses in the cell

$$l = \frac{\lambda_g}{4} \cdot (2q - 1) + \delta, \quad (6)$$

where δ is a value many times smaller than the thickness of the liquid in cell l .

We substitute expression (6) into (4) and expand the resulting expression for $th\gamma l$ into a series in terms of the value of δ . Let us limit ourselves to considering the first three terms of this series. Let us differentiate the resulting equation (4) by the value of δ and use condition (5). Then, discarding terms containing δ^2 as a factor, we obtain in a first approximation

$$\delta_{min} = \frac{\lambda_g}{2\pi} \cdot \frac{tg\frac{\Delta}{2}}{1+tg^2\frac{\Delta}{2}} \cdot \frac{1}{(\frac{\lambda_B}{\lambda_g})^2 \cdot (1+tg^2\frac{\Delta}{2})-1} \cdot \frac{1}{th[\frac{\pi}{2}(2p-1)tg\frac{\Delta}{2}]}. \quad (7)$$

Taking into account the correction δ , the first minimum of the dependence of η on l will occur at the thickness of the liquid in the cell:

$$l_1 = \frac{\lambda_g}{4} (1 + \delta_l), \quad (8)$$

$$\text{where } \delta_l = \frac{2}{\pi} \cdot \frac{tg\frac{\Delta}{2}}{1+tg^2\frac{\Delta}{2}} \cdot \frac{1}{(\frac{\lambda_B}{\lambda_g})^2 \cdot (1+tg^2\frac{\Delta}{2})-1} \cdot \frac{1}{th[\frac{\pi}{2}tg\frac{\Delta}{2}]}$$

In the general case, the distance between the nearby p and q minima of the dependence of η on l is determined by the relation:

$$l_q - l_p = \frac{\lambda_g}{2} \cdot (1 + \delta_{pq}), \quad (9)$$

$$\text{where } \delta_{pq} = \frac{1}{\pi} \cdot \frac{tg\frac{\Delta}{2}}{1+tg^2\frac{\Delta}{2}} \cdot \frac{1}{(\frac{\lambda_B}{\lambda_g})^2 \cdot (1+tg^2\frac{\Delta}{2})-1} \cdot \left\{ \frac{1}{th[\frac{\pi}{2}(2q-1)tg\frac{\Delta}{2}]} - \frac{1}{th[\frac{\pi}{2}(2p-1)tg\frac{\Delta}{2}]} \right\}.$$

The quantities δ_l and δ_{pq} included in formulas (8) and (9) depend on the values of the measured quantities λ and $tg\frac{\Delta}{2}$. For ease of calculation, the values of δ_l , δ_{12} and δ_{23} were calculated. According to the calculation data, the correction δ_l always has a positive sign, while δ_{pq} has negative signs. The values of δ_l and δ_{pq} increase sharply with increasing λ_g of the measured liquid. However, as the numbers p and q increase, the correction values decrease noticeably; they turn out to be significant only when the wavelength λ_g in the waveguide with the liquid under study is measured from the positions of the first three minima of the dependence of η on l .

It should be noted that for most polar liquids with values of $tg\frac{\Delta}{2} > 0,25$ in the ultrahigh frequency range, the dependence of η on l has, as a rule, 2–3 well-resolved minima of η .

3. RESULTS AND DISCUSSION

Table 1 gives the values of the dielectric constant of acetic acid ϵ' and dielectric losses ϵ'' . Explicitly, the spectrum contains only one absorption region of the relaxation type (Fig. 1, 2).

Table 1. Dielectric coefficients of acetic acid

T, °C	20		30		40		50	
λ cm	ϵ'	ϵ''	ϵ'	ϵ''	ϵ'	ϵ''	ϵ'	ϵ''
40.0	5.75	0.96	5.91	0.89	6.12	0.80	6.32	0.73
30.0	5.48	1.15	5.70	1.08	5.93	0.99	6.17	0.91
20.0	5.05	1.23	5.30	1.21	5.56	1.19	5.83	1.14
10.0	4.40	1.11	4.60	1.17	4.81	1.22	5.06	1.28
6.40	4.11	0.97	4.25	1.06	4.44	1.14	4.63	1.23
4.40	3.85	0.89	4.00	0.96	4.14	1.06	4.30	1.16
2.12	3.52	0.76	3.60	0.82	3.70	0.88	3.78	0.97
1.20	3.28	0.62	3.34	0.70	3.41	0.77	3.50	0.85
0.75	3.08	0.52	3.12	0.58	3.19	0.67	3.26	0.75

The relaxation times corresponding to the peak of the $\epsilon''(\lambda)$ curves change with temperature according to the relation $\tau = \tau_0 \exp(U/RT)$, where $\tau_0 = 11.8 \cdot 10^{-14}$ cm, $U = 4.0$ kcal/mol. Found in this way relaxation parameters should be considered effective, which is proven by the clear resolution of the spectrum when using the linear representation method (Fig. 3,4).

To a first approximation, the frequency variation of the values ϵ' , ϵ'' can be described by a superposition of two independent relaxation processes (Fig. 5):

$$\varepsilon' - i\varepsilon'' = \varepsilon_{\infty 2} + (\varepsilon_{01} - \varepsilon_{\infty 2}) \{C_1(1 + i\omega\tau_1)^{-1} + C_2[(1 + i\omega\tau_2)^{1-\alpha_2}]^{-1}\}. \quad (10)$$

Where: $C_j = \frac{\varepsilon_{0j} - \varepsilon_{\infty j}}{\varepsilon_{01} - \varepsilon_{\infty 2}}$; $C_1 + C_2 = 1$; $\varepsilon_{\infty 1} = \varepsilon_{02}$; $\tau_1 > \tau_2$, α_2 – parameter of the symmetric distribution of dielectric relaxation time values around the most probable value τ .

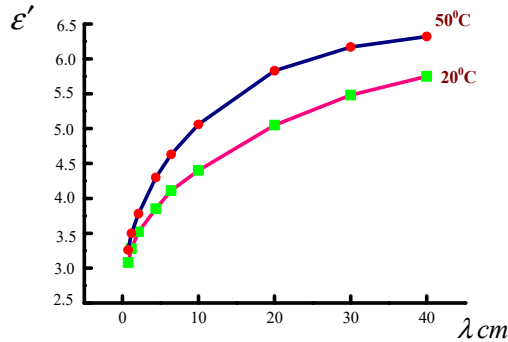


Figure 1. Dielectric constants ε' of acetic acid depending on the wavelength λ at 20 and 50°C

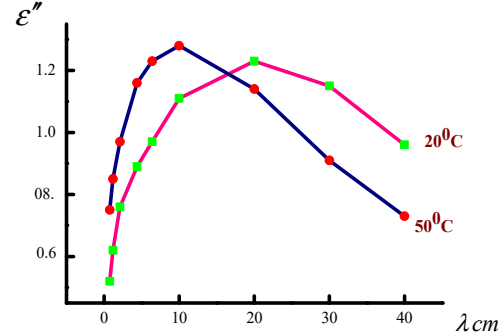


Figure 2. Dielectric losses ε'' of acetic acid depending on wavelength λ at 20 and 50°C

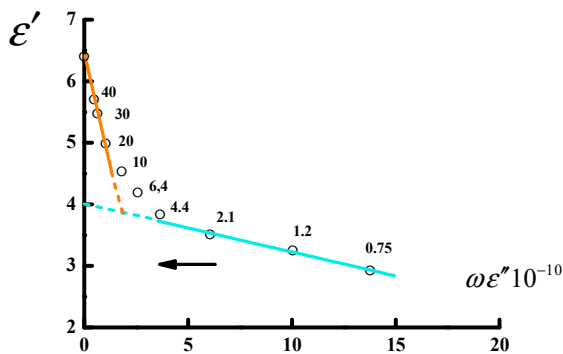


Figure 3. Line diagrams of acetic acid at 20°C. The numbers at the dots are wavelengths (cm)

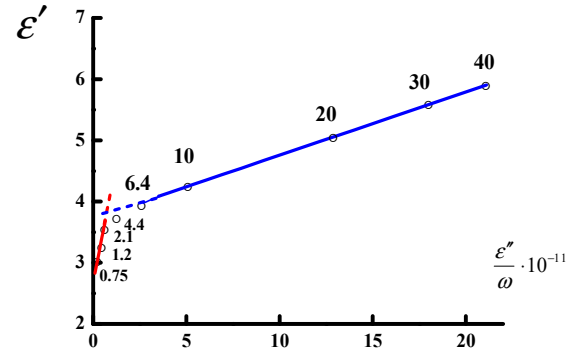


Figure 4. Line diagrams of acetic acid at 20°C. The numbers at the dots are wavelengths (cm)

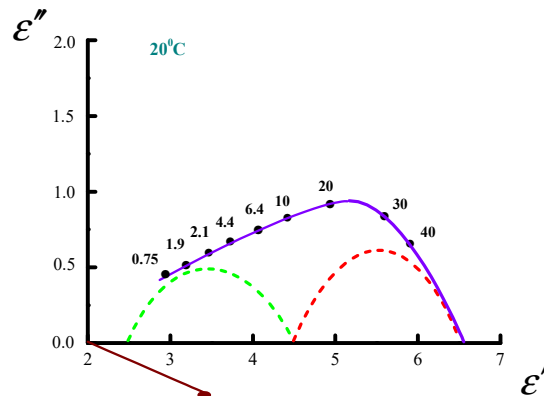


Figure 5. Arc diagrams of acetic acid when the spectrum is divided into two regions (20°C). The numbers at the dots are wavelengths (cm)

Table 2 gives the estimated parameters of equation (1) along with the measured values of ε_{01} . A comparison of the spectrum calculated from these values with the observed one shows [22] that the permissible limits of variation of the estimated parameters, in which the scatter does not exceed the experimental errors, are about 10% for τ and 0.05 for C .

Table 2. Relaxation parameters of the spectrum of acetic acid according to (1)

T, °C	ε_{01}	$\varepsilon_{\infty 2}$	$\tau_1 \cdot 10^{12} \text{sec}$	$\tau_2 \cdot 10^{12} \text{sec}$	α_2	C_1
20	6.30	2.58	122	11.5	0.29	0.50
30	6.38	2.57	100	10.0	0.28	0.49
40	6.46	2.56	81	8.8	0.27	0.46
50	6.54	2.56	66	7.8	0.26	0.48

Significant broadening of the high-frequency (HF) region makes its further division possible. Due to the large distribution parameter α of the dielectric relaxation time, attempts to describe this region using elementary Debye processes require the introduction of four relaxation time values. By analogy with monohydric alcohols [23], it seems advisable to limit ourselves to separating from the HF region only two contributions, each of which retains a certain distribution of relaxation times of a symmetrical type (Fig. 6). Table 3 gives the spectrum parameters according to the equation

$$\varepsilon' - i\varepsilon'' = \varepsilon_{\infty 3} + (\varepsilon_{01} - \varepsilon_{\infty 3}) \sum C_j [1 + (i\omega\tau_j)^{1-\alpha}]^{-1} j = 1, 2, 3. \quad (11)$$

Where $-\varepsilon_{\infty 1} = \varepsilon_{02}$; $\varepsilon_{\infty 2} = \varepsilon_{03}$; $\tau_1 > \tau_2 > \tau_3$, $\alpha_1 = 0$. The values of relaxation activation energy found from the lg graph are also given there $\tau - T^{-1}$

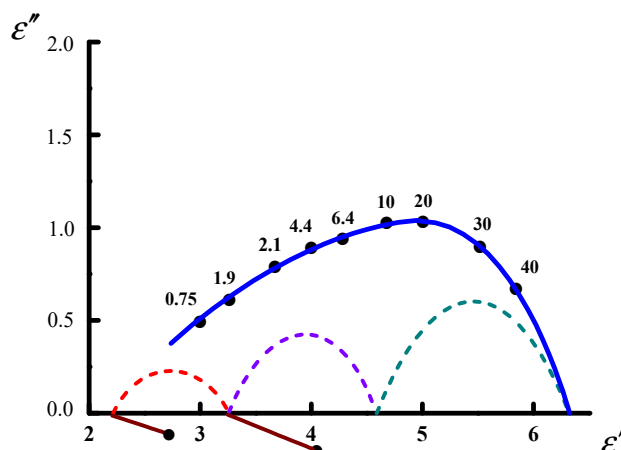


Figure 6. Arc diagrams of acetic acid when the spectrum is divided into three regions (20°C). The numbers at the dots are wavelengths (cm).

Table 3. Relaxation parameters of the spectrum of acetic acid according to equation (2)

T, °C	ε_{01}	ε_{02}	ε_{03}	$\varepsilon_{\infty 3}$	$\tau_1 \cdot 10^{12} \text{sec}$	$\tau_2 \cdot 10^{12} \text{sec}$	$\tau_3 \cdot 10^{12} \text{sec}$	α_2	α_3
20	6.30	4.42	3.26	2.58	122	25.0	2.8	0.11	0.13
30	6.38	4.48	3.28	2.57	100	21.5	2.5	0.11	0.12
40	6.46	4.54	3.29	2.56	81	19.0	2.2	0.10	0.11
50	6.54	4.60	3.30	2.56	66	17.0	2.0	0.10	0.10

The presence of an absorption spectrum contradicts the widespread opinion about the exclusively nonpolar dimeric type of clustering of liquid acetic acid. The presence of three absorption regions with relaxation times differing by a factor of 40 cannot be explained by the hypothetical interaction of monomers and cyclic dimers. At the same time, the value of the correlation parameter $g = 0.4$ (20°C) indicates a limited proportion of polar clusters. Taking this into account, as well as summarizing the results of spectrum analysis, identification should be carried out in terms of the equilibrium between non-polar clusters, polar multiverse and monomers.

The characteristics of the HF contribution give reason to believe that it is created by the reorientation of individual molecules as a whole, supplemented by internal rotation. The relative content of kinetic units involved in HF absorption (9%) found from the amplitude $\varepsilon_{03} - \varepsilon_{\infty 3}$ (at $g_3 = 1$) coincides with the concentration of acid monomers (12%) at 20°C, estimated from ultrasonic data. The attribution of the HF contribution to monomers is also confirmed by the closeness of the values of τ_3 , α_3 , and U_3 to those for ethyl acetate, where, with a comparable molecular structure, there are no directional interactions.

There is no doubt that the LF contribution is classified as multiverse. As for the intermediate contribution, its identification depends on the specific cluster model. For example, if we proceed from the model of linear highly polar clusters, then the most likely explanation will be the ratio of the intermediate contribution to the terminal molecules. Another model of clusters, proposed for alcohols [24-26], postulates an equilibrium between monomers, weakly polar dimers and highly polar cyclic (non-planar) multiverse (presumably tetramers). In this case, the HF and LF contributions, as before, are created by monomers and multiverse, respectively, and intermediate absorption is associated with polar dimers.

The main difference between linear and cyclic clustering models is that in the first case, the appearance of an intermediate region directly follows from the presence of chain multiverse. On the contrary, with cyclic clustering, the presence of kinetic units responsible for a given absorption region is not due to the existence of other types of relaxers.

4. CONCLUSIONS

1. The prerequisites for choosing between the two models are determined by comparing the expected and observed changes in the spectrum caused by the introduction of foreign molecules of acetic acid.

2. The linear clustering model predetermines the correlation between the amplitudes of low-frequency and intermediate contributions upon dilution of acetic acid.

3. It is obvious that the idea of an exclusively nonpolar type of clustering of liquid acetic acid is erroneous, as well as the possibility of two types of clusters, including open or ring polar multiverse.

4. From the dielectric data it is clear that there are two stable modifications in solid acetic acid, differing in orientation freedom.

ORCID

✉S.T. Azizov, <https://orcid.org/0000-0001-6252-1512>; ✉O.A. Aliyev, <https://orcid.org/0009-0000-5699-3054>

✉Kh.Kh. Hashimov, <https://orcid.org/0009-0002-9674-5578>

REFERENCES

- [1] T. Ganesh, D.J.S.A. Karunakaran, P. Udhayageetha, P. Jeevanandham and S. Kumar, "Microwave Dielectric Relaxation of Alcohols in non-polar solutions," *IOSR Journal of Applied Physics*, (IOSR-JAP) **6**(2), Ver. II 64-68 (2014)
- [2] C.D. Abeyrathne, M.N. Halgamuge, P.M. Farrell and E. Skafidas, "Dielectric Properties of Liquid Phase Molecular Clusters using External Field Method: Molecular Dynamics Study," *Physical Chemistry Chemical Physics*, **16**, 13943–13947 (2014). <https://doi.org/10.1039/C4CP00716F>
- [3] Y. Poplavko, "1 - The basics of dielectric spectroscopy," *Dielectric Spectroscopy of Electronic Materials*, Applied Physics of Dielectrics Woodhead Publishing Series in Electronic and Optical Materials, 1-40 (2021). <https://doi.org/10.1016/B978-0-12-823518-8.00003-7>
- [4] D.A. Skoog, D.M. West, F.J. Holler and S.R. Crouch, *Fundamentals of Analytical Chemistry*, 10th edition, (Cengage Learning, 2021).
- [5] C.J.F. Böttcher and P. Bordewijk, *Theory of Electric Polarization*, vol. 2, 2nd. edn. (Elsevier, Amsterdam, 1978). <https://doi.org/10.1002/bbpc.19800841128>
- [6] S.T. Azizov, "Investigation of the temperature dependence of the dielectric relaxation of chlorobenzene, bromobenzene and iodobenzene," *Journal «Bulletin of the Karaganda University», series «Physics»*, **29**(2), 36-42, (2024). <https://doi.org/10.31489/2024PH2/36-42>
- [7] S.R. Kasimova, "Improvement of the reflectivity of flat coatings," *Journal of Engineering Physics and Thermophysics*, **91**(6), 1592-1594 (2018). <https://doi.org/10.1007/s10891-018-1897-6>
- [8] S.T. Azizov, "Dielectric relaxation in solutions chlorobenzene - benzene and chlorobenzene – hexane," *Modern Physics Letters B*, **38**(20), 2450167 (2024). <https://doi.org/10.1142/S0217984924501677>
- [9] M.D. Lechner, editor, *Static Dielectric Constants of Pure Liquids and Binary Liquid Mixtures*, Landolt-Börnstein - Group IV Physical Chemistry, **27**, 668 (2015). <https://doi.org/10.1007/978-3-662-48168-4>
- [10] S.T. Azizov, O.A. Aliev and R.G. Abaszade, "Low – frequency dielectric properties of acetone," *International Journal of Latest Research in Science and Technology*, **5**(4), 58-62 (2016). https://www.mnkjournals.com/journal/ijlrst/pdf/Volume_5_4_2016/10678.pdf
- [11] E.Y. Salaev, E.R. Gasimov, Ch.O. Qajar and S.T. Azizov, "Resonans Reflectionless Absorption of Electromagnetic Waves in Solutions," *Turkish journal of Physics*, **XXII**(5), 389–393 (1998). <https://journals.tubitak.gov.tr/physics/vol22/iss5/4/>
- [12] P. Debye, *Dielectric properties of pure liquids*, (Berlin-Dahlem, Germany: Kaiser Wilhelm Institut für Physik, 171-182 (1986).
- [13] D. Kumar, S.K. Sit, S.N. Singh and S. Sahoo, "Investigation of dielectric relaxation in dipolar liquids from conductivity measurement," *Bulletin of Materials Science*, **45**, 37–49 (2022). <https://doi.org/10.1007/s12034-021-02597-x>
- [14] S. Sahoo and S.K. Sit, "Double relaxation phenomena of nicotinamide, benzamide and 1-propanol mixture dissolved in benzene measured at 9.385 GHz electric field," *Can. J. Phys.* **94**, 1–12 (2016). <https://doi.org/10.1139/cjp-2015-0477>
- [15] S.T. Azizov, "Temperature dependence of dielectric relaxation of absorption spectra in the chlorobenzene – iodobenzene system," *East Eur. J. Phys.* (1), 453–459 (2024). <https://doi.org/10.26565/2312-4334-2024-1-50>
- [16] F. Kremer and A. Schonhals, *Broadband Dielectric Spectroscopy*, (Springer, 2003). <https://link.springer.com/book/10.1007/978-3-642-56120-7>
- [17] Ch. Alexander and M. Sadiku, *Fundamentals of Electric Circuits*, (McGraw-Hill, New York, 2009).
- [18] D. Kumar, S.K. Sit, S.N. Singh and S. Sahoo, "Dielectric Relaxation Behavior of Amide and Phenol Mixtures in C₆H₆ Under Microwave Field," *Journal of Solution Chemistry*, **50**, 690–722 (2021). <https://doi.org/10.1007/s10953-021-01085-4>
- [19] T. Bachhar, S.K. Sit, S.H. Laskar and S. Sahoo, "Investigation of dielectric relaxation in tributyl phosphate from susceptibility and conductivity measurement under microwave field," *Bulletin of Materials Science*, **44**, (2021). <https://doi.org/10.1007/s12034-021-02366-w>
- [20] S. Sahoo, "Investigation of dielectric relaxation in dipolar liquids," *Indian J. Phys.* **94**, 17–29 (2020). <https://doi.org/10.1007/s12648-019-01437-3>
- [21] D. Kumar, S. Nand and S. Sahoo, *J. Solution Chem.* **50**, 690 (2021). <https://doi.org/10.1007/s10953-021-01085-4>
- [22] S.R. Kasimova, "Measurements of the Dielectric Properties of Strongly Absorbing Substances at Microwave Frequencies," *Measurement Techniques*, **58**(12), 1372-1375 (2016). <https://doi.org/10.1007/s11018-016-0901-9>
- [23] M. Malathi, R. Sabesan and S. Krishnan, "Dielectric studies of H-bonded complexes of formamide and acetamide with substituted phenols," *J. Mole. Liq.* **109**, 11–18 (2004). <https://doi.org/10.1016/j.molliq.2003.08.020>
- [24] S. Sahoo and S.K. Sit, "Dielectric relaxation of amides and tetrahydrofuran polar mixture in C₆H₆ from conductivity measurement under 990 GHz electric field," *Pramana J. Phys.* **88**, 1–12 (2017). <https://doi.org/10.1007/s12043-016-1314-7>
- [25] R.Z. Ibaeva, G.B. Ibragimov, A.S. Alekperov and R.E. Huseynov, "Obtained and studied structural aspects of the Ge_{0.9}Er_{0.1}S compound with Ge → Er substitutions," *East European Journal of Physics*, (4), 360–363 (2024). <https://doi.org/10.26565/2312-4334-2024-4-41>
- [26] R.Z. Ibaeva, V.N. Jafarova, V.I. Eminova, I.-C. Scurtu, S. Lupu, "First-principles study of electronic and magnetic properties of Ag- and Au-doped single-walled (6,0) SiC nanotubes: DFT study," *Journal of Nanoparticle Research*, **26**, 203 (2024). <https://doi.org/10.1007/s11051-024-06109-w>

ДІЕЛЕКТРИЧНА РЕЛАКСАЦІЯ ТА МОЛЕКУЛЯРНІ ВЗАЄМОДІЇ В ОЦТОВІЙ КИСЛОТІ

С.Т. Азізов^{a,b}, О.А. Алієв^{a,b}, Х.Х. Гашімов^b^aМіністерство науки та освіти Азербайджанської Республіки, Інститут фізики,
пр. Х. Джавіда 131, AZ-1143 Баку, Азербайджан^bАзербайджанський державний університет нафти та промисловості, Азадлігаве, 34, Баку AZ1010, Азербайджан

У цій статті представлені результати вимірювань діелектричних коефіцієнтів оцтової кислоти та її розчинів. Вимірювання проводилися на довжинах хвиль $\lambda = 40,0; 30,0; 20,0; 10,0; 6,4; 4,4; 2,1; 1,2$; та в діапазоні температур $20 \div 500^\circ\text{C}$. Моделі молекулярної кластеризації в рідкій оцтовій кислоті досліджувалися на основі аналізу спектру діелектричного поглинання. Результати дослідження спектру радіочастотного поглинання оцтової кислоти вказують на наявність двох поліморфних форм цієї сполуки. Визначено характерні температурні залежності діелектричної проникності ϵ' оцтової кислоти, з яких чітко видно два ізотермічні обертальні переходи. Перший – у температурі плавлення – супроводжується різким зменшенням кількості діелектрично активних одиниць. Другий, при температурі нижче точки плавлення, призводить до значень діелектричної проникності ϵ' , близьких до височастотної (HF) межі загального орієнтаційного внеску для мікрохвильового поглинання в рідкій кислоті. При температурах вище першого та нижче другого переходів значення діелектричної проникності ϵ' не залежать від частоти електромагнітної хвилі; навпаки, спостерігається виражена дисперсія в інтервалі між двома переходами.

Ключові слова: діелектрична спектроскопія; діелектрична релаксація; комплексна діелектрична проникність; діелектричні властивості; оцтова кислота

POLYPHENOL INTERACTIONS WITH AMYLOID FIBRILS: A MOLECULAR DOCKING STUDY

 **Uliana Malovytsia^{a*}**,  **Valeriya Trusova^a**,  **Mette Thomsen^b**,  **Kateryna Vus^a**,
 **Olga Zhytniakivska^a**,  **Galyna Gorbenko^a**

^a*Department of Medical Physics and Biomedical Nanotechnologies, V.N. Karazin Kharkiv National University
4 Svobody Sq., Kharkiv, 61022, Ukraine*

^b*AAU Energy, Aalborg University, Niels Bohrs Vej 8, 6700 Esbjerg, Denmark*

**Corresponding Author E-mail: uliana.tarabara@karazin.ua*

Received June 2, 2025, revised July 21, 2025; accepted August 15, 2025

Polyphenols, a versatile group of naturally occurring compounds with many favorable biological properties currently attract increasing research interest in the context of their ability to inhibit the formation and to destabilize special protein aggregates, amyloid fibrils, associated with a number of human diseases. In the present study the molecular docking technique was used to gain insights into molecular details of the interactions between polyphenolic compounds such as quercetin, curcumin, resveratrol, sesamin, salicylic and gallic acids with the mature amyloid fibrils from Abeta peptide, islet amyloid polypeptide, insulin, apolipoprotein A-I and apolipoprotein A-II. All examined polyphenols displayed the highest binding affinities for amyloid fibrils from apolipoprotein A-II and insulin, while the lowest affinities were observed for the fibrillar apolipoprotein A-I. The hydrophobicity/hydrophilicity analysis of amino acid composition of the binding sites showed that hydrophobic and neutral residues play a predominant role in the polyphenol complexation with amyloid fibrils from apolipoprotein A-I, apolipoprotein A-II and insulin, the basic residues essentially contribute to polyphenol association with fibrillar Abeta and islet amyloid polypeptides, while the involvement of acidic residues was revealed only for the complexes sesamin + apolipoprotein A-I / Abeta fibrils and curcumin keto + insulin fibrils. The results obtained may prove useful in the development of novel polyphenol-based anti-amyloid strategies.

Keywords: *Amyloid fibrils; Polyphenols; Binding sites; Binding affinity; Molecular docking*

PACS: 87.14.C++c, 87.16.Dg

Amyloid fibrils, specific protein aggregates with a core β -sheet structure, in the past decades continue to attract enormous attention in two main aspects associated with amyloid involvement in pathogenesis of more than forty human diseases [1] and great nanotechnological potential of amyloid assemblies [2]. Considerable research efforts are currently focused on the development of anti-amyloid strategies and searching for small molecule inhibitors of amyloid formation [3]. One class of such inhibitors is represented by polyphenols, naturally occurring compounds with a wide range of biological activities [4, 5]. Growing evidence indicates that polyphenols can interfere with the process of amyloid formation through: i) preventing the structural transitions of protein molecules into the aggregation-prone states; ii) hindering the conversion of oligomeric intermediates into mature amyloid fibrils; and iii) disrupting and remodeling the preformed fibrillar assemblies [6-9]. To exemplify, epigallocatechin gallate displayed the abilities not only to inhibit the growth of fibrils from Abeta and α -synuclein, but also to induce their remodeling into nontoxic amorphous aggregates [10, 11]. Resveratrol has been reported to prevent large-scale Abeta fibrillization without affecting the oligomer formation [12, 13]. Polyphenols baicalein, epigallocatechin gallate, rutin and gallic acid have been found to produce disassembly of glycation-mediated mature amyloid fibrils from bovine serum albumin (BSA) [14]. The inhibition of amyloid formation from insulin, lysozyme and A β 1-40 peptide, and disassembly of the preformed fibrils were revealed for rottlerin. It was hypothesized that this polyphenol is capable of interrupting the fibril-stabilizing bonds of β -sheets [15]. Gallic acid, caffeic acid, rutin and quercetin suppressed the fibrillization of the islet amyloid polypeptide (IAPP), while rutin and quercetin disaggregated the preformed amyloid fibrils of IAPP [16]. It has been proposed that improvement of the water solubility and bioavailability of polyphenols through nanonization enhances their anti-amyloid activities, as was demonstrated for the nanosheet form of polyphenolic fraction from propolis which displayed more efficient inhibition of amyloid growth and clearance of the preformed fibrils of bovine insulin [17]. It has been also shown that polyphenol association with fibrillized proteins is governed by hydrogen bonding, π - π stacking and hydrophobic interactions, and may lead to self-assembly of amyloid fibrils into complex hierarchical structures [9]. All the above findings point to the necessity of a more thorough investigation of the mechanisms underlying the interactions between polyphenols and proteins, especially the amyloid protein aggregates. For this reason, the aim of the present study was to scrutinize the interactions between a series of chemically diverse polyphenols (PF) with mature amyloid fibrils from structurally different proteins using the molecular docking technique. The group of the examined polyphenolic compounds included quercetin (QR), curcumin (CR), gallic acid (GA), salicylic acid (SA), sesamin (SES) and resveratrol (RES), while the amyloid-forming proteins were represented by Abeta peptide (Abeta), islet amyloid polypeptide, insulin (Ins), apolipoprotein A-I (apoA-I) and apolipoprotein A-II (apoA-II).

METHODS

The structures of polyphenols were prepared in MarvinSketch software, v.18.10, ChemAxon with subsequent geometry optimization in Avogadro 1.1.0 software using the Universal Force Field21. The insulin fibril model was taken from the archive provided by M. Sawaya (<http://people.mbi.ucla.edu/sawaya/jmol/fibrilmodels/>). The model amyloid fibrils of apolipoprotein A-I were constructed using the CreateFibril tool based on the translational and rotational affine transformations providing several copies of a certain fragment of fibril core, whose subsequent stacking produces the elongated fibrillar aggregate. The input structures for CreateFibril were generated from the monomers in the β -strand conformation with PatchDock. The structures of the amyloid fibrils from Abeta, IAPP and ApoAII were taken from the Protein Data Bank using the following PDB IDs: 8OT4 (A β amyloid fibrils from Alzheimer's brain tissue), 6Y1A (IAPP) and 8OQ4 (ApoAII). The docking of polyphenols to amyloid fibrils was performed using the web-based server HDOCK [18]. The selected docking poses were visualized with the UCSF Chimera software (version 1.14).

RESULTS AND DISCUSSION

The molecular docking study of the interactions between the selected polyphenolic compounds and amyloid fibrils provided evidence for the presence of different types of polyphenol binding sites on the amyloid aggregates (Figs.1-3). The association of polyphenols with fibrillar Abeta (Fig. 1, A, B,) and ApoAII (Fig. 3) occurs mainly through the dry surface of the fibrils, while the PF binding sites on the fibrils of IAPP (Fig. 1, C, D) and ApoAI (Fig. 2, A) are located on the wet surface of amyloid assemblies. The insulin fibrils appear to contain the binding sites for PF on both the dry and wet surfaces (Fig. 2, B).

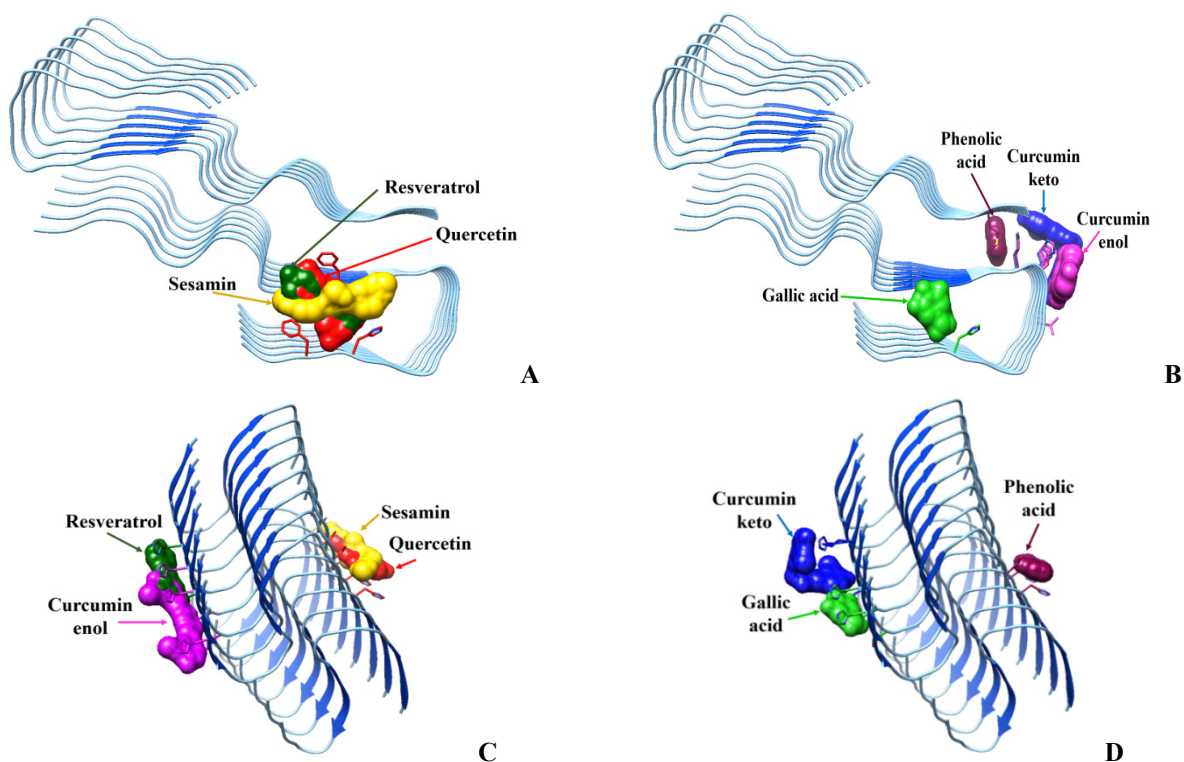


Figure 1. The best-score complexes of Abeta (A, B) and IAPP (C, D) fibrils with polyphenols.

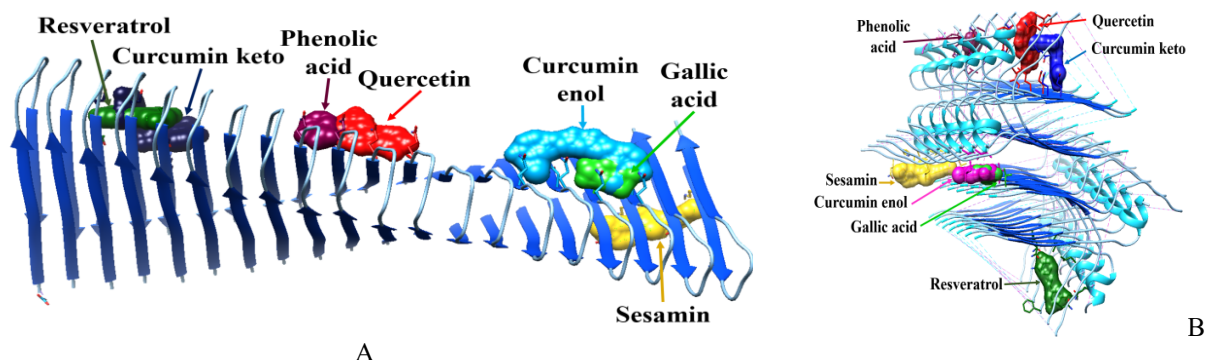


Figure 2. The best-score complexes of the fibrillar ApoAI (A) and insulin (B) with polyphenols.

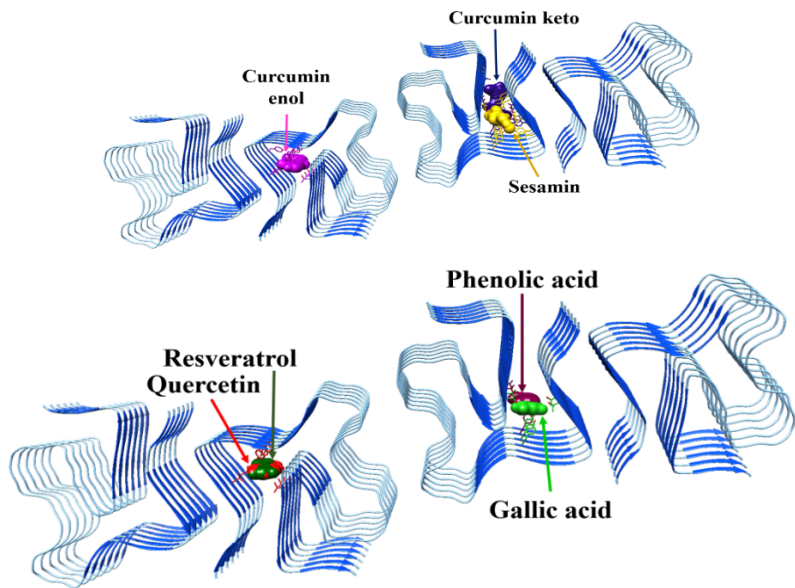


Figure 3. The best-score complexes of the fibrillar ApoAII with polyphenols.

As judged from the comparison of the best score values (Table 1), all polyphenols form the strongest complexes with the fibrils from ApoAII and insulin, with the binding affinities decreasing in the rows: **Quercetin:** ApoAII >Ins > IAPP > ApoAI ≥ Abeta; **Curcumin enol;** ApoAII >Ins ≥ IAPP > Abeta ≥ ApoAI; **Curcumin keto:** ApoAII >Ins > Abeta ≥ IAPP > ApoAI; **Phenolic acid:** ApoAII >Ins > IAPP ≥Abeta ≥ ApoAI; **Gallic acid:** ApoAII >Ins > IAPP≥ Abeta ≥ ApoAI; **Sesamin:** ApoAII >Ins > IAPP > Abeta ≥ ApoAI; **Resveratrol:** ApoAII >Ins > IAPP > Abeta ≥ ApoAI.

Table 1. The best score values for the complexes of polyphenols with amyloid fibrils

Polyphenol	Abeta	InsF	ApoAI	ApoAII	IAPP
Quercetin	-121.18	-163.80	-122.73	-211.93	-139.19
Curcumin enol	-135.49	-169.26	-118.84	-239.82	-163.48
Curcumin keto	-118.42	-140.44	-104.32	-161.14	-118.00
Salicylic (phenolic) acid	-71.07	-91.79	-70.36	-103.85	-73.63
Gallic acid	-80.34	-110.86	-78.72	-123.75	-83.94
Sesamin	-117.59	-153.37	-109.44	-220.44	-147.60
Resveratrol	-91.71	-115.26	-80.58	-164.03	-109.11

Presented in Tables 2-8 are the amino acid compositions of polyphenol binding sites on the examined amyloid fibrils. The hydrophobicity/hydrophilicity analysis performed using the Peptide 2.0 software (https://www.peptide2.com/N_peptide_hydrophobicity_hydrophilicity.php) allowed to identify the types of amino acid residues that predominantly determine the complexation of polyphenols with the fibrillized proteins. As seen in Table 2, the fibril binding sites for quercetin are composed mainly of hydrophobic and neutral residues, with their content being the highest for Abeta and ApoA-I fibrils, respectively. An exception is the fibrillar IAPP in which there are no hydrophobic residues at the quercetin binding sites. The association of quercetin with amyloid fibrils from Abeta, IAPP and Ins is mediated also by the basic residues, especially, histidine. Notably, the strongest complexes formed by quercetin with ApoA-II and Ins, are stabilized mainly by the interactions of this polyphenol with hydrophobic and neutral amino acid residues.

Table 2. The interface residues in the complexes between amyloid fibrils and quercetin

	Amyloid fibrils	Amino acid residues forming the fibril binding sites for quercetin
1	ApoA-I	GLN ₂₇₁ I, LEU ₂₇₂ J, ASN ₂₇₃ I, GLN ₂₉₈ K, LEU ₂₉₉ K, ASN ₃₀₀ K, GLN ₃₂₅ L, LEU ₃₂₆ L, ASN ₃₂₇ L, ASN ₃₅₄ M <i>Hydrophobic: 30%, Acidic: 0%, Basic: 0%, Neutral: 70%</i>
2	ApoA-II	LEU ₁₀ H, THR ₁₂ H, TYR ₁₄ H, TYR ₂₁ H, ALA ₅₆ H, GLY ₅₇ H, THR ₅₈ H, LEU ₁₀ N, THR ₁₂ N, TYR ₁₄ N, TYR ₂₁ N, ALA ₅₆ N, GLY ₅₇ N, THR ₅₈ N, LEU ₁₀ R, THR ₁₂ R, TYR ₁₄ R, TYR ₂₁ R, ALA ₅₆ R, GLY ₅₇ R, THR ₅₈ R, LEU ₁₀ V, TYR ₂₁ V, ALA ₅₆ V, THR ₅₈ V <i>Hydrophobic: 32%, Acidic: 0%, Basic: 0%, Neutral: 68%</i>

	Amyloid fibrils	Amino acid residues forming the fibril binding sites for quercetin
3	Abeta	PHE _{4K} , ARG _{5K} , HIS _{6K} , VAL _{18K} , PHE _{19K} , PHE _{20K} , ALA _{21K} , VAL _{24K} <i>Hydrophobic: 75%, Acidic: 0%, Basic: 25%, Neutral: 0%</i>
4	IAPP	HIS _{18D} , SER _{19D} , SER _{20D} , HIS _{18F} , SER _{19F} , SER _{20F} , HIS _{18H} , SER _{19H} , SER _{20H} , HIS _{18J} , SER _{19J} <i>Hydrophobic: 0%, Acidic: 0%, Basic: 36.36%, Neutral: 63.64%</i>
5	Ins	GLN _{115G} , PHE _{201G} , VAL _{202G} , ASN _{203G} , GLN _{204G} , HSD _{205G} , ILE ₂₁ , LEU ₁₃₁ , GLN ₁₅₁ , LEU ₁₁₃₁ , VAL ₂₀₂₁ , ASN ₂₀₃₁ , GLN ₂₀₄₁ , HSD ₂₀₅₁ , LEU ₂₀₆₁ , GLN _{5K} <i>Hydrophobic: 43.75%, Acidic: 0%, Basic: 12.5%, Neutral: 43.75%</i>

As judged from Table 3, all amyloid fibrils except Abeta possess the binding sites for salicylic acid containing the neutral amino acid residues in rather large amounts (from 44 % to 70 %). The hydrophobic amino acids do not participate in the SA association with IAPP, while the basic amino acids contribute to the complexation of SA with Abeta, IAPP and Ins fibrils.

Table 3. The interface residues in the complexes between amyloid fibrils and salicylic acid

	Amyloid fibrils	Amino acid residues forming the fibril binding sites for salicylic acid
1	ApoA-I	GLN _{217H} , GLN _{244I} , LEU _{245I} , ASN _{246I} , GLN _{271J} , LEU _{272J} , ASN _{273J} <i>Hydrophobic: 28.57%, Acidic: 0%, Basic: 0%, Neutral: 71.43%</i>
2	ApoA-II	LEU _{10F} , THR _{12F} , TYR _{14F} , TYR _{21F} , ALA _{56F} , GLY _{57F} , THR _{58F} , TYR _{21L} , ALA _{56L} , GLY _{57L} , THR _{58L} , THR _{58P} <i>Hydrophobic: 25%, Acidic: 0%, Basic: 0%, Neutral: 75%</i>
3	Abeta	GLN _{15A} , LYS _{16A} , LEU _{17A} , MET _{35B} , GLN _{15C} , LYS _{16C} , LEU _{17C} <i>Hydrophobic: 42.86%, Acidic: 0%, Basic: 28.57%, Neutral: 28.57%</i>
4	IAPP	SER _{19F} , HIS _{18H} , SER _{19H} , SER _{20H} , HIS _{18J} , SER _{19J} , SER _{20J} , HIS _{18L} <i>Hydrophobic: 0%, Acidic: 0%, Basic: 37.5%, Neutral: 62.5%</i>
5	Ins	VAL _{202A} , ASN _{203A} , GLN _{204A} , HSD _{205A} , ILE _{2C} , ASN _{203C} , GLN _{204C} , HSD _{205C} , LEU _{206C} , GLN _{5E} <i>Hydrophobic: 30%, Acidic: 0%, Basic: 20%, Neutral: 50%</i>

The types of amino acids in the amyloid binding sites for gallic acid are largely similar to those for salicylic acid, however, in contrast to SA, the basic residues do not participate in the GA interaction with fibrillar insulin (Table 4).

Table 4. The interface residues in the complexes between amyloid fibrils and gallic acid

	Amyloid fibrils	Amino acid residues forming the fibril binding sites for gallic acid
1	ApoA-I	GLN _{433P} , LEU _{434P} , ASN _{435P} , GLN _{460Q} , LEU _{461Q} , ASN _{462Q} , GLN _{487R} , LEU _{488R} , ASN _{489R} <i>Hydrophobic: 33.33%, Acidic: 0%, Basic: 0%, Neutral: 66.67%</i>
2	ApoA-II	LEU _{10L} , THR _{12L} , TYR _{14L} , TYR _{21L} , ALA _{56L} , LEU _{10P} , THR _{12P} , TYR _{14P} , TYR _{21P} , ALA _{56P} , GLY _{57P} , THR _{58P} , ALA _{56T} , GLY _{57T} , THR _{58T} <i>Hydrophobic: 33.33%, Acidic: 0%, Basic: 0%, Neutral: 66.67%</i>
3	Abeta	PHE _{4K} , ARG _{5K} , HIS _{6K} , VAL _{18K} , PHE _{19K} , PHE _{20K} <i>Hydrophobic: 66.67%, Acidic: 0%, Basic: 33.33%, Neutral: 0%</i>
4	IAPP	HIS _{18G} , SER _{19G} , SER _{20G} , HIS _{18I} , SER _{19I} , SER _{20I} , HIS _{18K} , SER _{19K} , SER _{20K} <i>Hydrophobic: 0%, Acidic: 0%, Basic: 33.33%, Neutral: 66.67%</i>
5	Ins	ILE _{102I} , CYS _{307I} , LEU _{217J} , VAL _{218J} , CYS _{219J} , LEU _{317J} , VAL _{318J} , CYS _{319J} , LEU _{306K} , CYS _{307K} , GLY _{308K} , LEU _{217L} , VAL _{218L} , CYS _{219L} <i>Hydrophobic: 57.14%, Acidic: 0%, Basic: 0%, Neutral: 42.86%</i>

Both hydrophobic and neutral amino acids account for the binding of resveratrol to amyloid fibrils from ApoA-I, ApoA-II and Ins, while the basic amino acids play a marked role in the complexation of this polyphenol with fibrillar Abeta, IAPP and Ins (Table 5).

Table 5. The interface residues in the complexes between amyloid fibrils and resveratrol

	Amyloid fibrils	Amino acid residues forming the fibril binding sites for resveratrol
1	ApoA-I	GLN _{55B} , ASN _{57B} , GLN _{82C} , LEU _{83C} , ASN _{84C} , GLN _{109D} , LEU _{110D} , ASN _{111D} , GLN _{136E} , LEU _{137E} , ASN _{138E} , ASN _{165F} <i>Hydrophobic: 25%, Acidic: 0%, Basic: 0%, Neutral: 75%</i>

	Amyloid fibrils	Amino acid residues forming the fibril binding sites for resveratrol
2	ApoA-II	LEU _{10H} , THR _{12H} , TYR _{14H} , TYR _{21H} , LEU _{10N} , THR _{12N} , TYR _{14N} , TYR _{21N} , ALA _{56N} , THR _{58N} , LEU _{10R} , THR _{12R} , TYR _{14R} , TYR _{21R} , ALA _{56R} , GLY _{57R} , THR _{58R} , LEU _{10V} , TYR _{21V} , ALA _{56V} , GLY _{57V} , THR _{58V} <i>Hydrophobic: 31.82%, Acidic: 0%, Basic: 0%, Neutral: 68.18%</i>
3	Abeta	PHE _{4K} , ARG _{5K} , HIS _{6K} , VAL _{18K} , PHE _{19K} , PHE _{20K} , ALA _{21K} , GLU _{22K} , ASP _{23K} , VAL _{24K} <i>Hydrophobic: 60%, Acidic: 20%, Basic: 20%, Neutral: 0%</i>
4	IAPP	HIS _{18C} , SER _{19C} , SER _{20C} , HIS _{18E} , SER _{19E} , SER _{20E} , HIS _{18G} , SER _{19G} , SER _{20G} , HIS _{18I} , SER _{19I} , SER _{20I} <i>Hydrophobic: 0%, Acidic: 0%, Basic: 33.33%, Neutral: 66.67%</i>
5	Ins	GLN _{115H} , PHE _{201H} , VAL _{202H} , ASN _{203H} , GLN _{204H} , HSD _{205H} , ILE _{2J} , LEU _{13J} , GLN _{15J} , VAL _{202J} , ASN _{203J} , GLN _{204J} , HSD _{205J} , LEU _{206J} , GLN _{5L} <i>Hydrophobic: 40%, Acidic: 0%, Basic: 13.33%, Neutral: 46.67%</i>

Interestingly, the molecular docking analysis revealed noticeable differences between the two tautomeric forms of curcumin in their fibril-associating abilities: i) the binding affinities of enol form of CR appeared to be markedly higher than those of the keto form, especially for ApoA-II fibrils (Table 1); ii) the basic amino acids are present in the binding sites of ApoA-I and Ins for CR enol, but not for keto CR; iii) the contribution of the basic residues in the stabilization of Abeta-CR complexes decreases in the case of keto CR in favor of the neutral residues; iv) the hydrophobic residues participate in the association of only CR keto with IAPP fibrils; v) in contrast to enol CR, the acidic residues are involved in the binding of keto CR to InsF (Table 6, 7).

Table 6. The interface residues in the complexes between amyloid fibrils and curcumin enol

	Amyloid fibrils	Amino acid residues forming the fibril binding sites for curcumin enol
1	ApoA-I	GLN _{379N} , GLN _{406O} , LEU _{407O} , ASN _{408O} , GLN _{433P} , LEU _{434P} , ASN _{435P} , GLN _{460Q} , LEU _{461Q} , ASN _{462Q} , GLN _{487R} , LEU _{488R} , ASN _{489R} , ASN _{516S} <i>Hydrophobic: 28.57%, Acidic: 0%, Basic: 0%, Neutral: 71.43%</i>
2	ApoA-II	THR _{12D} , LEU _{10H} , THR _{12H} , TYR _{14H} , TYR _{21H} , LEU _{10N} , THR _{12N} , TYR _{14N} , TYR _{21N} , ALA _{56N} , GLY _{57N} , THR _{58N} , LEU _{10R} , THR _{12R} , TYR _{14R} , TYR _{21R} , ALA _{56R} , GLY _{57R} , THR _{58R} , LEU _{10V} , THR _{12V} , TYR _{14V} , TYR _{21V} , ALA _{56V} , GLY _{57V} , THR _{58V} , TYR _{21K} , ALA _{56K} , THR _{58K} <i>Hydrophobic: 27.59%, Acidic: 0%, Basic: 0%, Neutral: 72.41%</i>
3	Abeta	HIS _{13C} , HIS _{14C} , VAL _{12E} , HIS _{13E} , HIS _{14E} , VAL _{12G} , HIS _{13G} , HIS _{14G} , VAL _{12I} , HIS _{13I} , HIS _{14I} , VAL _{12K} , HIS _{13K} , HIS _{14K} <i>Hydrophobic: 28.57%, Acidic: 0%, Basic: 71.43%, Neutral: 0%</i>
4	IAPP	HIS _{18E} , SER _{19E} , HIS _{18G} , SER _{19G} , SER _{20G} , HIS _{18I} , SER _{19I} , SER _{20I} , HIS _{18K} , SER _{19K} , SER _{20K} , HIS _{18M} , SER _{19M} , SER _{20M} , HIS _{18O} <i>Hydrophobic: 0%, Acidic: 0%, Basic: 40%, Neutral: 60%</i>
5	Ins	ILE _{102G} , LEU _{306G} , CYS _{307G} , GLY _{308G} , LEU _{217H} , VAL _{218H} , CYS _{219H} , LEU _{317H} , VAL _{318H} , CYS _{319H} , ILE _{102I} , LEU _{306I} , CYS _{307I} , GLY _{308I} , LEU _{217I} , VAL _{218I} , CYS _{219I} , LEU _{317I} , VAL _{318I} , CYS _{319I} , LEU _{306K} , CYS _{307K} , GLY _{308K} , LEU _{217L} , VAL _{218L} , CYS _{219L} <i>Hydrophobic: 57.69%, Acidic: 0%, Basic: 0%, Neutral: 42.31%</i>

Table 7. The interface residues in the complexes between amyloid fibrils and curcumin keto

	Amyloid fibrils	Amino acid residues forming the fibril binding sites for curcumin keto
1	ApoA-I	GLN _{82C} , LEU _{83C} , ASN _{84C} , GLN _{109D} , LEU _{110D} , ASN _{111D} , LYS _{113D} , ASN _{138E} , LYS _{140E} , ASN _{165F} , LYS _{167F} <i>Hydrophobic: 18.18%, Acidic: 0%, Basic: 27.27%, Neutral: 54.55%</i>
2	ApoA-II	LEU _{10B} , THR _{12B} , TYR _{14B} , TYR _{21B} , ALA _{56B} , GLY _{57B} , THR _{58B} , SER _{59B} , LEU _{60B} , LEU _{10F} , THR _{12F} , TYR _{14F} , TYR _{21F} , ALA _{56F} , GLY _{57F} , THR _{58F} , LEU _{10L} , TYR _{21L} , THR _{58L} <i>Hydrophobic: 31.58%, Acidic: 0%, Basic: 0%, Neutral: 68.42%</i>
3	Abeta	HIS _{13A} , HIS _{14A} , GLN _{15A} , GLY _{37B} , VAL _{12C} , HIS _{13C} , HIS _{14C} , GLN _{15C} , VAL _{12E} , HIS _{13E} , HIS _{14E} <i>Hydrophobic: 18.18%, Acidic: 0%, Basic: 54.55%, Neutral: 27.27%</i>
4	IAPP	LEU _{16E} , HIS _{18E} , SER _{19E} , SER _{20E} , LEU _{16G} , HIS _{18G} , SER _{19G} , SER _{20G} , LEU _{16I} , HIS _{18I} <i>Hydrophobic: 30%, Acidic: 0%, Basic: 30%, Neutral: 40%</i>
5	Ins	PHE _{201G} , VAL _{202G} , ASN _{203G} , GLN _{204G} , HSD _{205G} , ILE _{2I} , GLN _{15I} , LEU _{16I} , GLU _{17I} , GLN _{115I} , LEU _{116I} , GLU _{117I} , VAL _{202I} , ASN _{203I} , GLN _{204I} , HSD _{205I} , GLN _{15K} <i>Hydrophobic: 35.29%, Acidic: 11.76%, Basic: 11.76%, Neutral: 41.18%</i>

The contact residues of sesamin complexes with ApoA-I fibrils are represented by the acidic and basic residues, with the amino acid composition of the binding sites being completely different from that of the other polyphenols (Table 8). Likewise, the acidic residues take part in the association of sesamin with Abeta fibrils.

Table 8. The interface residues in the complexes between amyloid fibrils and sesamin

	Amyloid fibrils	Amino acid residues forming the fibril binding sites for sesamin
1	ApoA-I	ARG _{445Q} , ARG _{446Q} , ASP _{447Q} , ARG _{472R} , ARG _{473R} , ASP _{474R} , ARG _{499S} , ARG _{500S} , ASP _{501S} , ARG _{526T} , ARG _{527T} , ASP _{528T} <i>Hydrophobic: 0%, Acidic: 33.33%, Basic: 66.67%, Neutral: 0%</i>
2	ApoA-II	LEU _{10F} , THR _{12F} , TYR _{21F} , ALA _{56F} , GLY _{57F} , THR _{58F} , LEU _{10L} , THR _{12L} , TYR _{14L} , TYR _{21L} , ALA _{56L} , GLY _{57L} , THR _{58L} , LEU _{10P} , THR _{12P} , TYR _{14P} , TYR _{21P} , ALA _{56P} , THR _{58P} , LEU _{10T} , THR _{12T} , TYR _{14T} , TYR _{21T} <i>Hydrophobic: 30.43%, Acidic: 0%, Basic: 0%, Neutral: 69.57%</i>
3	Abeta	PHE _{4K} , HIS _{6K} , LYS _{16K} , LEU _{17K} , VAL _{18K} , PHE _{19K} , PHE _{20K} , ALA _{21K} , GLU _{22K} <i>Hydrophobic: 62.5%, Acidic: 12.5%, Basic: 25%, Neutral: 0%</i>
4	IAPP	SER _{19B} , HIS _{18D} , SER _{19D} , SER _{20D} , HIS _{18F} , SER _{19F} , SER _{20F} , HIS _{18H} , SER _{19H} , SER _{20H} , HIS _{18J} , SER _{19J} , SER _{20J} <i>Hydrophobic: 0%, Acidic: 0%, Basic: 30.77%, Neutral: 69.23%</i>
5	Ins	ILE _{102A} , VAL _{103A} , GLN _{304A} , HSD _{305A} , LEU _{306A} , CYS _{307A} , VAL _{218B} , CYS _{219B} , LEU _{317B} , VAL _{318B} , CYS _{319B} , GLN _{304C} , HSD _{305C} , LEU _{306C} , CYS _{307C} , LEU _{217D} , VAL _{218D} , CYS _{219D} <i>Hydrophobic: 50%, Acidic: 0%, Basic: 11.11%, Neutral: 38.89%</i>

Overall, PF association with Abeta fibrils is governed mainly by the hydrophobic and basic residues, while acidic residues make some contribution to stabilization of the Abeta complexes with sesamin and resveratrol. The binding of polyphenols to fibrillar ApoA-I and ApoA-II is mediated predominantly by hydrophobic and neutral amino acids, although in some cases the basic residues are also involved (*viz.* in the complexes ApoA-I + curcumin keto / sesamin, Ins + curcumin keto). The hydrophobic, basic and neutral residues account for the interactions of polyphenols with the insulin fibrils, while the basic and neutral amino acids play a key role in polyphenol complexation with IAPP fibrils.

CONCLUSIONS

In summary, the molecular docking study of the complexes between the representatives of the six groups of polyphenolic compounds such as flavonoids (quercetin), phenolic acids and derivatives (salicylic acid acid), stilbenes (resveratrol), curcuminoids (curcumin), lignans (sesamin), tannins (gallic acid) and the five types of amyloid fibrils showed that all examined polyphenols have the highest binding affinities for the fibrillar forms of apolipoprotein A-II and insulin, while the lowest affinities were observed for the fibrillar apolipoprotein A-I. The hydrophobicity/hydrophilicity analysis of the amino acid composition of the binding sites revealed that hydrophobic and neutral residues dominate in the association of polyphenols with amyloid fibrils from apoA-I, apoA-II and insulin, the basic residues to a large extent control polyphenol binding to Abeta and IAPP fibrils, whereas the involvement of the acidic residues was revealed only for the complexes sesamin + ApoA-I / Abeta and curcumin keto + Ins. These findings may be of value for deeper understanding of polyphenol ability to destroy or remodel the mature amyloid fibrils and the development of novel anti-amyloid strategies.

Acknowledgements

This project has received funding through the EURIZON project, which is funded by the European Union under Grant Agreement No. 3049.

ORCID

© Uliana Malovytsia, <https://orcid.org/0000-0002-7677-0779>; © Valeriya Trusova, <https://orcid.org/0000-0002-7087-071X>;
© Mette Hedegaard Thomsen, <https://orcid.org/0000-0001-6805-7247>; © Kateryna Vus, <https://orcid.org/0000-0003-4738-4016>
© Olga Zhytniakivska, <https://orcid.org/0000-0002-2068-5823>; © Galyna Gorbenko, <https://orcid.org/0000-0002-0954-5053>

REFERENCES

- [1] E. Chatani, K. Yuzu, Y. Ohhashi, and Y. Goto, *Int. J. Mol. Sci.* **22**, 4349 (2021). <https://doi.org/10.3390/ijms22094349>
- [2] B. Liu, H. Zhang, and X. Qinn, *Nanomaterials* **15**, 255 (2025). <https://doi.org/10.3390/nano15040255>
- [3] W. Yao, H. Yang, and J. Yang, *Front. Aging Neurosci.* **14**, 1019412 (2022). <https://doi.org/10.3389/fnagi.2022.1019412>
- [4] P. Bhosale, S. Ha, P. Vetrivel, H. Kim, S. Kim, and G. Kim, *Transl. Cancer Res.* **9**, 7619 (2020). <https://doi.org/10.21037/tcr-20-2359>
- [5] A. Rana, M. Samtiya, T. Dhewa, V. Mishra, and R. Aluko, *J. Food. Chem.* **46**, e14264 (2022). <https://doi.org/10.1111/jfbc.14264>
- [6] Y. Han, H. Yin, C. Xiao, M. Bernards, Y. He, and Y. Guan, *ACS Chem. Neurosci.* **14**, 4051–4061 (2023). <https://doi.org/10.1021/acscchemneuro.3c00586>
- [7] G. Martins, C. Nascimento, and N. Galamba, *ACS Chem. Neurosci.* **14**, 1905–1920 (2023). <https://doi.org/10.1021/acscchemneuro.3c00162>
- [8] F. Zaidi, and R. Bhat, *J. Biomol. Struct. Dyn.* **40**, 4593–4611 (2020). <https://doi.org/10.1080/07391102.2020.1860824>

- [9] Y. Nian, Y. Zhang, C. Ruan, and B. Hu, *Curr. Opin. Food Sci.* **43**, 99 (2022). <https://doi.org/10.1016/j.cofs.2021.11.005>
- [10] J. Bieschke, J. Russ, R. Friedrich, D. Ehrnhoefer, H. Wobst, K. Neugebauer, and E. Wanker, *Proc. Natl. Acad. Sci. U.S. A.* **107**, 7710–7715 (2010). <https://doi.org/10.1073/pnas.0910723107>
- [11] D. Ehrnhoefer, J. Bieschke, A. Boeddrich, M. Herbst, L. Masino, R. Lurz, S. Engemann, A. Pastore, and E. Wanker, *Nat. Struct. Mol. Biol.* **15**, 558–566 (2008). <https://doi.org/10.1038/nsmb.1437>
- [12] Z. Fu, D. Aucoin, M. Ahmed, M. Ziliox, W. Van Nostrand, and S. Smith, *Biochemistry* **53**, 7893–7903 (2014). <https://doi.org/10.1021/bi500910b>
- [13] R. Mishra, D. Sellin, D. Radovan, A. Gohlke, and R. Winter, *ChemBioChem* **10**, 445–449 (2009). <https://doi.org/10.1002/cbic.200800762>
- [14] G. Prasanna, and P. Jing, *Spectrochim Acta A Mol Biomol Spectrosc.* **246**, 119001 (2021). <https://doi.org/10.1016/j.saa.2020.119001>
- [15] K. Siposova, T. Kozar, V. Huntosova, S. Tomkova, and A. Musatov, *Biochim. Biophys. Acta - Proteins Proteom.* **1867**, 259–274 (2019). <https://doi.org/10.1016/j.bbapap.2018.10.002>
- [16] R. Abioye, O. Okagu, and C. Udenigwe, *J. Agric. Food Chem.* **70**, 392–402 (2022). <https://doi.org/10.1021/acs.jafc.1c06918>
- [17] M. Ramezani, M. Hesami, Y. Rafiei, E. Ghareghozloo, A. Meratan, and N. Nikfarjam, *ACS Appl. Bio Mater.* **4**, 3547–3560 (2021). <https://doi.org/10.1021/acsabm.1c00068>
- [18] Y. Yan, H. Tao, J. He, and S-Y. Huang, *Nat. Protoc.* **15**, 1829–1852 (2020). <https://doi.org/10.1038/s41596-020-0312-x>

**ВЗАЄМОДІЯ ПОЛІФЕНОЛІВ З АМІЛОЇДНИМИ ФІБРИЛАМИ:
ДОСЛІДЖЕННЯ МЕТОДОМ МОЛЕКУЛЯРНОГО ДОКІНГУ**

Уляна Маловиця^a, Валерія Трусова^a, Метте Томсен^b, Катерина Вус^a, Ольга Житняківська^a, Галина Горбенко^a

^a*Кафедра медичної фізики та біомедичних нанотехнологій, Харківський національний університет імені В.Н. Каразіна
м. Свободи 4, Харків, 61022, Україна*



^b*Університет Аалборг, вул. Нільса Бора 8, 6700 Есб'єрг, Данія*

Поліфеноли, група різноманітних сполук природного походження, які мають цілу низку корисних біологічних властивостей, наразі привертають все більший інтерес в контексті їх здатності інгібувати утворення і викликати дестабілізацію особливих білкових агрегатів, амілоїдних фібрил, пов'язаних із багатьма захворюваннями людини. У даній роботі метод молекулярного докінгу був застосований для з'ясування молекулярних деталей взаємодії між поліфенольними сполуками, включаючи кверцетин, куркумін, ресвератрол, сесамін, саліцилову та галову кислоти зі зрілими амілоїдними фібрилами із Абета пептиду, амілоїдного поліпептиду, інсуліну, аполіпопротеїнів А-I та А-II. Усі досліджені поліфеноли мали найвищу спорідненість до амілоїдних фібрил із аполіпопротеїну А-II та інсуліну, тоді як найнижча спорідненість спостерігалась до фібрилярного аполіпопротеїну А-I. Аналіз амінокислотного складу сайтів зв'язування з використанням шкали гідрофобності/гідрофільності показав, що гідрофобні та нейтральні залишки відіграють ключову роль у комплексоутворенні поліфенолів з амілоїдними фібрилами із аполіпопротеїну А-I, аполіпопротеїну А-II та інсуліну, позитивно заряджені залишки у значній мірі визначають зв'язування поліфенолів з фібрилярними формами Абета та амілоїдного поліпептидів, тоді як внесок негативно заряджених залишків був виявлений тільки для комплексів сесамін + фібрили аполіпопротеїну А-I /Абета та куркумін кето + фібрили інсуліну. Отримані результати можуть бути корисними при розробці нових анти-амілоїдних стратегій на основі поліфенолів.

Ключові слова: амілоїдні фібрили; поліфеноли; сайти зв'язування; спорідненість зв'язування; молекулярний докінг

COMPUTATIONAL STUDY OF DRUG DELIVERY SYSTEMS WITH RADIONUCLIDE AND FLUORESCENCE IMAGING MODALITIES.

IV. DOXORUBICIN DELIVERY SYSTEMS BASED ON ALBUMIN AND HEMOGLOBIN

 V. Trusova^{a*},  U. Malovytsia^a,  P. Kuznietsov^b,  I. Yakymenko^b, I. Karnaukhov^c,
 A. Zelinsky^c,  B. Borts^c, I. Ushakov^c, L. Sidenko^c,  G. Gorbenko^a

^aDepartment of Medical Physics and Biomedical Nanotechnologies, V.N. Karazin Kharkiv National University
 4 Svobody Sq., Kharkiv, 61022, Ukraine

^bO.I. Akhiezer Department for Nuclear Physics and High Energy Physics, V.N. Karazin Kharkiv National University
 4 Svobody Sq., Kharkiv, 61022, Ukraine

^cNational Science Center "Kharkiv Institute of Physics and Technology", Kharkiv, Ukraine

*Corresponding Author E-mail: valerija.trusova@karazin.ua

Received June 2, 2025, revised July 29, 2025; accepted August 21, 2025

The development of multifunctional drug delivery systems that integrate therapeutic and diagnostic capabilities remains a major challenge in oncology. In the present work we investigated hybrid carriers composed of human serum albumin and hemoglobin (HSA-Hb) for doxorubicin (DOX) delivery combined with radionuclide and fluorescence imaging. Using molecular docking simulations, we systematically evaluated the interactions of HSA-Hb assemblies with twelve technetium-99m (^{99m}Tc)-labeled radiopharmaceuticals, DOX, and four near-infrared (NIR) dyes. The results revealed that hemoglobin markedly expands the binding landscape, providing exclusive and high-affinity sites for several ^{99m}Tc complexes (notably TcMEB and TcDIS), while also serving as the primary scaffold for DOX and NIR dyes. Two distinct DOX-binding pockets were identified within Hb subunits, suggesting enhanced drug stability and potential responsiveness to tumor hypoxia. Fluorescent dyes, including methylene blue, indocyanine green, AK7-5, and SQ1, exhibited preferential binding to Hb with affinities higher than those observed for albumin, indicating superior suitability for optical imaging. Importantly, the partitioning of radiopharmaceuticals to albumin and therapeutic/imaging ligands to hemoglobin reduced binding competition and enabled the simultaneous integration of multimodal functions within a single construct. These findings highlight HSA-Hb nanocarriers as promising candidates for next-generation theranostic platforms, combining efficient DOX delivery with non-invasive radionuclide and fluorescence monitoring.

Keywords: Protein-based drug delivery nanosystems, Human serum albumin, Hemoglobin, Doxorubicin, Technetium complexes, Near infrared dyes, Molecular docking

PACS: 87.14.C++c, 87.16.Dg

Advancing the design of multifunctional drug delivery systems remains a pivotal objective in oncological research, particularly when addressing the therapeutic limitations of cytotoxic agents such as doxorubicin (DOX) [1,2]. The challenge lies in achieving targeted delivery with minimal off-target effects, while simultaneously enabling real-time visualization of drug distribution [3]. Protein-based nanocarriers have garnered significant attention due to their favorable pharmacological profiles, including biodegradability, low immunogenicity, and the ability to accommodate both therapeutic and diagnostic payloads. Among these, human serum albumin (HSA) continues to serve as a cornerstone in drug delivery strategies, owing to its high binding capacity, extended systemic half-life, and preferential accumulation in tumor tissues via the enhanced permeability and retention (EPR) effect [4]. Building upon our prior investigations into albumin-based hybrid systems incorporating transferrin or lysozyme [5-7], we now turn our focus to hemoglobin (Hb) as a co-carrier in the development of DOX delivery platforms. Hemoglobin, a tetrameric metalloprotein with intrinsic oxygen-carrying functionality, presents unique physicochemical properties that may be harnessed for drug encapsulation and release [8]. Its quaternary structure, redox-active heme groups, and responsiveness to pH and oxidative stress render it a compelling candidate for tumor-targeted delivery, particularly in hypoxic microenvironments where conventional carriers may falter. In this study, we employ computational modeling techniques to elucidate the molecular architecture and binding energetics of DOX within albumin-hemoglobin hybrid systems. Furthermore, we investigate the feasibility of integrating radionuclide and fluorescent imaging modalities into the carrier architecture, aiming to establish a dual-functional system capable of both therapeutic action and non-invasive biodistribution tracking. Through this approach, we seek to expand the repertoire of protein-based theranostic agents and contribute to the rational design of next-generation delivery vehicles tailored for precision oncology.

METHODS

To construct the protein-based drug delivery systems (PDDS), the dimeric structure of human serum albumin (HSA) was utilized as the foundational scaffold, retrieved from the Protein Data Bank (PDB ID: 1AO6). Hemoglobin (Hb, human deoxyhemoglobin, PDB ID: 2DN2) was introduced as a secondary protein component to explore its potential synergistic

role in doxorubicin (DOX) transport and imaging agent integration. A panel of twelve technetium-99m-labeled radiopharmaceuticals was selected to evaluate the compatibility of the PDDS with nuclear imaging modalities. Complete characteristics as well as the structures of the employed complexes are given in [5-7]. To enable dual-modality imaging, these radiotracers were paired with four near-infrared (NIR) fluorescent dyes: methylene blue (MB), indocyanine green (IG), cyanine derivative AK7-5, and squaraine-based SQ1. Molecular docking simulations were performed using the HDOCK platform to identify favorable interaction sites for DOX, technetium-labeled compounds, and NIR dyes within the HSA-Hb assemblies. Ligand structures were generated using MarvinSketch (version 18.10.0) and subsequently refined through energy minimization in Avogadro (version 1.1.0). The resulting docking poses were visualized and examined using UCSF Chimera (version 1.14), and protein-ligand interactions were further characterized using the Protein-Ligand Interaction Profiler tool [9].

RESULTS AND DISCUSSION

Our previous investigations have examined the versatility of albumin-centered drug delivery platforms for transporting doxorubicin (DOX), particularly in combination with technetium-99m-based radiotracers (TCC) and near-infrared (NIR) fluorescent dyes to enable multimodal imaging [5-7]. In our initial study, human serum albumin (HSA) was identified as a robust carrier capable of forming stable complexes with both radionuclide agents and optical probes. Computational analyses, including molecular docking and short-timescale molecular dynamics simulations, confirmed the structural integrity and high-affinity interactions of these hybrid nanocarriers, underscoring their potential for theranostic applications. Building upon this framework, subsequent works expanded the carrier design by introducing transferrin (TRF) and lysozyme (Lz) as auxiliary protein partners to albumin, thereby probing their capacity to enhance tumor targeting and cellular uptake. Both HSA-TRF and HSA-Lz hybrid platforms demonstrated preserved compatibility with TCC agents and NIR dyes, confirming their potential to optimize the therapeutic precision and overall performance of DOX delivery systems. In continuation of this line of research, the present study directs attention to albumin-hemoglobin (HSA-Hb) assemblies. By characterizing their molecular interactions with DOX, technetium-based radiopharmaceuticals, and fluorescent probes, we evaluate the suitability of HSA-Hb complexes as next-generation multimodal carriers. Particular emphasis is placed on binding energetics, conformational stability, and their potential to advance the dual goals of effective therapy and non-invasive imaging.

Molecular docking simulations revealed a distinct hierarchy in the binding affinities of technetium-99m-labeled compounds (TCC) to the HSA-Hb complexes (Fig. 1, left panel). Analysis of the best docking scores (BDS) indicated that TcHYN exhibited the strongest interaction, followed by TcDIS, TcDTPA, and TcMEB.

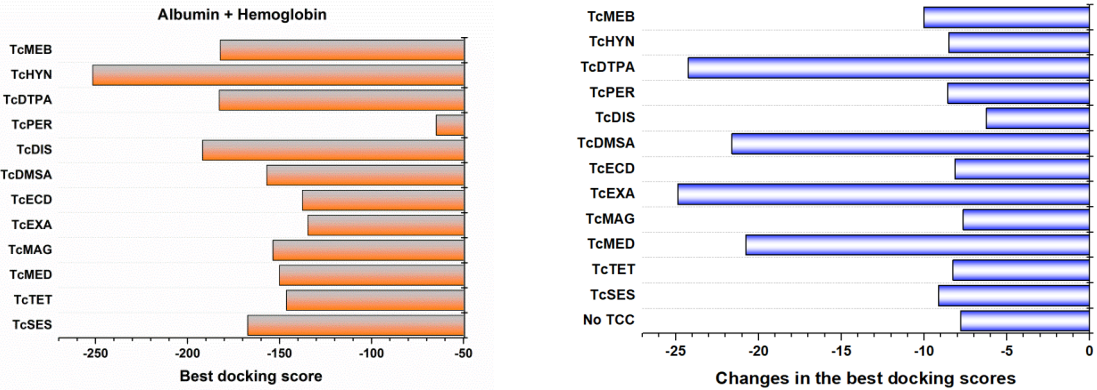


Figure 1. Absolute values (left panel) and changes (right panel) in the best docking score values obtained for the TCC complexes with HSA in the absence and presence of Hb

Intermediate affinities were observed for TcSES, TcDMSA, TcMAG, and TcMED, while TcTET, TcECD, TcEXA, and TcPER showed comparatively weaker binding. The top BDS values for HSA-Hb complexes reached -251.54, corresponding to 38 interface residues contributing to ligand stabilization (Table 1).

Table 1. The interface amino acid residues and the types of interactions involved in the binding of technetium 99m complexes (TCC) to the albumin-hemoglobin (Hb) associates

TCC	HSA-Hb-TCC interface residues			Type of interactions
	HSA	Hb		
TcSES		ASP _{99B} *, ARG _{104B} , HSD _{143B} , PRO _{37C} , ARG _{104D} , ALA _{128D} , VAL _{134D} , ALA _{135D} , ASN _{139D}	PRO _{100B} , ASN _{139B} , TYR _{145B} , LEU _{100C} , LEU _{105D} , GLN _{131D} , ALA _{135D} , ASN _{108D} , LYS _{132D}	GLU _{101B} , ALA _{142B} , PHE _{36C} , GLU _{101D} , ASN _{108D}
				Hydrophobic interactions, hydrogen bonds

TCC	HSA-Hb-TCC interface residues		Type of interactions
	HSA	Hb	
TcTET		GLN _{39B} , ARG _{40B} , GLU _{43B} , HSD _{97B} , PRO _{44C} , ARG _{92C}	Hydrophobic interactions
TcMED	ALA _{300B} , ASP _{301B} , LEU _{302B}	THR _{38A} , THR _{41A} , TYR _{42A} , LEU _{28D} , LEU _{31D} , LEU _{32D} , THR _{38D} , PHE _{41D} , PHE _{42D} , HSD _{63D} , VAL _{67D} , LEU _{96D} , HSD _{97D} , VAL _{98D} , ASP _{99D} , ASN _{102D} , PHE _{103D} , LEU _{106D}	Hydrogen bonds
TcMAG	ALA _{300B} , ASP _{301B}	THR _{41A} , TYR _{42A} , LEU _{28D} , LEU _{31D} , LEU _{32D} , THR _{38D} , PHE _{41D} , PHE _{42D} , HSD _{63D} , VAL _{67D} , HSD _{97D} , VAL _{98D} , ASP _{99D} , ASN _{102D}	Hydrogen bonds
TcEXA	LEU _{115A} , VAL _{116A} , ARG _{117A} , PRO _{118A} , MET _{123A} , PHE _{134A} , LYS _{137A} , TYR _{138A} , LEU _{139A} , GLU _{141A} , ILE _{142A} , ARG _{145A} , TYR _{161A} , PHE _{165A} , LEU _{182A} , ARG _{186A}		Hydrophobic interactions, hydrogen bonds
TcECD	LEU _{115B} , ARG _{117B} , PRO _{118B} , MET _{123B} , PHE _{134B} , LYS _{137B} , TYR _{138B} , GLU _{141B} , ILE _{142B} , TYR _{161B} , LEU _{182B} , ASP _{183B} , LEU _{185B} , ARG _{186B}		Hydrophobic interactions, hydrogen bonds, salt bridges
TcDMSA	LEU _{115A} , VAL _{116A} , ARG _{117A} , PRO _{118A} , MET _{123A} , TYR _{138A} , ILE _{142A} , HSD _{146A} , PHE _{149A} , LEU _{154A} , PHE _{157A} , TYR _{161A} , LEU _{182A} , LEU _{185A} , ARG _{186A} , ASP _{187A} , GLU _{188A} , GLY _{189A} , LYS _{190A}		Hydrogen bonds, salt bridges
TcDIS		PRO _{37A} , THR _{38A} , GLN _{131B} , LYS _{132B} , ALA _{135B} , ASN _{139B} , ASN _{139D} , ALA _{142D}	Hydrophobic interactions, hydrogen bonds, salt bridges
TcPER	ALA _{26B} , TYR _{30B} , LEU _{66B} , HSD _{67B} , PHE _{70B} , GLY _{71B} , ASN _{99B} , HSP _{247B} , GLY _{248B} , ASP _{249B} , LEU _{250B}		Hydrogen bonds
TcDTPA	LEU _{115A} , VAL _{116A} , ARG _{117A} , PRO _{118A} , MET _{123A} , PHE _{134A} , LEU _{135A} , LYS _{137A} , TYR _{138A} , GLU _{141B} , ILE _{142B} , TYR _{161A} , LEU _{182A} , ARG _{186A}		Hydrogen bonds, salt bridges
TcHYN	GLU _{383A} , LEU _{387A} , ASN _{391A} , LEU _{394A} , LEU _{430A} , LEU _{453A} , SER _{489A} , GLU _{492A} , ALA _{406A} , LEU _{407A} , VAL _{409A} , ARG _{410A} , TYR _{411A} , LYS _{541A} , GLU _{542A} , LYS _{545A}		Hydrogen bonds, π -stacking, salt bridges
TcMEB		LEU _{34A} , SER _{35A} , PHE _{36A} , PRO _{37A} , THR _{38A} , VAL _{1B} , GLN _{131B} , LYS _{132B} , ALA _{135B} , ASN _{139B} , PRO _{100D} , ARG _{104D} , ALA _{138D} , ASN _{139D} , ALA _{142D} , HSD _{143D} , LYS _{144D} , TYR _{145D} , HSD _{146D}	Hydrophobic interactions, hydrogen bonds

*A, B, C, D denote hemoglobin subunits

The incorporation of hemoglobin into the albumin scaffold significantly altered the ligand-binding landscape. Notably, the presence of Hb enhanced the binding affinity for several TCC agents, particularly TcMEB and TcDIS, suggesting that Hb introduces novel interaction sites or stabilizes conformational states favorable for ligand accommodation. Moderate affinity improvements were also observed for TcSES, TcMAG, and TcMED when bound to Hb-containing assemblies. Interestingly, four radiopharmaceuticals, TcSES, TcTET, TcMEB, and TcDIS, exhibited exclusive binding to the Hb component within the HSA-Hb complex (Fig. 2), with affinities surpassing those observed for albumin alone (Fig. 1, right panel).

This selective binding implies that hemoglobin not only complements HSA carrier function but may also serve as a primary docking site for certain radiopharmaceuticals. From a mechanistic perspective, tetrameric structure of Hb and its diverse subunit interfaces likely contribute to the formation of deeper or more electrostatically favorable pockets for TCC binding. Moreover, the redox-active nature of the heme groups may influence the local electronic environment, potentially stabilizing technetium complexes through transient coordination or polar interactions. These findings underscore the value of hemoglobin as a co-carrier in multimodal drug delivery systems, particularly for radiolabeled agents.

To assess the therapeutic potential of the HSA-Hb platform, we constructed ternary complexes by docking doxorubicin (DOX) onto the most favorable protein-TCC assemblies. The results revealed that DOX binding was significantly influenced by the presence of hemoglobin. Specifically, systems containing TcDTPA, TcDMSA, TcEXA,

and TcMED exhibited marked increases in DOX affinity when Hb was present. This suggests a cooperative effect, where the initial TCC binding induces conformational changes or exposes cryptic sites on Hb that are conducive to DOX interaction. In contrast, lysozyme-based systems analyzed in previous studies [5-7] showed only modest improvements in DOX binding, limited to TcTET and TcMED complexes. This comparison highlights the superior adaptability of hemoglobin in accommodating multiple ligands simultaneously, likely due to its larger surface area and more flexible quaternary structure.

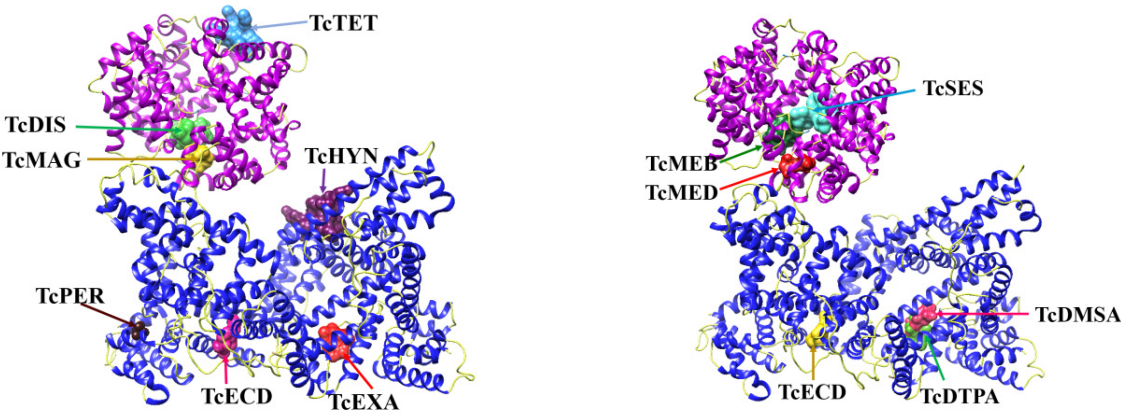


Figure 2. Best docking poses for TCC complexation with HSA-Hb systems

Detailed mapping of DOX binding sites within the HSA-Hb complexes revealed two distinct regions, both located exclusively on the hemoglobin molecule. The first site, observed in TcDIS and TcMEB systems, involved 15 residues from the A, B, and D subunits. The second, more extensive site, present in all other ternary complexes, comprised 25 residues spanning the A, B, and C subunits (Fig. 3; Table 2). These sites are likely stabilized by a combination of hydrophobic interactions and hydrogen bonding, facilitated by the amphipathic nature of DOX and the diverse chemical environment of Hb.

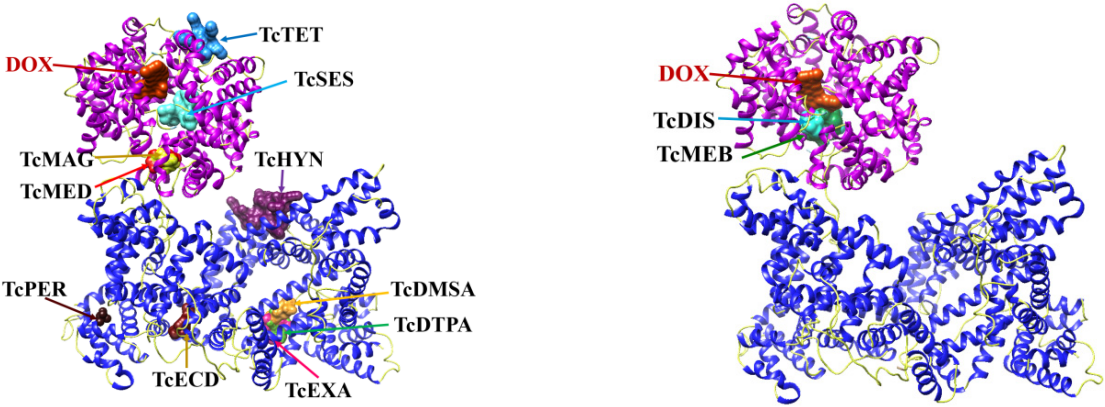


Figure 3. The highest affinity binding sites for DOX in HSA-Hb assemblies

Functionally, this Hb-mediated interaction may have twofold significance. First, Hb could act as a stabilizing scaffold that shields DOX from premature release in circulation, potentially lowering systemic toxicity. Second, the multivalent subunit interactions may facilitate drug retention within the hypoxic tumor microenvironment, where Hb oxygen-binding properties could further influence drug pharmacodynamics.

Table 2. The interface amino acid residues and the types of interactions involved in the binding of DOX to HSA-Hb-TCC complexes

Complex	HSA-Hb-TCC-DOX interface residues		Type of interactions
	HSA	Hb	
HSA-Hb-DOX		VAL _{1A} *, LEU _{2A} , LYS _{99A} , LEU _{100A} , SER _{102A} , HSD _{103A} , LEU _{106A} , ASP _{126A} , LYS _{127A} , ALA _{130A} , SER _{131A} , TYR _{35B} , TRP _{37B} , GLU _{101B} , LEU _{105B} , ASN _{108B} , ASP _{94C} , PRO _{95C} , VAL _{96C} , THR _{137C} , SER _{138C} , LYS _{139C} , TYR _{140C} , ARG _{141C}	Hydrophobic interactions, hydrogen bonds
HSA-Hb-TcSES-DOX		VAL _{1A} , LEU _{2A} , LYS _{99A} , LEU _{100A} , SER _{102A} , HSD _{103A} , LEU _{106A} , ASP _{126A} , LYS _{127A} , ALA _{130A} , SER _{131A} , TYR _{35B} , TRP _{37B} , GLU _{101B} , LEU _{105B} , ASN _{108B} , ASP _{94C} , PRO _{95C} , VAL _{96C} , THR _{137C} , SER _{138C} , LYS _{139C} , TYR _{140C} , ARG _{141C}	Hydrophobic interactions, hydrogen bonds

Complex	HSA-Hb-TCC-DOX interface residues		Type of interactions
	HSA	Hb	
HSA-Hb-TcTET-DOX		VAL _{1A} , LEU _{2A} , LYS _{99A} , LEU _{100A} , SER _{102A} , HSD _{103A} , LEU _{106A} , ASP _{126A} , LYS _{127A} , ALA _{130A} , SER _{131A} , TYR _{35B} , TRP _{37B} , GLU _{101B} , LEU _{105B} , ASN _{108B} , ASP _{94C} , PRO _{95C} , VAL _{96C} , THR _{137C} , SER _{138C} , LYS _{139C} , TYR _{140C} , ARG _{141C}	Hydrophobic interactions, hydrogen bonds
HSA-Hb-TcMED-DOX		VAL _{1A} , LEU _{2A} , LYS _{99A} , LEU _{100A} , SER _{102A} , HSD _{103A} , LEU _{106A} , ASP _{126A} , LYS _{127A} , ALA _{130A} , SER _{131A} , TYR _{35B} , TRP _{37B} , GLU _{101B} , LEU _{105B} , ASN _{108B} , ASP _{94C} , PRO _{95C} , VAL _{96C} , THR _{137C} , SER _{138C} , LYS _{139C} , TYR _{140C} , ARG _{141C}	Hydrophobic interactions, hydrogen bonds
HSA-Hb-TcMAG-DOX		VAL _{1A} , LEU _{2A} , LYS _{99A} , LEU _{100A} , SER _{102A} , HSD _{103A} , LEU _{106A} , ASP _{126A} , LYS _{127A} , ALA _{130A} , SER _{131A} , TYR _{35B} , TRP _{37B} , GLU _{101B} , LEU _{105B} , ASN _{108B} , ASP _{94C} , PRO _{95C} , VAL _{96C} , LYS _{99C} , THR _{137C} , SER _{138C} , LYS _{139C} , TYR _{140C} , ARG _{141C}	Hydrophobic interactions, hydrogen bonds
HSA-Hb-TcEXA-DOX		VAL _{1A} , LEU _{2A} , LYS _{99A} , LEU _{100A} , SER _{102A} , HSD _{103A} , LEU _{106A} , ASP _{126A} , LYS _{127A} , ALA _{130A} , SER _{131A} , TYR _{35B} , TRP _{37B} , GLU _{101B} , LEU _{105B} , ASN _{108B} , ASP _{94C} , PRO _{95C} , VAL _{96C} , THR _{137C} , SER _{138C} , LYS _{139C} , TYR _{140C} , ARG _{141C}	Hydrophobic interactions, hydrogen bonds
HSA-Hb-TcECD-DOX		VAL _{1A} , LEU _{2A} , LYS _{99A} , LEU _{100A} , SER _{102A} , HSD _{103A} , LEU _{106A} , ASP _{126A} , LYS _{127A} , ALA _{130A} , SER _{131A} , TYR _{35B} , TRP _{37B} , GLU _{101B} , LEU _{105B} , ASN _{108B} , ASP _{94C} , PRO _{95C} , VAL _{96C} , THR _{137C} , SER _{138C} , LYS _{139C} , TYR _{140C} , ARG _{141C}	Hydrophobic interactions, hydrogen bonds
HSA-Hb-TcDMSA-DOX		VAL _{1A} , LEU _{2A} , LYS _{99A} , LEU _{100A} , SER _{102A} , HSD _{103A} , LEU _{106A} , ASP _{126A} , LYS _{127A} , ALA _{130A} , SER _{131A} , TYR _{35B} , TRP _{37B} , GLU _{101B} , LEU _{105B} , ASN _{108B} , ASP _{94C} , PRO _{95C} , VAL _{96C} , THR _{137C} , SER _{138C} , LYS _{139C} , TYR _{140C} , ARG _{141C}	Hydrophobic interactions, hydrogen bonds
HSA-Hb-TcDIS-DOX		PHE _{36A} , LYS _{99A} , LEU _{100A} , SER _{102A} , HSD _{103A} , ASP _{126A} , TYR _{35B} , GLU _{101B} , ARG _{104B} , LEU _{105B} , ASN _{108B} , GLN _{131B} , VAL _{134B} , ALA _{135B} , GLU _{101D}	Hydrophobic interactions, hydrogen bonds
HSA-Hb-TcPER-DOX		VAL _{1A} , LEU _{2A} , LYS _{99A} , LEU _{100A} , SER _{102A} , HSD _{103A} , LEU _{106A} , ASP _{126A} , LYS _{127A} , ALA _{130A} , SER _{131A} , TYR _{35B} , TRP _{37B} , GLU _{101B} , LEU _{105B} , ASN _{108B} , ASP _{94C} , PRO _{95C} , VAL _{96C} , THR _{137C} , SER _{138C} , LYS _{139C} , TYR _{140C} , ARG _{141C}	Hydrophobic interactions, hydrogen bonds
HSA-Hb-TcDTPA-DOX		VAL _{1A} , LEU _{2A} , LYS _{99A} , LEU _{100A} , SER _{102A} , HSD _{103A} , LEU _{106A} , ASP _{126A} , LYS _{127A} , ALA _{130A} , SER _{131A} , TYR _{35B} , TRP _{37B} , GLU _{101B} , LEU _{105B} , ASN _{108B} , ASP _{94C} , PRO _{95C} , VAL _{96C} , THR _{137C} , SER _{138C} , LYS _{139C} , TYR _{140C} , ARG _{141C}	Hydrophobic interactions, hydrogen bonds
HSA-Hb-TcHYN-DOX		VAL _{1A} , LEU _{2A} , LYS _{99A} , LEU _{100A} , SER _{102A} , HSD _{103A} , LEU _{106A} , ASP _{126A} , LYS _{127A} , ALA _{130A} , SER _{131A} , TYR _{35B} , TRP _{37B} , GLU _{101B} , LEU _{105B} , ASN _{108B} , ASP _{94C} , PRO _{95C} , VAL _{96C} , THR _{137C} , SER _{138C} , LYS _{139C} , TYR _{140C} , ARG _{141C}	Hydrophobic interactions, hydrogen bonds
HSA-Hb-TcMEB-DOX		PHE _{36A} , LYS _{99A} , LEU _{100A} , SER _{102A} , HSD _{103A} , ASP _{126A} , TYR _{35B} , GLU _{101B} , ARG _{104B} , LEU _{105B} , ASN _{108B} , GLN _{131B} , VAL _{134B} , ALA _{135B} , GLU _{101D}	Hydrophobic interactions, hydrogen bonds

To assess the feasibility of multimodal imaging, the ternary HSA-Hb-TCC-DOX systems were subsequently docked with four near-infrared dyes: methylene blue (MB), indocyanine green (IG), AK7-5, and squaraine SQ1. The results underscored that the incorporation of Hb reshaped fluorophore binding preferences relative to albumin-only carriers. For MB, the canonical albumin binding site encompassing residues LEU115-ARG186 (site HSA115-186) was preserved in HSA-DOX and HSA-TCC-DOX complexes (Fig. 4). However, in HSA-Hb hybrids, MB predominantly engaged residues from both proteins, suggesting cooperative binding interfaces. Interestingly, MB affinity generally increased in HSA-Hb complexes compared to albumin alone, with exceptions observed in systems containing TcMED, TcEXA, TcDMSA, and TcDTPA.

In contrast, IG exhibited exclusive interactions with Hb, binding primarily within a site composed of 20 amino acids from the A, C, and D subunits (Fig. 5). Moreover, IG affinity was consistently higher in Hb-containing systems compared to albumin, highlighting hemoglobin as a superior scaffold for NIR dye incorporation. A similar trend was observed for the emerging fluorophores AK7-5 and SQ1 (data not shown), whose binding pockets were localized exclusively on Hb subunits.

This preferential dye association with hemoglobin is particularly noteworthy for theranostic design. By concentrating fluorescent reporters on Hb subunits, the hybrid carriers may achieve enhanced optical signal intensity and improved imaging contrast. Additionally, the spatial segregation of DOX and fluorophores within different Hb domains could reduce steric hindrance, ensuring that therapeutic and diagnostic functions are maintained simultaneously.

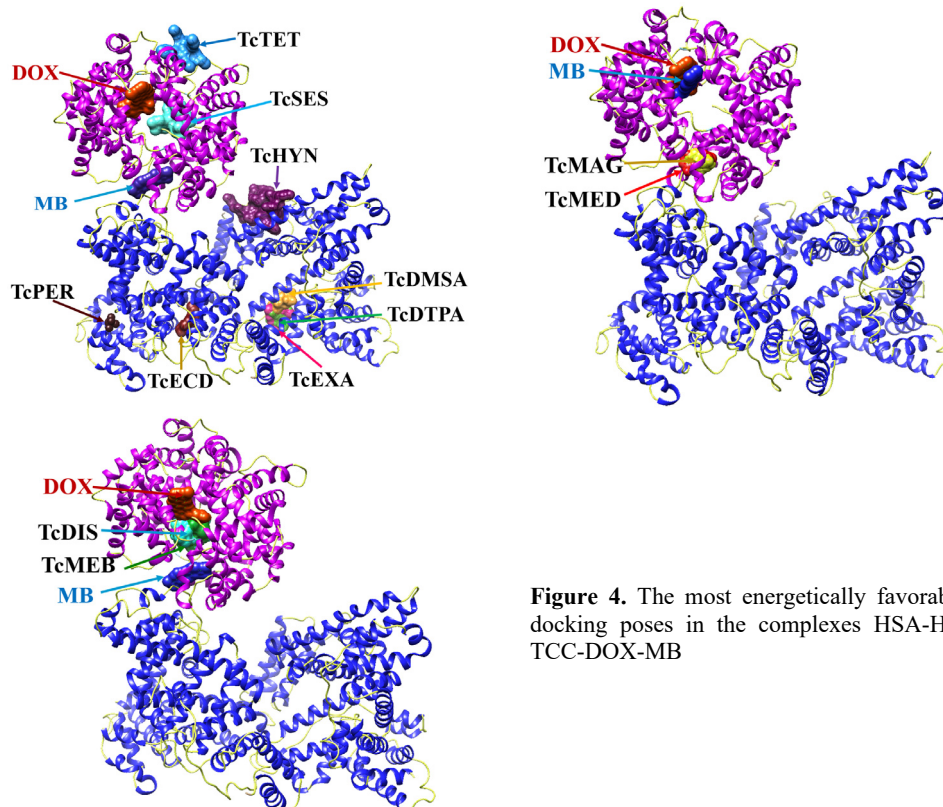


Figure 4. The most energetically favorable docking poses in the complexes HSA-Hb-TCC-DOX-MB

Taken together, these results highlight the transformative role of Hb when integrated with albumin in protein-based carriers. By expanding the available binding landscape, Hb improves affinity for key radiopharmaceuticals (notably TcMEB and TcDIS), provides exclusive and stable pockets for DOX, and preferentially anchors fluorescent dyes. The observed behavior of ligands within the hybrid nanosystems suggest that albumin primarily stabilizes technetium-based radiopharmaceuticals, while hemoglobin serves as the dominant host for DOX and NIR dyes. Such separation may optimize loading efficiency, minimize interference between ligands, and allow simultaneous therapeutic and diagnostic functions.

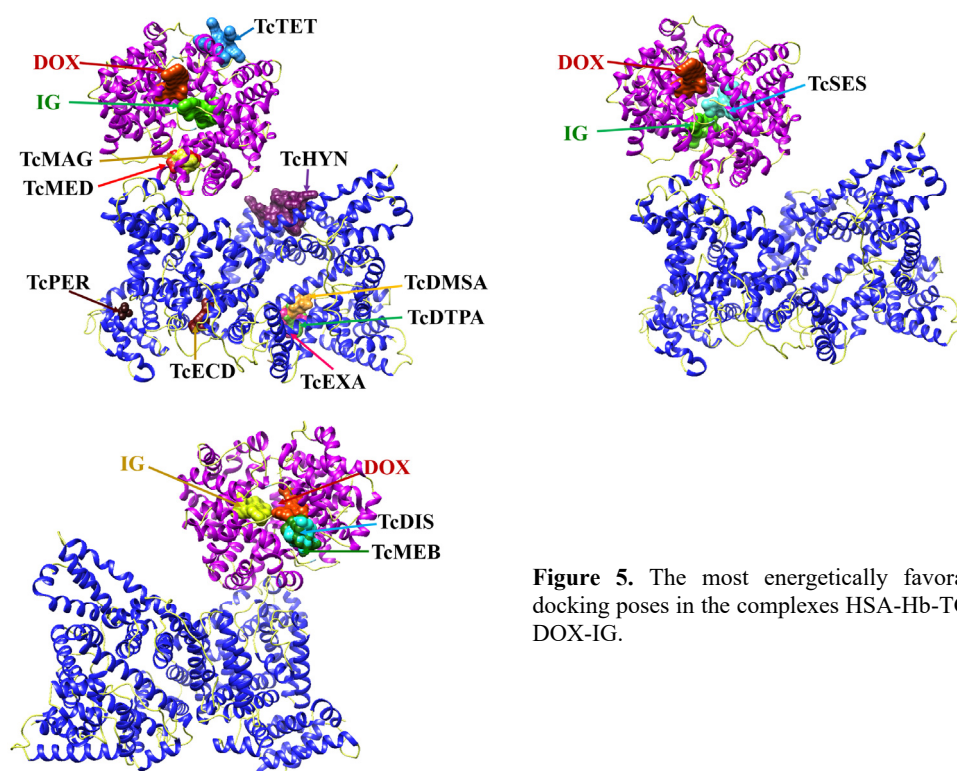


Figure 5. The most energetically favorable docking poses in the complexes HSA-Hb-TCC-DOX-IG.

From a clinical standpoint, HSA–Hb hybrids may offer several advantages over existing platforms. Intrinsic oxygen transport properties of Hb could modulate drug release in hypoxic tumors, addressing one of the most intractable barriers in chemotherapy. The preferential fluorophore binding observed for Hb also suggests superior fluorescence imaging capabilities, which are crucial for real-time surgical navigation and longitudinal monitoring of drug biodistribution. Finally, the strong and specific interactions predicted computationally provide a rationale for experimental development of HSA-Hb carriers as theranostic systems.

Future work should focus on validating these computational findings through experimental assays, including in vitro binding studies, cellular uptake analyses, and in vivo biodistribution imaging. Additionally, the potential immunogenicity and metabolic fate of hemoglobin-based carriers warrant careful evaluation to ensure clinical viability.

CONCLUSIONS

In conclusion, the present study demonstrates that hybrid assemblies of human serum albumin and hemoglobin (HSA-Hb) provide a versatile platform for doxorubicin delivery with integrated radionuclide and fluorescence imaging functionalities. Computational docking revealed that hemoglobin significantly expands the binding landscape, enabling preferential and stronger interactions with several technetium-99m radiopharmaceuticals while also serving as the dominant binding site for both doxorubicin and near-infrared fluorophores. This redistribution of ligand affinities between albumin and hemoglobin reduces competition for binding pockets and allows simultaneous incorporation of therapeutic and diagnostic agents within a single carrier. The spatial separation of ligands across albumin and hemoglobin subunits suggests a functional complementarity that could enhance drug stability, facilitate controlled release under tumor-specific conditions, and improve imaging contrast for multimodal theranostics. Taken together, our findings highlight HSA-Hb systems as promising candidates for the rational design of next-generation protein-based nanocarriers that combine therapeutic efficacy with real-time monitoring, paving the way for their further experimental validation and translational development.

Acknowledgements

This work was supported by the Ministry of Education and Science of Ukraine (Project No. ДЗ/174-2025).

ORCID

Valeriya Trusova, <https://orcid.org/0000-0002-7087-071X>; Uliana Malovytsia, <https://orcid.org/0000-0002-7677-0779>
Galyna Gorbenko, <https://orcid.org/0000-0002-0954-5053>; Andrey Zelinsky, <https://orcid.org/0000-0002-4110-8523>
Borys Borts, <https://orcid.org/0000-0002-1492-4066>; Pylyp Kuznietsov, <https://orcid.org/0000-0001-8477-1395>
Ivan Yakymenko, <https://orcid.org/0000-0002-0194-8376>

REFERENCES

- [1] C. Ferraro, M. Dattilo, F. Patitucci, S. Prete, G. Scopelliti, O. Parisi, and F. Puoci, *Pharmaceutics*, **16**, 1172 (2024). <https://doi.org/10.3390/pharmaceutics16091172>
- [2] J. Gao, J. Karp, R. Langer, and N. Joshi, *Chem Mater.* **35**, 359 (2023). <https://doi.org/10.1021/acs.chemmater.2c03003>
- [3] A. Prajapati, E. Garcia-Garrido, and A. Somoza, *Cancers (Basel)*. **13**, 3011 (2021). <https://doi.org/10.3390/cancers13123011>
- [4] A. Spada, J. Emami, J. Tuszynski, and A. Lavasanifar, *Mol. Pharmaceut.* **18**, 1862 (2021). <https://doi.org/10.1021/acs.molpharmaceut.1c00046>
- [5] V. Trusova, U. Tarabara, I. Karnaukhov, A. Zelinsky, B. Borts, I. Ushakov, L. Sidenko, and G. Gorbenko, *East Eur. J. Phys.* (4), 447 (2024). <https://doi.org/10.26565/2312-4334-2024-4-54>
- [6] V. Trusova, U. Malovytsia, P. Kuznietsov, I. Karnaukhov, A. Zelinsky, B. Borts, I. Ushakov, L. Sidenko, and G. Gorbenko, *East Eur. J. Phys.* (1), 376 (2025). <https://doi.org/10.26565/2312-4334-2025-1-46>
- [7] V. Trusova, U. Malovytsia, P. Kuznietsov, I. Karnaukhov, A. Zelinsky, B. Borts, I. Ushakov, L. Sidenko, and G. Gorbenko, *East Eur. J. Phys.* (2), 398 (2025). <https://doi.org/10.26565/2312-4334-2025-2-48>
- [8] J. Lukin, and C. Ho, *Chem. Rev.* **104**, 1219 (2004). <http://dx.doi.org/10.1021/cr940325w>
- [9] M.F. Adasme, K.L. Linnemann, S.N. Bolz, F. Kaiser, S. Salentin, V.J. Haupt, and M. Schroeder, *Nucl. Acids Res.* **49**, W530-W534 (2021). <https://doi.org/10.1093/nar/gkab294>

КОМП'ЮТЕРНЕ ДОСЛІДЖЕННЯ СИСТЕМ ДОСТАВКИ ЛІКІВ З РАДІОНУКЛІДНИМИ ТА ФЛЮОРЕСЦЕНТНИМИ МОДАЛЬНОСТЯМИ ВІЗУАЛІЗАЦІЇ.

IV. СИСТЕМИ НА ОСНОВІ АЛБУМІНУ ТА ГЕМОГЛОБІНУ ДЛЯ ДОСТАВКИ ДОКСОРУБІЦИНУ

В. Трусова^а, У. Маливиця^а, П. Кузнєцов^б, І. Якименко^б, І. Карнаухов^с, А. Зелінський^с, Б. Борц^с,
І. Ушаков^с, Л. Сіденко^с, Г. Горбенко^а

^аКафедра медичної фізики та біомедичних нанотехнологій, Харківський національний університет імені В.Н. Каразіна
м. Свободи 4, Харків, 61022, Україна

^бКафедра фізики ядра та високих енергій імені О.І. Ахієзера, Харківський національний університет імені В.Н. Каразіна
м. Свободи 4, Харків, 61022, Україна

^сНаціональний науковий центр «Харківський фізико - технічний інститут», Харків, вул. Академічна, 1, 61108, Україна
Розробка мультифункціональних систем доставки лікарських засобів, що поєднують терапевтичні та діагностичні можливості, залишається одним із ключових викликів сучасної онкології. У даній роботі досліджено гібридні носії на основі

сироваткового альбуміну людини та гемоглобіну (HSA-Hb) для доставки доксорубіцину (DOX), що містили радіонуклідні та флуоресцентні молекули-репортери. За допомогою методу молекулярного докінгу було проаналізовано взаємодію комплексів HSA-Hb із дванадцятьма радіофармпрепаратами на основі технецію-99m (^{99m}Tc), DOX та чотирма барвниками ближньої інфрачервоної (NIR) області. Результати показали, що гемоглобін суттєво розширює спектр зв'язування, забезпечуючи унікальні та високоафінні сайти для кількох комплексів ^{99m}Tc (зокрема TcMEB та TcDIS), а також виступає основним матричним білком для DOX і NIR-барвників. Усередині субодиниць Hb були ідентифіковані два окремі сайти зв'язування DOX, що вказує на підвищену стабільність препарату та потенційну чутливість до гіпоксії пухлин. Флуоресцентні барвники, включно з метиленовим синім, індоціаніновим зеленим, AK7-5 та SQ1, демонстрували переважне зв'язування з Hb із більшою спорідненістю, ніж до альбуміну, що свідчить про кращу придатність для оптичної візуалізації. Важливо, що афінність радіофармпрепаратів до альбуміну, а терапевтичних та діагностичних агентів – до гемоглобіну знижувала конкуренцію за сайти зв'язування та забезпечувала одночасну інтеграцію мультимодальних функцій в межах однієї наноплатформи. Отримані результати свідчать, що HSA-Hb наноносії є перспективними кандидатами для створення новітніх тераностичних платформ, що поєднують ефективну доставку DOX з неінвазивним радіонуклідним та флуоресцентним моніторингом.

Ключові слова: *наносистеми доставки ліків на основі білків; людський сироватковий альбумін; гемоглобін; доксорубіцин; комплекси технецію; інфрачервоні барвники; молекулярний докінг*

INFLUENCE OF RADIO-FREQUENCY MAGNETRON SPUTTERING PARAMETERS ON THE STRUCTURE AND PERFORMANCE OF Al AND Al₂O₃ THIN FILMS

 **R. Ramos Blazquez^{a*}**,  **F. Solís-Pomar^{a*}**,  **A. Fundora^b**,  **M.A. Ruiz-Robles^a**, Amilkar Fragiél^c,
 **Eduardo Pérez-Tijerina^a**

^aUniversidad Autónoma de Nuevo León, Centro de Investigación en Ciencias Físico Matemáticas, Facultad de Ciencias Físico-Matemáticas, Av. Universidad S/N. Ciudad Universitaria, 66451, San Nicolás de los Garza, Nuevo León, México

^bInstituto Superior de Tecnologías y Ciencias Aplicadas, Universidad de la Habana,
Ave. Salvador Allende N° 1110 CP 10400, La Habana, Cuba

^cCentro de Física, Instituto Venezolano de Investigaciones Científicas – IVIC, Apartado 20632, Caracas 1020-A, Venezuela

Corresponding Authors E-mail: francisco.solispm@uanl.edu.mx; rmos9708@gmail.com

Received June 13, 2025; revised August 22, 2025; accepted August 28, 2025

In this work, the structural, morphological and optical properties of aluminum (Al) and aluminum oxide (Al₂O₃) thin films deposited by radio-frequency (RF) magnetron sputtering were studied. The films were grown using a high-purity Al target in controlled atmospheres containing varying flows of argon (Ar) and oxygen (O₂). Particular attention was given to how the target-substrate distance and the Ar/O₂ flow ratios influence the films' structural properties, surface features, and optical response. Characterization techniques included X-ray diffraction (XRD) for phase identification and crystallite size estimation, Atomic Force Microscopy (AFM) for surface morphology and roughness analysis, and UV-Vis Spectroscopy for optical transmittance measurements. The results showed that reducing the target-substrate distance led to films with increased surface roughness, thickness, grain size and crystallite size, likely due to enhanced energetic bombardment and adatom mobility. Optical measurements revealed that Al₂O₃ films grown at higher O₂ flow rates (around 5 sccm) were highly transparent, exhibiting transmittance values close to 100% across the UV-visible range (190-900 nm). In contrast, films deposited under low O₂ flow conditions (0.6-1.4 sccm) were nearly opaque, indicating incomplete oxidation or metallic behavior. The XRD analysis revealed that higher O₂ flows tended to suppress crystallinity, resulting in amorphous Al₂O₃ films, while lower flows preserved some degree of crystalline order. Additionally, increasing the Ar flow rate during deposition promoted films growth, as evidenced by increased film thickness, which may be attributed to enhanced sputtering efficiency and target atom flux. These findings highlight the critical role of deposition parameters in tailoring the properties of Al-based thin films for optical and electronic applications.

Keywords: Aluminum; Thin films; Magnetron sputtering; Target-substrate distance; Ar flow rate

PACS: 81.15.Cd, 68.37.Ps, 61.05.cp, 78.66.Bz

INTRODUCTION

In recent years, thin film technology has emerged as a significant research area worldwide, driving the development of innovative techniques for film growth [1]. The structural properties of thin films depend on their synthesis method, with a preference in the literature for physical methods, primarily thermal and vapor deposition [1]. Physical deposition methods produce films with higher adhesion and require lower substrate temperatures. In contrast, the main drawback of chemical methods is their reliance on toxic solvents [2]. The properties of the resulting films depend on the deposition conditions used; in sputtering, these conditions include power [3,4,5], deposition time [6,7], working pressure, gases used [8-10], substrate temperature [11,3], target-substrate distance [12, 13], and other factors.

Metallic coatings are versatile and suitable for a diverse range of applications. Pure metals such as aluminum, nickel, tungsten, and titanium are commonly used in optical and energy applications [14,15].

Al₂O₃ films are frequently applied in various fields, including optics [8], cutting tool applications [16], and as insulating layers in gate dielectric components [17]. Due to their low refractive index and high optical transparency, alumina films are often utilized as anti-reflective coatings in solar cells [18].

In solar-to-thermal conversion, the selective solar absorber plays a crucial role by efficiently absorbing solar radiation over a broad wavelength range while minimizing infrared re-radiation as the absorber's temperature increases [19–21]. To enhance the thermal stability of selective solar absorber multilayers, Al₂O₃ layers have been used in [22] via atomic layer deposition (ALD) to suppress metal atom diffusion from the underlying reflective layer.

Al₂O₃ also has significant potential as a coating in thermonuclear fusion applications due to its high permeation reduction factor (PRF), good irradiation resistance, compatibility with Pb-Li, and strong corrosion resistance, mechanical durability, and wear resistance [23, 24].

Magnetron sputtering technology enables the deposition of thin films over large areas with high deposition rates and good adhesion, making it a preferred method for producing thin-film metallic coatings with less environmental impact than chemical methods [25].

To optimize the application of these films and coatings, it is essential to understand how deposition conditions affect their properties. The impact of sputtering power on film properties has been widely studied [1,4,5]. In this article, we

investigate the relationship between target-substrate distance, Ar and O₂ flow rates, and the resulting morphological, crystallographic, and optical properties of the films.

METHODOLOGY

Thin film synthesis

The films were deposited onto glass substrates by magnetron sputtering using a 13.56 MHz radio-frequency (RF) source with an Al target in an environment of high-purity Ar (99.999%) and O₂. The Al target, 99.99% pure, measured 2 inches in diameter and 0.25 inches in thickness and was cleaned by pre-sputtering for 40 minutes. The substrate surfaces were treated with Ar before deposition. A base pressure of 3.5×10^{-5} Torr was achieved using a mechanical pump and a turbomolecular pump.

For the characterization of the films by X-ray diffraction (XRD), an X'Pert³ Powder diffractometer was used at 45 kV and 40 mA with a wavelength of $\lambda = 1.5406 \text{ \AA}$. Data processing was performed using the X'Pert HighScore Plus software, and the patterns were indexed with assistance from the International Center for Diffraction Data (ICDD) database. Crystallite size calculations were performed using the Scherrer equation.

Atomic force microscopy (AFM) results were obtained with a Park Systems Corp. NX10 microscope in non-contact mode, equipped with an SiO₂ tip. Optical characterization was performed using a Jasco V-750 UV-Vis spectrophotometer over a wavelength range of 190-900 nm.

Table 1 presents the deposition conditions used for Al and Al₂O₃ thin films, illustrating the various parameters employed to investigate the effects of target-substrate distance, as well as argon and oxygen flow rates.

Table 1. Deposition parameters for Al and Al₂O₃ thin films synthesized by RF magnetron sputtering.

Deposition Parameter	Al films (Target-substrate distance study)	Al films (Ar flow study)	Al ₂ O ₃ films (O ₂ flow study)
Target-substrate distance (cm)	6, 9, 12	9	9
Argon Flow rate (sccm)	40	20, 40, 60	50
Oxygen Flow rate (sccm)			0.6, 1.0, 1.4, 5.0
Working pressure (mTorr)	5.0	3.5, 5.0, 7.0	5.0, 5.1, 5.2, 5.5
Deposition time (min)	15	15	30
Power (W)	150	150	270

RESULTS AND DISCUSSION

Al thin film grown at different target-substrate distances

The AFM technique enabled us to characterize the surface and thickness of the films. **Figure 1** displays the 2D AFM images of the films, while **Figure 2** illustrates the dependence of roughness and thickness on the target-substrate distance.

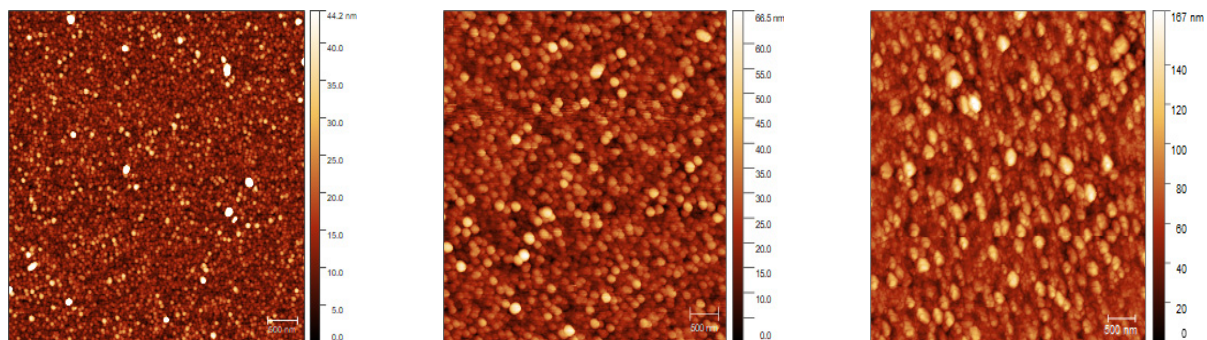


Figure 1. 2D AFM images of films grown (from left to right) at: 12, 9 and 6 cm target-substrate distance, the root mean square roughness turned out to be: 6.3, 8.0 and 20.4 nm, respectively

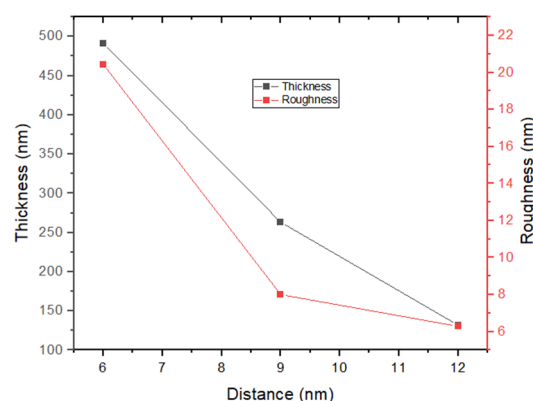


Figure 2. Decrease in the thickness and roughness of the films by increasing the target-substrate distance.

As shown in Figures 1 and 2, roughness, grain size, and thickness decrease as the target-substrate distance increases (**Table 2**). With a greater target-substrate distance, the eroded atoms travel farther before deposition, resulting in an increased number of collisions along their trajectory. This reduces both the kinetic energy with which they reach the substrate or growing film and the number of atoms that complete the entire path to deposition [26, 27].

Statistical analysis was conducted to quantify the increase in grain size, using the software XEI from Park Systems.

Table 2. Summary of AFM results for film characterization

Target-substrate distance (cm)	6	9	12
Thickness (nm)	491	263	132
Deposition rate (nm/min)	32.7	17.5	8.8
Root mean square roughness (nm)	20.4	8.0	6.3
Average grain length (nm)	155	125	90
Average grain perimeter (nm)	468	390	271

The diffraction patterns of the films grown at different target-substrate distances were analyzed. Using X'Pert HighScore Plus software and the Scherrer equation, the crystallite size was calculated for each family of planes present in the pattern.

Figure 3 shows the obtained diffraction patterns. These correspond to a cubic system with space group Fm-3m. As shown in the graph, decreasing the target-substrate distance results in higher peak intensities, which reflects an improved signal-to-noise ratio. This makes the fluctuations less noticeable, giving the diffraction lines a clearer and sharper appearance. This effect can be attributed to a higher deposition rate and larger crystallite formation at shorter distances. The increased kinetic energy of aluminum atoms enhances their mobility on the surface and along grain boundaries, promoting grain coalescence and growth [27].

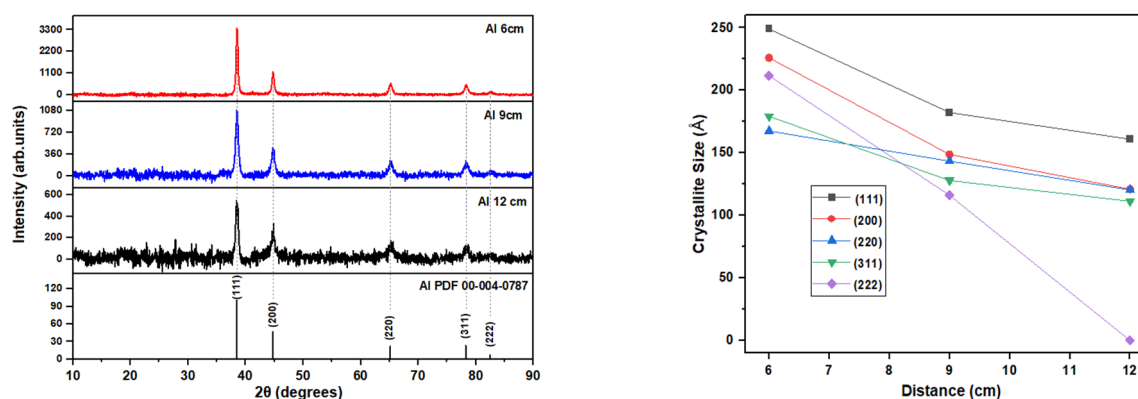


Figure 3. XRD patterns and decrease in crystallite size with the increasing in target-substrate distance for Al thin films

Al thin films grown at different Ar flow rates

Figure 4 shows the 2D AFM images obtained for these films, along with the root mean square roughness. The roughest film, as well as the one with the largest grain size, was obtained with 40 sccm of Ar (**Table 3**).

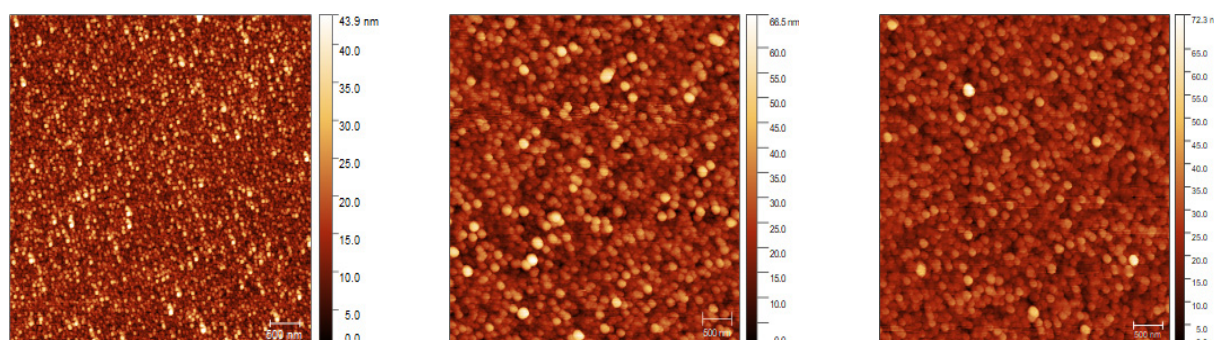


Figure 4. 2D AFM images of films grown (from left to right) at: 20, 40 and 60 sccm of Ar flow rate, the root mean square roughness was found to be: 5.8, 8.0 and 6.6 nm, respectively

Figure 5 shows an increase in thickness with the Ar flow rate. As the argon flow rate increases, a greater number of atoms are sputtered from the target, generally leading to an increase in thickness. However, when the argon flow becomes too high, the mean free path of the sputtered particles is reduced due to more frequent collisions, which can limit their ability to reach the substrate and consequently reduce the films thickness [28, 29]. Therefore, the thickness of the Al films is a competition of the above-mentioned effects. A decrease in roughness for the film grown at 60 sccm is also observed

in Figure 5. Similar behavior was reported by Chavan et al [28] in RF-sputtered Mo thin films. At 60 sccm, the higher flow reduces adatom energy and surface mobility, which limits the formation of large islands and promotes more uniform layer-by-layer growth, resulting in smoother films and lower roughness compared to 40 sccm, where higher mobility favors larger grains and a rougher surface.

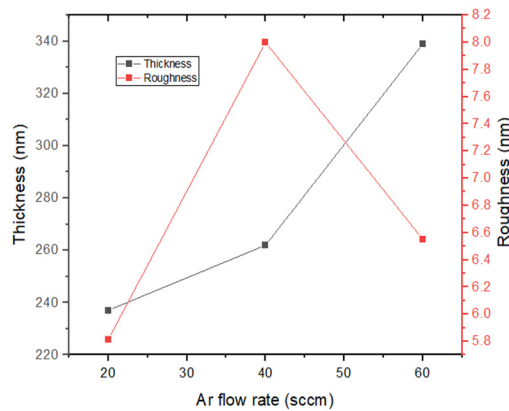


Figure 5. Behavior of the thickness and roughness of the films grown at different Ar fluxes.

Table 3. Summary of AFM results for film characterization.

Ar flow rate (sccm)	20	40	60
Thickness (nm)	237	263	339
Deposition rate (nm/min)	15.8	17.5	22.6
Root mean square roughness (nm)	5.8	8.0	6.6
Average grain length (nm)	102	125	119
Average grain perimeter (nm)	282	390	377

Figure 6 shows the diffraction patterns obtained. The film synthesized at 40 sccm of Ar exhibits a larger grain size, which translates into an improvement in crystalline properties, such as crystallite size (Figure 8). An analogous behavior in crystallite size was observed by Akhtaruzzaman et al. [30] in their study of WS₂ films deposited at different argon flow rates. The XRD peak intensities are governed by a combination of factors [31]. At low Ar flow (20 sccm), smoother surfaces and higher adatom mobility enhance coherent diffraction, producing the highest intensities. At 40 sccm, larger crystallites and good texture maintain relatively high peaks despite higher roughness, while at 60 sccm, defects and reduced mobility lower the peak intensities even for thicker films.

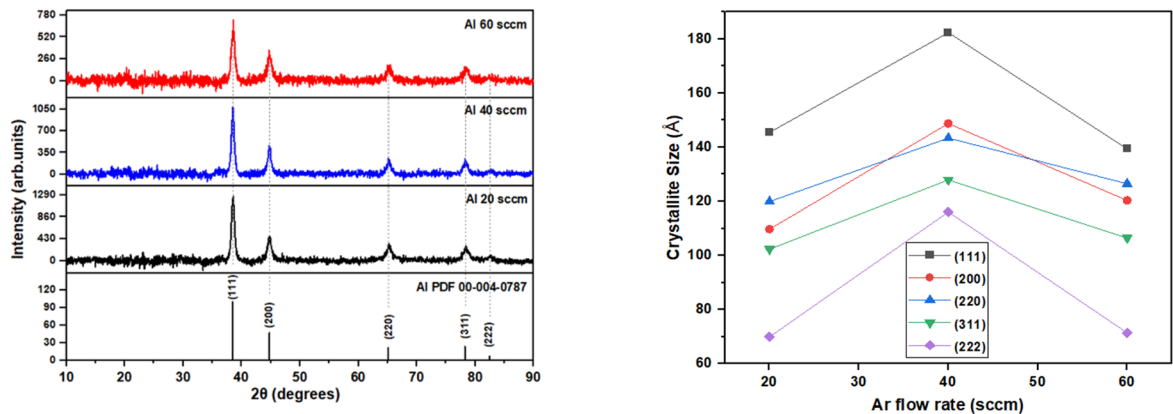


Figure 6. XRD patterns of Al samples grown at different Ar fluxes

Al₂O₃ thin films grown at different O₂ flow rates

The crystalline properties of Al₂O₃ films grown with an Al target in an Ar and O₂ environment, at different O₂ flow rates, were studied. Table 1 shows the deposition parameters used.

Figure 7 shows the obtained diffraction patterns, where we can observe a considerable decrease in crystalline properties as the amount of oxygen increases. The structural evolution of the films with oxygen flow can be described as follows: the samples grown at 0.6 and 1.0 sccm exhibit clear diffraction peaks corresponding to metallic Al, indicating that these films are crystalline. The sample deposited at 1.4 sccm shows weaker and broader peaks, consistent with a significant reduction in crystallite size and amorphization due to the incorporation of oxygen. Finally, the film grown at 5.0 sccm exhibits no discernible diffraction peaks, indicating a fully amorphous structure. In addition, a slight angular

shift of the diffraction peaks was observed, which can be attributed to changes in the lattice parameters. This progressive loss of crystallinity and peak displacement are expected, as oxygen incorporation disrupts the ordered arrangement of Al atoms in the metallic lattice and promotes the formation of an amorphous Al-O network. [32, 33].

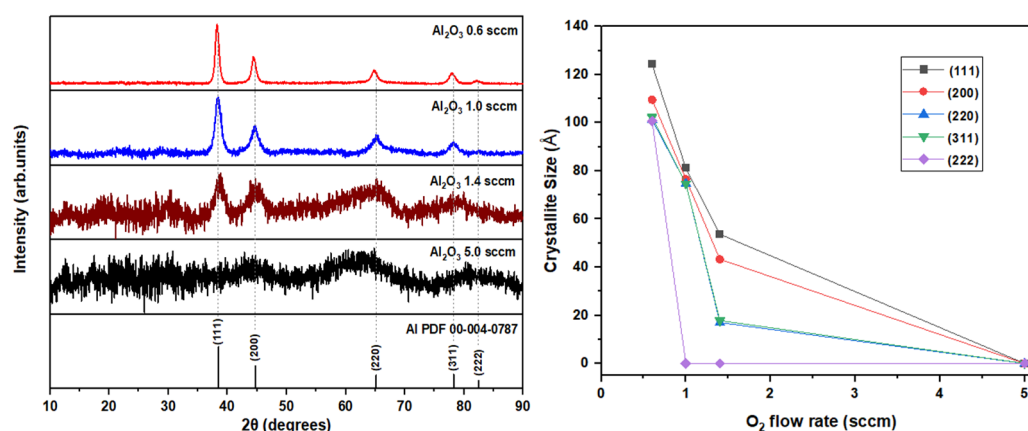


Figure 7. XRD patterns of Al_2O_3 samples grown at different O_2 flow rates. Decrease in crystallite size with increasing O_2 flow rate.

The optical properties of these films strongly depend on the O_2 flow rate. In **Figure 8**, we can observe that the film grown at the highest oxygen flow rate (5 sccm) has a transmittance of almost 100%, while the films synthesized at 0.6, 1.0, and 1.4 sccm have almost 0% transmittance across the range 290-900 nm and decreasing from $\approx 8\%$ to nearly 0% in the 190-290 nm range. These values reflect the strong absorption of the films. The spectral shape is further modulated by the onset of absorption in the glass substrate, which produces small oscillations in this range. Such oscillations are also visible for the 5 sccm sample despite its high transparency.

The depression in transmittance near 300 nm for the film grown at 5 sccm is consistent with interference in the near-UV and is mainly attributed to thin-film optical interference (film/substrate coupling). This interpretation is supported by the calculation of an interference minimum at 300 nm for a film thickness of 132.4 nm, which closely matches the experimental thickness of our film (133.8 nm).

The thickness of the samples was measured using the height difference between the film and the substrate in AFM. As shown in **Figure 9**, the film thickness decreases as the O_2 flow rate increases. At low O_2 flows, the aluminum target remains largely metallic, allowing a high sputtering yield and resulting in thicker films. As the O_2 flow increases, a layer of aluminum oxide forms on the target surface, which has a much lower sputtering yield compared to metallic Al. Although RF sputtering allows stable plasma operation even when the target becomes partially insulating, the deposition rate still decreases significantly because the sputtering efficiency of the oxidized target is lower. This process is known as poisoned target effect in reactive sputtering [34]. Consequently, films deposited under higher O_2 flow are thinner.

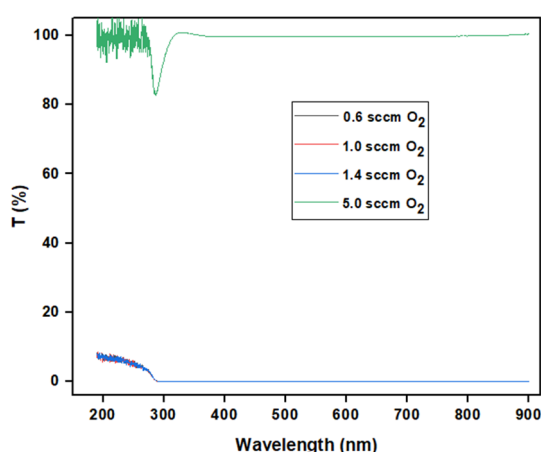


Figure 8. Transmittance of Al_2O_3 films grown at different O_2 flow rates

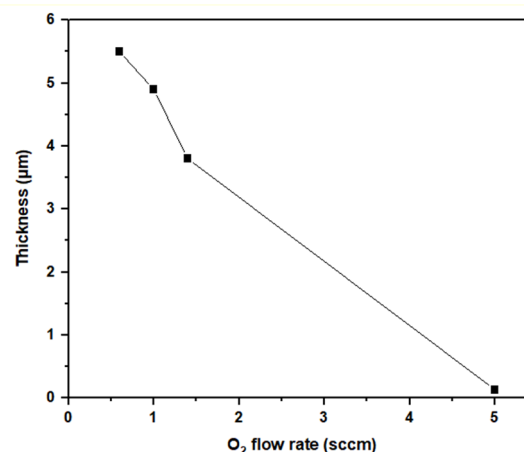


Figure 9. Behavior of the thickness of the Al_2O_3 films grown at different O_2 fluxes

CONCLUSIONS

In this work, Al and Al_2O_3 films were deposited by magnetron sputtering with a radio-frequency source. For the Al films, we used an Ar environment, while for the Al_2O_3 films, a mixture of Ar and O_2 was used. In the first case, we studied the influence of the target-substrate distance (6, 9, 12 cm) on the morphological and crystallographic properties of the films. AFM analysis revealed an increase in roughness, thickness, and grain size as the target-substrate distance decreased. XRD results showed that the crystalline properties of the samples improved as the target was brought closer to the

substrate, which is associated with the intentional increase in substrate temperature and grain fusion, contributing to the formation of a more uniform crystalline structure with fewer grain boundaries.

In the second case, we examined the influence of Ar flow rate (20, 40, 60 sccm). The film grown at 40 sccm was the roughest, with the largest grain and crystallite size. Furthermore, increasing the Ar flow rate led to an increase in film thickness.

For the Al_2O_3 samples, we studied the influence of O_2 flow rate, using a fixed Ar flow of 50 sccm while varying the O_2 flow (0.6, 1.0, 1.4, 5.0 sccm). We observed a significant decrease in crystalline properties as the oxygen flow increased, due to the introduction of oxygen atoms disrupting the orderly arrangement of atoms in the crystal lattice. The film grown at the highest oxygen flow exhibited a transmittance of almost 100%, while the films synthesized at 0.6, 1.0 and 1.4 sccm showed nearly 0% transmittance across the 290–900 nm range. In addition, the film thickness decreased with increasing O_2 flow due to the poisoning of the target during reactive sputtering.

Acknowledgements

R. Ramos Blazquez acknowledges CONAHCYT for his master studies scholarship (843048).

ORCID

✉ R. Ramos Blazquez, <https://orcid.org/0009-0008-6274-7640>; ✉ F. Solis-Pomar, <https://orcid.org/0000-0002-4536-6538>
✉ A. Fundora, <https://orcid.org/0000-0001-8809-7529>; ✉ M. A. Ruiz-Robles, <https://orcid.org/0000-0003-4834-8025>
✉ E. Pérez-Tijerina, <https://orcid.org/0000-0001-9742-4093>

REFERENCES

- [1] F.M. Mwema, O.P. Oladijo, S.A. Akinlabi, and E.T. Akinlabi, “Properties of physically deposited thin aluminium film coatings: A review,” *Journal of Alloys and Compounds*, **747**, (2018) 306–323. <https://doi.org/10.1016/j.jallcom.2018.03.006>
- [2] J. Tao, J. Liu, L. Chen, H. Cao, X. Meng, Y. Zhang, C. Zhang, *et al.*, “7.1% efficient Co-electroplated $\text{Cu}_2\text{ZnSnS}_4$ thin film solar cells with sputtered CdS buffer layers,” *Green Chem.* **18**(2), 550–557 (2016). <https://doi.org/10.1039/C5GC02057C>
- [3] S. Ponmudi, R. Sivakumar, C. Sanjeeviraja, and C. Gopalakrishnan, “Influences of sputtering power and annealing temperature on the structural and optical properties of $\text{Al}_2\text{O}_3\text{:CuO}$ thin films fabricated by radio-frequency magnetron sputtering technique,” *Journal of Materials Science: Materials in Electronics*, **30**, 18315–18327 (2019). <https://doi.org/10.1007/s10854-019-02185-0>
- [4] M. Lee, *et al.*, “Influence of sputtering conditions on the properties of aluminum-doped zinc oxide thin film fabricated using a facing target sputtering system,” *Thin Solid Films*, **703**, 137980 (2020). <https://doi.org/10.1016/j.tsf.2020.137980>
- [5] S. Asgary, *et al.*, “Magnetron sputtering technique for analyzing the influence of RF sputtering power on microstructural surface morphology of aluminum thin films deposited on SiO_2/Si substrates,” *Applied Physics A*, **127**, 752 (2021). <https://doi.org/10.1007/s00339-021-04892-0>
- [6] A. Tchenka, *et al.*, “Effect of RF sputtering power and deposition time on optical and electrical properties of indium tin oxide thin film,” *Advances in Materials Science and Engineering*, **2021**(1), 5556305 (2021). <https://doi.org/10.1155/2021/5556305>
- [7] V. Karoutsos, *et al.*, “On the Effect of Randomly Oriented Grain Growth on the Structure of Aluminum Thin Films Deposited via Magnetron Sputtering,” *Coatings*, **14**, 1441 (2024). <https://doi.org/10.3390/coatings14111441>
- [8] M. Akhtaruzzaman, M. Shahiduzzaman, N. Amin, G. Muhammad, M.A. Islam, K.S.B. Rafiq, and K. Sopian, “Impact of Ar flow rates on micro-structural properties of WS₂ thin film by RF magnetron sputtering,” *Nanomaterials*, **11**(7), 1635 (2021). <https://doi.org/10.3390/nano11071635>
- [9] J. Wang, *et al.*, “Enhanced formation of $\alpha\text{-Al}_2\text{O}_3$ at low temperature on Cr/Al coating by controlling oxygen partial pressure,” *Applied Surface Science*, **515**, 146053 (2020). <https://doi.org/10.1016/j.apsusc.2020.146053>
- [10] M.K. Sandager, C. Kjeldse, and V. Popok, “Growth of thin AlN films on Si wafers by reactive magnetron sputtering: Role of processing pressure, magnetron power and nitrogen/argon gas flow ratio,” *Crystals*, **12**(10), 1379 (2022). <https://doi.org/10.3390/cryst12101379>
- [11] Y. Gao, H. Leiste, S. Heissler, S. Ulrich, and M. Stueber, “Optical properties of radio-frequency magnetron sputtered $\alpha\text{-(Cr}_{1-x}\text{Al}_x)_2\text{O}_3$ thin films grown on $\alpha\text{-Al}_2\text{O}_3$ substrates at different temperatures,” *Thin Solid Films*, **660**, 439–446 (2018). <https://doi.org/10.1016/j.tsf.2018.06.053>
- [12] G. Zhu, Y. Yang, B. Xiao, and Z. Gan, “Evolution Mechanism of Sputtered Film Uniformity with the Erosion Groove Size: Integrated Simulation and Experiment,” *Molecules*, **28**(22), 7660 (2023). <https://doi.org/10.3390/molecules28227660>
- [13] Z. Wei, L. Shen, Y. Kuang, J. Wang, G. Yang, and W. Lei, “The evolution of preferred orientation and morphology of AlN films under various sputtering parameters,” *Journal of Crystal Growth*, **625**, 127439 (2024). <https://doi.org/10.1016/j.jcrysgro.2023.127439>
- [14] A. Baptista, *et al.*, “Sputtering Physical Vapour Deposition (PVD) Coatings: A Critical Review on Process Improvement and Market Trend Demands,” *Coatings*, **8**, 402 (2018). <https://doi.org/10.3390/coatings8110402>
- [15] J. Cheng, *et al.*, “Research on magnetron sputtering thin films as electrode materials for supercapacitors,” *Chemical Engineering Journal*, **509**, 161242 (2025). <https://doi.org/10.1016/j.cej.2025.161242>
- [16] M. Singh, *et al.*, “Deposition and Characterization of Aluminium Thin film Coatings using DC Magnetron Sputtering Process,” *Materials Today: Proceedings*, **5**, 2696–2704 (2018). <https://doi.org/10.1016/j.matpr.2018.01.050>
- [17] Y. Gao, *et al.*, “The process of growing Cr_2O_3 thin films on $\alpha\text{-Al}_2\text{O}_3$ substrates at low temperature by r.f. magnetron sputtering,” *Journal of Crystal Growth*, **457**, 158–163 (2017). <https://doi.org/10.1016/j.jcrysgro.2016.08.009>
- [18] J. Cheng Ding, *et al.*, “Low-temperature deposition of nanocrystalline Al_2O_3 films by ion source-assisted magnetron sputtering,” **149**, 284–290 (2018). <https://doi.org/10.1016/j.vacuum.2018.01.009>
- [19] K.C. Chung, and W.-H. Lee, “Effect of pretreatment on Al_2O_3 substrate by depositing Al_2O_3 film on the properties of Ni–Cr–Si based thin film resistor,” *Materials Chemistry and Physics*, **234**, 311–317 (2019). <https://doi.org/10.1016/j.matchemphys.2019.05.058>
- [20] Y. Ning, *et al.*, “NiCrAlO/ Al_2O_3 solar selective coating prepared by direct current magnetron sputtering and water boiling,” *Solar Energy Materials and Solar Cells*, **219**, 110807 (2021). <https://doi.org/10.1016/j.solmat.2020.110807>

- [21] Y. Wu, *et al.*, “Enhanced thermal stability of the metal/dielectric multilayer solar selective absorber by an atomic-layer-deposited Al_2O_3 barrier layer,” *Applied Surface Science*, **541**, 148678 (2021). <https://doi.org/10.1016/j.apsusc.2020.148678>
- [22] P. Li, *et al.*, “Copper-Doped Chromium Oxide Hole-Transporting Layer for Perovskite Solar Cells: Interface Engineering and Performance Improvement,” *Adv. Mater. Interfaces*, **3**, 1500799 (2016). <https://doi.org/10.1002/admi.201500799>
- [23] E.B. Kashkarov, D.V. Sidelev, M. Rombaeva, M.S. Syrtanov, and G.A. Bleykher, “Chromium coatings deposited by cooled and hot target magnetron sputtering for accident tolerant nuclear fuel claddings,” *Surface & Coatings Technology*, **389**, 125618 (2020). <https://doi.org/10.1016/j.surfcoat.2020.125618>
- [24] S. Ozen, V. Senay, “Optical, Morphological and Nano-Mechanical Properties of Chromium Oxide Thin Films Fabricated by Radio-Frequency (RF) Magnetron Sputtering,” *Optik*, **201**, 163433 (2020). <https://doi.org/10.1016/j.ijleo.2019.163433>
- [25] J. Li, *et al.*, “Facilitating Complex Thin Film Deposition by Using Magnetron Sputtering: A Review,” *JOM*, **74**, 3069–3081 (2022). <https://doi.org/10.1007/s11837-022-05294-0>
- [26] *Handbook of thin film deposition*, edited by K. Seshan, and D. Schepis, (William Andrew, 2018).
- [27] J.A. Lenis, M.A. Gómez, and F.J. Bolívar, “Effect of deposition temperature and target-substrate distance on the structure, phases, mechanical and tribological properties of multi-layer HA Ag coatings obtained by RF magnetron sputtering,” *Surface & Coatings Technology*, **378**, 124936 (2019). <https://doi.org/10.1016/j.surfcoat.2019.124936>
- [28] P. Yi, W. Zhang, F. Bi, L. Peng, and X. Lai, “Microstructure and properties of a-C films deposited under different argon flowrate on stainless steel bipolar plates for proton exchange membrane fuel cells,” *Journal of Power Sources*, **410–411**, 188–195 (2019). <https://doi.org/10.1016/j.jpowsour.2018.10.054>
- [29] K.B. Chavan, S.V. Desarada, and N.B. Chaure, “Influences of substrate temperature and Ar flow on the properties of RF sputtered Mo thin films,” *Journal of Materials Science: Materials in Electronics*, **31**(13), 10306–10314 (2020). <https://doi.org/10.1007/s10854-020-03578-2>
- [30] Md. Akhtaruzzaman, *et al.*, “Impact of Ar Flow Rates on Micro-Structural Properties of WS_2 Thin Film by RF Magnetron Sputtering,” *Nanomaterials*, **11**, 1635 (2021). <https://doi.org/10.3390/nano11071635>
- [31] H. Khan, A.S. Yerramilli, A. D'Oliveira, T.L. Alford, D.C. Boffito, and G.S. Patience, “Experimental methods in chemical engineering: X-ray diffraction spectroscopy—XRD,” *The Canadian journal of chemical engineering*, **98**(6), 1255–1266 (2020). <https://doi.org/10.1002/cjce.23747>
- [32] M. Sowjanya, *et al.*, “Impact of Ar:O₂ gas flow ratios on microstructure and optical characteristics of CeO₂-doped ZnO thin films by magnetron sputtering,” *EPL*, **135**, 67003 (2021). <https://doi.org/10.1209/0295-5075/ac2d55>
- [33] G. Angarita, C. Palacio, M. Trujillo, and M. Arroyave, “Synthesis of alumina thin films using reactive magnetron sputtering method,” *Journal of Physics: Conference Series*, **850**(1), 012022 (2017). <https://doi.org/10.1088/1742-6596/850/1/012022>
- [34] M. Arif, and C. Eisenmenger-Sittner, „In situ assessment of target poisoning evolution in magnetron sputtering,” *Surface and Coatings Technology*, **324**, 345–352 (2017). <https://doi.org/10.1016/j.surfcoat.2017.05.047>

ВПЛИВ ПАРАМЕТРІВ РАДІОЧАСТОТНОГО МАГНЕТРОННОГО РОЗПИЛЕННЯ НА СТРУКТУРУ ТА ХАРАКТЕРИСТИКИ ТОНКИХ ПЛІВОК Al ТА Al_2O_3

Р. Рамос Бласкес^a, Ф. Соліс-Помар^a, А. Фундора^b, М.А. Руйс-Роблес^a, Амілкар Фрагіель^c, Едуардо Перес-Тіхеріна^a

^aАвтономний університет Нуево-Леон, Центр досліджень фізико-математичних наук, факультет фізико-математичних наук
Авеню Педро де Альба, Університетське місто, Сан-Ніколас-де-лос-Гарса, Нуево-Леон, 66455, Мексика



^bВищий інститут прикладних наук і технологій Гаванського університету,
пр. Сальвадора Альєнде 1110 CP 10400, Гавана, Куба

^cФізичний центр, Венесуельський інститут наукових досліджень – IVIC, 20632, Каракас 1020-А, Венесуела

У цій роботі досліджувалися структурні, морфологічні та оптичні властивості тонких плівок алюмінію (Al) та оксиду алюмінію (Al_2O_3), нанесених методом радіочастотного (РЧ) магнетронного розпилення. Плівки вирощували з використанням високочистої мішені з Al у контрольованих атмосферах, що містили різні потоки аргону (Ar) та кисню (O_2). Особливу увагу приділяли тому, як відстань між мішенню та підкладкою та співвідношення потоків Ar/O_2 впливають на структурні властивості плівок, особливості поверхні та оптичну реакцію. Методи характеристики включали рентгенівську дифракцію (XRD) для ідентифікації фаз та оцінки розміру кристалітів, атомно-силову мікроскопію (АСМ) для аналізу морфології та шорсткості поверхні, а також УФ-спектроскопію для вимірювання оптичного пропускання. Результати показали, що зменшення відстані між мішенню та підкладкою призводить до отримання плівок зі збільшенням шорсткості поверхні, товщини, розміру зерен та розміру кристалітів, ймовірно, через посилене енергетичне бомбардування та рухливість атомів. Оптичні вимірювання показали, що плівки Al_2O_3 , вирощені при вищих швидкостях потоку O_2 (близько $5 \text{ куб. см}^3/\text{см}^3$), були дуже прозорими, демонструючи значення пропускання близькі до 100% у всьому УФ-видимому діапазоні (190–900 нм). На противагу цьому, плівки, осаджені в умовах низького потоку O_2 (0,6–1,4 $\text{куб. см}^3/\text{см}^3$), були майже непрозорими, що свідчить про неповне окислення або металеву поведінку. Рентгенівський дифракційний аналіз показав, що вищі потоки O_2 мали тенденцію пригнічувати кристалічність, що призводило до аморфних плівок Al_2O_3 , тоді як нижчі потоки зберігали певний ступінь кристалічного порядку. Крім того, збільшення швидкості потоку Ar під час осадження сприяло росту плівок, про що свідчить збільшення товщини плівки, що може бути пов'язано з підвищеною ефективністю розпилення та потоком атомів мішені. Ці результати підкреслюють критичну роль параметрів осадження у визначенні властивостей тонких плівок на основі Al для оптичних та електронних застосувань.

Ключові слова: алюміній; тонкі плівки; магнетронне розпилення; відстань між мішенню та підкладкою; швидкість потоку Ar

EXPLORING PLANE SYMMETRIC SPACE-TIME IN $f(R)$ MODIFIED GRAVITATIONAL THEORY

 **D.V. Dhote^{a*}**,  **S.D. Deo^{b§}**

^aPost Graduate Teaching Department of Mathematics, Gondwana University, Gadchiroli, India

^bMahatma Gandhi College of Science, Gadchandur, India.

*Corresponding Author E-mail: dhanshridhote20@gmail.com; §E-mail: shailendradeo36@gmail.com

Received May 17, 2025; revised July 4, 2025; in final form August 21, 2025; accepted August 23, 2025

This paper investigates a plane symmetric cosmological model (PSCM) in the context of modified $f(R)$ gravity theory, incorporating both vacuum and non-vacuum scenarios. A perfect fluid is assumed as the matter source. To obtain the solutions, we consider the premise of both constant and nonconstant scalar curvature. By applying the conservation law for Einstein's field equation, $T_{ij}^{;j} = 0$, and the power-law assumption, we retrieve some well-known solutions. We solved the field equations by making a specific assumption that involved a transformation $A^2B = U$. This study explores the physical and kinematic characteristics of specific cosmological models, along with an examination of the statefinder diagnostic—a key tool for analysing the Universe's evolutionary trajectory. The work provides important insights into the behaviour of anisotropic models within the context of modified $f(R)$ gravity. It highlights the interplay between matter distribution and spacetime geometry, particularly emphasizing how assuming constant and nonconstant scalar curvature aids in simplifying and solving the corresponding field equations. The resulting solutions enhance our understanding of cosmic evolution governed by modified $f(R)$ gravity.

Keywords: Plane symmetric; $f(R)$ gravitation theory; Perfect fluid; Statefinder; Anisotropic Universe

PACS: 04.20.-q; 04.20. Jb; 04.50. Kd

1. INTRODUCTION

The groundbreaking theory of modern physics called General Theory of Relativity (GR) brings numerous solutions to understand cosmic phenomena. The physical processes which GR explains are numerous yet there exist multiple unresolved astrophysical and cosmic problems outside its existing boundaries. One of the most significant challenges is the observed late-time acceleration of the Universe, which GR alone cannot adequately explain. To address such limitations, researchers have proposed modifications to the Einstein-Hilbert action—the foundational element of GR. Among these modifications, the $f(R)$ theory of gravity stands out. This theory generalizes the Einstein-Hilbert action by introducing a function $f(R)$, where R is the Ricci scalar representing spacetime curvature.

In the past decade, $f(R)$ gravity has become a leading approach to modifying General Relativity (GR). This theory helps scientists find new solutions to describe how the Universe evolves. By adding a function of the Ricci scalar, $f(R)$, to the gravitational action, the theory allows for more flexible models of gravity. These models can explain the observed cosmic acceleration without needing dark energy. $f(R)$ gravity extends GR and offers new ideas for understanding the Universe. A key aim of the theory is to explain both the rapid expansion in the early Universe and the current acceleration in a single framework.

Hans Adolph Buchdahl introduced the $f(R)$ gravity theory in 1970 [1]. Bertolami et al. [2] later extended it by coupling a function of the Ricci scalar R with the matter Lagrangian L_m , while Carroll et al. [3] used it to explain the Universe's late-time acceleration. A fundamentally different image of our Universe has been revealed by astrophysical data from a variety of sources, including Cosmic Microwave Background (CMB) variations [4], type-Ia supernovae experiments [5], X-ray experiments [6], as well as large-scale structure observations [7]. All these data point to a faster expansion of the cosmos.

Some astrophysicists believe that modified gravity theories could explain the phenomena of dark matter (DM) and dark energy (DE), which appear to be causing the continuous expansion of the Universe. Numerous astrophysical models with varying aspects have been developed and analysed over the past decade. Perlmutter et al. [8] provided the first evidence for a Universe with a positive cosmological constant, indicating its expansion, based on observations of 40 high-redshift supernovae. Bamba et al. [9] explored various methods for testing DE and alternative extended gravity models using cosmography. One approach to addressing this problem involves replacing the conventional Einstein-Hilbert action in the standard part of the Einstein field equations with a general function of Ricci Scalar R [10]. Mishra et al. [11] demonstrated a transition from early deceleration to significant late-time acceleration by using different deceleration values with a hybrid scale factor.

The investigation of DE can be examined through its equation of state (EoS) parameter $\omega = \frac{p}{\rho}$. It's important to note that perfect fluid is a significant component of the Universe, undergoes variation and contraction in its action. Fakhreh MD [12], studied the dynamical behaviour of an anisotropic Universe in extended gravity using two cosmological models.

Shamir [13], explored the Plane symmetric model in $f(R)$ gravity, and obtained some well-known solutions. Raut et al. [14], obtained vacuum solutions of plane symmetric model with the help of special form of deceleration parameter (DP) in $f(R)$ gravity theory. Agrawal et al. [15], studied gravitational baryogenesis models' comparison in $f(R)$ gravity by considering perfect fluid as a matter. Singh et al. [16], studied Bianchi type-I five-dimensional cosmological models with massive string in GR and found that sum of energy density and string tension density was null. Agrawal et al. [17], investigated black holes and wormholes by considering spherical symmetric space-time beyond classical GR. Karim MR [18], studied Bianchi type-I model in the context of an anisotropic Universe within the Saez-Ballester theory of gravitation and found the formula for computing the Universe's entropy in terms of viscosity. Al-Haysah and Hasmani [19], assumed $f(R) = R + \alpha R^2$ and obtained the solution for higher dimensional Bianchi type-I cosmological model by considering string as a matter field by combining $f(R)$ gravity theory and Kaluza-Klein (KK) theory. Ladke and Mishra [20,21], studied five-dimensional plane symmetric and static interior plane symmetric solutions in $f(R)$ gravity theory. Thakare et al. [22], derived the precise solutions of non-vacuum, higher-dimensional, plane symmetric model in $f(R, T)$ gravity theory by means of quadratic EoS. Sharma et al. [23], investigates the stability of the transition from early deceleration to recent acceleration in a perfect fluid LRS Bianchi-I cosmological model within $f(R, T)$ theory. Dabre et al. [24], explores a bulk viscous fluid with a cloud of strings using the plane symmetric LRS Bianchi type I metric in the context of $f(R)$ gravity. Pawar et al. [25], explored string cosmological plane symmetric model considering bulk viscosity and find solution using relation between metric potential $B = RA^n$. Turrión et al. [26], studied the physical non-viability of a wide class of $f(R)$ models and their constant-curvature solutions, and show that most $f(R)$ -exclusive constant-curvature solutions also exhibit a variety of unphysical properties. Larranaga A. [27], obtained a rotating charged solution in $f(R)$ theory of gravity with constant curvature representing a black hole. Calza et al. [28], studied vacuum $f(R)$ gravity solutions which are characterized by constant Ricci scalar and investigated black hole solutions in detail.

This paper explores vacuum and non-vacuum solutions for plane symmetric spacetime within the $f(R)$ gravity framework. We obtain general solutions for the field equations of plane symmetric spacetime under the premise of constant and nonconstant scalar curvature. Additionally, we applied Einstein's field equation, $T_{ij}^{ij} = 0$ to solve non-vacuum field equations. The physical behaviour of these solutions is analysed using various physical quantities.

2. $f(R)$ GRAVITATIONAL THEORY

The gravitational $f(R)$ theory is regarded as the best straightforward example of an extended gravity theory, first proposed by Hans Adolph Buchdahl.

The action for $f(R)$ gravity theory is given by [29,30,31],

$$s = \int \sqrt{-g} \left(\frac{1}{16\pi G} f(R) + L_m \right) d^4 x \quad (1)$$

Here, the Lagrangian matter is denoted by L_m , and a function that depends on the Ricci scalar R is represented as $f(R)$. The above action is formulated by simply replacing R with $f(R)$ in the traditional Einstein-Hilbert action expression.

Now, changing (1) with respect to the metric g_{ij} , we obtain

$$F(R)R_{ij} - \frac{1}{2}f(R)g_{ij} - \nabla_i \nabla_j F(R) + g_{ij} \square F(R) = kT_{ij} \quad (2)$$

Here, $F(R) = \frac{df(R)}{dR}$, $\square \equiv g^{ij} \nabla_i \nabla_j$ is the d'Alembert operator, ∇_i represent the covariant derivative operator, T_{ij} denotes the standard matter energy-momentum tensor derived from the Lagrangian L_m and k is the coupling constant in gravitational units.

Solving the above equation (2), we get

$$F(R)R - 2f(R) + 3\square F(R) = kT \quad (3)$$

In vacuum case (i.e., for $T = 0$) equation (3), reduce to

$$F(R)R - 2f(R) + 3\square F(R) = 0 \quad (4)$$

This connection between $f(R)$ and $F(R)$ is crucial for simplifying the field equations. With a constant Ricci scalar $R = R_0$, equation (4) becomes:

$$F(R_0)R_0 - 2f(R_0) = 0 \quad (5)$$

The term "constant curvature condition" describes this situation.

When we simplify equation (3), we obtain

$$f(R) = \frac{F(R)R + 3\square F(R) - kT}{2} \quad (6)$$

Solving equations (2) and (6), we get,

$$\left(\frac{F(R)R - \square F(R) - kT}{4}\right) = \frac{F(R)R_{ij} - \nabla_i \nabla_j F(R) - kT_{ij}}{g_{ij}} \quad (7)$$

As an LHS of equation (7) is not depend on index i , we have

$$K_i = \left(\frac{F(R)R_{ii} - \nabla_i \nabla_i F(R) - kT_{ii}}{g_{ii}}\right) \quad (8)$$

Where, $K_i - K_j = 0$, for all i and j , K_i just a notation of traced quantity.

For perfect fluid the energy-momentum tensor is,

$$T_{ij} = (p + \rho)u_i u_j - p g_{ij} \quad (9)$$

Which follows the EoS,

$$p = \omega \rho \quad (10)$$

Where $-1 \leq \omega \leq 1$, ρ and p represents energy density and pressure of dark energy.

It is widely accepted that by the end of the inflationary period, the geometry of the Universe was homogeneous and isotropic [32], where the FLRW models plays an important role in representing both spatially homogeneous and isotropic Universe. Observational studies have confirmed these symmetries. Yet, theoretical arguments and unexpected anomalies in the cosmic microwave background (CMB) suggest that an anisotropic phase may have existed in the early Universe. After the announcement of the Planck probe results [33], it is believed that the early universe may not have been exactly uniform. Thus, the existence of inhomogeneous and anisotropic properties of the universe has increased popularity when it is come to constructing cosmological models under the supervision of anisotropic background.

3. METRIC AND THE FIELD EQUATIONS

The general non-static, anisotropic and spatially homogeneous plane symmetric spacetime metric is given by [14],

$$ds^2 = dt^2 - A^2(dx^2 + dy^2) - B^2 dz^2 \quad (11)$$

Where $A = A(t)$, $B = B(t)$.

We denote the coordinates x, y, z, t as x^1, x^2, x^3, x^4 respectively.

The Ricci scalar of metric (11) is,

$$R = -2 \left[\frac{2\ddot{A}}{A} + \frac{\ddot{B}}{B} + \frac{\dot{A}^2}{A^2} + \frac{2\dot{A}\dot{B}}{AB} \right] \quad (12)$$

Where $\dot{A} = \frac{dA}{dt}$, $\ddot{A} = \frac{d^2A}{dt^2}$ etc.

From equations (8), for vacuum field,

$$K_i = \left(\frac{F(R)R_{ij} - \nabla_i \nabla_j F(R)}{g_{ij}}\right) \quad (13)$$

Where, $K_i - K_j = 0, \forall i, j$

For $K_4 - K_1 = K_4 - K_2 = 0$ and $K_4 - K_3 = 0$ we get

$$\left[\frac{\ddot{A}}{A} + \frac{\ddot{B}}{B} - \frac{\dot{A}^2}{A^2} - \frac{\dot{A}\dot{B}}{AB} \right] F + \frac{\dot{A}}{A} \dot{F} - \ddot{F} = 0 \quad (14)$$

$$\left[\frac{2\ddot{A}}{A} - \frac{2\dot{A}\dot{B}}{AB} \right] F + \frac{\ddot{B}}{B} \dot{F} - \ddot{F} = 0 \quad (15)$$

With three unknowns, A, B, and F, we are left with two non-linear DE (14) and (15). These are challenging, nonlinear equations to solve. However, we look into a few solutions utilizing the idea of constant curvature assumption.

4. SOLUTIONS WITH THE CONSTANT CURVATURE ASSUMPTION

Under the assumption of constant curvature, the field equations in $f(R)$ gravity are analysed. This approach allows for the recovery of several well-known solutions that are already established in GR, but now within the context of significant $f(R)$ gravity models.

Case-I:

Say for a constant curvature solution $R = R_0$, we have

$$\dot{F}(R_0) = 0 = \ddot{F}(R_0) \quad (16)$$

Equations (14) and (15) can be used to get the following form:

$$\frac{\ddot{A}}{A} + \frac{\ddot{B}}{B} - \frac{\dot{A}^2}{A^2} - \frac{\dot{A}\dot{B}}{AB} = 0 \quad (17)$$

$$\frac{2\ddot{A}}{A} - \frac{2\dot{A}\dot{B}}{AB} = 0 \quad (18)$$

The power law assumption can be used to solve these problems. i.e. $A \propto t^p$ and $B \propto t^q$, where p and q are real numbers.

Thus, $A = k_1 t^p$ and $B = k_2 t^q$, where k_1 and k_2 are proportionality constants.

From equations (17) and (18), we get,

$$p = \frac{2}{3}, q = -\frac{1}{3} \quad (19)$$

And hence from (11) and (19) the solution becomes

$$ds^2 = dt^2 - k_1^2 t^{\frac{4}{3}}(dx^2 + dy^2) - k_2^2 t^{-\frac{2}{3}} dz^2 \quad (20)$$

This can be shown that, these values of p and q leads to $R = 0$. This represents the simplest possible solution and is somewhat trivial in the case of constant scalar curvature.

We reinterpret the specifications, i.e. $k_1^2 dx^2 = dX^2, k_1^2 dy^2 = dY^2, k_2^2 dz^2 = dZ^2$

The above metric can be written as,

$$ds^2 = dt^2 - t^{\frac{4}{3}}(dX^2 + dY^2) - t^{-\frac{2}{3}} dZ^2 \quad (21)$$

This corresponds to Taub's Metric [13].

Case-II:

Now we assume that $B = A^n$. Then subtracting equation (17) from (18), we get

$$\frac{\ddot{A}}{A} - \frac{\ddot{B}}{B} + \frac{\dot{A}^2}{A^2} - \frac{\dot{A}\dot{B}}{AB} = 0 \quad (22)$$

After solving above equation we get,

$$A = [(n+2)(k_3 t + k_4)]^{\frac{1}{(n+2)}} \quad (23)$$

Hence

$$B = [(n+2)(k_3 t + k_4)]^{\frac{n}{(n+2)}} \quad (24)$$

Where k_3 and k_4 are constants of integration.

With these values of A and B , metric takes the form

$$ds^2 = dt^2 - [(n+2)(k_3 t + k_4)]^{\frac{2}{(n+2)}}(dx^2 + dy^2) - [(n+2)(k_3 t + k_4)]^{\frac{2n}{(n+2)}} dz^2 \quad (25)$$

This equation gives Taub's Metric for $n = -\frac{1}{2}$.

Case-III: For non-vacuum perfect fluid solutions:

In this instance, the metric in equation (11) has a non-vacuum solution.

The energy-momentum tensor for a single fluid source is

$$T_{ij} = (p + \rho)u_i u_j - p g_{ij} \quad (26)$$

With

$$g^{ij}u_i u_j = 1, u_i = (0,0,0,1) \quad (27)$$

where ρ is the fluid's energy density and p is the isotropic pressure.

u_i is the four-velocity of the time-like vector satisfying (27).

Using (8), (26) and (27), we get

For $K_1 - K_4 = K_2 - K_4 = 0$ and for $K_3 - K_4 = 0$, we get,

$$\left[-\frac{\ddot{A}}{A} - \frac{\ddot{B}}{B} + \frac{\dot{A}^2}{A^2} + \frac{\dot{A}\dot{B}}{AB} \right] F - \frac{\dot{A}}{A} \dot{F} + \ddot{F} + k(p + \rho) = 0 \quad (28)$$

$$\left[-\frac{2\ddot{A}}{A} + \frac{2\dot{A}\dot{B}}{AB} \right] F - \frac{\dot{B}}{B} \dot{F} + \ddot{F} + k(p + \rho) = 0 \quad (29)$$

Using equations (16), equations (28) and (29) becomes,

$$\left[-\frac{\ddot{A}}{A} - \frac{\ddot{B}}{B} + \frac{\dot{A}^2}{A^2} + \frac{\dot{A}\dot{B}}{AB} \right] + \frac{k}{F}(p + \rho) = 0 \quad (30)$$

$$\left[-\frac{2\ddot{A}}{A} + \frac{2\dot{A}\dot{B}}{AB} \right] + \frac{k}{F}(p + \rho) = 0 \quad (31)$$

Solving (30) and (31), we get

$$\frac{\ddot{A}}{A} - \frac{\ddot{B}}{B} + \frac{\dot{A}^2}{A^2} - \frac{\dot{A}\dot{B}}{AB} = 0 \quad (32)$$

Integrating (32), we obtain

$$\frac{\dot{A}}{A} - \frac{\dot{B}}{B} = \frac{k_5}{A^2 B} \quad (33)$$

where k_5 is the integration constant. Making use of (33) and the conversion

$$A^2 B = \mathcal{U} \quad (34)$$

Where $\mathcal{U} = \mathcal{U}(t)$ and $A = A(\mathcal{U})$, $B = B(\mathcal{U})$ are expressed as follows:

$$A = \beta \mathcal{U}^{(1/3)} e^{(k_5/3) \int (dt/\mathcal{U})}, B = \delta \mathcal{U}^{(1/3)} e^{(-2k_5/3) \int (dt/\mathcal{U})} \quad (35)$$

Where β and δ are integration constants.

$$ds^2 = dt^2 - \beta^2 \mathcal{U}^{(2/3)} e^{(2k_5/3) \int (dt/\mathcal{U})} (dx^2 + dy^2) - \delta^2 \mathcal{U}^{(2/3)} e^{(-4k_5/3) \int (dt/\mathcal{U})} dz^2 \quad (36)$$

The standard conservation law for Einstein's field equation $T_{;j}^{ij} = 0$ (Here semicolon (;) indicates covariant divergence) gives,

$$\dot{\rho} + (p + \rho) \left(2 \frac{\dot{A}}{A} + \frac{\dot{B}}{B} \right) = 0 \quad (37)$$

Solving (37), using equations (10) and (34) we obtain,

$$\rho = \xi \mathcal{U}^{-(1+\omega)} \quad (38)$$

Where ξ is integration constant and $-1 \leq \omega \leq 1$.

The cosmological parameters are given by,

Spatial volume, $V = \mathcal{U}$

Hubble parameter, $H = \frac{1}{3} \frac{\dot{\mathcal{U}}}{\mathcal{U}}$

Expansion scalar, $\theta = \frac{\dot{\mathcal{U}}}{\mathcal{U}}$

Shear scalar, $\sigma^2 = \frac{1}{3} \frac{k_5^2}{\mathcal{U}^2}$

Deceleration parameter, $q = \frac{[2 \dot{\mathcal{U}}^2 - 3 \ddot{\mathcal{U}} \mathcal{U}]}{\dot{\mathcal{U}}^2}$

Three different circumstances arise based on the parameter \mathcal{U} .

1. $\mathcal{U} = \text{constant} = c$.

In this case $A = \beta' e^{(k't/3)}$ and $B = \delta' e^{-(2k't/3)}$, $\rho = \xi c^{-(1+\omega)}$

where $\beta' = \beta c^{(1/3)}$, $\delta' = \delta c^{(1/3)}$, $k' = k_5/c$

Also $H = 0$, $\theta = 0$, $\sigma^2 = \frac{k'^2}{3}$, q is not defined. Here ρ and σ are constant. For $k_5 = 0$, A and B are constant and σ become significant. For $k_5 > 0$, A increases and B decreases exponentially with time.

2. $\mathcal{U} = t$

In this case $A = \beta t^{((k_5+1)/3)}$ and $B = \delta t^{((1-2k_5)/3)}$, $\rho = \xi t^{-(1+\omega)}$, scale factor $a = t^{(1/3)}$, $H = (1/3t)$, $\theta = (1/t)$, $\sigma^2 = (k_5^2/3t^2)$ and $q = 2$.

3. $\mathcal{U} = t^n$

In this case $A = \beta t^{(n/3)} e^{(k_5 t^{(1-n)}/3(1-n))}$, $B = \delta t^{(n/3)} e^{-(2k_5 t^{(1-n)}/3(1-n))}$, $\rho = \xi t^{-n(1+\omega)}$,

$\theta = (n/t)$, $\sigma^2 = (k_5^2/3t^{2n})$ and $q = ((3-n)/n)$, where $n \neq 1$.

The dimensionless rate of change of the third derivative of the field parameter with respect to the cosmic time is known as the jerk parameter in cosmology. It is given by

$$j(t) = q + 2q^2 - \frac{\dot{q}}{H} \text{ and hence } j(t) = (18/n^2) - (9/n) + 1$$

In this case, the expansion scalar θ remains positive for $n > 0$, confirming that the Universe is expanding. As cosmic time increases, θ decreases and asymptotically approaches zero, indicating a gradual slowdown in the expansion rate. The shear scalar σ^2 also diminishes over time and vanishes in the asymptotic limit, implying that the Universe evolves toward isotropy. The deceleration parameter is given by $q = ((3-n)/n)$, which becomes negative for $n > 3$, reflecting an accelerated expansion phase consistent with current cosmological observations. The energy density follows the relation

$\rho = \xi t^{-n(1+\omega)}$, and decreases with time for $\omega > -1$. Notably, for $\omega = -1$, the density remains constant, imitating the behaviour of a cosmological constant and aligning with the Λ CDM model. These results support a scenario in which the Universe transitions from an anisotropic, decelerating phase to an isotropic, accelerating one at late times.

5. SOLUTIONS WITHOUT THE CONSTANT CURVATURE ASSUMPTION

Field equations (28) and (29) are linearly independent with five unknowns A, B, p, ρ and F . The deceleration parameter describes the evolution of the universe. The cosmological models of the evolving universe transits from early deceleration phase. ($q > 0$) to the current accelerating phase ($q < 0$). Whereas the models can be classified based on the time dependence of DP. To solve the system of equations, we assume the deceleration parameter (q) varies linearly with the Hubble parameter [34,35].

$$q = -\frac{a\ddot{a}}{\dot{a}^2} = \gamma + \alpha H \quad (39)$$

Here γ and α are arbitrary constants.

For $\gamma = -1$ in equation (39)

$$q = -\frac{a\ddot{a}}{\dot{a}^2} = -1 + \alpha H$$

Which yields the following differential equation,

$$\frac{a\ddot{a}}{\dot{a}^2} + \alpha \frac{\dot{a}}{a} - 1 = 0 \quad (40)$$

Integrating equation (40) we get

$$a(t) = e^{\frac{1}{\alpha}\sqrt{2\alpha t+k_6}} \quad (41)$$

Where k_6 is a constant of integration.

Assuming the shear scalar σ is proportional to the expansion scalar θ we obtain the relationship between scale factor A and B as follows:

$$A = B^n \quad (42)$$

Where n is constant and $n \neq 1$

Using (34), (41) and (42) the metric components are

$$A(t) = e^{\frac{3n}{\alpha(2n+1)}\sqrt{2\alpha t+k_6}} \quad (43)$$

and

$$B(t) = e^{\frac{3}{\alpha(2n+1)}\sqrt{2\alpha t+k_6}} \quad (44)$$

The metric (11) is reduced to,

$$ds^2 = dt^2 - e^{\frac{6n}{\alpha(2n+1)}\sqrt{2\alpha t+k_6}}(dx^2 + dy^2) - e^{\frac{6}{\alpha(2n+1)}\sqrt{2\alpha t+k_6}}dz^2 \quad (45)$$

Equation (45) represents PSCM with variable deceleration parameter.

The directional Hubble parameter H_x, H_y and H_z are given by

$$H_x = H_y = \frac{3n}{(2n+1)\sqrt{2\alpha t+k_6}}$$

$$H_z = \frac{3}{(2n+1)\sqrt{2\alpha t+k_6}}$$

Hubble parameter (H) and expansion scalar (θ) is given by

$$H = \frac{1}{\sqrt{2\alpha t+k_6}} \quad (46)$$

$$\theta = \frac{3}{\sqrt{2\alpha t+k_6}} \quad (47)$$

The spatial volume (V) and anisotropic parameter (Δ) is given by

$$V = e^{\frac{3}{\alpha}\sqrt{2\alpha t+k_6}} \quad (48)$$

$$\Delta = \frac{2(n-1)^2}{(2n+1)^2} = \text{constant} \quad (\Delta \neq 0 \text{ for } n \neq 1) \quad (49)$$

The shear scalar (σ^2) is given by

$$\sigma^2 = \frac{3(n-1)^2}{(2n+1)^2(2at+k_6)} \quad (50)$$

From equations (47) and (50), we get

$$\lim_{t \rightarrow \infty} \frac{\sigma^2}{\theta^2} = \frac{(n-1)^2}{3(2n+1)^2} = \text{constant} (\neq 0 \text{ for } n \neq 1) \quad (51)$$

The energy density ρ and isotropic pressure p using equations (10) and (38) are given by

$$\rho = \xi \left[e^{\frac{-3(1+\omega)}{\alpha} \sqrt{2at+k_6}} \right] \text{ and } p = \omega \xi \left[e^{\frac{-3(1+\omega)}{\alpha} \sqrt{2at+k_6}} \right] \quad (52)$$

Where ξ is integration constant and $-1 \leq \omega \leq 1$.

The deceleration parameter (q) is given by

$$q = -1 + \frac{\alpha}{\sqrt{2at+k_6}} \quad (53)$$

From equation (12), the Ricci scalar R is found as

$$R = 6 \left\{ \frac{\alpha}{(2at+k_6)^{3/2}} - \frac{3(3n^2+2n+1)}{(2n+1)^2(2at+k_6)} \right\}, \quad (54)$$

In this model, the Universe's initial time is given by $t = -\frac{k_6}{2\alpha} = \mathcal{T}$ ($k_6 \geq 0, \alpha > 0$), which can be shifted to $t = 0$ by setting $k_6 = 0$. At this initial moment, the scale factor a remains constant, indicating that the Universe in this case begins from a non-singular state.

At the initial time ($t = \mathcal{T}$), the Hubble's parameter (H), expansion scalar (θ), shear scalar (σ) are all infinite. Additionally, the isotropic pressure (p) depends on EoS parameter (i.e. $p = \omega \xi$) while the energy density (ρ) remains constant (i.e. $\rho = \xi$).

Also, the energy density remains positive throughout cosmic evolution but gradually declines over time. In contrast, the isotropic pressure increases, it starts from a negative value in the early universe and approaches zero at the present epoch. Observationally, this negative pressure is attributed to dark energy, which, despite having positive energy density, drives accelerated cosmic expansion.

As time t progresses, the scale factor a increases, while the physical parameters H, θ, σ gradually decrease. In the limit of large t , the scale factor a becomes infinitely large, while the parameters H, θ, σ approach zero. This implies that the Universe in this model originates from a non-singular state and expands exponentially over cosmic time.

Furthermore, the deceleration parameter q is positive for $t < \frac{\alpha^2 - k_6}{2\alpha}$, indicating an early decelerating phase of the Universe. Conversely, q is negative for $t > \frac{\alpha^2 - k_6}{2\alpha}$, predicting the accelerating phase of the Universe's expansion in this model. However as $t \rightarrow \infty, q$ approaches -1 , which is characteristic of de Sitter-like exponential expansion. This indicates a transition from deceleration to acceleration, consistent with current observations of cosmic evolution.

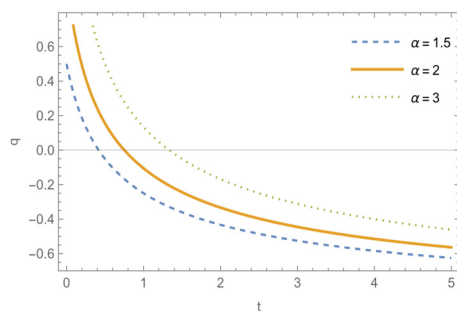


Figure 1. Plot of (q) vs. time t

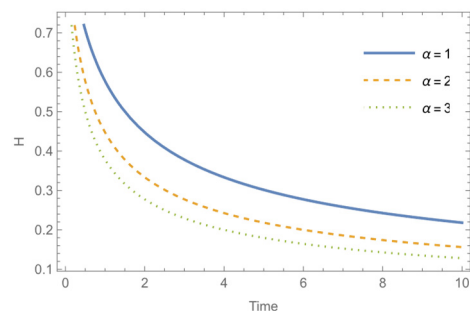


Figure 2. Plot of (H) vs. time t

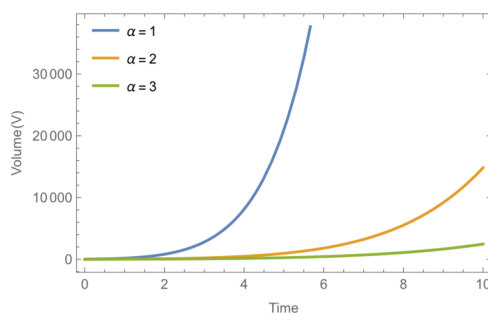


Figure 3. Plot of (V) vs. time t

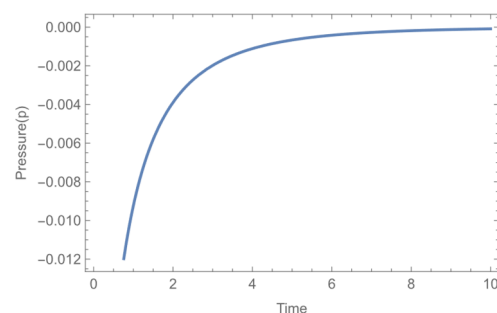


Figure 4. Plot of (p) vs. Time t

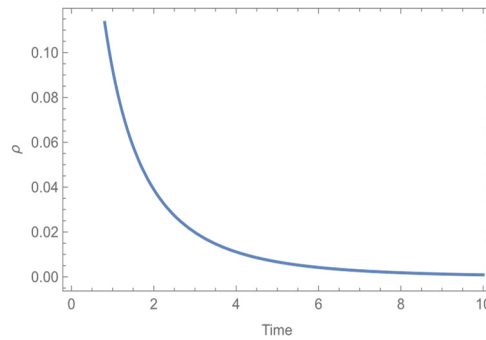


Figure 5. Plot of (ρ) vs. Time t

Statefinder diagnostic: A geometric statefinder pair $\{r, s\}$, whose notable characteristic is their dependence on the scale factor and its time derivatives, was introduced by Sahni et al. and Alam et al. [36,37]. The statefinder diagnostic method serves as effective tool for distinguishing different DE models in cosmology. This diagnostic pair also characterizes the Λ CDM model where the cosmological constant Λ act as DE. The Λ CDM model is considered the standard framework for studying the evolution of the accelerating Universe and is identified by the fixed point $\{r, s\} = \{1, 0\}$. The state-finder diagnostic pair is defined as [38,39,40]

$$r = \frac{\ddot{H}}{H^3} - 3q - 2 \text{ and } s = \frac{r-1}{3(q-\frac{1}{2})} \quad (55)$$

We employ the statefinder diagnostic method to evaluate our model's dynamics and contrast its behaviour with that of the Λ CDM model. The expressions for the statefinder parameters $\{r, s\}$ in our framework are derived as follows:

$$r = 1 + \frac{3\alpha^2}{2\alpha t + k_6} - \frac{3\alpha}{\sqrt{2\alpha t + k_6}} \text{ and } s = \frac{\left[\frac{\alpha}{\sqrt{2\alpha t + k_6}} - 1\right]}{\left[1 - \frac{3\sqrt{2\alpha t + k_6}}{2\alpha}\right]} \quad (56)$$

In our model, the state-finder pair $\{r, s\}$ tends toward $\{1, 0\}$ at late time, thus the model is compatible with Λ CDM model [41]

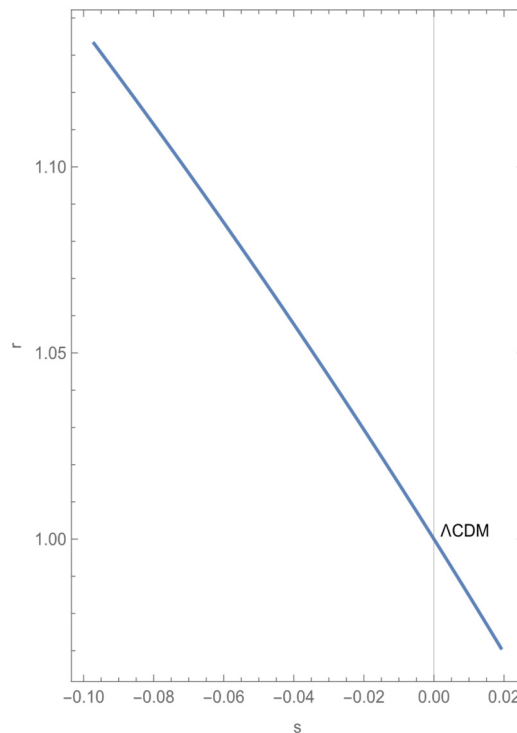


Figure 6. The figure shows the state-finder parameter

Energy conditions: Here, the time-varying behaviour of the energy conditions is explored. The energy conditions are used in many approaches to understand the evolution of the universe. The study of singularities in the spacetime was based on energy conditions. Some of the important energy conditions are given as follows:

Weak energy conditions (WEC) $\Rightarrow \rho \geq 0, \rho - P \geq 0$

Dominant energy conditions (DEC) $\Rightarrow \rho + P \geq 0$

Strong energy conditions (SEC) $\Rightarrow \rho + 3P \geq 0$

Using equation (52), we analyse the behaviour of above-mentioned energy conditions. Figures (7-9) show the behaviour of WEC, DEC and SEC with proper choice of constants respectively and it is observed that all the energy conditions are satisfied for this model.

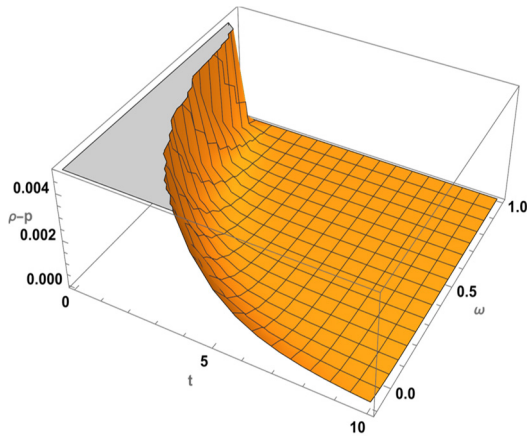


Figure 7. Behaviour of WEC vs. t and ω with $\xi = 1, \alpha = 2, k_6 = 1$

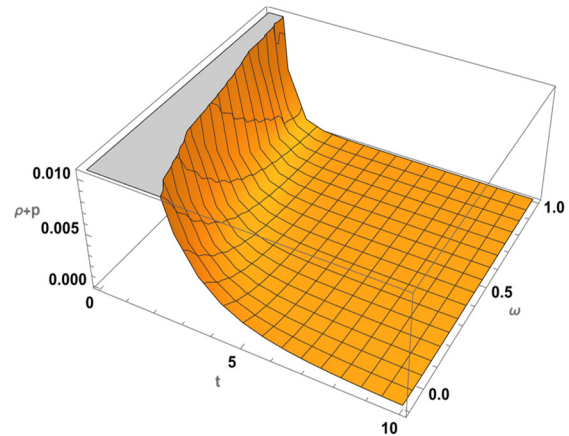


Figure 8. Behaviour of DEC vs. t and ω with $\xi = 1, \alpha = 2, k_6 = 1$

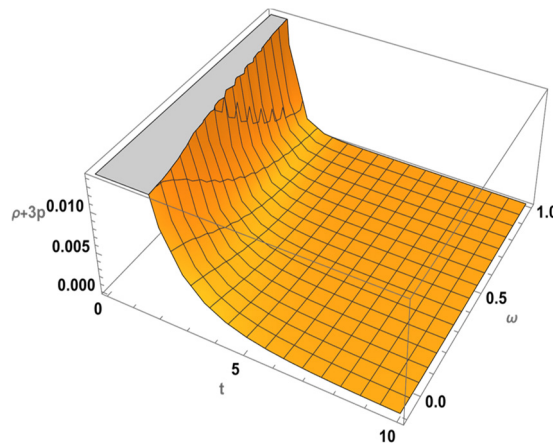


Figure 9. Behaviour of SEC vs. t and ω with $\xi = 1, \alpha = 2, k_6 = 1$

6. CONCLUSIONS

We have investigated non-static plane-symmetric model in the framework of $f(R)$ gravity theory in this work, looking at both scenarios with and without matter (vacuum and non-vacuum conditions). To determine precise answer to the field equations, we have taken into consideration the metric form of the theory.

In the first two cases, we considered vacuum conditions and found solutions using constant curvature and power law assumptions. These solutions matched the well-known Taub's solution.

In the third case, we considered non-vacuum condition and found solutions using the energy momentum tensor equation. We solved the field equations by making a specific assumption that involved a transformation $A^2 B = \mathcal{U}$ and using the EoS, $p = \omega\rho$. For the non-vacuum scenario, we considered three possibilities of \mathcal{U} , where \mathcal{U} is constant, t , and t^n . Particularly, in the case where $\mathcal{U} = t^n$ with $0 < n < 1$, we observed that the ratio σ/θ does not approach to zero as $t \rightarrow \infty$. This implies that the shear decreases at a slower rate compared to the expansion scalar, implying that anisotropic remains significant over time. This persistent anisotropy suggests that our model remains anisotropic, representing the early evolutionary phase of the Universe.

These findings underscore the potential of $f(R)$ gravity to effectively describe the Universe's dynamics, particularly during its early stages when anisotropic effects are expected to be prominent.

In this section, without assuming constant curvature, we assumed a scale factor $a(t) = e^{\frac{1}{\alpha}\sqrt{2\alpha t + k_6}}$ (where α and k_6 are positive constants), to derive an exact solution of the Einstein field equations. This model remains anisotropic throughout cosmic evolution for $n \neq 1$, as it is independent of the cosmic time t . It describes an exponentially expanding Universe that originates with a finite volume at the big bang ($t=0$) and later transitions into an accelerated expansion

phase. The behaviour of the DP is shown in Fig. 1 for $\alpha = 1.5, 2, 3$. The deceleration parameter q in this model is found to be time dependent, exhibiting a transition from an early decelerating phase to the current accelerating phase of the Universe. Fig. 2 and 3 represents the time-varying behaviour of the Hubble parameter (H) and volume (V), respectively. Fig. 4 and Fig. 5 illustrate the variation of isotropic pressure p and energy density ρ w.r.t. the cosmic time t . The energy density and pressure gradually diminish and approach zero as t becomes large. Fig. 6 shows the evolution of r - s trajectory. The state-finder pair $\{r, s\}$ tends towards $\{1, 0\}$ at late time, indicating that the model asymptotically behaves like the Λ CDM (cosmological constant Λ + Cold Dark Matter) model. Fig. 7, 8, and 9 represents the time varying behaviour of WEC, DEC, and SEC, showing that all the energy conditions (WEC, DEC, SEC) are satisfied throughout the evolution.

Acknowledgements

We are very indebted to the editor and anonymous referee for illuminating suggestions that have significantly improved our paper in terms of research quality as well as presentation.

ORCID

✉ D.V. Dhote, <https://orcid.org/0009-0009-1569-9161>; ✉ S.D. Deo, <https://orcid.org/0009-0008-5413-9485>

REFERENCES

- [1] H.A. Buchdahl, "Non-linear Lagrangians and Cosmological Theory". *Mon. Not. R. Astro. Soc.*, **150**, 1-8 (1970). <https://doi.org/10.1093/mnras/150.1.1>
- [2] O. Bertolami, F.G. Pedro, and M.L. Delliou, "Dark energy-dark matter interaction and putative violation of the equivalence principle from the Abell cluster A586," *Phys. Letters B*, **654**, 165-169 (2007). <https://doi.org/10.1016/j.physletb.2007.08.046>
- [3] Carroll, *et al.*, "Is cosmic speed-up due to new gravitational physics?" *Phys. Rev. D*, **70**, 043528 (2004). <https://doi.org/10.1103/PhysRevD.70.043528>
- [4] C.L. Bennet, *et al.*, *Astrophys. J. Suppl.* "First-Year Wilkinson Microwave Anisotropy Probe (WMAP)* Observations: Preliminary Maps and Basic Results," **148**, 1(2003). <https://doi.org/10.1086/377253>; Spergel, *et al.*, "First-Year Wilkinson Microwave Anisotropy Probe (WMAP)* Observations: Determination of Cosmological Parameters," *Astrophys. J. Suppl.* **148**, 175(2003). <https://doi.org/10.1086/377226>
- [5] Riess, *et al.* (Supernovae Search Team), *Astron. J.* "Observational Evidence from Supernovae for an Accelerating Universe and a Cosmological Constant," **116**, 1009 (1998). <https://doi.org/10.1086/300499>; *Astrophys. J.* "Type Ia Supernova Discoveries at $z > 1$ from the Hubble Space Telescope: Evidence for Past Deceleration and Constraints on Dark Energy Evolution," **607**, 665 (2004). <https://doi.org/10.1086/383612>; Perlmutter, S., *et al.*, *Astrophys. J.* "Measurements of Ω and Λ from 42 High-Redshift Supernovae," **517**, 565 (1999). <https://doi.org/10.1086/307221>; Astier, P., *et al.*, "The Supernova Legacy Survey: measurement of Ω_M , Ω_Λ and w from the first year data set," *Astron. Astrophys.* **447**, 31-48 (2006). <https://doi.org/10.1051/0004-6361:20054185>
- [6] S.W. Allen, *et al.*, "Constraints on dark energy from Chandra observations of the largest relaxed galaxy clusters," *Mon. Not. R. Astron. Soc.* **353**, 457-467 (2004). <https://doi.org/10.1111/j.1365-2966.2004.08080.x>
- [7] N. Tegmark, *et al.*, "Cosmological parameters from SDSS and WMAP," *Phys. Rev. D*, **69**, 103501 (2004). <https://doi.org/10.1103/PhysRevD.69.103501>
- [8] S. Perlmutter, "Cosmology from Type Ia Supernovae," *Bulletin of the American Astronomical Society*, **29**, 1351, (1997). <https://arxiv.org/pdf/astro-ph/9812473>
- [9] K. Bamba, S. Capozziello, S. Nojiri, and S.D. Odintsov, "Dark Energy Cosmology: The Equivalent Description via Different Theoretical Models and Cosmography Tests," *Astrophys. And Space Sci.* **342**, 155-228 (2012). <https://doi.org/10.1007/s10509-012-1181-8>
- [10] S. Nojiri, and S.D. Odintsov, "Unified Cosmic History in Modified Gravity: from $f(R)$ Theory to Lorentz Non-Invariant Models," *Phys. Report*, **505**, 59-144 (2011). <https://doi.org/10.1016/j.physrep.2011.04.001>
- [11] B. Mishra, and S.K. Tripathy, "Anisotropic Dark Energy Model with a Hybrid Scale Factor," *Modern Phys. Letters A*, **30**, 1550175 (2015). <https://doi.org/10.1142/S0217732315501758>
- [12] F.M.D. Esmaeili, "Dynamics of Bianchi I Universe in Extended Gravity with Scale Factor," *Journal of High Energy Physics, Gravitation and Cosmology*, **4**, 716-730 (2018). <https://doi.org/10.4236/jhepgc.2018.44040>
- [13] M.F. Shamir, "Exploring Plane-Symmetric Solutions in $f(R)$ Gravity," *Journal of Experimental and Theoretical Physics*, **122**, 331-337 (2016). <https://doi.org/10.1134/S106377611601009X>
- [14] V.B. Raut, *et al.*, "Plane Symmetric Vacuum Cosmological Model with a special form of Deceleration Parameter in $f(R)$ Theory of Gravity," *Physical Science International Journal*, **5**(1), 74-80 (2015). <https://doi.org/10.9734/PSIJ/2015/13999>
- [15] A.S. Agrawal, *et al.*, "Gravitational baryogenesis model's comparison in $f(R)$ gravity," *Chinese journal of physics*, **71**, 333-340 (2021). <https://doi.org/10.1016/j.cjph.2021.03.004>
- [16] K.P. Singh, J. Baro, A.J. Meitei, "Higher Dimensional Bianchi Type-I Cosmological Model with Massive String in General Relativity," *Front. Astron. Space Sci.* **8**, 777554 (2021). <https://doi.org/10.3389/fspas.2021.777554>
- [17] A.S. Agrawal, S. Zerbin, and B. Mishra, "Black Holes and Wormholes Beyond Classical General Relativity," *arXiv:2406.01241[gr-qc]*, (2024). <https://doi.org/10.48550/arXiv.2406.01241>
- [18] M.R. Karim, "Bianchi Type-I Anisotropic Universe with Meric Potential in Saez-Ballester Theory of Gravitation," *Journal of Applied Mathematics and Physics*, **10**, 3072-3082 (2022). <https://doi.org/10.4236/jamp.2022.1010205>
- [19] A.M. Al-Haysah, and A.H. Hasmani, "Higher dimensional Bianchi type-I string cosmological model in $f(R)$ theory of gravity," *Heliyon*, **7**, e08063 (2021). <https://doi.org/10.1016/j.heliyon.2021.e08063>
- [20] L.S. Ladke, and R.D. Mishra, "Higher Dimensional Plane Symmetric Solutions in $f(R)$ Theory of Gravitation," *Prespacetime journal*, **8**(5), 542-554 (2017). <https://prespacetime.com/index.php/pst/article/download/1259/1228>
- [21] L.S. Ladke, R.D. Mishra, and S.R. Gomkar, "Static Interior Plane Symmetric five-dimensional solutions in $f(R)$ gravity," *International Journal of Mathematical Archive*, **9**(4), 151-162 (2018).

- [22] V.A. Thakare, R.V. Mapari, and S.S. Thakre, "Five- Dimensional Plane Symmetric Cosmological Model with Quadratic Equation of State in $f(R, T)$ Theory of Gravity," East Eur. J. Phys. (3), 108-121 (2023). <https://doi.org/10.26565/2312-4334-2023-3-08>
- [23] U.K. Sharma, R. Zia, A. Pradhan, and A. Beesham, "Stability of LRS Bianchi type-I cosmological models in $f(R, T)$ -gravity," Research in Astronomy and Astrophysics, **19**(4), 55-68 (2019). <https://doi.org/10.1088/1674-4527/19/4/55>
- [24] A. Dabre, and P. Makode, "Viscous Plane Symmetric String Cosmological Model in $f(R)$ Gravity," Astrophysics, **67**, 161-177 (2024). <https://doi.org/10.1007/s10511-024-09826-1>
- [25] D.D. Pawar, and A.G. Deshmukh, "Bulk Viscous Fluid Plane Symmetric String Cosmological Model in General Relativity," Bulg. J. Phys. **37**, 56-63 (2010). https://www.bjp-bg.com/papers/bjp2010_1_56-63.pdf
- [26] A. Cassado-Turrión, A. de la Cruz-Dombriz, and A. Dobado, "Physical nonviability of a wide class of $f(R)$ models and their constant-curvature solutions," Phys. Rev. D, **108**, 064006 (2023). <https://doi.org/10.1103/PhysRevD.108.064006>
- [27] A. Larranaga, "A rotating charged black hole solution in $f(R)$ gravity," Pramana journal of physics, **78**(5), 697-703 (2012). <https://doi.org/10.1007/s12043-012-0278-5>
- [28] M. Calza, M. Rinaldi, and L. Sebastiani, "A special class of solutions in $F(R)$ - gravity," Eur. Phys. J. C, **78**, 178 (2018). <https://doi.org/10.1140/epjc/s10052-018-5681-8>
- [29] M. Sharif, and M.F. Shamir, "Non-Vacuum Bianchi Types I and V in $f(R)$ Gravity," Gen. Rel. Grav. **42**, 2643-2655 (2010). <https://doi.org/10.1007/s10714-010-1005-5>
- [30] M. Sharif, and M.F. Shamir, "Plane Symmetric Solutions in $f(R)$ Gravity," Mod. Phys. Lett. A, **25**, 1281-1288 (2010). <https://doi.org/10.1142/S0217732310032536>
- [31] D.R.K. Reddy, K.S. Adhav, and S.L. Munde, "Vacuum Solutions of Bianchi Type-I and V Models in $f(R)$ Gravity with a Special Form of Deceleration Parameter," Int. J. Sci. Adv. Tech. **4**, (2014).
- [32] A.D. Linde, "Inflationary Cosmology," in: *Inflationary Cosmology. Lecture Notes in Physics*, edited by M. Lemoine, J. Martin, and P. Peter, **738**, (Springer, Berlin, Heidelberg), (2008), pp. 1-54. https://doi.org/10.1007/978-3-540-74353-8_1
- [33] P.A.R. Ade, (Planck Collaboration), "Planck 2013 results. XVI. Cosmological Parameters," Astron. Astrophys. **571**, A16, (2014). <https://doi.org/10.1051/0004-6361/201321591>
- [34] R.K. Tiwari, R. Singh, and B.K. Shukla, "A Cosmological Model with Variable Deceleration parameter," The African Review of Physics, **10**, 395-402 (2015). <http://aphysrev.ictp.it/index.php/aphysrev/article/download/1137/460>
- [35] P.K. Ray, and R.R. Baruah, "Anisotropic cloud string cosmological model with five-dimensional Kaluza Klein space-time," Frontiers in Astronomy and Space Sciences, **9**, 869020 (2022). <https://doi.org/10.3389/fspas.2022.869020>
- [36] V. Sahni, T.D. Saini, A.A. Starobinsky, and U. Alam, "Statefinder – A new geometrical diagnostic of dark energy," J. Exp. Theor. Phys. Lett. **77**, 201-206 (2003). <https://doi.org/10.1134/1.1574831>
- [37] U. Alam, V. Sahni, T.D. Saini, and A.A. Starobinsky, "Exploring the Expanding Universe and Dark Energy using the Statefinder Diagnostic," Mon. Not. R. Astron. Soc. **344**, 1057 (2003). <https://doi.org/10.1046/j.1365-8711.2003.06871.x>
- [38] S. Appleby, R. Battye, and A. Starobinsky, "Curing singularities in cosmological evolution of $f(R)$ gravity," JCAP, **1006**, 005 (2010). <https://doi.org/10.1088/1475-7516/2010/06/005>
- [39] F. Yu, J.L. Cui, J.F. Zhang, and X. Zhang, "Statefinder hierarchy exploration of the extended Ricci dark energy," Eur. Phys. J. C, **75**, 274 (2015). <https://doi.org/10.1140/epjc/s10052-015-3505-7>
- [40] M.Z. Khurshudyan, and A.N. Makarenko, "On a phenomenology of the accelerated expansion with a varying ghost dark energy," Astrophys. Space Sci. **361**, 187 (2016). <https://doi.org/10.1007/s10509-016-2775-3>
- [41] B.K. Shukla, R.K. Tiwari, D. Sofuoglu, and A. Beesham, "Quintessence's Universe in $f(R, L_m)$ gravity with special form of deceleration parameter," (2023). <https://doi.org/10.48550/arXiv.2306.09387>

ДОСЛІДЖЕННЯ ПЛОСКОГО СИМЕТРИЧНОГО ПРОСТОРУ-ЧАСУ В МОДИФІКОВАНІЙ ГРАВІТАЦІЙНІЙ ТЕОРІЇ $f(R)$

Д.В. Дхоте^а, С.Д. Део^б

^аКафедра математики післядипломної освіти, Університет Гондвани, Гадчіролі, Індія

^бКоледж наук Махатми Ганді, Гадчандур, Індія

У цій статті досліджується плоскосиметрична космологічна модель (PSCM) у контексті модифікованої теорії гравітації $f(R)$, включаючи як вакуумні, так і невакуумні сценарії. Джерелом матерії вважається ідеальна рідина. Щоб отримати розв'язки, ми розглядаємо передумову як постійної, так і непостійної скалярної кривини. Застосовуючи закон збереження для рівняння поля Ейнштейна, $T_{;j}^{ij} = 0$, та припущення степеневого закону, ми отримуємо деякі відомі розв'язки. Ми розв'язали рівняння поля, зробивши специфічне припущення, яке включало перетворення $A^2B = \mathcal{U}$. Це дослідження досліджує фізичні та кінематичні характеристики конкретних космологічних моделей, а також розглядає діагностику за допомогою методу пошуку станів – ключового інструменту для аналізу еволюційної траєкторії Всесвіту. Робота надає важливе розуміння поведінки анізотропних моделей у контексті модифікованої $f(R)$ гравітації. Вона підкреслює взаємодію між розподілом матерії та геометрією простору-часу, особливо підкреслюючи, як припущення постійної та непостійної скалярної кривини допомагає спростити та розв'язати відповідні рівняння поля. Отримані рішення покращують наше розуміння космічної еволюції, що керується модифікованою $f(R)$ гравітацією.

Ключові слова: плоско-симетричний; теорія гравітації $f(R)$; ідеальна рідина; визначник станів; анізотропний Всесвіт

FLUORESCENT DETECTION OF HEAVY METAL IONS USING BENZANTHRONE DYE

 U. Malovytsia^{a*},  O. Zhytniakivska^a, K. Yeltsov^a,  K. Vus^a,  V. Trusova^a,  E. Kirilova^b,
 G. Gorbenko^a

^aDepartment of Medical Physics and Biomedical Nanotechnologies, V.N. Karazin Kharkiv National University
4 Svobody Sq., Kharkiv, 61022, Ukraine

^bDepartment of Applied Chemistry, Institute of Life Sciences and Technology, Daugavpils University, LV-5401 Daugavpils, Latvia

*Corresponding Author E-mail: uliana.tarabara@karazin.ua

Received June 3, 2025; revised July 16, 2025; accepted August 21, 2025

The development of sensitive, low-cost, and biocompatible sensors for detecting toxic heavy metals remains a pressing challenge in environmental monitoring. Protein-based nanostructures present unique opportunities in this regard. Coupling amyloid fibrils with amyloid-sensitive fluorescent dyes, which exhibit distinct spectral responses upon binding to amyloid structures and in the presence of metal ions, may lead to a promising sensing platform. In this study, the benzanthrone derivative ABM was examined as a fluorescent probe for detecting heavy metal ions in aqueous solutions and in the presence of β -lactoglobulin amyloid fibrils (β -lgf). In water, benzanthrone dye shows a broad emission spectrum dominated by a band at 690 nm. Binding to β -lgf produces a substantial increase in fluorescence intensity and a ~ 65 nm hypsochromic shift, indicating dye partitioning into the fibrillar hydrophobic environment. In aqueous solutions, ABM responds to heavy metals with characteristic spectral changes: Pb^{2+} and Ni^{2+} decrease the 690 nm emission band and generate a 560 nm band, while Cu^{2+} and Zn^{2+} cause complete quenching of the 690 nm emission with the appearance of a prominent 560 nm maximum, consistent with the formation of metal–ligand charge–transfer complexes. In the fibrillar environment, ABM displays a dominant emission at 560 nm; addition of heavy metals modulates the intensity and shape of this band in an ion-specific manner. Deconvolution of the emission spectra revealed two spectral components, whose amplitudes and shape descriptors were selectively altered by Ni^{2+} and Cu^{2+} , while Zn^{2+} and Pb^{2+} had lesser effects. These findings demonstrate that ABM fluorescence reports sensitively on the strength and specificity of heavy metal interactions with amyloid fibrils, supporting its potential as an optical sensor for probing protein–metal systems.

Keywords: Benzanthrone dyes; Metal detection; Heavy metals

PACS: 87.14.Cc, 87.16.Dg

Heavy metal ion contamination poses a significant environmental and public health challenge, as ions such as mercury (Hg^{2+}), lead (Pb^{2+}), cadmium (Cd^{2+}), and copper (Cu^{2+}) are highly toxic even at trace levels, persist in ecosystems, and readily bioaccumulate, with strong links to cancer and neurodegenerative disorders [1–3]. Accurate detection of these ions remains a critical priority for environmental monitoring and disease prevention related to heavy metals. Despite the high sensitivity and reliability of conventional analytical techniques, including atomic absorption spectroscopy (AAS) [4], inductively coupled plasma mass spectrometry (ICP-MS) [5], and electrochemical assays [6,7], their applications are limited by high costs, extensive sample preparation, and limited field portability. These constraints highlight the urgent need for novel sensing strategies, particularly for detecting water contamination. Recently, fluorescence-based sensing has emerged as an attractive alternative due to its high sensitivity, selectivity, and potential for real-time applications [8–11]. Numerous studies have documented advances in fluorescent sensors incorporating aptamers [8,9], quantum dots [10,11], and organic dyes [12–15] for detecting heavy metals in environmental matrices. Specifically, small-molecule fluorescent probes offer rapid response and high affinity through selective coordination with metal ions, enabling precise fluorescence modulation [8, 16].

Concurrently, protein-based nanomaterials are emerging as highly effective nanoscaffolds for heavy metal removal due to their diverse amino acid functional groups and ability to self-assemble into tunable supramolecular structures such as fibrils, gels, and spherical condensates. Recent advances in protein- and peptide-derived adsorbents demonstrate outstanding metal-binding efficiencies. For example, soy protein hydrogels efficiently captured $\text{Cu}(\text{II})$ even in the presence of competing ions [17], while a BSA/graphene oxide hybrid membrane achieved 90.4% mercury removal [18]. Additionally, elastin-like polypeptides with histidine clusters proved effective for $\text{Cd}(\text{II})$ [19]. Particularly, hybrid membranes combining activated carbon with amyloid fibrils from proteins such as β -lactoglobulin or soy protein removed over 99% of various metals, including gold, mercury, lead, palladium, arsenic, chromium, and nickel, in both model and real wastewater systems [20–22]. Despite the structural stability, high surface area, and abundant binding sites of amyloid fibrils—making them well-suited for functionalisation with optical reporters in biosensing applications—the convergence of amyloid fibril scaffolding and fluorescent dyes for heavy metal ion detection remains largely unexplored. This hybrid sensing approach could utilise the structural and binding capacity of amyloid frameworks with the optical sensitivity of fluorescent reporters, potentially enabling portable, low-cost detection systems with enhanced sensitivity and selectivity.

In this study, we present a feasibility investigation into the development of a sensor platform comprising β -lactoglobulin amyloid fibrils with the benzanthrone fluorescent dyes ABM for the detection of Cu^{2+} , Zn^{2+} , Ni^{2+} , and

Pb²⁺, heavy metal ions. More specifically, the aim of our study was to assess the ABM sensitivity to heavy metals and metal- β -lactoglobulin fibril interactions.

EXPERIMENTAL SECTION

Materials

Bovine β -lactoglobulin (β lg), copper(II) chloride dihydrate, nickel(II) chloride, lead(II) nitrate, zinc chloride and thioflavin T (ThT) were purchased from Sigma, USA. Benzanthrone dye ABM [23] was synthesized in the Daugavpils University. All other reagents were of analytical grade and used without the further purification.

Preparation of working solutions

The β -lactoglobulin stock solutions 10 mg/ml (β lgF) was prepared in distilled water with HCl (pH 2.0). The reaction of the protein (stock solutions) fibrillization was conducted at 90 °C for 2 days. The kinetics of amyloid formation was monitored using the Thioflavin T assay [24], revealing the dye fluorescence intensity increase at 480 nm *ca.* 7 times (data not shown). The working solutions of protein were prepared by dissolving a stock solution of the fibrillar β -lactoglobulin in distilled water (pH 6.07). The ABM stock solutions were prepared in ethanol, while ThT was dissolved in 10 mM Tris buffer (pH 7.4). The fluorimetric measurements were carried out in distilled water (pH 6.07).

Spectroscopic measurements

The absorption spectra of the examined dyes were recorded with the spectrophotometer Shimadzu UV-2600 (Japan) at 25°C. The dye concentrations were determined spectrophotometrically using the extinction coefficients $\varepsilon_{444}^{EtOH} = 9.3 \cdot 10^3 \text{ M}^{-1}\text{cm}^{-1}$ and $\varepsilon_{412}^{water} = 3.6 \cdot 10^4 \text{ M}^{-1}\text{cm}^{-1}$ for ABM and ThT, respectively. Steady-state fluorescence spectra were recorded with an RF-6000 spectrofluorimeter (Shimadzu, Japan). Fluorescence measurements were performed at 25°C using 10 mm pathlength quartz cuvettes. Fluorescence spectra were recorded within the range of 480–800 nm, with an excitation wavelength of 460 nm. The excitation and emission slit widths were set at 10 nm.

Fluorescence spectra analysis

The deconvolution of the dye absorption spectra was performed with Origin 9.0 (OriginLab Corporation, Northampton, USA) using the log-normal asymmetric function (LN) [25]:

$$I = I_{\max} \exp \left[-\frac{\ln 2}{\ln^2(\rho)} \ln^2 \left(\frac{a - \lambda}{a - \lambda_c} \right) \right], \quad (1)$$

where I is the fluorescence intensity, I_{\max} is the emission maximum, λ is the wavelength, λ_c is the position of the peak, ρ is the asymmetry of the function defined as:

$$\rho = \frac{\lambda_c - \lambda_{\min}}{\lambda_{\max} - \lambda_c} \quad (2)$$

where λ_{\min} and λ_{\max} denote the wavelength values at half-emission. The parameter a designates the limiting wavelength:

$$a = \lambda_c + \frac{(\lambda_{\max} - \lambda_{\min}) \cdot \rho}{\rho^2 - 1} \quad (3)$$

Binding model

Quantitative characteristics of the dye-protein binding were determined in terms of the Langmuir adsorption model by analyzing protein-induced changes in the probe fluorescence intensity at the wavelengths, corresponding to emission maximum for ABM (624 nm was selected for non-deconvoluted spectra). Assuming that the ABM fluorescence response is proportional to the amount of the protein-bound fluorophore B , the β -lgF-induced change in the probe fluorescence intensity ΔI at the fluorescence maximum can be written as:

$$\Delta I = I - I_0 = [\alpha_{\text{bound}} B + \alpha_{\text{free}} (Z - B)] - \alpha_{\text{free}} Z = (\alpha_{\text{bound}} - \alpha_{\text{free}}) B = F_{\text{mol}} B \quad (4)$$

where I_0 and I – fluorescence intensities of the dye in a buffer solution and in the presence of protein, respectively; F_{mol} is a coefficient proportional to the difference of the dye quantum yields in buffer and when bound to the macromolecule; α_{bound} and α_{free} – molar fluorescence of the bound and free dye, respectively, Z is the total concentration of the probe. If one protein molecule contains n dye binding sites, the association constant (K_a) is given by:

$$K_a = \frac{B}{(Z - B)(P - n - B)} \quad (5)$$

where P is total protein concentration.

The F_{mol} parameter was calculated from the fluorimetric titration of the dye by the fibrillar β -lactoglobulin. Specifically, at high protein concentrations, when $P/n \gg B$, from the combination of the Eqs. (4) and (5) one obtains:

$$\frac{1}{\Delta I} = \frac{1}{BF_{mol}} = \frac{1}{K_a P n Z F_{mol}} + \frac{1}{Z F_{mol}} \quad (6)$$

$$F_{mol} = 1/aZ \quad (7)$$

where a – the y-intercept of the linear fit of the plot $1/\Delta I = 1/P$.

Next, Eqs. (4) and (5) can be rearranged to give:

$$\Delta I = \frac{1}{2} F_{mol} \left[Z + nP + 1/K_a - \sqrt{(Z + nP + 1/K_a)^2 - 4nPZ} \right] \quad (8)$$

The approximation of the experimental dependencies ΔI (fluorescence intensity increase) on P (total protein concentration) by Eq. 8 allowed us to determine the other dye-protein binding parameters – association constant (K_a) and binding stoichiometry (n).

RESULTS AND DISCUSSION

In the initial phase of our study, we assessed the binding of ABM with β -lactoglobulin amyloid fibrils. As can be seen from Figure 1, a free dye in an aqueous environment is characterized by an emission maximum at 690 nm. The emission maximum of ABM shifts from 538 nm in nonpolar benzene to 650 nm in polar ethanol, arising from intramolecular charge transfer between the amine substituent and the carbonyl group, which increases the excited-state dipole moment and induces solvent relaxation [26]. The addition of fibrillar β -lactoglobulin to ABM in water caused a marked increase in fluorescence intensity, accompanied by a ~ 65 nm hypsochromic shift in the emission maximum, indicating dye transfer into a non-polar environment. To quantitatively evaluate the ABM binding, the fluorescence enhancement at 625 nm (ΔI) as a function of the protein concentration was fitted using the Langmuir adsorption model (Eq. 8), yielding the association constant $K_a = 1.9 \times 10^3 \text{ M}^{-1}$ and the number of binding sites $n = 7.5 \pm 0.3 \text{ mol/mol}$.

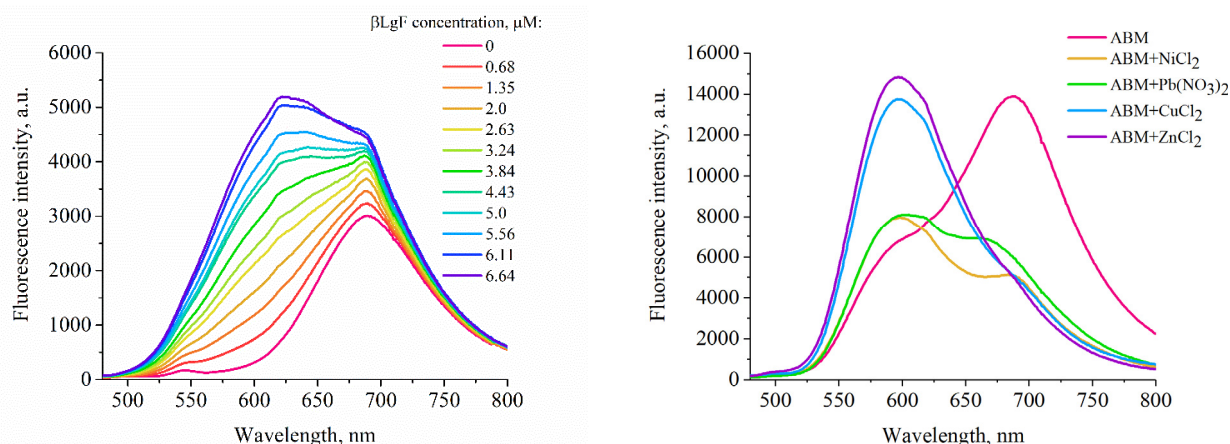


Figure 1. Emission spectra of ABM in the presence of β -lactoglobulin amyloid fibrils (A) and heavy metal ions (B). ABM concentration was 1 μM and 10 μM for ABM- β -lgF and ABM- β -lgF-heavy metal systems, respectively

Next, we evaluated ABM's ability to detect heavy metal ions in aqueous solution (Figure 1B). In water, the benzanthrone dye ABM displays a broad emission spectrum with a prominent peak at 690 nm and a shoulder at approximately 560 nm. When it binds to heavy metals, the 690 nm band diminishes, while emission at around 560 nm increases, with the extent of these changes depending on the specific ion. Particularly, binding with Ni^{2+} and Pb^{2+} results in about a 1.8-fold reduction in fluorescence intensity at 690 nm, a 20 nm blue shift of the emission maximum, and the emergence of a distinct band at 560 nm. Notably, ABM shows an even higher affinity for Cu^{2+} and Zn^{2+} , demonstrated by complete quenching of the 690 nm band and the appearance of a highly intense emission maximum at 560 nm. It is well known that the interaction between fluorescent dyes and heavy metal ions is mainly controlled by the presence of functional donor groups in their molecular structure (such as carbonyl, amine, nitrogen, hydroxyl, etc.), which act as coordination sites for metal binding [8]. The shift in emission peaks for ABM with metal ions likely arises from the formation of metal-ligand charge-transfer complexes involving electron transfer from molecular orbitals in the metal to those in the ligand. Our results indicate that Pb^{2+} and Ni^{2+} , probably, exhibit weaker metal-ligand charge-transfer complex. The strong quenching of the 690 nm maximum and the blue shift at around 560 nm can be explained by the formation of a metal-ligand charge transfer complex involving the amino and carbonyl groups of ABM, as numerous

studies indicate Cu^{2+} preference for these structural groups [8,27]. Conversely, Zn^{2+} tends to form stable coordination complexes mainly through the carbonyl oxygen [8,27], which is also present in the ABM structure. When interacting with the carbonyl group of ABM, Zn^{2+} likely stabilizes the dye's excited state, reducing non-radiative decay and leading to the emergence of a highly emissive band at 560 nm.

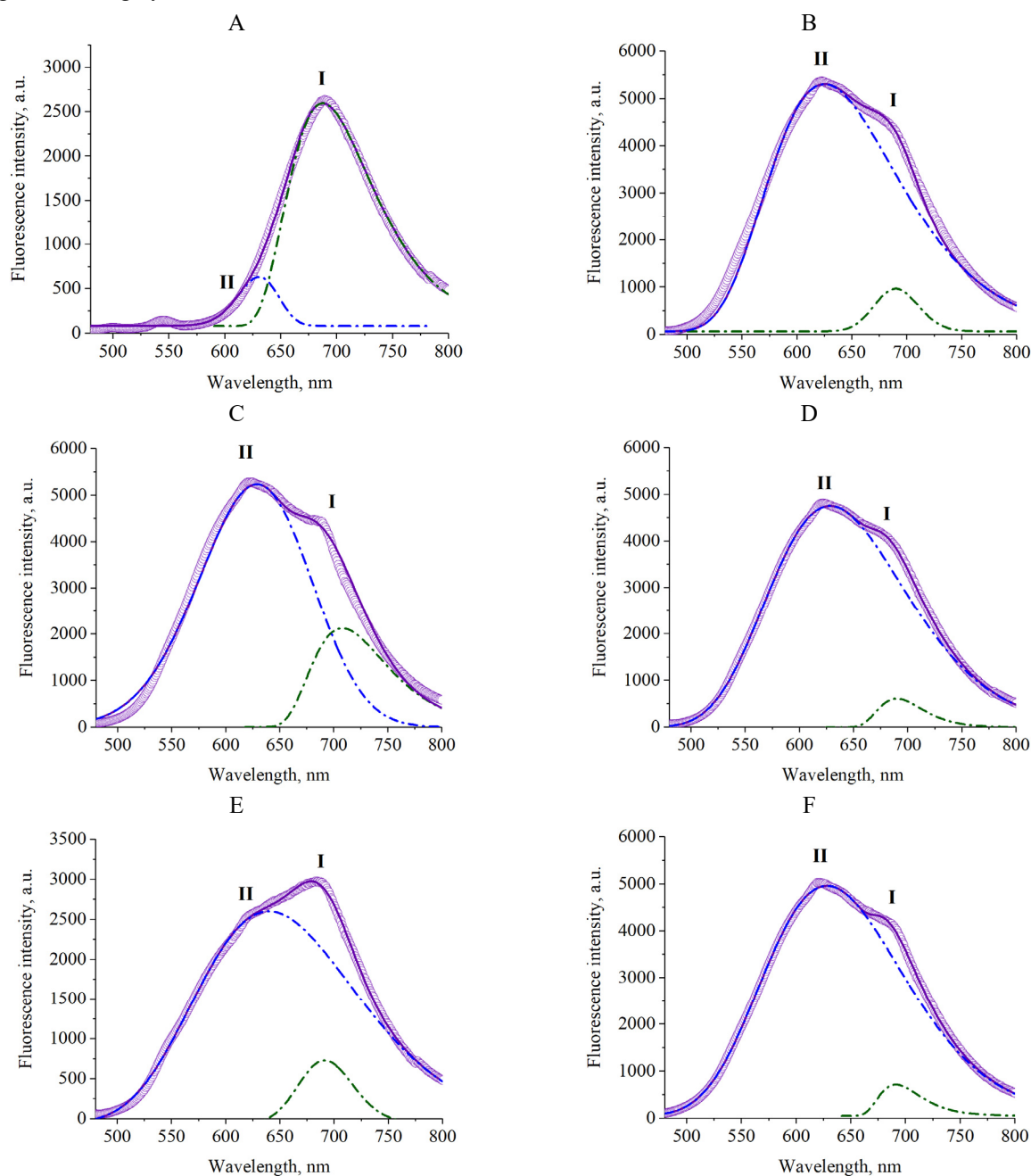


Figure 2. Deconvolution of ABM absorption spectra into two components in water (A), in the presence of 6.64 μM $\beta\text{-IgF}$ (B), ABM- $\beta\text{-IgF-Ni}$ system (C), ABM- $\beta\text{-IgF-Pb}$ system (D), ABM- $\beta\text{-IgF-Cu}$ system (E), ABM- $\beta\text{-IgF-Zn}$ system (F). Heavy metal concentration was 423 μM . Empty circles represent raw data. The solid line demonstrates the fitting of the experimental data by the asymmetric log-normal function

In the next phase of our study, we investigated the sensitivity of ABM to heavy metal ions in the presence of amyloid fibrils. Figure 2 illustrates the emission spectra of ABM in systems containing $\beta\text{-IgF}$ and heavy metals. When only $\beta\text{-IgF}$ is present, ABM shows a prominent emission peak at 560 nm along with a weaker shoulder around 690 nm. The addition of heavy metal ions altered the relative intensities of these bands in a metal-dependent manner. Specifically, the addition of Zn^{2+} , Ni^{2+} , and Pb^{2+} did not significantly change the overall shape of the emission spectra, whereas in the presence of Cu^{2+} , the 690 nm peak became dominant. To analyze the spectral behaviour of ABM in the combined amyloid-heavy metal systems, the dye's fluorescence spectra were decomposed using the log-normal (LN) function, which is well-suited for resolving asymmetric spectra [25]. It was found that the fluorescence spectra of ABM in water, in the presence of $\beta\text{-lactoglobulin}$ amyloid fibrils, and in the ABM- $\beta\text{-IgF}$ -heavy metal systems could be represented as a sum of two distinct

bands corresponding to short-wavelength and long-wavelength spectral components. From the deconvolution data, a set of parameters was obtained, including the amplitude and three shape descriptors: (i) the peak position, which reflects the polarity of the environment; (ii) the full width at half-maximum (FWHM); and (iii) the asymmetry parameter of the peak.

Table 1. Spectral characteristics of ABM in aqueous solution, β -lactoglobulin fibrils and β -IgF–metal systems

System	Band	A_{\max}	λ_c , cm ⁻¹	FWHM, cm ⁻¹	ρ , cm ⁻¹	R^2
ABM	I	2514.9	687.7	92.1	0.633	0.996
	II	551.7	630.8	43.3	1.152	
ABM_bLgF	I	903.5	690	47.2	0.950	0.999
	II	5240	625	142.3	0.708	
ABM_bLgF_Ni	I	2120	708	85	0.635	0.993
	II	5231.0	629	122.8	1.082	
ABM_bLgF_Pb	I	613.5	689.9	49.7	0.692	0.999
	II	4755.7	628.4	150.5	0.781	
ABM_bLgF_Cu	I	783.3	691.3	59.2	0.915	0.999
	II	2653.9	639.8	175.7	0.795	
ABM_bLgF_Zn	I	665.1	691.2	46.0	0.638	0.999
	II	4908.8	628.2	152.1	0.80	

As summarised in Table 1, the bathochromic band I (690 nm) dominates over the hypsochromic band II (630 nm) in aqueous ABM, whereas band II prevails in both ABM– β -IgF and ABM– β -IgF–metal systems. Upon addition of heavy metals, several characteristic changes were observed compared to ABM– β -IgF: (i) an increase in band I amplitude in the presence of Ni²⁺ and Cu²⁺, more pronounced for Ni²⁺; (ii) a slight decrease in band II amplitude for Zn²⁺ and Pb²⁺; and (iii) a 1.9-fold decrease in band II fluorescence intensity in the ABM– β -IgF–Cu²⁺ system. These spectral alterations were accompanied by broadening of band I (Ni²⁺ and Cu²⁺) and band II (Cu²⁺), as reflected in increased FWHM values, along with a rise in the asymmetry parameter of band II in the Cu²⁺ complex. The presence of heavy metals did not affect the position of the peaks, except for the band I of ABM_bLgF_Ni, where a slight long-wavelength shift was observed.

Overall, the results in Table 1 indicate that the addition of Ni²⁺ and Cu²⁺ influences the fluorescence response of fibril-bound ABM more strongly than other tested heavy metal ions. Given the highest fluorescence response of ABM in aqueous solution with Cu²⁺ and Zn²⁺, these findings suggest that both the dye's sensitivity to heavy metals and the interaction strength between heavy metals and amyloid fibrils are key factors in the spectral behaviour of the fibril-bound dye. Little is known about the mechanism of heavy metal ion interaction with β -lactoglobulin amyloid fibrils. However, Peydayesh et al. [21] demonstrated that adsorption of chromium, nickel, silver, and platinum to β -lactoglobulin amyloid fibrils is a highly exothermic and ion-specific process. Assuming that the accessibility of metal-binding sites for different ions in β -IgF varies, stronger binding of Cu²⁺ and Ni²⁺ to the fibrils can perturb the local environment of ABM, amplifying spectral shifts and intensity changes compared to Zn²⁺ and Pb²⁺. However, further studies are needed to elucidate the molecular mechanisms of metal–fibril binding and quantitatively assess binding affinities.

CONCLUSIONS

This study demonstrates the feasibility of using β -lactoglobulin amyloid fibrils in combination with the benzanthrone-based fluorescent dye ABM as a sensing platform for heavy metal ions, including Cu²⁺, Zn²⁺, Ni²⁺, and Pb²⁺. The results show that ABM exhibits distinct, metal-specific fluorescence responses in both aqueous solutions and fibril-bound environments. In particular, ABM undergoes pronounced spectral changes in aqueous solution upon binding Cu²⁺, Zn²⁺, Ni²⁺, and Pb²⁺, with Cu²⁺ and Zn²⁺ producing the most potent effects due to their preferential coordination to amino and carbonyl donor groups. The incorporation of ABM into β -lactoglobulin fibrils enhances dye fluorescence. It enables the selective modulation of emission signals upon metal binding, with Ni²⁺ and Cu²⁺ causing the most significant changes in spectral characteristics. Collectively, these results indicate that the fluorescence response of ABM reflects not only direct dye–metal binding but also the strength of metal interactions with amyloid fibrils. This dual sensitivity positions ABM as a promising optical probe for studying metal–protein interactions and for developing supramolecular platforms for heavy-metal sensing. Further studies are warranted to characterize the dye–fibril–metal complexation and expand its application to additional metal ions.

Acknowledgements

This work was supported by the Ministry of Education and Science of Ukraine (the project “Development of economically affordable nanosystems for rapid identification and purification of water from heavy metal ions based on carbon nanoallotropes and amyloids from organic waste” No. 0124U000968).

ORCID

Olga Zhytniakivska, <https://orcid.org/0000-0002-2068-5823>; Uliana Malovytsia, <https://orcid.org/0000-0002-7677-0779>

Kateryna Vus, <https://orcid.org/0000-0003-4738-4016>; Valeriya Trusova, <https://orcid.org/0000-0002-7087-071X>

Elena Kirilova, <https://orcid.org/0000-0002-9577-5612>; Galyna Gorbenko, <https://orcid.org/0000-0002-0954-5053>

REFERENCES

- [1] L. Järup, Br. Med. Bull. **68**, 167 (2003). <https://doi.org/10.1093/bmb/ldg032>
- [2] P. Zhang, M. Yang, J. Lan, Y. Huang, J. Zhang, et al. Toxics, **11**, 828 (2023). <https://doi.org/10.3390/toxics11100828>
- [3] J. Huff, R. Lunn, M. Waalkes, L. Tomatis, and P. Infante. Int. J. Occup. Environ. Health, **13**, 202 (2007). <https://doi.org/10.1179/oeh.2007.13.2.202>
- [4] F. Barbosa, F. Krug, and E.C. Lima. Spectrochimica Acta Part B: Atomic Spectroscopy, **54**(8), 1155 (1999). [https://doi.org/10.1016/S0584-8547\(99\)00055-5](https://doi.org/10.1016/S0584-8547(99)00055-5)
- [5] E.L. Silva, P. dos Santos Roldan, M.F. Giné. Journal of Hazardous Materials, **171**(1–3), 1133 (2009). <https://doi.org/10.1016/j.jhazmat.2009.06.127>
- [6] S. Fouziya Sulthana, U. Mohammed Iqbal, S.B. Suseela, et al., ACS Omega, **9**(24), 25493 (2024). <https://doi.org/10.1021/acsomega.4c00933>
- [7] R. Ding, Y.H. Cheong, A. Ahamed, G. Lisak. Anal. Chem. **93**, 4, 1880–1888 (2020) <https://doi.org/10.1021/acs.analchem.0c04247>
- [8] N. De Acha, C. Elosúa, J.M. Corres, and F.J. Arregui, Sensors, **19**, 599 (2019). <https://doi.org/10.3390/s19030599>
- [9] Y. Wen, F. Xing, S. He, S. Song, and L. Wang, Chem. Commun. **46**, 2596 (2010). <https://doi.org/10.1039/B924832C>
- [10] M. Zhou, J. Guo, and C. Yang, Sens. Actuators B Chem. **264**, 52 (2018). <https://doi.org/10.1016/j.snb.2018.02.119>
- [11] B. Rezaei, M. Shahshahanipour, A.A. Ensafi, and H. Farrokhpour, Sens. Actuators B Chem. **247**, 400 (2017). <https://doi.org/10.1016/j.snb.2017.03.082>
- [12] W.-B. Huang, W. Gu, H.-X. Huang, et al., Dye Pigment, **143**, 427 (2017). <https://doi.org/10.1016/j.dyepig.2017.05.001>
- [13] M. Saleem, and K.-H. Lee, J. Lumin. **145**, 843 (2014). <https://doi.org/10.1016/j.jlumin.2013.08.044>
- [14] X. Yang, W. Zeng, L. Wang, et al., RSC Adv. **4**, 22613 (2014). <https://doi.org/10.1039/C4RA02738H>
- [15] Y. Han, C. Yang, K. Wu, and Y. Chen. RSC Adv. **5**, 16723 (2015). <https://doi.org/10.1039/C4RA16479B>
- [16] A. Majhi, K. Venkateswarlu, and P. Sasikumar, J. Fluoresc. **34**, 1453 (2024). <https://doi.org/10.1007/s10895-023-03372-3>
- [17] J. Liu, D. Su, J. Yao, Y. Huang, J. Shao, and X. Chen, J. Mater. Chem. A, **5**, 4163 (2017). <https://doi.org/10.1039/C6TA10814H>
- [18] X. Yu, W. Liu, X. Deng, S. Yan, and Z. Su, Chemical Engineering Journal, **335**, 176 (2017). <https://doi.org/10.1016/j.ccej.2017.10.148>
- [19] J. Kostal, A. Mulchandani, and W. Chen, Macromolecules, **34**(7), 2257 (2001). <https://doi.org/10.1021/ma001973m>
- [20] S. Bolisetty, and R. Mezzenga, Nat. Nanotechnol. **11**, 365 (2016). <https://doi.org/10.1038/nnano.2015.310>
- [21] M. Peydayesh, S. Bolisetty, T. Mohammadi, and R. Mezzenga, Langmuir, **35**, 4161 (2019). <https://doi.org/10.1021/acs.langmuir.8b04234>
- [22] L.C. Ramírez-Rodríguez, L.E. Díaz Barrera, M.X. Quintanilla-Carvajal, et al., Membranes, **10**, 386 (2020). <https://doi.org/10.3390/membranes10120386>
- [23] E.M. Kirilova, I. Kalnina, G.K. Kirilov, and I. Meirovics, J. Fluoresc. **18**, 645 (2008). <https://doi.org/10.1007/s10895-008-0340-3>
- [24] M. Groenning, J. Chem. Biol. **3**, 1 (2010). <https://doi.org/10.1007/s12154-009-0027-5>
- [25] M. Bacalum, B. Zorila, and M. Radu. Anal Biochem. **440**, 123 (2013). <https://doi.org/10.1016/j.ab.2013.05.031>
- [26] G. Gorbenco, V. Trusova, E. Kirilova, et al., Chem. Phys. Lett. **495**, 275 (2010). <https://doi.org/10.1016/j.cplett.2010.07.005>
- [27] Z. Yan, Y. Cai, J. Zhang, Y. Zhao, et al., Measurements, **187**, 110355 (2022). <https://doi.org/10.1016/j.measure.2021.110355>

ФЛУОРЕСЦЕНТНЕ ДЕТЕКТУВАННЯ ІОНІВ ВАЖКИХ МЕТАЛІВ ЗА ДОПОМОГОЮ
БЕНЗАНТРОНОВОГО БАРВНИКА

У. Маловиця^а, О. Житняківська^а, К. Сльцов^а, К. Вус^а, В. Трусова^а, Е. Кірілова^б, Г. Горбенко^а

^аКафедра медичної фізики та біомедичних нанотехнологій, Харківський національний університет імені В.Н. Каразіна
м. Свободи 4, Харків, 61022, Україна

^бКафедра прикладної хімії, Інститут наук про життя та технологій, Даугавпільський університет, LV-5401 Даугавпілс, Латвія

Розробка чутливих, недорогих та біосумісних сенсорів для виявлення токсичних важких металів залишається актуальним завданням у сфері екологічного моніторингу. Наноструктури на основі білків надають унікальні можливості для створення таких сенсорів. Поєднання амілоїдних фібрил з амілоїд-чутливими флуоресцентними барвниками, які демонструють характерні спектральні зміни при взаємодії з амілоїдними структурами та іонами металів, може створити перспективну сенсорну платформу. В даній роботі досліджено чутливість бензантронного зонда АВМ до іонів важких металів у водних розчинах та у присутності амілоїдних фібрил β-лактоглобуліну (β-IgF). У воді зонд характеризується спектром випромінювання з домінуючим піком при 690 нм. Зв'язування з β-IgF спричиняє значне збільшення інтенсивності флуоресценції та ~ 65 нм гіпсохромний зсув положення максимуму, що вказує на перехід барвника у гідрофобне середовище фібрил. У водних розчинах АВМ реагує на важкі метали характерними спектральними змінами: Pb²⁺ та Ni²⁺ зменшують смугу випромінювання при 690 нм та формують смугу при 560 нм, тоді як Cu²⁺ та Zn²⁺ повністю гасять флуоресценцію при 690 нм, що супроводжується утворенням максимум на 560 нм, що, найбільш імовірно, є наслідком утворення комплексів переносу заряду метал–ліганд. У присутності амілоїдних фібрил АВМ має широкий спектр флуоресценції з максимумом на 560 нм. Додавання важких металів модулює інтенсивність і форму цієї смуги в іон-специфічний спосіб. Деконволюція спектрів випромінювання показала наявність двох спектральних компонентів, амплітуди та характеристики яких змінювались під дією Ni²⁺ та Cu²⁺, тоді як Zn²⁺ та Pb²⁺ мали менший вплив. Ці результати демонструють, що флуоресценція АВМ чутливо відображає специфічність взаємодії важких металів з амілоїдними фібрилами, підтверджуючи його потенціал як оптичного сенсора для вивчення систем «білок–метал».

Ключові слова: бензантронні барвники; детекція металів; важкі метали